Assessing the kinematics and subsurface geometry of the central Nepal Himalayas: Insights from thermokinematic modeling

by

Suryodoy Ghoshal

B.Sc. - Geology, University of Calcutta, 2012

M.Sc. – Applied Geology, Indian Institute of Technology - Bombay, 2014

Submitted to the Graduate Faculty of the

Dietrich School of Arts and Sciences in partial fulfillment

of the requirements for the degree of

Doctor of Philosophy

University of Pittsburgh

2021

UNIVERSITY OF PITTSBURGH

DIETRICH SCHOOL OF ARTS AND SCIENCES

This dissertation was presented

by

Suryodoy Ghoshal

It was defended on

May 3, 2021

and approved by

Dr. Todd Ehlers, Professor, Geosciences,
University of Tübingen

Dr. Charles E. Jones, Senior Lecturer, Geology and Environmental Sciences

Dr. Brian Stewart, Associate Professor, Geology and Environmental Sciences

Dr. Eitan Shelef, Assistant Professor, Geology and Environmental Sciences

Thesis Advisor/Dissertation Director: Dr. Nadine McQuarrie Professor, Geology and Environmental Sciences

Copyright © by Suryodoy Ghoshal

2021

Assessing the kinematics and subsurface geometry of the central Nepal Himalayas: Insights from thermokinematic modeling

Suryodoy Ghoshal, PhD

University of Pittsburgh, 2021

We couple detailed, sequentially forward modeled balanced cross-sections through the central Nepal Himalaya, including flexural isostasy and erosion with a thermokinematic model (PECUBE) to provide insight into the geometry of the Main Himalayan thrust (MHT), and its structural and thermal evolution. These models are constrained by new and existing geologic mapping at the surface and a large, high-resolution dataset of thermochronological ages. Our modeling shows that the location and temporal evolution of ramps exert a first-order control on the distribution of cooling ages, and that this can be used to invalidate proposed models for the subsurface in the Himalaya. We also show how the location, geometry and rates of uplift and exhumation in the Himalaya has responded to increases in the strength of the south Asian monsoon over time. We highlight the importance of out-of-sequence faulting on the distribution of cooling ages at the surface, and its effect on topography. Finally, combining the individual 2D kinematic models allows us to create a 3D kinematic model of central Nepal, and assess whether mapped changes in geology, and cooling ages are the result of along-strike changes in the geometry of the modern MHT ramp, or due to critical changes in the geometry of the MHT in the past.

Table of contents

Title Page i

Committee Page ii

Abstract iv

Table of contents v

List of tables xi

List of figures xii

1.0 Introduction 1

2.0 Constraining central Himalayan (Nepal) fault geometry through integrated thermochronology and thermokinematic modeling 4

2.1 Introduction 4

2.2 Geologic background 10

2.2.1 Tectonostratigraphy 11

2.2.1.1 Subhimalaya 11

2.2.1.2 Lesser Himalaya 11

2.2.1.3 Greater Himalaya 13

2.2.2 Gorkha earthquake and MHT geometries 15

2.3 Thermochronology 17

2.3.1 Muscovite $^{40}Ar/^{39}Ar$ data 18

2.3.1.1 Distribution of detrital muscovites 19

2.3.1.2 Zircon (U-Th)/He data 20

2.3.1.3 Apatite Fission Track (AFT) data 21

2.4 Cross sections and modeling 23

2.4.1 Balanced cross sections 23

2.4.2 Kinematic and flexural modeling 28

2.4.2.1 Kinematic sequence 31

2.4.3 Thermokinematic modeling and results 34

2.4.3.1 Effect of ramp angle on cooling ages 37

2.4.3.2 Effect of duplex geometry on cooling ages 38

2.4.3.3 Effect of décollement geometry on cooling ages 46

2.4.4 Velocity analysis 50

2.4.5 Effect of out-of-sequence thrusting 53

2.5 Discussion 54

2.5.1 Sensitivity of cooling ages to subsurface geometry 54

2.5.1.1 Duplex geometry 54

2.5.1.2 Décollement geometry 57

2.5.2 Thermal structure 62

2.5.3 Age of initiation vs. rate of motion 65

2.5.4 Out-of-sequence thrusting 66

2.6 Conclusions 67

2.7 Acknowledgements 68

2.8 Supplementary information 69

2.8.1 Geologic mapping 71

2.8.1.1 Siwalik Group/Subhimalaya 73

2.8.1.2 Lesser Himalaya 74

2.8.1.3 Greater Himalaya 77

2.8.2 Thermochronology 80

2.8.2.1 $^{40}Ar/^{39}Ar$ analysis 80

2.8.2.2 Zircon (U-Th)/He analysis 82

2.8.3 Sensitivity of ages to ramp location, ramp angle, heat production and velocity 86

2.8.3.1 Effect of geometry vs. heat production and velocity 88

2.8.3.2 Effects of e-folding depth 92

2.8.4 Data fitting 96

2.9 References 102

3.0 Erosional controls on the architecture and kinematics of the Himalaya: Insights from thermokinematic modeling 120

3.1 Introduction 120

3.2 Geologic background 126

3.2.1 Tectonostratigraphy 127

3.2.1.1 Subhimalayas 127

3.2.1.2 Lesser Himalayas 127

3.2.1.3 Greater Himalaya 129

3.2.1.4 Tethyan Himalaya 130

3.3 Thermochronology 133

3.4 Methods 135

3.4.1 Balanced cross-section 135

3.4.2 Kinematic and Flexural modeling 136

3.4.3 Thermokinematic modeling 138

3.5 Results..... 140

3.5.1 Balanced cross-section 140

3.5.1.1 Structural zones 140

3.5.2 Predicted cooling ages.....145

3.5.2.1 Effect of constant shortening rates..... 145

3.5.2.2 Effect of incision..... 148

3.5.2.3 Effect of out-of-sequence thrusting 150

3.5.2.4 Effect of variable shortening rates 152

3.6 Discussion 154

3.6.1 Out-of-sequence thrusting and topography.....154

3.6.2 Exhumation rates in the Marsyangdi valley.....158

3.6.3 South Asian monsoon and potential tectonic response.....160

3.7 Conclusions 162

3.8 Supplementary information 163

3.9 References 165

4.0 Assessing the geometry of the Main Himalayan thrust in central Nepal: Insights from thermokinematic modeling 181

4.1 Introduction 181

4.2 Geologic setting..... 186

4.2.1 Tectonostratigraphy of the Daraundi valley.....186

4.2.1.1 Subhimalayas 186

4.2.1.2 Lesser Himalayas 187

4.2.2 Greater Himalayas **188**

4.3 Thermochronology **191**

4.3.1 Spatial distribution of cooling ages **192**

4.3.2 Thermochronology of the Daraundi valley **193**

4.4 Methods **195**

4.4.1 Balanced cross-section **195**

4.4.2 Kinematic and flexural modeling **196**

4.4.3 Thermokinematic modeling **198**

4.5 Results **201**

4.5.1 Along-strike variations in surface geology **201**

4.5.2 Balanced cross-section along the Daraundi valley **203**

4.5.2.1 Structural zones **203**

4.5.3 Predicted cooling ages **208**

4.6 Discussion **214**

4.6.1 Kinematic evolution of the central Nepal Himalayas **214**

4.6.2 Controls/drivers of along-strike changes of upper plate geometry **221**

4.6.3 Lateral changes in the geometry of the MHT **224**

4.7 Conclusions **225**

4.8 Supplementary information **226**

4.8.1 Geologic mapping **226**

4.8.2 Satellite-assisted mapping **228**

4.8.3 Kriging **229**

4.9 References **233**

Appendix A Mapping data **247**

Appendix B Muscovite $^{40}Ar/^{39}Ar$ (Mar) ages **255**

Appendix C Zircon Fission Track (ZFT) ages **261**

Appendix D Zircon (U-Th)/He (ZHe) ages **262**

Appendix E Apatite Fission Track (AFT) ages **264**

List of tables

Table 2.1: Sample locations and cooling ages from central Nepal 17

Table 2.2: Model geologic and flexural parameters, along with initiation times for major structures at long-term constant rates. 28

Table 2.3: Mechanical and thermal parameters for PECUBE 32

Table 2.4: Velocity profiles for the hinterland-dipping model based on the Whipple et al. (2016) décollement geometry 48

Table 2.5: Model statistics 101

Table 3.1: Mechanical and thermal properties for PECUBE 140

Table 3.2: Velocity profiles for final OOS models 153

Table 4.1: Mechanical and thermal parameters for PECUBE 198

Table 4.2: Velocity profiles for final models along the Daraundi..... 207

List of figures

Figure 2.1: Geologic map of the Kathmandu region of central Nepal 9

Figure 2.2: Cross-sectional projection of data along the Budhi Gandaki transect. 14

Figure 2.3: Comparison between new cross-sectional geometries. 22

Figure 2.4: Structural and thermochronologic evolution of the hinterland- and foreland-dipping cross-sections 30

Figure 2.5: Plots comparing thermochronometric ages predicted by the hinterland-dipping and foreland-dipping duplexes. 33

Figure 2.6: Plot comparing thermochronometric ages predicted by the hinterland-dipping and foreland-dipping duplexes using the best-fit thermal parameters for the geometry. 37

Figure 2.7: Predicted MAr, ZHe, and AFT ages compared to measured data for the cross section proposed by Hubbard et al. (2016). 43

Figure 2.8: Predicted MAr, ZHe, and AFT ages compared to measured data for geometry based on the Elliott et al. (2016) décollement. 45

Figure 2.9: Plots comparing the best-fit predicted ages for the Whipple et al., 2016 geometry and that of the Elliott et al. (2016). 46

Figure 2.10: Effects of variable velocities and out-of-sequence motion on the predicted cooling ages. 49

Figure 2.11: Comparison between predicted and measured Peak temperature and pressure. 60

Figure 2.12: Comparison between the predicted thermal field, cross section geometry, and location of high-frequency seismic sources, the Gorkha Earthquake, and the modeled transition zone between creeping and locked portions of the MHT (Ader et al., 2012). 61

Figure 2.13: Geological map of central Nepal, showing detailed mapping from the region.70

Figure 2.14: Outcrop photographs from mapping along Budhi Gandaki and Trishuli valleys in central Nepal. 72

Figure 2.15: Data projected along the Trishuli section line. 79

Figure 2.16: $^{40}Ar/^{39}Ar$ age spectra 80

Figure 2.17: Map of estimated drainage basins for detrital MAr samples (yellow diamonds) from Wobus et al. (2006). 84

Figure 2.18: Restored cross-sectional geometries. 85

Figure 2.19: Comparison between a constant crustal heat production and an e-folding depth. 87

Figure 2.20: Effect of changing ramp angle, crustal heat production and velocity on cooling ages. 91

Figure 2.21: Statistical comparisons between modeled and measured MAr, ZHe and AFT ages respectively. 95

Figure 2.22: Changes in shortening rate with time for models shown in Figure 2.10A. 96

Figure 2.23: Comparison between different velocity profiles tested for the Hinterland-dipping duplex based on the Elliott et al., 2016 decollement geometry. 99

Figure 2.24: Comparison between different velocity profiles tested for the Foreland-dipping duplex based on the Whipple et al., 2016 decollement geometry. 100

Figure 2.25: Effect of OOS thrusting on cooling ages using a constant velocity (red). 101

Figure 3.1: Plots of monsoon proxies through time. 125

Figure 3.2: Geological map along the Marsyangdi transect of central Nepal. 131

Figure 3.3: Plots of projected data along the Marsyangdi transect. 132

Figure 3.4: Structural and thermochronologic evolution of the Marsyangdi cross-section. 145

Figure 3.5: Predicted cooling ages using a constant velocity of 21 mm/yr. and an A_0 value of 2.00 μW m^{-3}. 145

Figure 3.6: Effect of incision on modeled topography and predicted cooling ages. 148

Figure 3.7: Plots showing the effect of out-of-sequence thrusting on the predicted cooling ages. 150

Figure 3.8: Plots showing the effect of variable rates of thrusting on the predicted cooling ages. 152

Figure 3.9: Plots showing the effect of out-of-sequence thrusting on modeled topography. 154

Figure 3.10: Plot of measured exhumation rates through time (starting at 23 Ma) for rocks exposed at the surface in the model. 158

Figure 3.11: Restored cross-section geometry for the Marsyangdi transect 164

Figure 4.1: Geologic map of central Nepal. 186

Figure 4.2: Predictive cooling age maps of central Nepal. 191

Figure 4.3: Plots of projected data along the Daraundi transect. 193

Figure 4.4: Plots comparing best-fit predicted cooling ages to measured data. 200

Figure 4.5: Evolution of the central Nepal Himalayas through time, showing predicted cooling ages for each transect. 213

Figure 4.6: Thermal evolution of the Daraundi transect. 218

Figure 4.7: Thermal evolution of the Marsyangdi transect. 219

Figure 4.8: Thermal evolution of the Budhi Gandaki transect. 220

Figure 4.9: Restored cross-section geometry for the Daraundi transect 231

Figure 4.10: Integration of new geologic mapping with remote sensing. 232

1.0 Introduction

In 2015, the Mw 7.8 Gorkha EQ ruptured on the Main Himalayan thrust (MHT) in central Nepal, causing major devastation and loss of life (USGS, 2015). The earthquake nucleated ~80 km WNW of the capital Kathmandu, with the rupture propagating eastwards over a 150 km-long segment, interpreted to be part of the flat of the MHT (Avouac *et al.*, 2015; USGS, 2015). While the geometry of the MHT in central Nepal is broadly known to be a gently-dipping plane that increases in depth towards the north and includes a steeper-dipping ramp underneath the high Himalaya, the details are disputed, including how it varies laterally in space (Herman *et al.*, 2010; Khanal and Robinson, 2013; Avouac *et al.*, 2015; Elliott *et al.*, 2016; Hubbard *et al.*, 2016; Whipple *et al.*, 2016). After the earthquake, InSAR and GPS data from the rupture allowed for new quantitative estimates for the geometry of the MHT in central Nepal (Elliott *et al.*, 2016; Hubbard *et al.*, 2016; Qiu *et al.*, 2016; Whipple *et al.*, 2016) along with models for how it changes from east to west. These lateral changes in geometry were proposed to have restricted the propagation of the rupture (Hubbard *et al.*, 2016; Mugnier *et al.*, 2017). We use new mapping in the region, and a large, high-resolution dataset of thermochronological cooling ages to model the age and rates of deformation of major thrust sheets in central Nepal and extract detailed exhumation histories for the rocks. This allows us to assess and propose best-fit 2D geometries for the MHT along the Budhi Gandaki, Marsyangdi and Daraundi river valleys in central Nepal. In addition, connecting exhumation and structural deformation allows us to quantify the importance of recent out-of-sequence faulting, a mechanism that has been proposed as one of the primary drivers of uplift in the Himalaya. Finally, we propose a new 3D kinematic model for the central Nepal Himalaya that shows how the lateral changes in geology and the distribution of cooling ages

at the surface are not the result of variations in the geometry of the modern MHT ramp, but rather a critical change in the geometry of the MHT in the late Miocene.

In the Kathmandu region, our research focuses on using the relationship between ramps, exhumation and thermochronological cooling ages to assess the geometry of the MHT, and the temporal and kinematic evolution of the overlying duplex. Using a thermokinematic model, we evaluate four possible cross-sectional geometries, based on three new estimates for the MHT in central Nepal (e.g., Elliott et al., 2016; Hubbard et al., 2016; Whipple et al., 2016). To assess these geometries, we created three new balanced cross-sections constrained by the mapped geology at the surface and the newly proposed estimates for the MHT as the décollement. The restored sections are then sequentially deformed, flexurally loaded and eroded, with the motion tracked using a grid of points. This sequence of grids is used by PECUBE to recreate the time-temperature paths for these rocks and predict cooling ages at the surface (Braun, 2003; Ehlers *et al.*, 2005). With exhumation focused at ramps (Lock and Willett, 2008; McQuarrie and Ehlers, 2015), we can use the predicted cooling ages to locate and track the timing of the exhumation. This method allows us to separate the evolution of the duplex from that of the modern MHT ramp and assess the relative roles that they play in producing the distribution of cooling ages at the surface. The degrees of fit between the measured and predicted cooling ages allows us to identify the combination of duplex and décollement geometry that is best able to reproduce the distribution of cooling ages at the surface and invalidate proposed geometries that are unsuccessful.

In the Marsyangdi valley, we extend this method to identify the best-fit subsurface geometry, and its temporal evolution to assess whether the location or mechanism of active uplift changes in response to climate-modulated erosion. To address this, we created a new balanced cross-section through the Marsyangdi valley. Combining this forward-modeled this cross-section

with the thermokinematic model allowed us to evaluate how exhumation has varied through time, and how these changes have affected the cooling history of the rocks. We compare the resulting predicted cooling ages to existing measured ages to identify the best-fit geometry and its kinematic history. This kinematic sequence allows us to evaluate how drivers of uplift and exhumation have changed through time and assess the importance of out-of-sequence thrusting on the distribution of cooling ages as well as its effect on topography. In addition, we quantify the rates at which exhumation occurs in our model and compare the periods of fast exhumation to proposed windows of enhanced monsoon precipitation. This allows us to evaluate whether changes in the behavior of faulting in the Himalaya (e.g., increasing rates of uplift over active ramps or out-of-sequence motion in the hinterland) occurs in response to periods of stronger erosional exhumation driven by the monsoon.

Finally, in the Daraundi valley, we create a third cross-section, and combine it with the best-fit models for the Budhi Gandaki and Marsyangdi to create a 3D kinematic model of the central Nepal Himalaya. We use this 3D model to explore the formation of a mapped southward step in surface geology and a corresponding offset in the distribution of reset MAr ages and assess whether they are the result of variations in the geometry of the modern MHT ramp, or due to critical changes in the geometry of the MHT in the past. This also allows us to evaluate whether a major lateral structure exists in the MHT that may have been responsible for restricting the propagation of the Gorkha earthquake towards the west. Finally, we evaluate the geometry and timing of out-of-sequence thrusting across the region, and its relationship to the MHT.

2.0 Constraining central Himalayan (Nepal) fault geometry through integrated thermochronology and thermokinematic modeling

2.1 Introduction

Constraining the subsurface structural geometry of the central Himalaya continues to prove difficult, even after the 2015 Gorkha earthquake and the resulting insights into the trajectory of the Main Himalayan thrust (MHT). To this end, we apply a thermokinematic model to evaluate four possible balanced cross section geometries based on three estimates of the MHT in central Nepal. We compare the effect of different décollement and duplex geometries on predicted cooling ages and compare these to new and published ages. We find that the best-fit geometry able to reproduce the cooling ages at the surface is a hinterland-dipping duplex, which has been translated over a mid-crustal ramp located ~110 km north of the Main Frontal thrust. We find that the temporal evolution of the duplex and MHT mid-crustal ramp both play an integral role in producing the observed cooling ages, implying that the common assumption that the active décollement and ramp geometry solely control the distribution of cooling ages is incorrect. Furthermore, results indicate that the Ramgarh-Munsiari thrust was emplaced between 17 and ~10 Ma, followed by the Trishuli thrust. Duplex growth occurs between 6.5 Ma and 0.75 Ma, with its constituent thrust sheets moving at variable rates between 10 – 42 mm/yr. Young out-of-sequence thrusting (5 km of displacement) in the hinterland produces a slightly improved fit to the cooling ages. Finally, the resulting thermal field modeled from our best-fit geometry suggests a possible basis for the nucleation and rupture characteristics of the Gorkha earthquake.

Thermochronometer cooling ages measured at the surface of compressional orogens are a function of the thermal history of rocks from their burial to exhumation. This thermal history is fundamentally influenced by the geometry and location of ramps in the active décollement over time. The size and angle of ramps control the magnitude of burial that the rocks underlying the fault experience, as well as the amount and location of rock uplift and resulting exhumation of the overriding thrust sheet. Ramps therefore, are a primary control on the distribution of cooling ages (e.g., Shi and Wang, 1987; Ruppel and Hodges, 1994; Rahn and Grasemann, 1999; Huntington et al., 2007; Lock and Willett, 2008; Robert et al., 2011; McQuarrie and Ehlers, 2017). Because of the first-order control that ramps impart to thermochronometer cooling ages, the along-strike distribution of cooling ages may be used to test a proposed ramp location, geometry and evolution with time (Lock and Willett, 2008; Herman *et al.*, 2010; Robert *et al.*, 2011; Coutand *et al.*, 2014; Rak, McQuarrie and Ehlers, 2017; Gilmore *et al.*, 2018). Geologic cross sections have long been a tool for projecting mapped relationships of rocks, folds, and faults into potential subsurface geometries that could produce the mapped patterns seen in the Himalaya (Gansser, 1964; Fuchs, 1980), Alps (Argand, 1916; Trümpy, 1980; Marchant, 1993) and the North American Cordillera (Bally, Gordy and Stewart, 1966; Price, 1981; Bally, 1984). Balanced cross sections, grew from the need to evaluate the plausibility of these proposed subsurface geometries (Bally, Gordy and Stewart, 1966; Dahlstrom, 1969; Boyer and Elliott, 1982) and require cross sections to be restored to an undeformed state (Elliott, 1983). A balanced section eliminates a suite of proposed subsurface geometries that are geologically not possible (e.g., Woodward et al., 1989); however, the same surface and subsurface data may have several different solutions, all of which allow restoration and are admissible (e.g., Boyer and Elliott, 1982; Woodward et al., 1989). The most nonunique components to a balanced cross section are the geometry of subsurface faults, and the

kinematics (or sequence) of faulting. Although nonunique, a balanced cross section presents a hypothesis for how a ramp's geometry, magnitude, and location change through time to produce the surface geology. The sensitivity of the across-strike distribution of a suite of thermochronometer samples to these same metrics (ramp geometry, magnitude, and location) provides another dataset to test the hypothesized cross section geometry against (i.e., can the geometry and resulting kinematic evolution reproduce the measured cooling ages?). The dataset becomes especially powerful if we can invalidate proposed cross section geometries because the resulting thermal histories do not produce the measured cooling ages.

Ongoing debates regarding the subsurface geometry in central Nepal (Lavé and Avouac, 2001; Pearson, 2002; Wobus, Hodges and Whipple, 2003; Pearson and DeCelles, 2005; Wobus, Whipple and Hodges, 2006; Herman *et al.*, 2010; Khanal and Robinson, 2013; Elliott *et al.*, 2016; Hubbard *et al.*, 2016; Whipple *et al.*, 2016) make it an ideal setting to test this hypothesis. The first-order geometry of the central Nepal Himalaya has the ~70 km wavelength Gorkha-Pokhara antiform that exposes Lesser Himalayan rocks and separates two regions where Greater Himalayan rocks are exposed, the Kathmandu synform to the south and the high Himalaya to the north (Gansser, 1964; Fuchs, 1980; Stöcklin, 1980) (Figure 2.1). This configuration strongly suggests a duplex at depth, as illustrated by all published cross sections (Pandey *et al.*, 1995; Lavé and Avouac, 2001; Pearson, 2002; Avouac, 2003; Robinson *et al.*, 2003; Khanal and Robinson, 2013). While there is consensus regarding the existence of a duplex in central Nepal, the rocks exposed at the surface are carried by the roof thrust of the duplex. Thus, the duplex geometry (e.g., foreland-dipping vs. hinterland-dipping vs. antiformal stack), the stratigraphic units and the resulting stratigraphic thickness carried by repeating thrust faults are unknown. Duplexes form when ramps sequentially develop between lower (floor thrust) and upper (roof thrust) detachment surfaces

(Boyer and Elliott, 1982; Mitra, 1986). Therefore, the duplex cooling history should reflect both the magnitude and sequential development of these ramps (Lock and Willett, 2008; McQuarrie and Ehlers, 2017). In addition to the presence of a duplex to account for the Gorkha-Pokhara antiform, all published cross sections through central Nepal show a 10-15 km ramp in the Main Himalayan thrust (MHT). Although the presence of the ramp is ubiquitous in these models, the proposed location ranges from the southern edge of the antiform (Pearson, 2002; Robinson *et al.*, 2003; Pearson and DeCelles, 2005; Khanal and Robinson, 2013), through the center of the antiform (Pandey *et al.*, 1995; Lavé and Avouac, 2001; Herman *et al.*, 2010), to the northern limb of the antiform (Elliott *et al.*, 2016; Hubbard *et al.*, 2016). In addition, the existence of a major mid-crustal ramp has been argued as necessary to sustain the topography of the high Himalaya (Seeber and Armbruster, 1981; Ni and Barazangi, 1984; Lyon-Caen and Molnar, 1985; Pandey *et al.*, 1995).

The location, depth and propagation of the 2015 Gorkha earthquake illuminated the ruptured MHT and required the mid-crustal ramp to be located significantly farther north (15 – 45 km) than previously thought, automatically invalidating a number of previous estimates for the subsurface (Pearson, 2002; Herman *et al.*, 2010; Khanal and Robinson, 2013) and narrowing the permissible range for a valid geometry. However, even with the added hypocentral, InSAR and GPS data from the earthquake, different interpretations for the MHT geometry and ramp locations remain due to uncertainties in locating the rupture plane in the vertical direction and the sensitivity of the solutions to the location of the crustal ramp north of the earthquake rupture (Elliott *et al.*, 2016; Hubbard *et al.*, 2016; Whipple *et al.*, 2016). In addition to questions regarding the shape of the active décollement, the duplex geometry itself is unknown.

We propose that the relationship between ramps, exhumation, and mineral cooling ages can be exploited to further constrain both the geometry of the MHT and the geometry of the overlying duplex in central Nepal. A large, well-distributed dataset of thermochronological ages (Hubbard and Harrison, 1989; Copeland *et al.*, 1991; Wobus, Hodges and Whipple, 2003; Herman *et al.*, 2010; Robert *et al.*, 2011) is available through this part of central Nepal (Figures 2-1 and 2-2a). We augment this dataset with 25 new cooling ages to extend the spatial coverage and maximize the resolution of available thermochronometers (see Appendices for full list). We show a suite of balanced cross sections that incorporate proposed geometries for the MHT (Elliott *et al.*, 2016; Hubbard *et al.*, 2016; Whipple *et al.*, 2016), complete with end-member duplex geometries. The new cross sections presented here follow the Budhi Gandaki valley in central Nepal (Figure 2.1; A-A'), 40 km west of an existing cross section along the Trishuli River valley (Hubbard *et al.*, 2016) that we also evaluate (Figure 2.1; B-B'). Each section was forward modeled and used as input into the thermokinematic model (PECUBE; Braun, 2003) using the modified version presented in Whipp et al., (2009) and McQuarrie and Ehlers (2015) to predict thermochronological ages. The predicted ages are compared to measured cooling ages. Quantifying the relationship between the different structural drivers of uplift-driven exhumation (i.e., mid-crustal ramps, duplex formation, and out-of-sequence thrusting) and their resulting patterns of exhumation, allows us to assess if a robust dataset of cooling ages can be used to invalidate different proposed cross section models to gain a fuller understanding of the modern fault geometry and fault evolution of the central Nepal Himalaya.

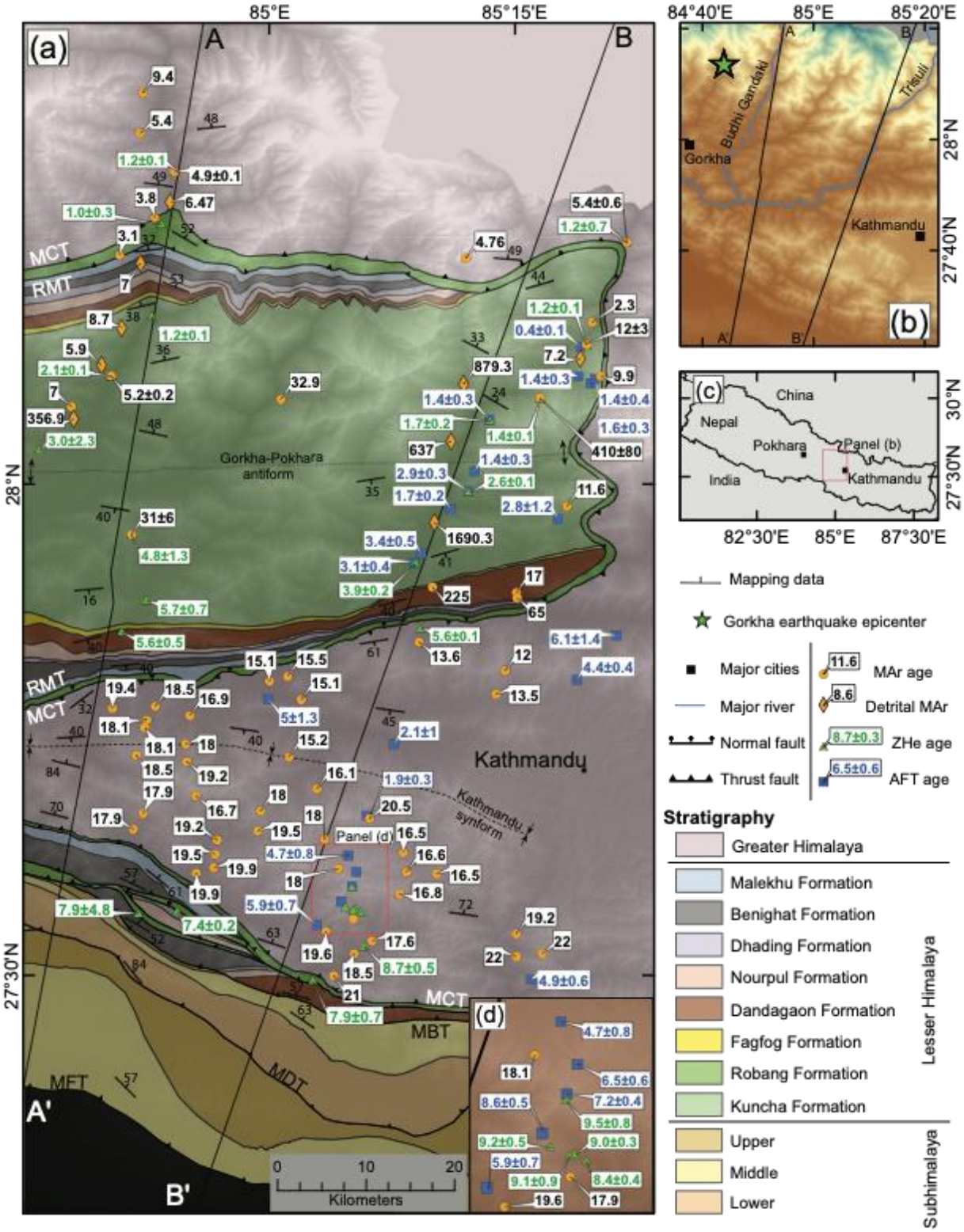

Figure 2.1: Geologic map of the Kathmandu region of central Nepal

(a) Geologic map of the Kathmandu region of central Nepal showing the distribution of measured MAr (black text), ZHe (green text), and AFT (blue text) thermochronological ages. The detrital MAr samples (yellow diamonds) show the first-quartile age (Wobus, Whipple and Hodges, 2006). Geology shown is based on new mapping in the region, combined with past mapping from Lavé and Avouac (2000); Pearson (2002); Khanal and Robinson (2013). (b) Regional map of central Nepal showing the location of the epicenter of the Gorkha earthquake (green star), and the two main rivers (blue). The two cross section lines (A-A' and B-B') are shown in black. The topography shown in panels (a) and (b) are from an SRTM DEM of Nepal. (c) Inset map showing the position of the field area in Nepal.

2.2 Geologic background

The Himalaya formed as a result of the collision between the Indian and Asian Plates that occurred ~58 Ma (Garzanti, Baud and Mascle, 1987; DeCelles *et al.*, 2014; Orme, Carrapa and Kapp, 2015; Hu *et al.*, 2016). The ongoing collision moves India towards the Tibetan Plateau at a rate of ~2.0 cm/yr, with most of the convergence accommodated along the MHT (Bilham *et al.*, 1997; Lavé and Avouac, 2000; Jouanne *et al.*, 2004; Bettinelli *et al.*, 2006; Ader *et al.*, 2012). The collision has led to the translation of India-derived sedimentary and metasedimentary rocks southwards relative to the Indian Plate along major thrust faults and shear zones, dividing the resulting orogen into four tectonostratigraphic zones, which are from south to north, the Subhimalaya, Lesser Himalaya, Greater Himalaya, and the Tethyan Himalaya.

2.2.1 Tectonostratigraphy

2.2.1.1 Subhimalaya

The Subhimalaya are composed of the Siwalik Group and represent the most recent foreland basin sediments deposited from the growing and eroding thrust belt to the north (Gansser, 1964; Tokuoka *et al.*, 1986; Harrison *et al.*, 1993; Quade *et al.*, 1995; Burbank, Beck and Mulder, 1996; DeCelles *et al.*, 1998; Gautam and Rösler, 1999; Ojha *et al.*, 2000, 2009). This sequence is bound to the south by the Main Frontal thrust (MFT), the southernmost surface expression of the MHT, and places the Subhimalayan sedimentary rocks (Section 2.8.1.1, Figure 2.14a) on the modern foreland basin sediments to the south. In central Nepal, the Siwalik Group contains two discrete thrust sheets, one carried by the MFT, and the other by the Main Dun thrust (MDT) (Mugnier *et al.*, 1998; Lavé and Avouac, 2000). The northern extent of the Siwalik Group is defined by the Main Boundary thrust (MBT), which places the Lesser Himalayan (LH) rocks over the Subhimalaya.

2.2.1.2 Lesser Himalaya

In central Nepal, the Lesser Himalayan sequence consists of eight mappable formations with a total thickness of ~8-13 km that are designated as the Paleoproterozoic lower LH and the Mesoproterozoic upper LH strata (Sakai, 1983; Harutaka Sakai, 1985; Upreti, 1996; Khanal and Robinson, 2013). The lower LH is composed of greenschist facies metasedimentary rocks of the Kuncha Formation (Section 2.8.1.2.1, Figure 2.14c), and its older, more northern distal facies, the Robang Formation (Section 2.8.1.2.1, Figure 2.14d-e) (Martin *et al.*, 2011). The mapped thickness of the Robang increases from ~0.5 km in the south to ~2.5 km in the north (Section 2.8.1.2.1, Figure 2.13). The basal Kuncha Formation makes up ~30% of the rocks exposed along the transect

and forms the core of the Gorkha-Pokhara antiform (Pêcher, 1977) (Figure 2.1). The base of the Kuncha Formation is never exposed at the surface, and therefore its thickness is unknown, but mapped relations require it to be 3-8 km thick (Pearson, 2002; Khanal and Robinson, 2013)(SM1). Structurally, the Robang Formation is mapped above the upper LH with the contact interpreted as the Ramgarh-Munsiari thrust (RMT) (Pearson and DeCelles, 2005; Robinson and Pearson, 2013). The Main Boundary thrust (MBT) places the Robang Formation, and the underlying upper LH stratigraphy, against the Siwalik Group to the south. The Robang is exposed again on both the southern and northern edges of the Kathmandu synform. The northernmost mapped location of the Robang Formation is structurally under Greater Himalayan rocks carried by the northern trace of the MCT (Figure 2.14b). In the Budhi Gandaki valley the RMT places the Robang Formation directly over upper LH rocks (Figure 2.14f), in the Trishuli valley it is directly over the Kuncha Formation (Figures 2.1 and 2.13).

The upper LH is made up of six units: the Fagfog, Dandagaon, Nourpul, Dhading, Benighat and Malekhu Formations with a total thickness of ~4.5 km and is metamorphosed to lower greenschist facies in the south and upper greenschist to amphibolite facies in the north (Pearson, 2002; Khanal, 2009) (Section 2.8.1.2.2; Figure 2.14g-l). North of the MBT, along the Budhi Gandaki transect (A-A'), an out-of-sequence thrust lifts the younger Benighat Formation from structurally below the RMT and places it on top of the Robang Formation (Khanal and Robinson, 2013) (Figures 2.1 and 2.13). Upper LH rocks are encountered again to the north of the Kathmandu synform, exposed in the northern and southern limbs of the Gorkha-Pokhara antiform, above the lower LH Kuncha Formation and below the RMT.

The Gorkha-Pokhara antiform has been interpreted to reflect a duplex at depth (Pandey *et al.*, 1995; Lavé and Avouac, 2001; Pearson, 2002; Avouac, 2003; Khanal and Robinson, 2013;

Hubbard *et al.*, 2016), with a roof thrust (the Trishuli thrust) that carries the LH rocks exposed at the surface (Khanal and Robinson, 2013; Robinson and Martin, 2014). The southern extent of the Trishuli thrust reaches the surface at the MBT (Pearson and DeCelles, 2005; Khanal and Robinson, 2013; Hubbard *et al.*, 2016), although along the Budhi Gandaki section, it is immediately under the RMT (Khanal and Robinson, 2013) (Figures 2.1 and 2.13).

2.2.1.3 Greater Himalaya

The contact between the Greater Himalayan (GH) and LH rocks is defined as the Main Central thrust (MCT). In central Nepal, the MCT places the ~15 km thick GH sequence structurally above the LH Robang Formation. The northern exposure of GH rocks carried by the MCT reached temperatures (650-750 °C) and pressures (9-12 kbar) that are consistent with burial depths between 35-50 km (Kohn *et al.*, 2004; Kohn, 2008). The Kathmandu synform is composed of crystalline gneisses located south of the LH duplex (Section 2.8.1.3.1; Figure 2.14m-n). It has been interpreted to be an erosional outlier of the GH (Gansser, 1964; Johnson *et al.*, 2001; Pearson, 2002; Khanal and Robinson, 2013), with the rocks metamorphosed to chlorite-amphibolite facies, that experienced lower peak temperatures (500 – 630 °C) but potentially similar peak pressures (8-~12 kbar) as the rocks exposed above the MCT to the north (Johnson et al., 2001) (Section 2.8.1.3.2; Figure 2.14o-p). Both pressures (6-9.5 kbar) and temperatures (~500 °C) are lower on the southern limb but pressure and temperature data are unavailable for the basal-most part of the section (Johnson *et al.*, 2001; Pearson, 2002).

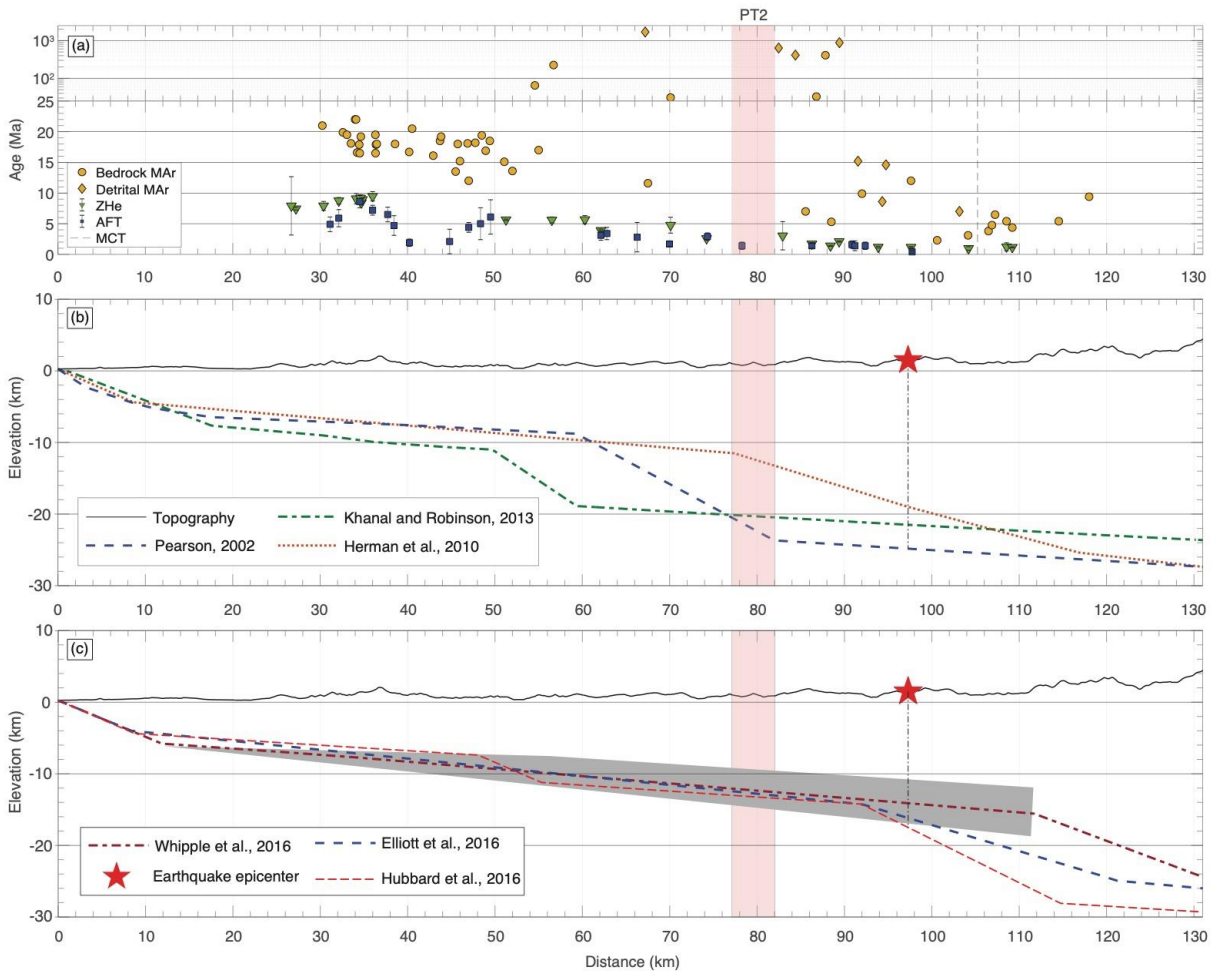

Figure 2.2: Cross-sectional projection of data along the Budhi Gandaki transect.

(a) Combined MAr (yellow), ZHe (green), and AFT (blue) thermochronometer data plotted along the Budhi Gandaki section line, parallel to the direction of transport. The location of the MCT is marked by a black, dashed line, while the origin is the location of the MFT. (b) Pre-Gorkha published MHT geometries for the region. Khanal and Robinson, (2013) **(green, dash-dot), Herman et al. (2010) (orange, dot), and Pearson, (2002) (blue, dash). (c) Newly proposed geometries for the MHT in the region after the Gorkha EQ in 2015. Elliott et al. (2016) (blue, dash), Whipple et al. (2016) (red, dash-dot), and Hubbard et al. (2016) (orange, dash). The margin of error for the Whipple et al. décollement is shown in grey. The red star shows the epicenter of the Gorkha EQ. The topographic profile along the section (A-A') is shown in black (no vertical exaggeration), with the location of the Physiographic Transition 2 (PT2) marked by the red zone.**

2.2.2 Gorkha earthquake and MHT geometries

The 7.8 Mw Gorkha earthquake in 2015 ruptured the MHT, with the epicenter located ~80 km WNW of Kathmandu (Figure 2.1b), and propagated for ~140 km towards the east on a ~10°N dipping plane (Avouac *et al.*, 2015; USGS, 2015). Focal mechanism studies estimate the hypocentral depth to be between 7-23 km (USGS, 2015). The earthquake, although devastating, provides a rare glimpse into the geometry of the MHT, allowing the use of geodetic and seismic data to provide constraints on the MHT depth, dip and ramp location (Avouac *et al.*, 2015; Yagi and Okuwaki, 2015; Duputel *et al.*, 2016; Elliott *et al.*, 2016; Whipple *et al.*, 2016). Compared to previous estimates for the MHT (Pandey *et al.*, 1995; Lavé and Avouac, 2001; Pearson, 2002; Herman *et al.*, 2010; Khanal and Robinson, 2013), the new estimates place the mid-crustal ramp 15-45 km farther to the north (Figure 2.2b-c). Elliott et al. (2016) propose a best-fit geometry with a 75 km flat that dips 7°N (from horizontal). This flat ends in a mid-crustal ramp, dipping 20°N from horizontal, located immediately south of the surface trace of the MCT (Figure 2.2c, blue dashed line). Whipple et al. (2016) argue for a 4-7N° flat that extends north of the surface trace of the MCT, along with a steeper mid-crustal ramp, dipping ~26°N (Figure 2.2c, dark red, dot-dashed line). A third geometry by Hubbard et al. (2016) and Qiu et al. (2016) divides the flat of the MHT into two distinct parts, a southern flat, dipping at 2-5°N from the Siwalik Group to the Kathmandu synform, and a northern flat dipping 7°N under the Gorkha-Pokhara antiform. These two flats are joined by a short (~6 km, 26°N) ramp, located ~50 km from the MFT, at the southern extent of the earthquake rupture (Figure 2.2c, light red dashed line). The mid-crustal ramp, dipping 26°N is located at approximately the same position (~90-92 km from the MFT) as that proposed by Elliott et al. (2016) (Figures 2.2 and 2. 3).

The geometry of the MHT, particularly the location of ramps and active faults, is also responsible for the progressive development of the topography of the Himalaya. A marked change in topography and slope from lower elevations and slopes to the south to the higher topography and steep slopes of the high Himalaya is referred to as Physiographic Transition 2 (PT2). This zone, located ~80 km from the MFT (Hodges, Hurtado and Whipple, 2001; Wobus, Hodges and Whipple, 2003), is interpreted to reflect a major change in the rate of uplift due to the mid crustal ramp of the MHT or an out-of-sequence fault (Wobus, Hodges and Whipple, 2003; Wobus, Whipple and Hodges, 2006; Herman *et al.*, 2010). Therefore, in addition to testing the three proposed geometries for the MHT, we also test the effect of a young out-of-sequence thrust located 80 km from the MFT on the predicted cooling ages. The geometry of the out-of-sequence thrust and permissible displacement is constrained by the requirement that only the LH Kuncha Formation can be exposed at the surface after fault movement.

Sample name	Latitude (dd.ddddd)	Longitude (dd.ddddd)	Elevation (m)	Map unit	MAr Median Age (Ma)	MAr 2σ Error (Ma)	ZHe age (Ma)	ZHe 2σ Error (Ma)
CN16 - 004	27.85350	85.15397	1612.5	GH	-	-	5.6	0.1
CN16 - 007	28.24641	85.36367	1731.6	GH	5.4	0.6	1.2	0.7
CN16 - 016	28.14202	85.32276	1731.6	Kuncha	12	3	1.2	0.1
CN16 - 017	28.08754	85.27541	1983.8	Kuncha	410	80	1.4	0.1
CN16 - 018	28.06546	85.22443	2030.1	Kuncha	-	-	1.7	0.2
CN16 - 019	27.99270	85.20262	1496.9	Kuncha	-	-	2.6	0.1
CN16 - 020	27.92009	85.14891	589.0	Kuncha	-	-	3.9	0.2
CN16 - 032	27.85012	84.84991	437.0	Fagfog	-	-	5.6	0.5
CN16 - 033	27.88244	84.87545	575.6	Kuncha	-	-	5.7	0.7
CN16 - 034	27.94910	84.86010	1196.6	Kuncha	31	6	4.8	1.3
CN16 - 036	28.11037	84.83924	689.5	Kuncha	5.2	0.2	2.1	0.1
CN16 - 037	28.31831	84.90406	284.8	GH	4.9	0.1	1.2	0.1
CN16 - 048	28.26517	84.89064	353.1	Robang	-	-	1.0	0.3
CN16 - 064	28.17197	84.88042	1277.9	Kuncha	-	-	1.2	0.1
CN16 - 069	28.03586	84.76636	353.0	Kuncha	-	-	3.0	2.3
CN16 - 084	27.56566	84.90636	471.1	Robang	-	-	7.4	0.2

CN16 - 092	27.56350	84.86703	213.4	Robang	-	-	7.9	4.8
CN16 - 102	27.52990	85.09667	840.1	GH	-	-	8.7	0.5
CN16 - 103	27.49513	85.04448	601.0	Robang	-	-	7.9	0.7

Table 2.1: Sample locations and cooling ages from central Nepal

Latitudes and longitudes are based on the WGS84 datum. MAr: Muscovite $^{40}Ar/^{39}Ar$; ZHe: Zircon (U-Th)/He.

2.3 Thermochronology

We present new muscovite $^{40}Ar/^{39}Ar$ (MAr) and zircon (U-Th)/He (ZHe) cooling ages collected along the Budhi Gandaki and the Trishuli (~40 km to the east) transects between the MBT and the MCT (Tables 2.1, 2.5, 2.6, 2.7). The MAr analyses were performed at the U.S. Geological Survey Argon Geochronology laboratory in Denver (Morgan, 2020), and ZHe analyses were performed at the University of Arizona Radiogenic Helium Dating Laboratory (Schmitz and Bowring, 2001; Reiners *et al.*, 2004; Hourigan, Reiners and Brandon, 2005; Reiners, 2005; Renne *et al.*, 2005; Kuiper *et al.*, 2008) (see Section 2.8.2 for MAr and ZHe methods). We project the new and existing thermochronological data onto the two cross section lines along strike, maintaining their relative structural positions (Figure 2.2a). We limit this projection to samples less than 50 km away from either cross-section line to avoid the effects of any lateral structures on the thermochronometer ages. The distance along the section is calculated using the traces of the MCT (both the northern boundary and the edges of the Kathmandu synform) as the reference frame because the MFT shows multi-scale salients and recesses (Lavé and Avouac, 2000; Avouac, 2003; Robinson *et al.*, 2003) that can significantly change the distance between the MFT and structures to the north (MBT or MCT). Where we focus in central Nepal, the MFT is located ~5 km farther south along the Trishuli cross section than the Budhi Gandaki (Figure 2.1). The trace of the MCT

north of the duplex maintains a trend that is roughly perpendicular to the shortening direction of the Himalaya (Figure 2.1), allowing us to use it as a fixed frame of reference. Maintaining the relationship between data location and structure also required adjusting how data are plotted south of the antiform axis where the broad structural plunge to the east changes the mapped extent of the Kathmandu synform between the Budhi Gandaki and Trishuli sections. As a result, the distribution of cooling ages projected to the Trishuli section is slightly different than that of the Budhi Gandaki section, so that the distances between measured ages reflect mapped changes in the surface geology (Figure 2.15).

2.3.1 Muscovite $^{40}Ar/^{39}Ar$ data

We present six new white mica $^{40}Ar/^{39}Ar$ (MAr) ages, collected from LH and GH rocks along the Budhi Gandaki and Trishuli transects (Table 2.1), where the reported uncertainty on the age represents a 2-sigma analytical uncertainty for each sample (Morgan, 2020). Of the ages collected from the GH, one was collected in the Budhi Gandaki valley (CN16-037), 5 km north of the trace of the MCT (Figure 2.2a), while the other was collected from the Trishuli valley, 1 km north of the MCT (CN16-007). The measured ages are 4.9 ± 0.1 Ma and 5.4 ± 0.6 Ma, respectively. The $^{40}Ar/^{39}Ar$ data collected from the LH Kuncha Formation all show complicated age spectra. Although we report an integrated age and the associated age-release spectra (Figure 2.16), we emphasize that these integrated ages (and errors) do not represent cooling ages through a closure isotherm. We report the integrated age from LH rocks because they show a pattern of young ages in the north to older ages in the south that we think reflect real changes in the thermal histories of these samples. Sample CN16-016 from ~3 km south of the MCT in the Trishuli valley shows a range in ages from 100 Ma to 5 Ma, which we combine for an integrated age of 12 ± 3 Ma (Figures

2.13 and 2.16). Sample CN16-017 from ~10 km south of the MCT displays ages from 840 to 80 Ma with an integrated age of 410 ± 80 Ma. To the west in the Budhi Gandaki valley, ages range from 5.2 ± 0.2 Ma (CN16-036, ~12 km south of the MCT) to a broader range of ages (100 Ma to 10 Ma) from sample CN16-034 (~30 km south of the MCT), which combine for an integrated age of 31 ± 6 Ma. Full analytical details and argon geochronology data are available in Morgan (2020). We merge these new cooling ages with 47 existing MAr ages (Hubbard and Harrison, 1989; Copeland *et al.*, 1991; Wobus, Hodges and Whipple, 2003; Herman *et al.*, 2010), and project them together onto the section lines (Figure 2.2a). Along the section line, the bedrock MAr ages cluster into three distinct populations of ages. From south to north, the first suite of data is located in the Kathmandu synform and ranges in age between 20 Ma - 15 Ma. In the Gorkha-Pokhara antiform, where LH rocks are exposed, published MAr bedrock ages range from 225 to 11.6 Ma and represent integrated ages as discussed for samples CN16-016, CN16-017, and CN16-034. Farther north (100-105 km north from the MFT, ~5 km south of the trace of the MCT), reset cooling ages range from 10-2 Ma with the youngest ages (~2 Ma) located 3 km to the south of the surface trace of the MCT. North of the MCT, the ages become steadily older, reaching a maximum measured age of ~10 Ma, at a distance of ~15 km north of the MCT.

2.3.1.1 Distribution of detrital muscovites

In addition to the bedrock ages discussed above, we also include a group of nine detrital MAr ages (Wobus, Whipple and Hodges, 2006) obtained from modern river sediments in tributaries to the Budhi Gandaki and Trishuli River valleys (Figure 2.1, yellow diamonds). Unlike the bedrock ages reported by the other samples, these detrital samples present a range of measured ages (Figure 2.17), which are interpreted to represent an aggregate of bedrock ages over the drainage area of the sampled stream (Brewer, Burbank and Hodges, 2003; Hodges *et al.*, 2005;

Wobus, Whipple and Hodges, 2006). The ages shown in Figure 2.1 indicate the youngest quartile of the detrital age population. Due to the uncertainty in both the original location, and age for any individual grain, the young, reset detrital samples (<9 Ma) are not used in our analysis. However, the older detrital ages show that both unreset (1.8 – 2.9 Ga) and partially reset (40 Ma - 1.8 Ga) white mica are found over a significant areal extent within the Gorkha-Pokhara antiform (Figure 2.17). As a result, we plot the median age of these older detrital samples in Figure 2.2 and subsequent plots of thermochronometric data. These detrital ages elucidate the breadth of permissible MAr ages in the Gorkha-Pokhara antiform between 55 km and 90 km north from the MFT. Here, LH rocks have $^{40}Ar/^{39}Ar$ ages that are highly variable. Young, clearly reset cooling ages (~5 Ma) located 90-100 km from the MFT transition to unreset and partially reset ages as old as 1.8 Ga immediately to the south. Across the Gorkha-Pokhara antiform, detrital MAr samples define an ~40 km (north-south) zone of unreset to partially reset ages that vary from older than 2.9 Ga to 40 Ma (Wobus, Whipple and Hodges, 2006). This range in ages requires that none of these detrital samples underwent prolonged heating above the closure temperature for MAr during Himalayan orogenesis (Wobus, Hodges and Whipple, 2003).

2.3.1.2 Zircon (U-Th)/He data

We present 19 new ZHe ages from four GH and 15 LH samples (Table 2.1). These new ages are reported as an arithmetic mean age, calculated from two to three zircon grains and their associated 2σ analytical errors. The reported error for each sample includes the full age dispersion in the measured single grain ages. Two of the GH samples were collected north of the MCT. One GH sample (CN16-037) was collected in the Budhi Gandaki valley, ~1 km north of the MCT, while the other (CN16-007) was collected to the north-east along the Trishuli valley. The samples yield ages ranging between 1.2 ± 0.1 Ma and 1.2 ± 0.7 Ma. The remaining GH samples were

collected from rocks in the Kathmandu synform (CN16-004 and CN16-102) and yield ages that range between 5.6 ± 0.1 Ma and 8.7 ± 0.5 Ma. Of the 15 LH samples, four were collected from the Robang Formation. Three of the Robang samples were collected south of the synform, yielding ages of 7.9 ± 4.8, 7.4 ± 0.2, and 7.91 ± 0.7 Ma. The remaining Robang sample was collected north of the Gorkha-Pokhara anticline in the MCT footwall, yielding a very young age of 1 ± 0.3 Ma. The remaining 11 samples were collected from LH rocks across the anticlinorium between the MCT in the north and the Kathmandu synform in the south and yield ages that systematically increase in age from 1.2 ± 0.1 Ma in the north to 5.7 ± 0.7 Ma in the south. These new ages were combined with an existing age/elevation transect (Figure 2.1d) in GH rocks exposed in the southern limb of the Kathmandu synform (Herman *et al.*, 2010). This transect has the oldest measured ZHe age of 9.5 ± 0.8 Ma located ~36 km north of the MFT (Figure 2.2a).

2.3.1.3 Apatite Fission Track (AFT) data

We also include 15 existing AFT ages from the same region (Figure 2.2a, blue squares) (Herman *et al.*, 2010; Robert *et al.*, 2011). The AFT data show a broadly southward increasing trend in the measured ages with the youngest ages (~1.4 ± 0.8 Ma) found at the MCT, and the oldest age, 8.6 ± 1 Ma, located 35 km north of the MFT. However, this trend in increasing age is broken within the synform, with AFT ages as young as 1.9 ± 0.6 Ma, forming a trough of young ages between 35 and 50 km from the MFT. While these AFT ages have been reported as 1σ errors in the original studies, we plot the data here with a 2σ error.

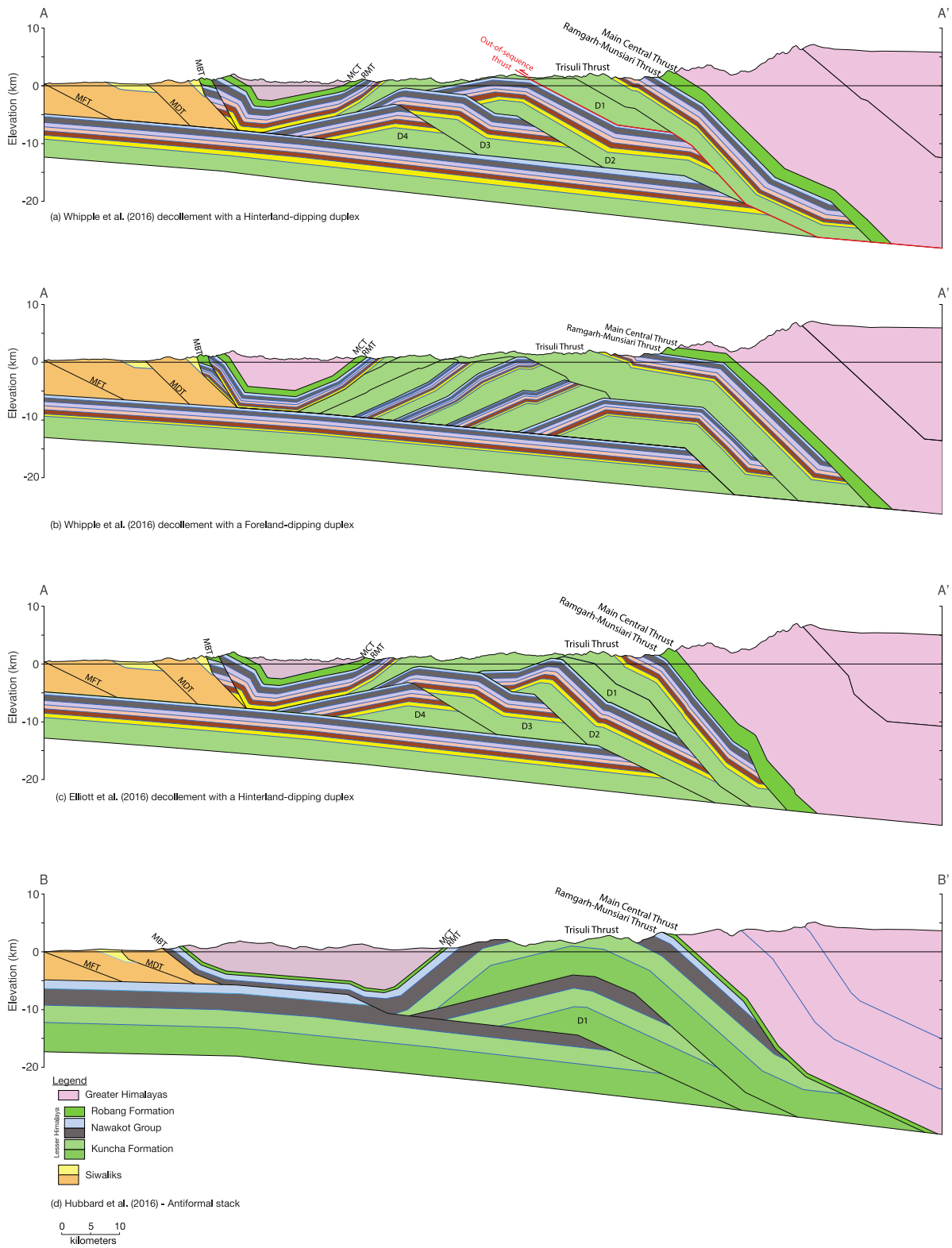

Figure 2.3: Comparison between new cross-sectional geometries.

(a) Simplified balanced cross section along the Budhi Gandaki transect based on the Whipple et al. 2016 décollement geometry, with a hinterland-dipping duplex. (b) Simplified balanced cross section along the Budhi Gandaki transect based on the Whipple et al. (2016) décollement geometry, with a foreland-dipping duplex. (c) Simplified balanced cross section along the Budhi Gandaki transect based on the Elliott et al. (2016) décollement geometry, with a hinterland-dipping duplex. (d) Balanced cross section proposed by Hubbard et al. (2016) for the Trishuli transect. Legend shows the units represented in the Hubbard et al. (2016) section. The deformed sections are all at the same scale (no vertical exaggeration), indicated on the figure. The topographic profiles shown for (a-c) are extracted from A-A', and for (d) extracted from B-B' using an SRTM DEM.

2.4 Cross sections and modeling

2.4.1 Balanced cross sections

We present three new cross sections along the Budhi Gandaki Valley, based on the two décollement geometries proposed after the Gorkha earthquake (Elliott *et al.*, 2016; Whipple *et al.*, 2016) and constrained by new and existing mapping of surface geology (Pearson, 2002; Khanal and Robinson, 2013) (Section 2.8.1; Figure 2.13). New mapping was concentrated along the Budhi Gandaki and Trishuli River valleys, and integrated with published maps from central Nepal (Lavé and Avouac, 2000; Pearson, 2002; Khanal and Robinson, 2013) and maps referenced therein. A detailed description of the mapped units is given in section 2.8.1. The section line along the Budhi Gandaki is oriented approximately 10° from N, perpendicular to the Himalayan front, and parallel to the direction of transport as revealed by regional strike and mineral stretching lineations (this study, Bollinger *et al.*, 2004). Orientations measured in the field were projected onto the line of

section (Figure 2.1) and used to limit permissible geometries. The line lengths of each of the tectonostratigraphic units in the deformed sections were measured and balanced in the restored sections (Figure 2.18). We do not account for any small-scale folding or any ductile deformation (penetrative strain) within formations, or internal thrusting that may exist within Greater Himalayan rocks. Both Greater and Lesser Himalayan rocks preserve pervasive penetrative strain above and immediately below the MCT (Macfarlane, Hodges and Lux, 1992; Hodges, Parrish and Searle, 1996; Pearson, 2002; Pearson and DeCelles, 2005; Larson, Godin and Price, 2010; A. J. Parsons, Ferré, *et al.*, 2016). The MCT and RMT both initially deform at high temperatures (650-700 °C and 500-600 °C, respectively) (Johnson *et al.*, 2001; Kohn *et al.*, 2004; Kohn, 2008; Larson, Godin and Price, 2010; Larson and Cottle, 2014; A. J. Parsons, Law, *et al.*, 2016). Penetrative strain recorded in the LH rocks largely records layer-normal flattening with respect to both the original stratigraphy and thrusts that displace the strata (Larson, Godin and Price, 2010; A. J. Parsons, Ferré, *et al.*, 2016). This flattening predates displacement on discrete thrusts for the lower temperature LH (e.g., Long et al., 2011) and either predates or is concurrent with displacement in the higher temperature GH rocks (Corrie *et al.*, 2012; Law *et al.*, 2013; Long *et al.*, 2016). All faults (MCT, RMT and the modern MHT) transition from ductile to brittle processes as thrust and shear systems approach the surface, with a transition temperature of ~350 °C (Avouac, 2003). These cooler processes, i.e. friction on brittle faults and erosional exhumation, control modeled fault rates (Beaumont *et al.*, 2001; Avouac, 2003; Jamieson *et al.*, 2004) and are the processes that are recorded by the suite of thermochronometers in this study. Discrete structures, such as ramps, can exist at temperatures that range from 300-550 °C as is shown by the existence of the modern MHT ramp. Estimates for its depth and temperature range from 12-28 km and ~300-550° C, respectively (Pandey *et al.*, 1995; Bollinger *et al.*, 2004; Herman *et al.*, 2010; Robert *et al.*, 2011).

In the kinematic models we present here (section 2.4.2), all thrust sheets are treated as rigid bodies that were translated by discrete structures, and incremental strain that precedes or is concurrent with displacement is not incorporated. However, the integration of the cross section geometry and evolution with a thermal model allows us to evaluate where and when peak temperatures occur, compare modeled deformation temperatures with published peak and deformation temperature estimates (Johnson *et al.*, 2001; Kohn *et al.*, 2004; Kohn, 2008; Larson and Godin, 2009; Larson, Godin and Price, 2010; Larson and Cottle, 2014; A. J. Parsons, Ferré, *et al.*, 2016; A. J. Parsons, Law, *et al.*, 2016) and assess whether the temperature histories of the rocks can be replicated without the inclusion of penetrative grain-scale strain (e.g. Long et al., 2016).

While the strata and stratigraphic thickness repeated by the duplex are unknown, the most recent fault in the duplex originated from the footwall of the MHT and is thus required to carry a thickness of rocks that correspond to the modern ramp thickness (8-16 km thick depending on the proposed MHT geometry) (Figure 2.2). Ramps are identified in mapped geology by the sequence of rocks that that are commonly seen together at the surface (e.g. Rich, 1934; Rodgers, 1950; Gwinn, 1970; Woodward et al., 1989), such as the entire GH package of rocks, which sets the height of the initial MCT ramp, or the entire sequence of LH rocks that are mapped on the northern and southern limbs of the Gorkha-Pokhara antiform along the Budhi Gandaki valley. This repetition of the entire LH stratigraphy at the surface presents a strong argument that the ramps associated with these thrust faults cut through the entire LH stratigraphy, setting the ramp height. The mapped thickness of exposed LH rocks is ~10 km (Khanal and Robinson, 2013), consistent with estimates of the MHT ramp height. Where the Trishuli thrust breaches the surface at the MBT, available space between the décollement depth and the GH rocks exposed in the Kathmandu synform limits the thickness of Lesser Himalayan strata that is carried by the frontal portion of the

Trishuli thrust to the thickness of only the upper LH section, while the mapped geology on the northern and southern limbs of the Gorkha-Pokhara antiform requires that the main portion of the thrust sheet carries the entire LH section (Figures 2.1 and 2.13). Additionally, the hanging wall cutoff for the Trishuli thrust sheet is exposed at the MBT, along with the cutoff for the out-of-sequence thrust immediately north of the MBT (Figures 2.1 and 2.13). These observations determine the southernmost extent of the MBT and do not permit additional shortening on that structure. They also limit the range of permissible duplex thickness variations to thicknesses that either contain just the lower Kuncha formation (e.g., D1, Figure 2.3) or thicknesses that contain the entire section (e.g., D3-4, Figure 2.3). Only the minimum permissible displacements on the RMT and MCT exist for this region. Both thrusts have had their hanging wall cutoffs eroded away. Exposures of the RMT structurally above upper LH rocks carried by the Trishuli thrust at the MBT indicate that the RMT must have covered the entire Trishuli sheet. Similarly, the hanging wall cutoff for the MCT sheet is also not preserved, and the shortening amount used to build the cross section is the minimum amount required to bury the entire RMT sheet. Finally, both Subhimalayan thrust sheets have hanging wall cutoffs that are eroded, so they are restored using their minimum shortening estimates. In the Trishuli transect, where the Hubbard et al. (2016) section is located, the entire hanging wall cutoff for the Trishuli thrust has been eroded away allowing for a displacement amount that is higher than the minimum. In this cross section, a higher-than-minimum displacement on the Trishuli thrust is required by the location of the southern ramp proposed on the northern side of the Kathmandu synform (Hubbard *et al.*, 2016).

To evaluate the influence of duplex geometry on cooling ages, we designed two cross sections with the same underlying décollement geometry (Whipple *et al.*, 2016), one with a hinterland-dipping duplex (Figure 2.3a) and the other with a foreland-dipping duplex (Figure

2.3b). While the location of the top of the ramp remains the same in both cross sections, the angle of the mid-crustal ramp varies with the foreland-dipping duplex showing a steeper ramp (40°), which is required to balance the steeper south-dipping horses of the foreland-dipping duplex. These two duplex geometries were created to fill the same amount of space under the exposed Trishuli thrust sheet in the Gorkha-Pokhara antiform and above the proposed MHT décollement. The geometry of the third cross section, based on the MHT geometry proposed by Elliott et al. (2016) was kept as similar as possible to the hinterland-dipping duplex geometry cross section that used the Whipple et al. (2016) décollement (Figure 2.3c). A similar duplex geometry was chosen to ensure differences in modeled cooling ages reflect the location of the mid-crustal ramp, rather than duplex formation. The final cross section geometry that we model to evaluate the influence of duplex geometry on cooling ages is the antiformal stack geometry proposed by Hubbard et al. (2016), located along the Trishuli valley (Figure 2.3d).

The distance between the Budhi Gandaki and Trishuli sections is 30-40 km. Over this distance there are changes in the southern extent of the MFT (~5 km), the number and geometry of structures immediately north of the MBT, and the north-south extent of the Kathmandu synform, which has a 20 km extent in the west and 40 km extent in the east (Figure 2.1). While these differences will undoubtably affect the cooling history of rocks in the southern limb of the synform and to the south, we argue that the similar north-south 40-45 km extent of the Gorkha-Pokhara antiform), the east-west trend of the MCT, which is perpendicular to the transport direction, and the similar north-south pattern of cooling ages supports treating the first-order geometry and structural evolution as two-dimensional. In particular, our chosen study area avoids significant along-strike changes that include the lateral edge of exposed LH rocks in the Gorkha-Pokhara antiform to the east and the termination of the Kathmandu synform to the west.

Geometry		Total shortening (km)	Effective elastic thickness (km)	MCT initiates (Ma)	RMT initiate (Ma)	TT initiates (Ma)	Duplex initiates (Ma)	MDT initiates (Ma)	MFT initiates (Ma)
MHT geometry	Duplex geometry								
Whipple et al. (2016)	Hinterland-dipping	447.0	50	23.00	16.47	9.78	7.2	0.79	0.41
	Foreland-dipping	442.2	70	23.00	16.03	9.34	8.8	0.75	0.34
Elliott et al. (2016)	Hinterland-dipping	372.8	50	20.00	14.16	8.37	5.69	0.62	0.23
Hubbard et al. (2016)	Antiformal stack	464	50	25.50	15.61	5.28	2.14	1.65	0.55

Table 2.2: Model geologic and flexural parameters, along with initiation times for major structures at long-term constant rates.

MCT: Main Central thrust; RMT: Ramgarh-Munsiari thrust; TT: Trishuli thrust; MDT: Main Dun thrust; MFT: Main Frontal thrust.

2.4.2 Kinematic and flexural modeling

Each of our newly restored cross sections (Figures 2.3 and 2.18), along with the balanced cross section from Hubbard et al. (2016) were kinematically and flexurally forward modeled using the structural modeling software Move (Midland Valley/Petex), to recreate the final deformed cross-sectional geometry. The forward modeling was performed in ~10 km increments using the fault-parallel flow algorithm that best replicates displacement on compressional faults where displacement occurs on discrete structures and the fault-bend angles do not exceed 45° (Ziesch, Tanner and Krawczyk, 2014). Following each 10 km increment, flexural loading and erosional unloading is applied. The magnitude of the flexural load applied at each step was calculated using the difference between the deformed topography produced by a 10 km increment of shortening and the estimated topography from the step immediately prior (McQuarrie and Ehlers, 2015). To determine the magnitude of erosion at each incremental step and the resulting estimated

topography, we use a ‘responsive topography’ method (McQuarrie and Ehlers, 2015; Gilmore *et al.*, 2018), where the new topography is defined by a topographic taper angle that increases in elevation towards the north, at an angle similar to that of modern topography in regions where active uplift has occurred. In areas that did not experience uplift, the new topography follows the existing, isostatically loaded topography. Each model begins with an initial topography that increases at an angle of 2° towards the north, reaching an elevation of 5 km above the southern limit of GH rocks. This simplified initial topography simulates a preexisting fold and thrust belt made up of a ~15 km thick section of Tethyan rocks exposed in southern Tibet (Brookfield, 1993; Ratschbacher *et al.*, 1994; Zhang and Guo, 2007) and places the initial base of the Greater Himalayan section ~45 km below the surface. The flexural response of the crust to the building of topography and subsequent erosion allows the décollement to steepen and thus deepen with time. The steepening is dependent upon the effective elastic thickness, crustal density, and the starting dip of the décollement of the models, all of which were systematically varied until a best-fit combination was found to replicate the surface geology, foreland basin depth, and the proposed décollement angles. The range of parameters used in these models is listed in Table 2.2.

We use a 2D point grid with a resolution of 0.5 km that is deformed sequentially with each cross section to create a displacement field. Assigning an age to each of these increments converts the displacement field to a velocity field, which is then used as input into a University of Tübingen modified version of PECUBE (see Whipp et al., 2009; McQuarrie and Ehlers, 2015). We also applied temporally varying velocities by controlling the age at which the faults initiate, providing an opportunity to evaluate the timing and rate of faulting that best reproduces the measured cooling ages.

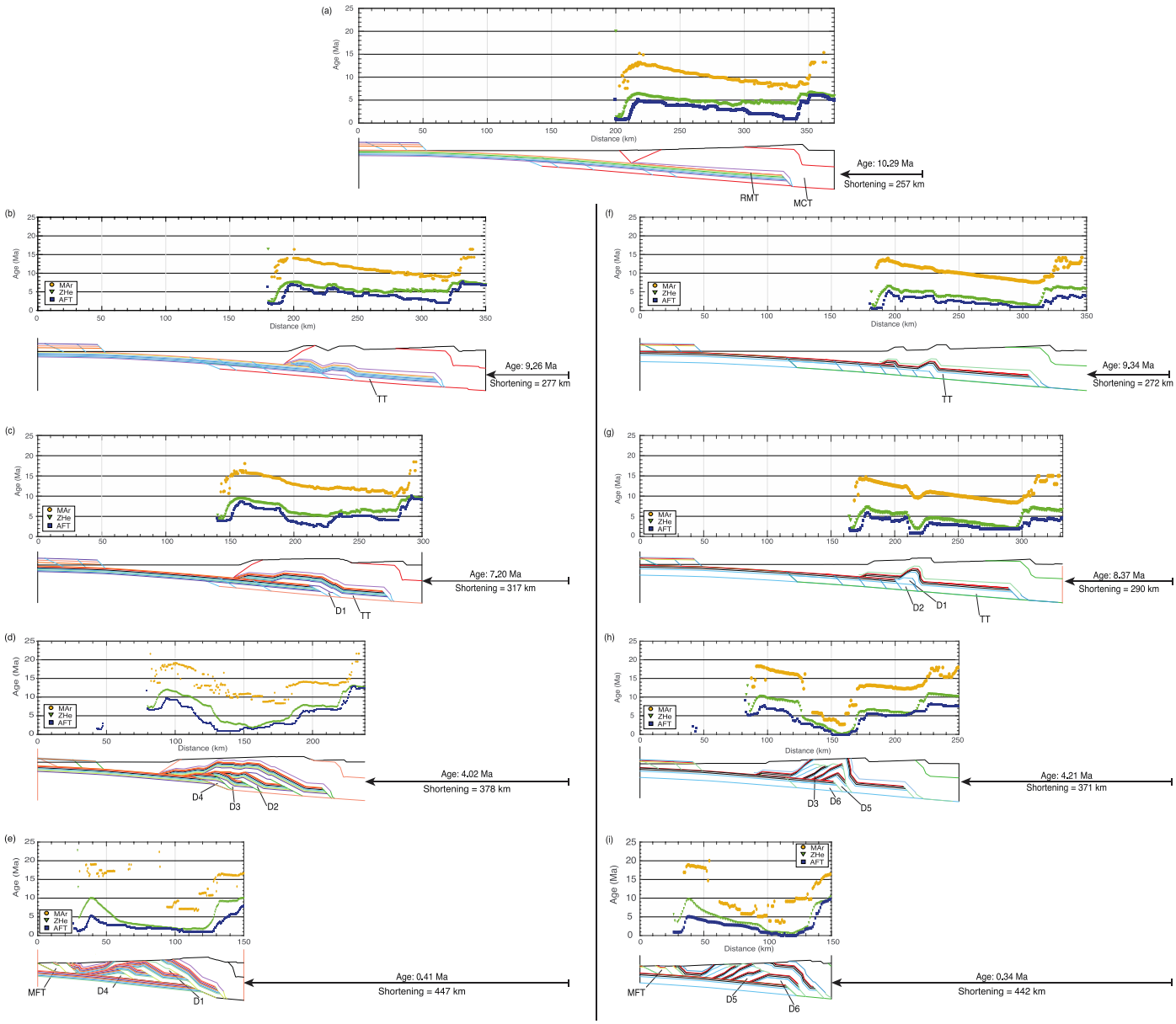

Figure 2.4: Structural and thermochronologic evolution of the hinterland- and foreland-dipping cross-sections

(a-d) Sequential cross section reconstructions and associated predicted cooling ages based on the Whipple et al. (2016) MHT geometry and the hinterland-dipping duplex. The sequence assumes a constant shortening rate starting at 23 Ma (19.44 mm/yr.). (e-h) Sequential cross section reconstructions and associated predicted cooling ages based on the Whipple et al. (2016) MHT geometry and the foreland-dipping duplex. The sequence assumes a constant shortening rate starting at 23 Ma (19.23 mm/yr.).

2.4.2.1 Kinematic sequence

In the kinematic and flexural analysis of all our models, the MCT emplaces the GH sequence over the rocks of the LH Robang Formation (Pearson, 2002; Pearson and DeCelles, 2005). The RMT emplaces Robang and GH rocks over the rocks that will be carried by the Trishuli thrust sheet (Pearson, 2002; Khanal and Robinson, 2013), completely burying it. The Trishuli thrust places these overlying thrust sheets on top of the rocks that will form the LH duplex (Pearson, 2002; Khanal and Robinson, 2013; Hubbard *et al.*, 2016).

The faults that create the LH duplex vary in number and displacement amount depending on the geometry of the duplex (Figure 2.3). Variability also exists in the fault length and the stratigraphic thickness of each fault-bound thrust sheet (horse). In the hinterland-dipping duplex, the first horse (D1) to move only carries the Kuncha Formation. Three more horses follow (D2, D3, and D4), all of which are composed of the entire LH section. The foreland-dipping duplex is made up of six horses, where the first two horses (D1 and D2) carry only the Kuncha Formation, and the remaining four (D3, D4, D5, and D6) contain the entire LH section. Once the Trishuli thrust is emplaced, slip is successively transferred to the horses of the duplex, promoting uplift and exhumation of the overlying rocks and erosionally stranding GH rocks in the Kathmandu synform from those exposed above the main MCT sheet to the north. The shortening that builds the duplex is transferred to the surface along the MBT and along an out-of-sequence thrust mapped in the Budhi Gandaki transect (Khanal and Robinson, 2013). The MBT and associated thrusts stop moving when the deformation front steps forward into the foreland basin, emplacing the Subhimalayan thrust sheets (MDT and MFT) and moving the duplex into its final position.

Parameter	Input value
Material properties	
Crustal density (kg m^{-3})	2650
Mantle density (kg m^{-3})	3300
Specific heat capacity (J kg^{-1} K)	800
Crustal volumetric heat production (mW m^{-3})	1.0 – 3.5
E-folding depth (km)	20
Thermal conductivity (W m^{-1} K)	2.5
Numerical properties	
Temperature at base (°C)	1300
Model thickness (km)	110
Surface temperature (°C)	20
Atmospheric lapse rate (°C km^{-1})	7
Kinematic grid spacing (km)	0.5
Horizontal node spacing (km)	0.5
Vertical node spacing (km)	1 km
Model domain (km)	Variable x 110 x 5
Model start time (Ma)	500

Table 2.3: Mechanical and thermal parameters for PECUBE

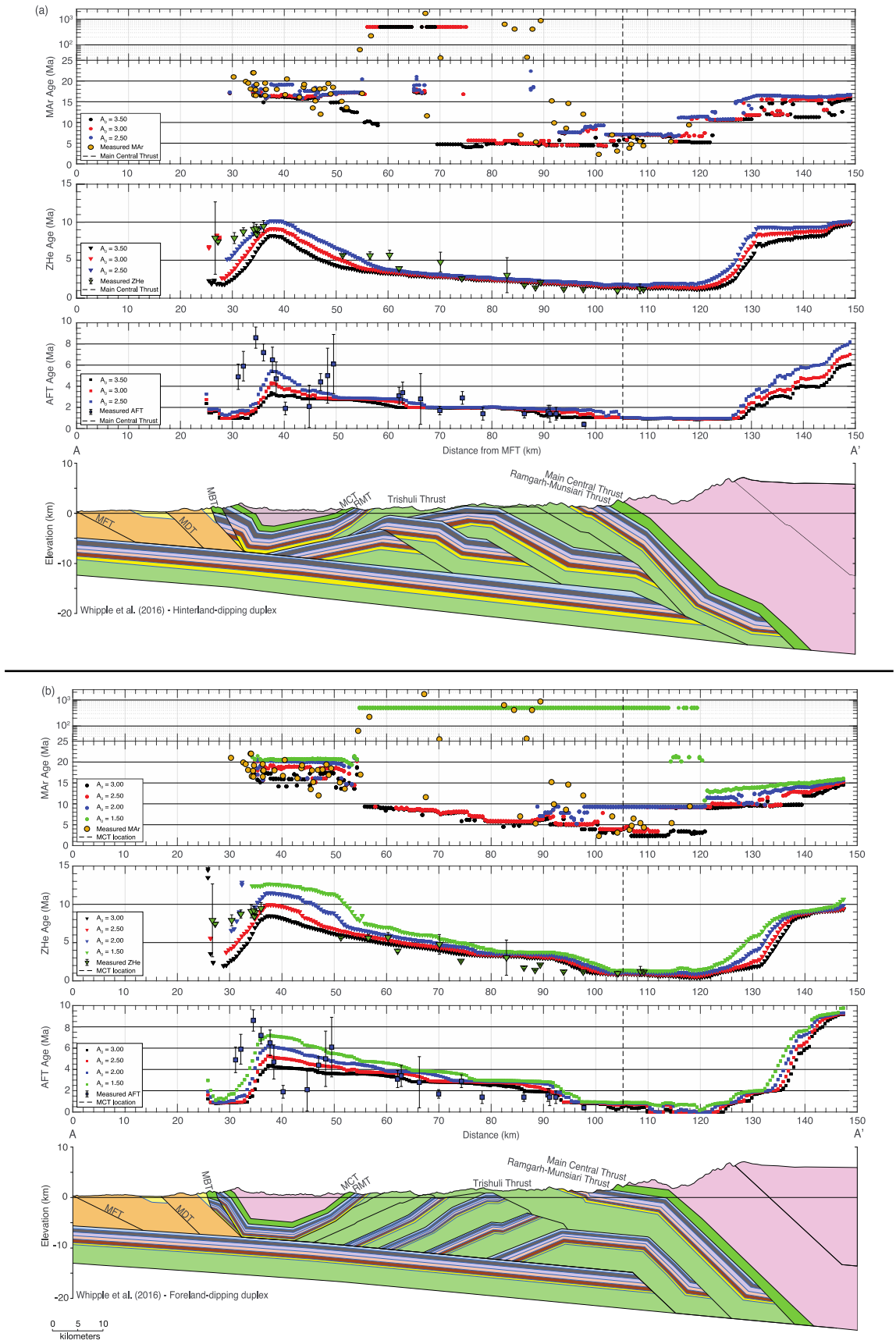

Figure 2.5: Plots comparing thermochronometric ages predicted by the hinterland-dipping and foreland-

dipping duplexes.

The décollement geometry is kept constant. (a) Output from thermokinematic models comparing three A_0 values (red: 2.50, blue: 3.00, black: 3.50) for the hinterland-dipping duplex. (b) Output from thermokinematic models comparing four A_0 values (green: 1.50, blue: 2.00, red: 2.50, black: 3.00) for the foreland-dipping duplex. The shortening rates are constant at ~19 mm/yr. All plots are age vs. distance from MFT (km).

2.4.3 Thermokinematic modeling and results

The thermokinematic modelling is made up of three components. A kinematic component describing the velocities of thrust sheets, using the displacement point grids imported from Move. A transient thermal component that calculates the evolving thermal field using crustal thermophysical properties, thermal boundary conditions, the imported velocity vectors, and erosion at the topographical surface. The topographic surface used is the same one that is generated in Move and represents the final topography at the end of each 10 km incremental step. Finally, age prediction algorithms are used to predict the surface cooling ages at each of the tracked points as they are exhumed and brought to the surface (Braun, 2003; Ehlers *et al.*, 2005). To calculate these ages, we do not use a predetermined value for the closure temperature, rather the closure temperature is calculated from the rock cooling rate and kinetic parameters for each thermochronometer system. For this version of PECUBE, the kinetics for the AFT system come from the Durango apatite parameters calculated in Crowley et al. (1991). The ZHe kinetic model is from Reiners et al. (2004). The MAr ages are calculated using thermally activated diffusion (e.g. Dodson, 1973), with parameters from Hames and Bowring (1994) using a cylindrical geometry (Hodges, 2014). These parameters produce a MAr closure temperature of 395 °C using a cooling rate of 10°C/Myr. Laboratory-derived diffusion parameters (assuming spherical diffusion at 5

kbar) suggest a moderately higher MAr closure temperature of 405 °C at 10°C/Myr (Harrison *et al.*, 2009).

The initial thermal state of the crust simulated by PECUBE is dependent on heat flow from the mantle, and the material properties of the crust (thermal conductivity, density, heat capacity, and radiogenic heat production). The model parameters include a surface heat production value (A_0) that decreases exponentially to a value of 1/e of the surface. This decay occurs over a distance specified by a parameter called the 'e-folding depth' (McQuarrie and Ehlers, 2017), allowing us to honor the nonlinear decline of heat production with depth, and measured heat production values from the region (e.g. England et al., 1992; Ketcham, 1996; Menon et al., 2003; Brady et al., 2006; Whipp et al., 2007). We test our new cross-sectional geometries by systematically varying the surface heat production value between 2.0 – 3.5 $\mu W\ m^{-3}$ to find values that can reproduce the best-fit cooling signal for each geometry using an e-folding depth of 20 km. Crustal material properties (e.g., heat production, thermal conductivity, and thermal capacity) are not advected by the imposed displacement fields, but remain static throughout our simulations, using average representative values for the setting. Specifically, the values for thermal conductivity and heat capacity used in our models (2.5 $W\ m^{-1}\ K^{-1}$ and 800 $J\ kg^{-1}\ K^{-1}$ respectively), are based on measured values from the Himalaya (Ehlers, 2005; Ray, Bhattacharya and Roy, 2007; Whipp *et al.*, 2007). To evaluate the sensitivity of both peak temperatures and predicted cooling ages to a prescribed e-folding depth, we also evaluated peak temperatures, predicted cooling ages and the final predicted temperature field using a constant heat production value through the entire crust (Section 2.8.3; Figure 2.19). Prior to any shortening being accommodated, a static, steady-state thermal field is generated, which produces a near-surface geothermal gradient that is independent of geometry, only depending on the assigned value of crustal heat production. Increasing the heat production value

from 2 μW m^{-3} to 3.5 μW m^{-3} increases the near-surface gradient from 21.5 °C/km from 27.3 °C/km. When a constant surface heat production is applied to the crust, the steady-state geothermal gradient is 25.1 °C/km. The respective parameters used to set up the thermal model in PECUBE are listed in Table 2.3.

We evaluate the fit of these modeled results by calculating the differences between the observed ages and predicted ages at the same location. The difference in age or 'residual' is positive if the measured age is younger than the predicted age and negative if the measured age is older. These residuals are used to calculate the root mean square error (RMSE) for each model run (see section 2.8.4 for details). We calculate a separate RMSE value for each of the three thermochronometer systems and take the mean of the three to produce a single value that can be compared across all of the models, without placing emphasis on the fit of a particular system. To reinforce this result, we also conducted a statistical comparison between the modeled and measured data using a two-sample Kolmogorov-Smirnov Test (Massey, 1951). This test compares the predicted and measured ages by calculating and comparing their Cumulative Density functions (CDFs), to check whether they come from the same distributions. This fit is expressed as a p-value. The model is rejected if the p-value is less than a significance level of 0.05. We explore a suite of model solutions to minimize the RMSE and increase the p-value and determine the best-fit model for the cross section (Table 2.5). We initiate our models at 500 Ma, which produces 500 Ma unreset MAr ages where the MAr system has not been reset by ~25 Ma and younger deformation. For this zone of unreset ages, we consider the modeled and measured age to be a match and increase the p-value if these 500 Ma model ages coincide spatially with median detrital or measured MAr ages that range from 400 Ma - 1.9 Ga (see section 2.8.4).

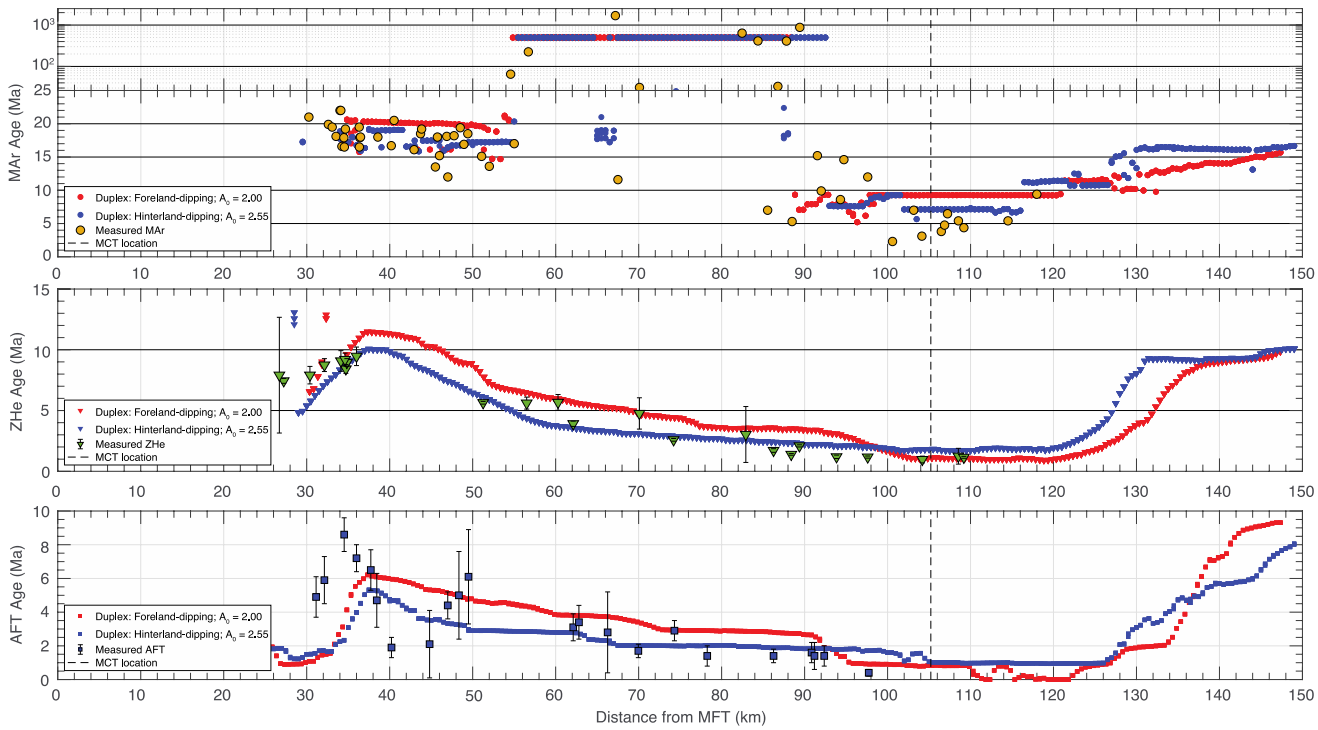

Figure 2.6: Plot comparing thermochronometric ages predicted by the hinterland-dipping and foreland-dipping duplexes using the best-fit thermal parameters for the geometry.

The décollement geometry is kept constant.

2.4.3.1 Effect of ramp angle on cooling ages

The effect of changing ramp angles on the resulting cooling ages was first explored by Lock and Willett (2008). They looked at modeled AHe and AFT systems and showed that the reset age is the same regardless of the ramp angle. However, the across-strike distance over which the ages are reset widen with lower angles (Lock and Willett, 2008) (Figure 2.20). Because changing the duplex geometry changes the angles of both the modern MHT ramp as well as the angles of the ramps that form the duplex (Figures 2-3 and 2-18), we ran similar simulations, adjusting ramp angle with the ramp magnitude set to the size of the MCT ramp in our models. Similar to what Lock and Willett (2008) observed, all ramp angles produce the same reset chronometer age. A key difference is while the zones of reset AFT and ZHe widen with lower ramp angles, particularly

increasing the northern (down dip) extent of reset ages, the zone of reset MAr ages narrows with decreasing ramp dip (Section 2.8.3; Figure 2.20).

2.4.3.2 Effect of duplex geometry on cooling ages

To understand the effect of duplex geometry on the predicted cooling ages, we model hinterland-dipping and foreland-dipping duplexes using the same basal décollement, a constant velocity of ~19 mm/yr. (Ader *et al.*, 2012), varying the value of A_0 from 2.5 to 3.5 μW m^{-3}. We also test the antiformal stack geometry illustrated by the Hubbard et al. (2016) cross section.

Hinterland-dipping duplex

We show the sequential deformation of a hinterland-dipping duplex, along with the cooling ages predicted at key steps to illustrate the relationship between geometry and predicted cooling ages (Figure 2.4a-e; **Error! Reference source not found.**). As the RMT is emplaced on LH rocks, t he pattern of predicted ages shows the youngest ages at the ramp and a systematic increase in predicted ages towards the south in the direction of transport (Figure 2.4a). After emplacement of the MCT and RMT, young MAr ages at the active ramp represent the cooling during motion of the MCT while the youngest AFT ages at the ramp are a function of emplacement of the RMT (**Error! R eference source not found.**: timesteps 1-27). The oldest reset ages are always located at the front of the system, in the MCT and RMT hanging walls, and indicate the approximate age of deformation initiation of the MCT (MAr ages) or RMT (AFT ages). As the Trishuli thrust sheet is emplaced (Figure 2.4b and c; **Error! Reference source not found.**: timesteps 28-33), and initiates n ew ramps, the resulting exhumation in the model predicts younger ZHe and AFT ages in these locations. As the duplex develops, the position of the active ramp systematically migrates south producing a southward younging pattern of predicted ZHe and AFT ages with the youngest ages

located above the active ramp (Video 2.1: timesteps 34-41). The increase in erosional exhumation above the duplex, produces a pattern of reset MAr ages that record an earlier exhumational event (McQuarrie and Ehlers, 2017) during the emplacement of the Trishuli thrust (Figure 2.4b). The youngest MAr ages (<10 Ma) in the north are focused above the Trishuli thrust footwall ramp and increase in age to its southern extent (Figure 2.4d; Video 2.1: timesteps 34-40). As exhumation continues and erosionally removes the overlying GH rocks, we see a zone of unreset MAr ages, increasing in width with time, separating the reset ages in the Kathmandu synform from the reset ages in the north (Figure 2.4e, 55 – 90 km; Video 2.1: timesteps 40-48).

At the end of the sequential model, the youngest MAr ages (<10 Ma) are located at the top of the ramp and increase in age northwards (Figure 2.4e). Within the Kathmandu synform 40-60 km north of the MFT, MAr ages are reset cooling ages reflecting the age of RMT initiation. The predicted ZHe ages increase steadily towards the south from their minimum age (~1 Ma) above the active ramp. The slope of the predicted ages sharply increases 60 km north of the MFT, reaching the oldest predicted age at the Kathmandu synform ~40 km from the MFT. The AFT system produces a similar trend, with the youngest ages predicted at the ramp, increasing steadily towards the south, with the oldest ages predicted at ~40 km from the MFT in the core of the synform (Figure 2.4e).

The modeled ages produced by an A_0 value of 2.5 μW m^{-3} fit the measured data well (Figure 2.5a, red). The model is able to match the MAr ages measured in the Kathmandu synform, along with the zone of unreset ages above the duplex. The predicted ages are also able to reproduce the pattern of increasing MAr ages, north of 110 km from the MFT. However, the model fails to predict MAr ages of <5 Ma immediately south of the MCT. Increasing the surface heat production value from 2.5 μW m^{-3} to 3.5 μW m^{-3} in steps of 0.5 μW m^{-3} results in higher upper crustal

thermal gradients, and as expected, younger predicted ages in all three thermochronometer systems (Figure 2.5a) including <5 Ma MAr ages at the MCT. However, increasing heat production increases the spatial extent of reset MAr ages at the surface. Consequently, the zone of partial resetting observed between the MCT and Kathmandu synform becomes narrower and ~5 Ma MAr ages are predicted farther south of the MCT with increased radiogenic surface heat production. At A_0 = 3.5 μW m^{-3}, ~5 Ma MAr ages are found across the Gorkha-Pokhara antiform and no unreset ages are predicted between 70-95 km north of the MFT (Figure 2.5a, black). In the ZHe system, the higher heat production changes the age of the inflection point representing the oldest predicted age located 39 km north of the MFT as A_0 values increase from 2.5 μW m^{-3} to 3.5 μW m^{-3}. In addition, increasing radiogenic heat production decreases the predicted ZHe ages by ~1 Ma providing a better fit to the cooling ages across the antiform. However, a lower A_0 value of 2.55 μW m^{-3} is able to produce the best-fit of modeled to measured ages for all three thermochronometer systems (p-value = 0.32, RMSE = 2.22; Figures 2.6 and 2.22; Table 2.5). Even with our best fit model, the ages that are not matched well are the AFT ages and to a lesser degree the ZHe ages on the southern limb of the Kathmandu syncline. The model predicts AFT ages that are 2 to 6 Ma younger than the southern four measured ages, and ZHe ages that are ~1 Ma younger than measured ages between 30 and 35 km from the MFT.

Foreland-dipping duplex

Similar to the formation of the hinterland-dipping duplex, the patterns of predicted cooling ages for the foreland-dipping duplex show the youngest cooling ages above the active ramps (Figure 2.4a, f-i; Video 2.2). The cooling ages produced at the end of the emplacement of the RMT are very similar to that in the hinterland-dipping duplex model, with the youngest ages located at the ramp, increasing towards the south with reset MAr ages representing the emplacement of the

MCT (Video 2.2: timestep 1-28). Emplacement of the Trishuli thrust shows reset young AFT and ZHe ages above the active ramps (Figure 2.4f; Video 2.2: timestep 29). Initiation of duplex formation occurs with the emplacement of D1 over what becomes D2. The exhumation caused by this motion is seen in the predicted reset AFT and ZHe cooling ages (Figure 2.4g; Video 2.2: timesteps 30-31). The youngest AFT and ZHe ages are always over the active ramp, which remains in the north (Figure 2.4h). The stepwise pattern of the predicted ZHe and AFT ages track the systematic southward migration of the preceding active ramp after it is transferred to the upper plate (Figure 2.4g-h; Video 2.2: 30-38). Even with exhumation sufficient to expose the Trishuli thrust sheet above the duplex, the foreland-dipping model still retains young reset MAr cooling ages across the duplex (Figure 2.4i) that also show a stepwise pattern of increasing ages to the south.

The final cooling ages predicted by the foreland-dipping duplex geometry share the first-order shape of the ages predicted by the hinterland-dipping duplex using an A_0 value of 2.50 μW m^{-3}, because the southward translation of the hinterland duplex over the active ramp produces a similar pattern to a foreland-dipping duplex where the ramp is always in the north (Figures 2.4, 2.5 and 2.6). The most significant difference between the predicted cooling ages of the two models is the slope of the age versus distance trend from north to south (Figure 2.5). The predicted age versus distance slope from the foreland-dipping duplex is due to the development of the duplex over ~8 Ma creating a slope for all three chronometers that is notably steeper than the southward slope of AFT and ZHe ages produced by the translation of the hinterland dipping duplex over the ramp in the last 3-4 Ma. Like the hinterland dipping duplex, the youngest MAr ages (~5 Ma) for the foreland model are located at the top of the ramp. Even though the steeper ramp should produce a wider swath of young reset age (Figure 2.20) than a shallower ramp, the youngest reset ages only

span a 10-15 km distance before systematically getting older to the south (Figure 2.5b) due to uplift and exhumation over earlier ramps (Figure 2.4h-i). This additional exhumation produces reset MAr ages that extend 40 km south of the MCT (Figure 2.5b) in contrast to the swath of unreset and partially reset ages across the duplex in the hinterland dipping model.

Evaluating the fit of the predicted to measured ages shows that while this geometry predicts MAr ages that are similar in age to the measured data near the northern trace of the MCT (90-120 km) and in the Kathmandu synform (30-55 km) with an A0 value of 2.50 μW m−3, it cannot produce a zone of partially reset MAr ages between 55-90 km from the MFT. As expected, increasing the value of A0 to 3.00 only exacerbates the problem. Therefore, the heat production was decreased from 2.5 μW m−3 to 1.5 μW m−3 in steps of 0.5 to reach a balance between the width of the zone of partial resetting and retaining young reset MAr ages at the MCT. However, decreasing the value of A0 to 2.00 μW m−3 leads to reset MAr ages near the northern trace of the MCT that are 9 Ma, 4-5 Ma older than the measured ages, and systematically older ZHe and AFT ages (Figure 2.5b; Video 2.2). All of these differences lead to an increased mismatch between the predicted and measured ages. Even with these misfits, an A_0 value of 2.00 μW m−3 produces the best fit to the measured ages (Figures 2.6 and 2.21b; Video 2.2), with a p-value of 0.2, and a RMSE value of 2.589 (Table 2.5). Like the hinterland dipping duplex, the foreland-dipping model does not reproduce the trend of AFT ages in the southern limb Kathmandu syncline. The southern limit of reset and partially reset ZHe ages overlaps with measured ZHe age in GH rocks but misses the southern two ZHe samples at the MBT (Figures 2.5 and 2.6).

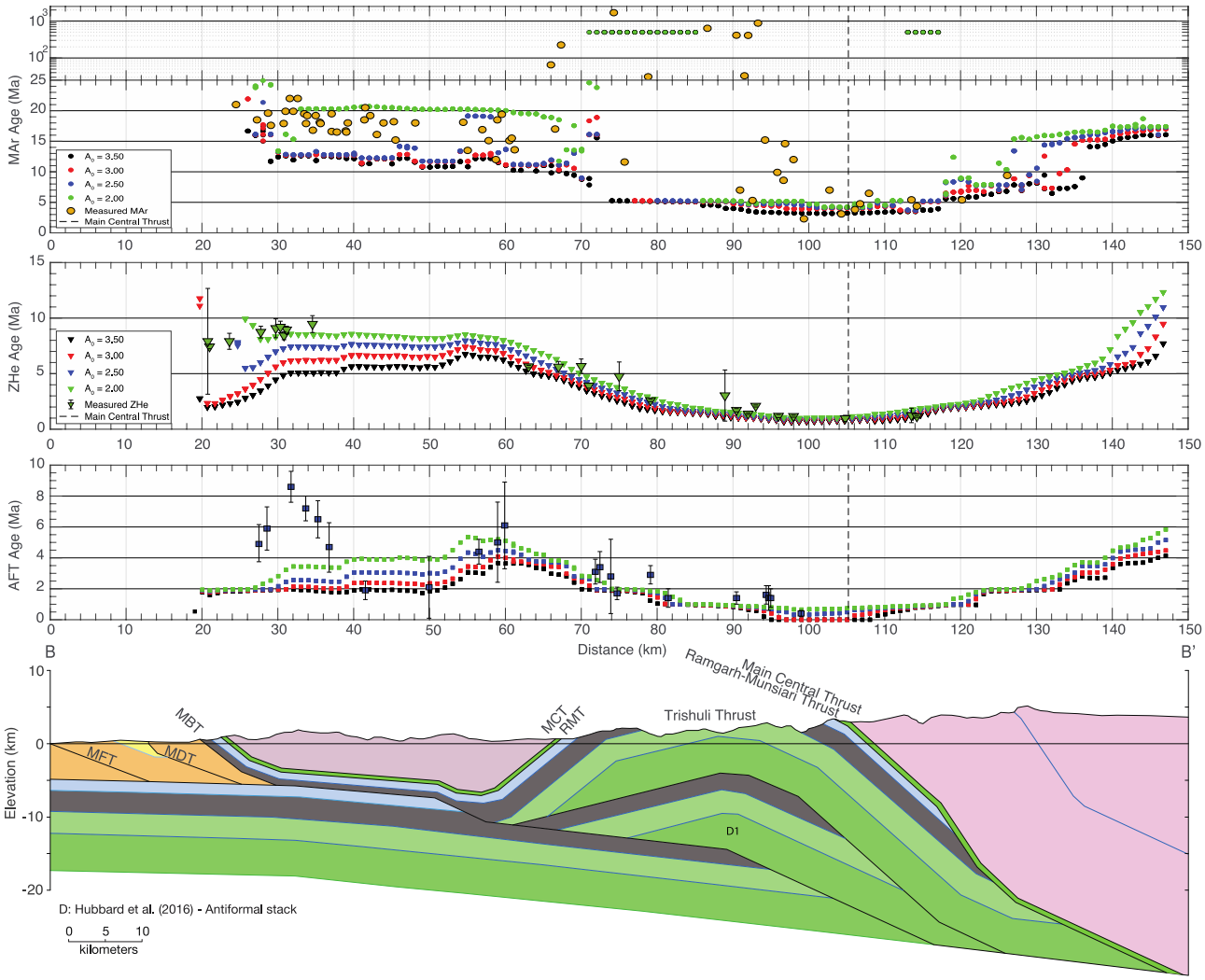

Figure 2.7: Predicted MAr, ZHe, and AFT ages compared to measured data for the cross section proposed by Hubbard et al. (2016).

The data shown are for four A_0 values (green: 2.00, blue: 2.50, red: 3.00, black: 3.50).

Antiformal stack

The antiformal stack geometry proposed by Hubbard et al. (2016) predicts the youngest cooling ages 5-10 km south of the MCT with predicted MAr cooling ages becoming progressively older north of the MCT, matching the ages and trend of the measured data (Figure 2.7). South of 70 km north of the MFT, in the region of the Kathmandu synform, the model predicts ages that are

~13 Ma rather than the 15-20 Ma measured ages using an A_0 value of 2.5 μW m^{-3} or greater. Of greater significance, predicted MAr ages between the MCT and the Kathmandu synform are young (3-5 Ma), and extend ~25 km south of the MCT. The focused uplift and erosion driven by the antiformal stack predict uniformly young reset ages in sharp contrast to the scattered, significantly older, partially reset measured MAr ages in the Gorkha-Pokhara antiform, 70-105 km north of the MFT (Video 2.3). This geometry predicts ~2 Ma ZHe ages at the MCT, which become older towards the south, matching the measured ages. However, the model predicts younger-than-measured ages between 20-35 km north of the MFT. Predicted AFT ages are 2-6 Ma younger than the measured ages between 25-40 km north of the MFT (Figure 2.7).

Increasing the value of the surface heat production from 2.5 μW m^{-3} to 3.5 μW m^{-3} decreases the match to measured AFT and ZHe ages between 20-35 km north of the MFT and to measured MAr ages between 65 and 95 km north of the MFT (Figure 2.7). Decreasing A_0 to 2.0 μW m^{-3} increases the width of the zone of predicted unreset MAr ages in the Gorkha-Pokhara antiform. However, even with an A_0 value of 2.0 μW m^{-3}, young, reset MAr ages are still predicted 20 km south of the MCT, such that the predicted zone of partially reset ages is too narrow to fit the measured data. The predicted ages in the Kathmandu synform increase to ~20 Ma and fit the oldest measured MAr data between 30-50 km from the MFT. The lower surface heat production values produce a better match to the measured ZHe data less than 40 km from the MFT, but the predicted cooling ages still miss the three southern measured ZHe ages and all AFT ages between 25 and 45 km north of the MFT (Figure 2.7). Even though a surface heat production value A_0 = 2.0 μW m^{-3} produces the best-fit for the geometry (Video 2.3), the fit is poor (p-value = 0.11), higher than the minimum threshold of 0.05 but significantly lower than the Whipple et al. (2016) hinterland-dipping model (0.32). Specifically, in the MAr system, the combination of exclusively

young (~5 Ma) ages predicted between 85-95 km north of the MFT, and a small cluster of unreset ages north of the MCT (112-118 km from the MFT) lowers the fit significantly. In addition, the very young predicted AFT ages (<4 Ma) between 25-45 km north of the MFT, which are the result of the southern ramp at 50 km north of the MFT, increases the statistical mismatch between measured and modeled ages (Figure 2.7). These two features ultimately result in a significantly higher RMSE (6.52) than either the hinterland- or foreland-dipping models (Figure 2.21a-b; Table 2.5), indicating that the antiformal stack is not a match to the data (Figure 2.21c).

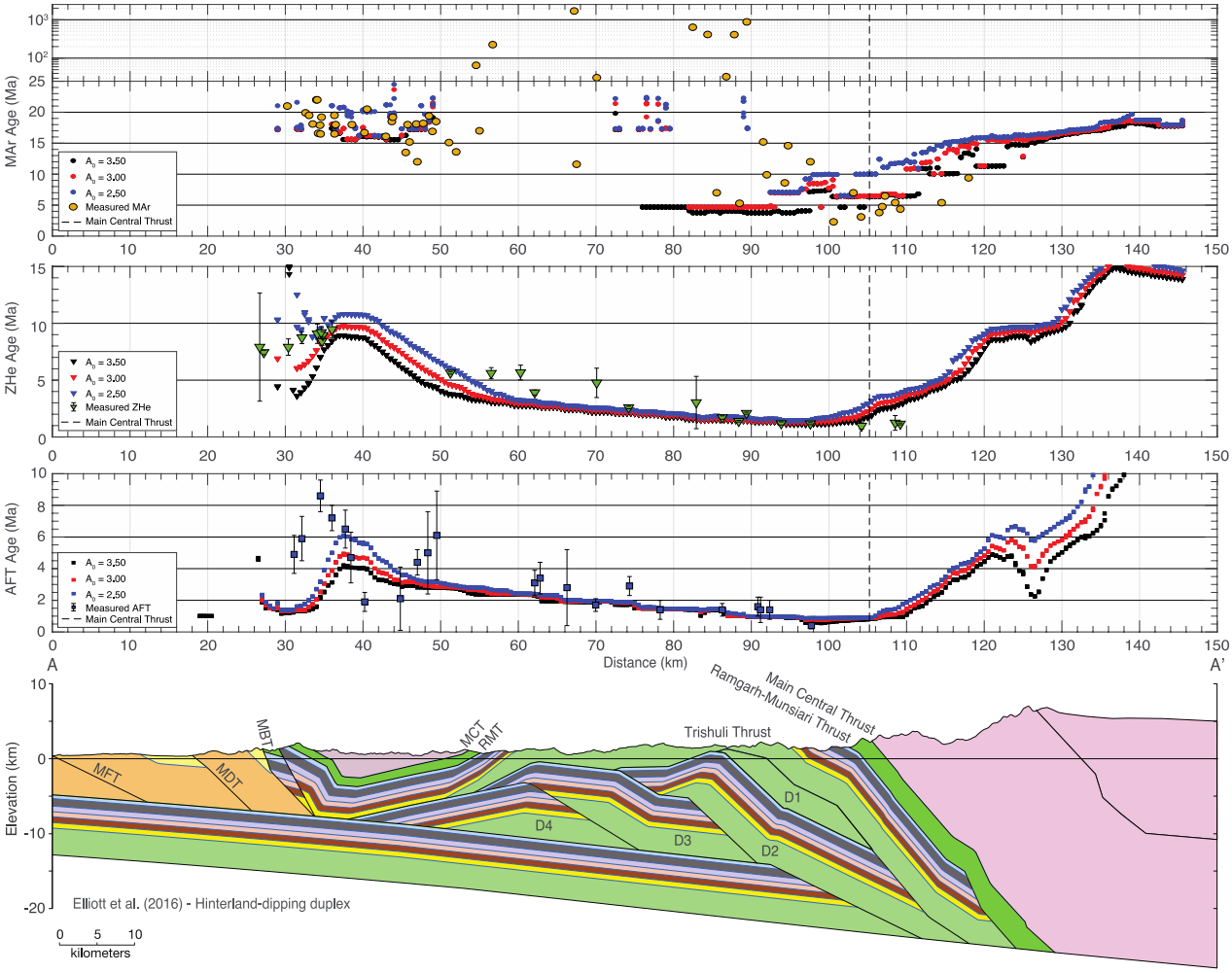

Figure 2.8: Predicted MAr, ZHe, and AFT ages compared to measured data for geometry based on the Elliott et al. (2016) décollement.

The data shown is for three A_0 values (red: 2.50, blue: 3.00, black: 3.50).

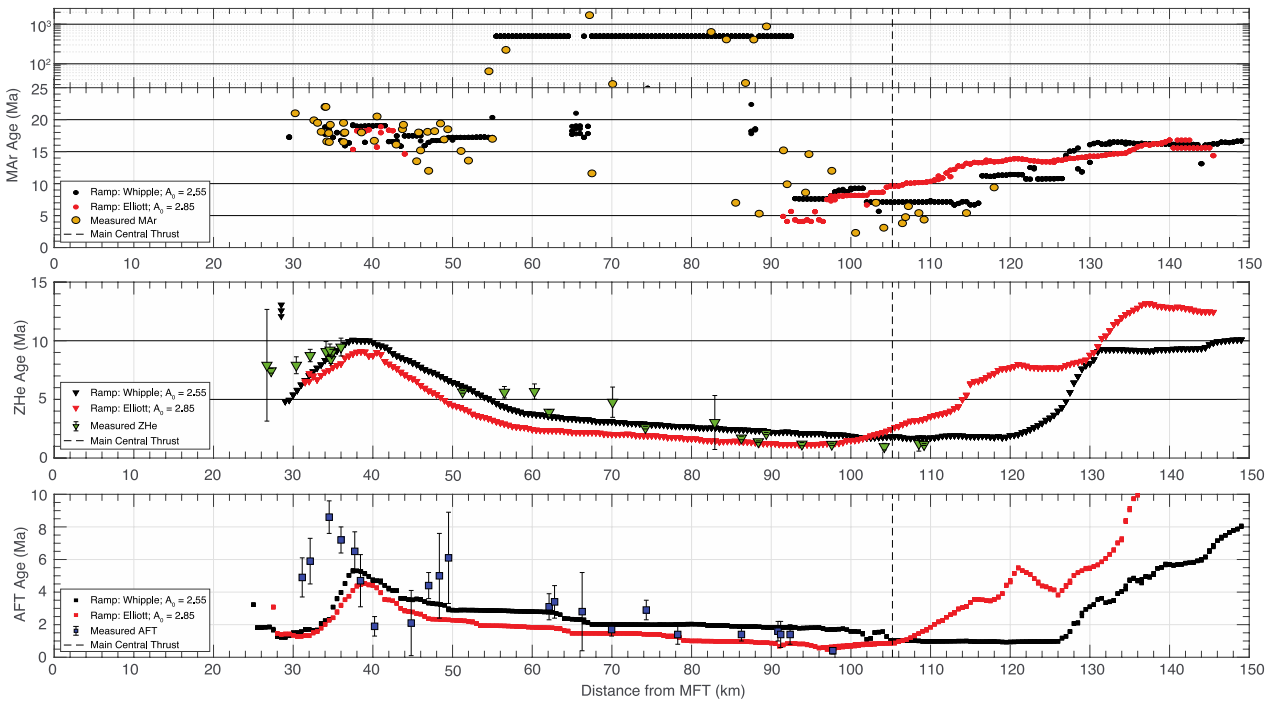

Figure 2.9: Plots comparing the best-fit predicted ages for the Whipple et al., 2016 geometry and that of the Elliott et al. (2016).

(red) Whipple et al. (2016) at A_0 = 2.55; (black) Elliott et al. (2016) at A_0 = 2.85. The data shown are at the same constant rate.

2.4.3.3 Effect of décollement geometry on cooling ages

To test the effect of the active ramp location, we compare the predicted cooling ages from a hinterland-dipping duplex based on the MHT geometry proposed by Elliott et al. (2016) to the predicted cooling ages from the hinterland-dipping duplex based on the Whipple et al. (2016) MHT geometry described above. The model based on the Elliott et al. (2016) ramp geometry was run with a constant convergence rate of ~19 mm/yr. using a range of A_0 values (2.5 – 3.5 μW m^{-3}; Figure 2.8; Video 2.4).

The final ages predicted using an A_0 = 2.50 show that the youngest cooling ages are located above the mid-crustal ramp, the top of which is located ~12 km south of the MCT (Figure 2.8).

The predicted MAr and ZHe ages systematically increase in age from the ramp northward from 3 Ma to 18 Ma (MAr), and from 1 Ma to ~15 Ma (ZHe). This contrasts with the measured ages, which are the youngest between the MCT and 4 km to the south (Figure 2.8). Similar to the décollement geometry of Whipple et al. (2016), the predicted ZHe and AFT ages gradually increase to the south until they reach an inflection point at 60 km (ZHe) and 45 km (AFT) north of the MFT, where the slope increases, reaching the oldest predicted ages of ~12 Ma (ZHe) and 6 Ma (AFT) at 39 km north of the MFT. The modeled ZHe and AFT ages fit the measured data well between 75 – 100 km north of the MFT, with low residuals. However, the mismatch is the greatest between 50-70 km (AFT and ZHe) and 105-110 km (ZHe) north of the MFT, where the residuals increase to ~2-3 Ma.

Increasing the heat production from 2.5 to 3.5 μW m^{-3} produces younger predicted MAr ages at the MCT, increasing the match between the modeled and measured ages between 100 and 120 km north of the MFT. However, this change also predicts young MAr ages south of the MCT, narrowing the width of the zone of predicted partial resetting (Figure 2.8). An A_0 value of 2.85 μW m^{-3} provides the best fit between the predicted ages (Video 2.4) and measured ages (p-value = 0.27, RMSE = 2.50; Figures 2.9 and 2.22d; Table 2.5). With this best fit, the youngest predicted MAr ages between 90 and 120 km north of the MFT are 10 km farther south and 5-10 Ma older than the youngest measured ages (Figure 2.9). The northernmost extent of predicted young ZHe ages does not align with measured ages. Predicted ZHe ages 100-110 km north of the MFT are 10 km farther south and 2-3 Ma older than the youngest measured ages.

Structure	Constant rate		Young Trishuli		Best-fit profile	
	Initiation (Ma)	Rate (mm/yr.)	Initiation (Ma)	Rate (mm/yr.)	Initiation (Ma)	Rate (mm/yr.)
MCT	23	19.44	20	31.75	23	21.17
RMT	16.47	19.44	16	12.62	17	18.01
TT	9.78	19.44	5.7	41.67	9.78	15.24
D1	7.2	19.44	4.5	41.18	6.5	38.3
D2	5.23	19.44	3.57	41.34	5.5	42.38
D3	4.36	19.44	3.16	41.75	5.1	41.75
D4_start	4.02	19.44	3	27.91	4.94	9.55
D4-mid	-	-	-	-	1.8	40
D4-end	-	-	-	-	1.3	18.18
OOS	0.93	19.44	0.85	28	0.75	18.67
MDT	0.79	19.44	0.75	20.28	0.6	25.17
MFT	0.41	19.44	0.39	20.51	0.31	25.81

Table 2.4: Velocity profiles for the hinterland-dipping model based on the Whipple et al. (2016) décollement geometry

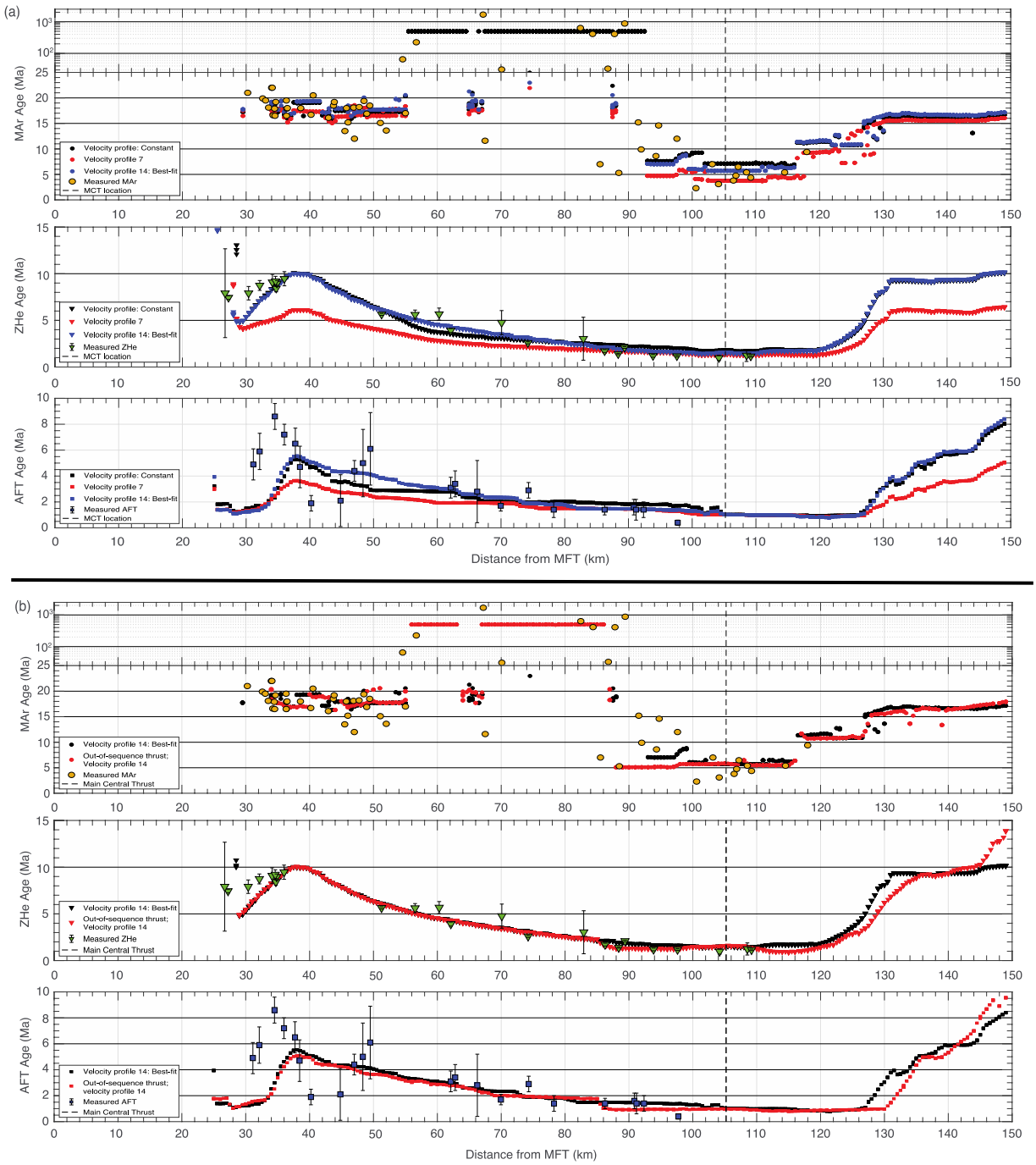

Figure 2.10: Effects of variable velocities and out-of-sequence motion on the predicted cooling ages. (a) Effect of variable velocities on predicted cooling ages. Plots compare three velocity profiles (Table 2.4) on the predicted cooling ages using the Hinterland-dipping duplex based on the Whipple et al. (2016) geometry. Black: Constant, Blue: Young Trishuli, Green: Best fit. (b) Plots comparing the effect of an out-of-sequence thrust uplifting material above the duplex (~85 km). Predicted ages comparing the effect of the out-of-

sequence thrust on the same duplex geometry are shown at the same A_0 (2.55) value, using the best-fit velocity profile. Black: No out-of-sequence thrust; Red: With out-of-sequence thrust.

2.4.4 Velocity analysis

Although the hinterland-dipping duplex based on the MHT geometry proposed by Whipple et al. (2016) produces a good fit to the measured data using a constant convergence velocity (~20 mm/yr.), several discrepancies remain. In this section, we consider the effect of variable shortening rates on the predicted cooling ages using the best-fit A_0 value of 2.55 μW m^{-3}. While the rate of displacement on faults controls the slope of the age-distance curve, the ages that define the curve are controlled by the initiation of fault motion (McQuarrie and Ehlers, 2015; Gilmore *et al.*, 2018). This relationship is seen by comparing the predicted ages in the constant-rate models to the time at which different structures initiate (Figures 2.5, 2.6, 2.7, 2.8, 2.9 and 2.23; Table 2.4).

We first attempt to decrease the predicted MAr ages at, and to the north of, the MCT to match the measured ages, which are at their youngest just south of the MCT and become steadily older to the north (Figure 2.10a). Changing the initiation age for the Trishuli thrust (TT) and the duplex (D1) to 5.7 Ma and 4.5 Ma (Table 2.4; Young Trishuli; Figure 2.22), respectively, reproduces the magnitude and trend of the MAr ages north of the MCT. The zone of partially reset ages between 55-95 km north of the MFT is also accurately reproduced. However, a 5.7 Ma initiation age for the Trishuli thrust also decreases the ages of the oldest ZHe age predicted at the front of the system (40 km north of the MFT) to 5.7 Ma, which is ~4 Ma younger than the measured ages between 30-60 km north of the MFT. The 5.7 Ma start for the TT also decreases the predicted AFT ages ~40 km north of the MFT, producing a residual of ~3 Ma (Figure 2.10a).

The best-fit velocity profile (Table 2.4; Figure 2.22) corrects these discrepancies. Because the MAr ages in the Kathmandu synform are set by the age at which the RMT initiates, setting the RMT to start at 17 Ma matches the data in the synform. Increasing the initiation age from 5.7 to 9.8 Ma for the Trishuli thrust decreases the fit of the MAr ages north of 110 km north of the MFT but improves the fit to the measured ZHe ages 30-40 km north of the MFT. Changing the duplex initiation age to 6.5 Ma predicts 6.5 Ma MAr ages at the MCT, while allowing the fourth horse of the duplex (D4) to initiate earlier (~5 Ma) and not exceed admissible convergence velocities. The age of initiation for the first and last horses in the duplex requires duplex formation to be fast, with the two middle horses moving at ~40 mm/yr (Table 2.4). This ensures that the trend of the predicted ZHe ages south of the MCT remains largely flat, matching the slope of the measured ages. The displacement on the fourth horse (D4) is what translates the duplex over the ramp a total of 60 km (Figures 2.4 and 2.5). Allowing the last 60 km of displacement to vary in velocity continues to improve the fit of measured to modeled ages. The first 20 km (D4_start) is slow at a rate of ~9 mm/yr. from 4.94 Ma to 1.8 Ma and matches the trend of steeper measured ages between 50-70 km north of the MFT. The middle part of the displacement (D4_mid) is significantly faster at 40 mm/yr. (Table 2.4, Figure 2.22). This allows the model to reproduce the flat trend of the young measured ZHe ages between 90-110 km north of the MFT. The final motion of D4 moves at ~18 mm/yr. from 1.3-0.6 Ma to best match modern convergence rates (Bilham *et al.*, 1997; Ader *et al.*, 2012). The p-value reaches a high of 0.62, along with a low RMSE of 0.974, making it the best-fit solution (Figure 2.21e, Table 2.5).

Because the velocity field in the model domain has a significant effect on chronometer age by setting the time at which rocks cool, we also evaluated whether applying variable velocities to the other duplex and ramp models (Figure 2.3) notably changed the match of predicted ages to

measured data. The results of this analysis are shown in Figures 2.24 and 2.25. To increase the match of young MAr ages located near and north the MCT for the Elliott et al. (2016) hinterland dipping model required initiation of the TT at 5 Ma as well as a RT initiating at 11 Ma to better fit predicted MAr ages north of the MCT (Figure 2.23, blue). However, these changes also produce MAr ages that are too young in the Kathmandu synform and south of the MCT (80-90 km north of the MFT) and ZHe and AFT ages between 30-70 km from the MFT that are much too young. A best-fit model (Figure 2.23, red) has the TT active from 7-10 Ma to match the ZHe ages between 30 and 40 km from the MFT and has a window of slow shortening rates (~1-3 Ma) during initial translation of the duplex over the ramp to match the slope of ages versus distance of AFT and ZHe ages between 50-70 km from the MFT. Problematically, this velocity field completely fails to reproduce the ages north of the MCT and produces modeled ages that are 3-4 Ma older than the northern three ZHe ages between 100-110 km from the MFT (Figure 2.23). Thus, changing velocities permit us to find a better fit to the hinterland ages, or a better fit to the foreland ages, but not both. It also highlights the strong control of the ramp position on the location of the youngest ages. The mix of poorly matched hinterland ages with a good fit south of the MCT leads to a reasonably high p-value (0.32), and a low RMSE (1.8).

For the foreland-dipping duplex model, increasing the fit to the MAr ages at and to the north of the MCT also requires an older start for RT initiation and a young age for TT initiation at 15 Ma and 6 Ma, respectively (Figure 2.24, Blue). Similar to the velocity changes for the southern ramp model (based on Elliott et al., 2016), this increases the fit of the MAr ages >100 km north of the MFT; however, it predicts significantly younger ZHe and AFT ages between 30-70 km north of the MFT. Additionally, while the 1.9 Ma initiation age and ~58 mm/yr. velocity of the final duplex horse helps increase the fit of the ZHe and AFT ages between 85-110 km north of the MFT,

the significantly high rate of exhumation created by the duplex emplacement (Figure 2.24, blue) causes the model to predict young, reset MAr ages between 60-80 km north of the MFT, and AFT ages that are <3 Ma between 30-50 km north of the MFT. The best-fit profile (Figure 2.24, green-dashed) that fits the measured ZHe and AFT ages in the foreland produces a much lower match (3-5 Ma difference) to measured MAr ages between 100 and 115 km north of the MFT and results in a high p-value of 0.43, and low RMSE of 1.6. The lower mismatch between measured and modeled ages obtained by the foreland-dipping geometry (when compared with the results from the best fit velocity from the southern ramp geometry proposed by Elliott et al., 2016) is largely due to the northerly location of the mid-crustal ramp, further reinforcing our hypothesis that the ramp location is the primary control on the location of young cooling ages. While still important, the geometry of the duplex is a secondary control.

2.4.5 Effect of out-of-sequence thrusting

We test the sensitivity of the cooling ages by adding an out-of-sequence thrust located ~85 km north of the MFT using the hinterland-dipping geometry based on the best-fitting Whipple et al. (2016) MHT geometry. This out-of-sequence thrust was proposed to explain the rapid increase in topographic elevation, slope and river steepness termed the Physiographic Transition 2 (PT2) and has been argued as having significant control on the pattern of cooling ages (Wobus, Hodges and Whipple, 2003; Wobus, Whipple and Hodges, 2006; Whipple *et al.*, 2016). In the constant-rate model (~19 mm/yr.), the out-of-sequence thrust is active from ~0.25 Ma until the end of the model, moving a total of 5 km. The effect of out-of-sequence thrusting is most clearly visible in the predicted ages north of 85 km from the MFT, with the predicted MAr ages 1-3 Ma younger, predicted ZHe ages 0.5 to 1 Ma younger and AFT ages 1 Ma younger (Figure 2.25). This change

increases the fit of the model by decreasing the residuals for both the ZHe and the AFT ages at distances greater than 85 km north of the MFT producing a higher p-value, 0.41 (compared to 0.32), and an RMSE of 1.975 (compared to 2.221) (Table 2.5). We also added the out-of-sequence thrust to the best-fit velocity profile (Figure 2.10b, red) and see a similarly small shift in the revised fit, increasing the p-value from 0.62 to 0.7, and decreasing the RMSE from 0.974 to 0.852.

2.5 Discussion

2.5.1 Sensitivity of cooling ages to subsurface geometry

Cooling ages in active fold-and-thrust belts are dependent on location of active erosional exhumation. In the Himalaya, this uplift-induced erosion is thought to be driven by an active duplex (DeCelles et al., 2001; Robinson et al., 2003; Khanal and Robinson, 2013), a major ramp in the décollement (Bollinger, Henry and Avouac, 2006; Herman *et al.*, 2010; Long *et al.*, 2012; Gilmore *et al.*, 2018; McQuarrie *et al.*, 2019), and/or out-of-sequence thrusting in the hinterland (Wobus, Hodges and Whipple, 2003; Hodges *et al.*, 2004; Wobus *et al.*, 2005; Wobus, Whipple and Hodges, 2006). Each of these mechanisms creates a distinct pattern of exhumation, and thus, a distinct pattern of cooling ages that can be used to assess the viability of proposed drivers of uplift.

2.5.1.1 Duplex geometry

One of the most distinctive trends visible in the across-strike pattern of cooling ages in central Nepal is a zone of unreset to partially reset MAr ages distributed between ~60-105 km

north of the MFT, where the ages range from ~2.0 Ga to 204 Ma and require that none of these rocks underwent prolonged heating above the MAr closure temperature during Himalayan orogenesis (Wobus, Hodges and Whipple, 2003; Wobus, Whipple and Hodges, 2006) (Figures 2.2a and 2.15). The transition between predicted unreset to reset MAr ages in our best-fitting model is coincident with a shift in peak modeled temperatures from 340°C (unreset) to 380°C (reset) indicating they cooled at rates below 5°C/Myr early in duplex formation. The zone of unreset and partially reset MAr ages is over the LH duplex, where the MCT and RMT sheets have been eroded, leaving the LH rocks of the Trishuli thrust sheet exposed. Whether the Trishuli thrust reaches the temperatures and exhumation rates required to reset MAr ages depends on the duplex geometry. Formation of an antiformal stack as proposed by Hubbard et al. (2016) focuses exhumation in the middle of the antiform at rates that keep temperatures high in the Trishuli thrust, predicting young ages (<5 Ma) throughout the partially reset zone, in contrast to the large, partially reset age range in the measured data (Figure 2.7; Video 2.3). Similarly, the formation of a foreland-dipping duplex also concentrates high exhumation rates over the active ramp, which remains at the northern edge of the duplex maintaining elevated temperatures in this region (Figure 2.4). Only the lowest surface radiogenic heat production values prevent reset modeled MAr ages (Figure 2.5b; Video 2.2); however, the resulting youngest predicted MAr ages at the MCT are also 4-5 Ma older than measured ages (Figure 2.5b). The broader exhumation pattern combined with the two-part exhumation history of the hinterland dipping duplex (initial duplex formation followed by the translation of the duplex over the ramp) based on the décollement geometries of Whipple et al. (2016) and Elliott et al., (2016) can reproduce the large zone of unreset MAr ages above the duplex (Figures 2.5a, 2.8 and 2.9; Videos 2.1 and 2.4).

The kinematics and rate of duplex formation are important for the shape of the predicted ZHe cooling age curve. The measured ZHe ages have the youngest ages located in the north, characteristic of a foreland-dipping duplex (McQuarrie and Ehlers, 2017). Although the foreland-dipping duplex can reproduce the first-order shape of the ZHe cooling signal, rapid rates of thrusting (>45 mm/yr.) are required in the last 1-3 Ma to match the young ZHe ages south of the MCT (Figure 2.23). Our hinterland dipping duplex model reproduces the ZHe age pattern by translating the duplex over the ramp across a narrower window of time. However, in our best fit hinterland-dipping duplex model, fast rates (~40 mm/yr. between 4 - 6.5 Ma and 1-2 Ma) are also required to most closely match the measured ZHe ages (Figures 2.10 and 2.22). The rate of the translation sets the slope of the age versus distance trend in the ZHe system.

All four models fail to match the sinusoidal curve of AFT ages between 30 and 50 km from the MFT. The measured AFT ages are incongruous with the first-order shape of the Kathmandu synform with the youngest ages (~2 Ma) in the syncline core and older ages (4-6 Ma) on the outer limbs. Combined with this first-order pattern are ages as old as 7-9 Ma on the southern limb of the synform (Figure 2.1). The ZHe ages are limited to 26-36 km and 50-60 km north of the MFT, have a much narrower range in ages, and are very similar in age to the AFT ages at ~35 and 50 km north of the MFT. However, the lack of overlap in AFT and ZHe chronometers between 35-50 km from the MFT makes it impossible to discern if the young AFT ages in the syncline core are a result of young shallow exhumation processes or if exhumation was sufficient to reset ZHe ages (Figure 2.5). The Hubbard et al. (2016) geometry with its southern ramp provides a mechanism to match the youngest AFT ages in the syncline but predicts ages that are 2-6 Ma too young farther to the south between 28 and 38 km north of the MFT (Figure 2.7). The foreland and hinterland models miss the youngest AFT age in the syncline core, as well as the four southern AFT ages that are

distinctly older than the predicted ages (Figures 2.5 and 2.6). The mismatch between predicted ages and measured ages at the southern limb of the Kathmandu synform and MBT highlight that there are structures and geometries that are not accurately modeled by any of the four cross sections. Throughout Nepal, the geometry of the MBT is not a simple, recent thrust fault (Robinson, DeCelles and Copeland, 2006; Khanal and Robinson, 2013; Riesner *et al.*, 2019) (Figures 2.1 and 2.13). In particular, our mapping highlights a normal fault between the trace of the MBT and the MCT at the southern edge of the Kathmandu synform between the two cross section lines (Figure 2.1). A structure such as this one has the potential to alter exhumation paths of AFT samples in its immediate hanging wall (Figure 2.1) depending on the age and magnitude of displacement. The location and limited lateral extent of this and other out-of-sequence faults have the potential to impart lateral differences in the shallow cooling history and argues that the exhumation paths for frontal portions of the two cross sections should be evaluated independently.

2.5.1.2 Décollement geometry

Horizontal convergence in fold-and-thrust belts is converted into uplift and exhumation by displacement over active ramps. The active ramp location determines where exhumation is focused in the system, and as a result, the location of the youngest cooling ages (Lock and Willett, 2008). In the past, a number of different locations have been proposed for the active ramp of the MHT, based on a variety of constraints like the concentration of microseismicity (Pandey *et al.*, 1995), stratigraphic requirements from balanced cross sections (Pearson, 2002; Khanal and Robinson, 2013), and inverse modeling of thermochronometer data (Herman *et al.*, 2010; Robert *et al.*, 2011) (Figure 2.2b). Critically, the Gorkha earthquake showed that past estimates for the location of the mid-crustal ramp in central Nepal were incorrect, placing it between 15 – 45 km north of the previously proposed locations (Figure 2.2c).

Elliott et al. (2016) proposed an updated MHT geometry with a mid-crustal ramp located ~90 km north of the MFT (Figure 2.2c). They used a combination of geodetic measurements from the earthquake, microseismicity (Pandey *et al.*, 1995), magnetotelluric data, where the zone of high resistivity was interpreted as the fault zone (Lemonnier *et al.*, 1999), and river incision rates (Lavé and Avouac, 2000). Hubbard et al. (2016) proposed their mid-crustal ramp in a similar location, based on the same data used by Elliott et al. (2016), and its location at the northern boundary of the zone of greatest slip (4-5 m) during the earthquake (Avouac *et al.*, 2015). They also used this location of the active ramp to explain the formation of the Gorkha-Pokhara anticlinorium. In both the Elliott et al. (2016) and Hubbard et al. (2016) geometries, the youngest ZHe and AFT ages are predicted ~5 km south of the MCT, located at the upper 5 km of the ramp (Figures 2.7 and 2.8; Videos 2.3 and 2.4). The two geometries differ with respect to the youngest MAr ages. In the Hubbard et al. (2016) model, the youngest MAr age (~4 Ma) is predicted in the middle of the active ramp, at the surface trace of the MCT, whereas the Elliott et al. (2016) geometry has the youngest ages located at the top of the ramp ~10 km south of the MCT (Figure 2.8). The stacking of the previous ramp (active until ~1.7 Ma; Hubbard et al., (2006}) on top of the currently active ramp in the Hubbard et al. (2016) geometry leads to the concentration of the youngest MAr ages (~4 Ma) in the middle of the ramp, but also predicts equally young ages 20-30 km south of the MCT. The translation of the previous ramp ~30 km over the newly active ramp in the Elliott et al. (2016) model leads to the prediction of the young MAr ages at the top of the active ramp ~10 km south of the MCT when a low surface heat production is used. With increasing values of A_0 young ages are predicted even farther to the south.

A more northern location for the mid-crustal ramp as proposed in the Whipple et al. (2016) geometry pushes the center of exhumation north of the MCT thereby leading to the concentration

of the youngest MAr ages at the MCT (Figure 2.9: 100-110 km north of the MFT). The similar duplex geometry in the Elliott et al. (2016) and Whipple et al. (2016) hinterland-dipping models ensures that the observed differences in the cooling ages are solely due to the effect of the different ramp locations (Videos 2.1 and 2.4). In the hinterland-dipping duplex model, the locations of the youngest cooling ages are highly sensitive to the location of the ramp (Figure 2.9). The location and angle of the ramp defines the location and slope of the increasing ages to the north of the MCT. The ~10 km misfit between the youngest predicted ages and the measured ages in the Elliott et al. (2016) model requires that the ramp be located at least 10 km farther to the north, potentially 20 km north (Figures 2.2 and 2.9).

The demonstrated link between exhumation and the location of ramps in convergent systems strongly suggests that thermochronometer data can be inverted using an ensemble inversion (Sambridge, 1999) to determine a décollement depth and ramp geometry that best matches the measured cooling ages at the surface (Herman *et al.*, 2010; Robert *et al.*, 2011; Coutand *et al.*, 2014). In this method, the best-fit geometry for the main décollement is determined based on iteratively recalculating the probability distribution functions to lower the misfit between predicted ages and the measured ages at the surface, assuming that the décollement geometry is the only control on the final cooling ages. If this assumption were true, then changing the geometry of the duplex would not have any effect on the chronometers most sensitive to the active ramp location (i.e., ZHe and AFT). The differences in the final cooling ages predicted by the hinterland- and foreland-dipping duplex models (Figures 2.5 and 2.6) indicate that a large component of the cooling signal is the result of duplex formation and the associated evolution of ramps and ramp locations that preceded the final modern ramp. The final cooling ages are therefore a combination of both the duplex geometry and the modern ramp location. The effect of changing the duplex

geometry on the predicted cooling ages while maintaining the same ramp location is also apparent in the Elliott et al. (2016) and Hubbard et al. (2016) models, which have the same southern mid-crustal ramp location but different duplex geometries (Figures 2.7 and 2.8). These two sets of models all produce different predicted AFT and ZHe ages over and in front of the décollement ramp. These discrepancies highlight that caution is needed when using inverse techniques to determine the subsurface geometry.

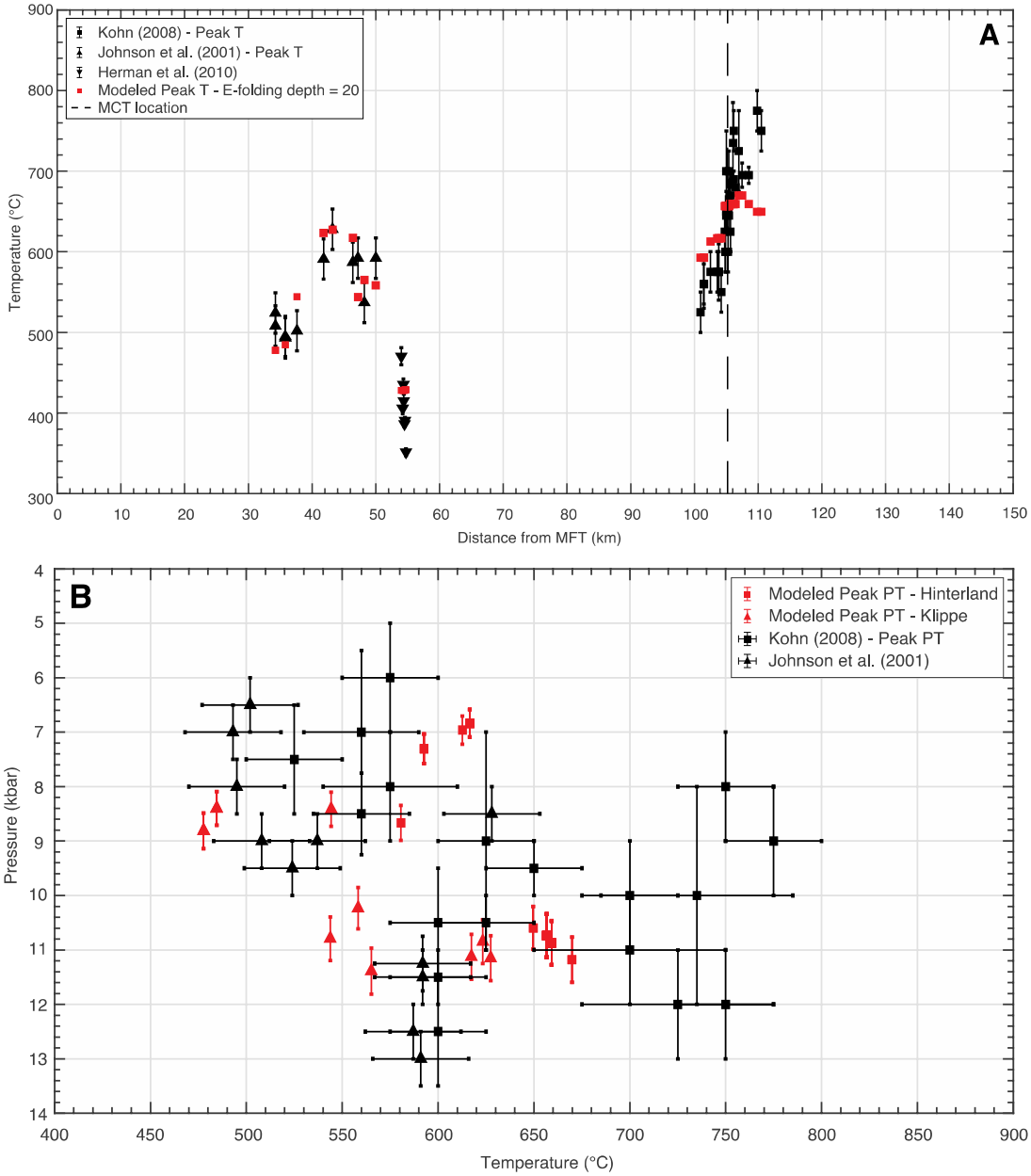

Figure 2.11: Comparison between predicted and measured Peak temperature and pressure.

(A) Plot comparing modeled peak temperatures (red) with measured values (black) from the region. (B) Comparison between modeled (red) and measured (black) peak PT values for the region. All results shown here are from the best-fit model. Measured data shown here are from Johnson et al. (2001); Kohn (2008) and Herman et al. (2010).

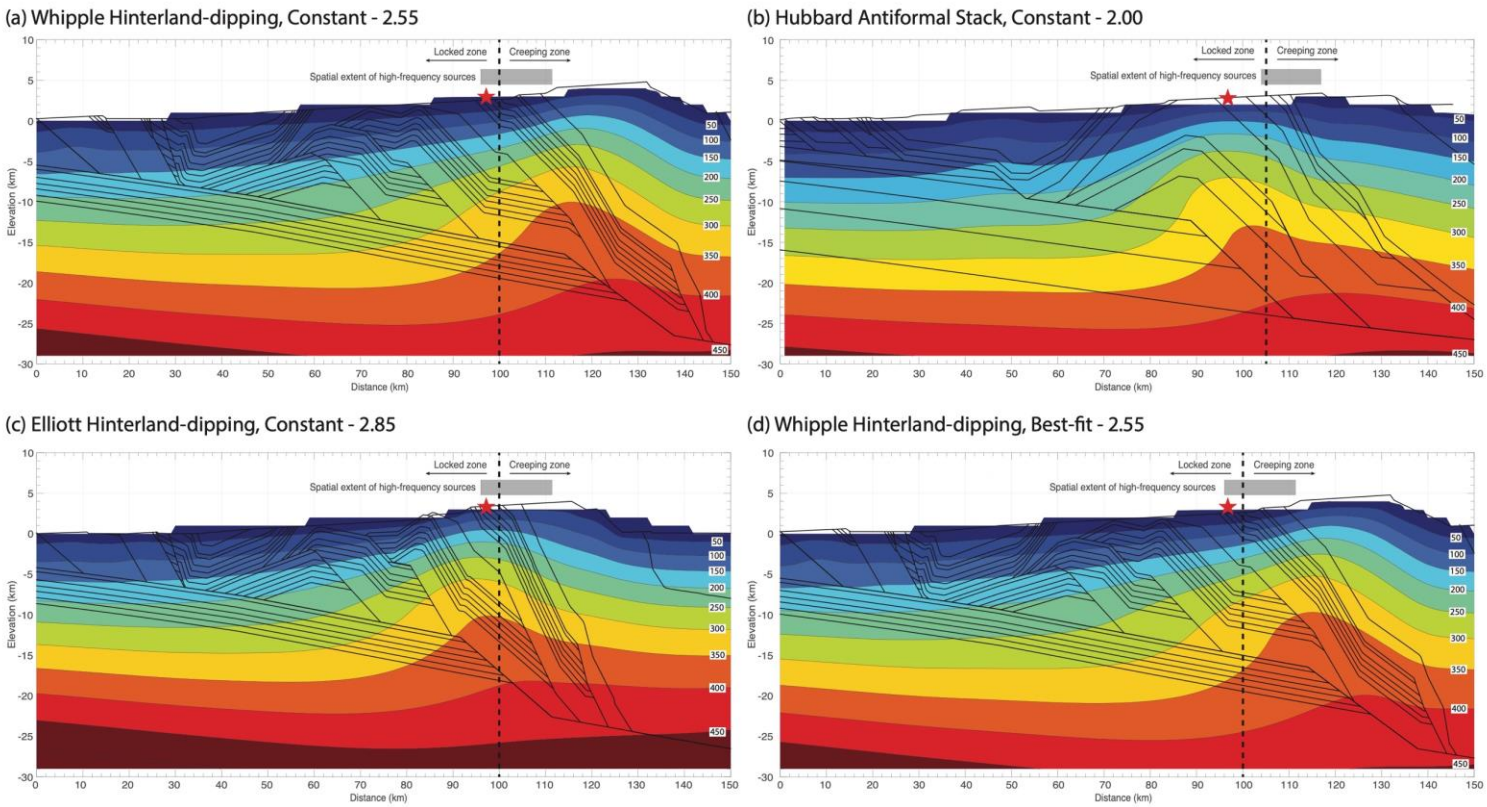

Figure 2.12: Comparison between the predicted thermal field, cross section geometry, and location of high-frequency seismic sources, the Gorkha Earthquake, and the modeled transition zone between creeping and locked portions of the MHT (Ader et al., 2012).

The red star marks the location of the epicenter of the Gorkha earthquake. Grey zone shows the spatial extent of the high-frequency sources for the Gorkha earthquake (from Grandin et al., 2015). (A) Whipple et al. (2016) décollement – Hinterland-dipping duplex, Constant rate, A_0 = 2.55; (B) Hubbard et al. (2016) décollement, Antiformal stack, Constant rate, A_0 = 2.00; (C) Elliott et al. (2016) décollement, Hinterland-dipping duplex, Constant rate, A_0 = 2.85; (D) Whipple et al. (2016) décollement, Hinterland-dipping duplex, Best-fit velocities, A_0 = 2.55. Contour values are in °C.

2.5.2 Thermal structure

Altering the model thermal properties results in a hotter or cooler subsurface thermal field. A result of this thermal change is that predicted cooling ages become younger and/or occupy a wider extent as surface heat production (A_0) increases from 2.0 to 3.5 (Figures 2.5, 2.7, and 2.8). The first-order constraint on how warm the subsurface thermal field can be for a given cross section model is whether the model predicts reset MAr ages where measured MAr data are unreset and partially reset between 54 and 92 km north of the MFT for the Whipple et al. (2016) and Elliott et al. (2016) models (Figures 2.1, 2.5 and 2.8) or between 66 and 94 km for the Hubbard et al. (2016) model (Figs. 1 and 7). As mentioned in the previous section (2.5.1.2), there is a strong correlation between the location of the mid-crustal ramp and the youngest MAr cooling ages, as well as between the applied surface radiogenic heat production value (A_0) and the ability of the model to reproduce the zone of partially reset MAr ages between the MCT and the Kathmandu synform (Figures 2.5, 2.7 and 2.8). The resulting subsurface thermal fields that are required to best reproduce the measured thermochronometers can also be compared to measured peak temperatures and modern geothermal gradients.

We compare the predicted thermal evolution of our best-fit model to existing deformation and peak temperature estimates from central Nepal (Figure 2.11A; Video 2.1). Due to the potential sensitivity of the evolving thermal field to our initial thermal structure, we also compare the predicted to measured temperatures using a constant heat production value (Section 2.8.3.2, Figure 2.19). GH rocks carried by the MCT are exposed in the Kathmandu synform to the south and north of the MCT. While they both originate from the same thrust sheet, thermobarometry suggests that the rocks in the synform experience lower temperatures (~500-630 °C) but potentially the same peak pressures (~9-12 kb) as the rocks exposed in the north (Johnson *et al.*, 2001; Kohn *et al.*,

2004; Kohn, 2008) (Figure 2.11B). The thermal field predicted by our best-fit model shows a temperature gradient through the frontal portion of the thrust sheet (which will become the Kathmandu synform) and ranges from 650 °C at the base (~43 km deep) to 500 °C at the top of the GH section at a depth of ~22 km. The depth increases to ~50 km in the north with this northern portion experiencing temperatures in excess of 650 °C during motion on the MCT (Figure 2.12). Although initial emplacement of the MCT over the RMT occurs at ~500 °C, the front half of the thrust sheet quickly cools to below 450°C. Burial of the RMT sheet by the MCT means that the rocks experience peak temperatures of ~600°C in the north, similar to that measured along the Trishuli River (Figures 2.1 and 2.13) near Langtang (Kohn *et al.*, 2004; Kohn, 2008), while the southern half of the RMT reached temperatures from 400°C (southern limit) to 500°C (Figure 2.11A). These temperatures and the load of the overlying GH rocks lead to the layer-normal flattening observed within the RMT rocks (Larson, Godin and Price, 2010; Larson and Cottle, 2014). Emplacement of the RMT rocks over the Trishuli thrust sheet and the associated exhumation cools the rocks exposed in the RMT to <350 °C. Rocks exposed in the Trishuli thrust sheet, as well as each duplex thrust are displaced at temperatures of 300-400 °C, and only the northernmost horse and northern edge of the Trishuli thrust deformed at the upper temperature range (400-450°C). Modeled LH rocks carried by the Trishuli thrust and exposed at the surface reached temperatures of 260-400°C, with the highest temperatures (450-620°C) within 5 km of the MCT (Figure 2.11A). Most of the faults which deform LH rocks were displaced at or below the brittle-ductile transition (Video 2.1). Quartz deformation structures and vorticity analyses from LH rocks directly south of the RMT show that these rocks underwent layer-normal flattening at temperatures of 350-450°C (Larson and Godin, 2009; Larson, Godin and Price, 2010; A. J. Parsons, Ferré, *et al.*, 2016; A. J. Parsons, Law, *et al.*, 2016) due to the overburden of structurally

higher thrust sheets (Long et al., 2011; 2016). Because the highest temperatures and resulting layer-normal flattening occurs prior to thrust motion, the resulting penetrative strain has minimal to no effect on the cooling ages driven by exhumation. The final thermal field shows a geothermal gradient of 35°C/km above the northern ramp while maintaining a cool gradient of 15°C/km at the southern edge of the model similar to heat flow measurements in the Indian Shield (Roy and Rao, 2000) (Figure 2.12).

In addition to the thermal evolution through time, we evaluate how the final predicted thermal structure relates to the thermal conditions that have been argued as necessary to control the location where the MHT transitions from locked to creeping (Ader *et al.*, 2012), as well as compare the structure of the thermal field to the location of high frequency emissions, which may identify the downdip limit of the seismogenic domain (Lay *et al.*, 2012). Maps of coseismic slip from the 2015 Gorkha earthquake show a rapid decrease of slip in the downdip direction with the lower limit of slip (≤2 m) coincident in space with the locations of high-frequency source emissions and a marked decrease in the percentage of interseismic coupling (Grandin *et al.*, 2015). These observations are consistent with decreased coupling limiting the propagation of the Gorkha earthquake rupture to greater depths (Grandin *et al.*, 2015). Laboratory experiments on quartzo-feldspathic rocks emphasize the control of temperature on the transition from frictional sliding to stable creep, highlighting that the critical temperature is 350°C (Blanpied, Lockner and Byerlee, 1995; Marone, 1998; Hsu *et al.*, 2009). Figure 2.12 shows the relationship between the modeled temperature field, fault geometry, the boundary between where interseismic coupling is greater or less than 75% (Grandin *et al.*, 2015) and the location of the Gorkha earthquake. The strong correlations in space between the 350°C contour on the Whipple et al. (2016) model, the transition of the MHT from creeping to locked, the Gorkha earthquake and the high frequency sources

strongly suggest a thermal-rheological control rather than a geometric-structural control as the underlying cause of the seismic coupling gradient. The more southerly position of the ramp in the Elliott et al. (2016) and Hubbard et al. (2016) models place the boundary in interseismic coupling on the ramp and at higher temperatures, much closer to 400°C (Figure 2.12).

2.5.3 Age of initiation vs. rate of motion

Cooling ages are produced by rock uplift and associated erosion as a thrust sheet moves over a ramp. The ages are sensitive to when exhumation began and the rate at which it occurred. Because of this relationship, the trends in the measured MAr, ZHe, and AFT ages can be used to extract information about the initiation and rates of development of major structures in a fold-and-thrust belt. We find a better fit to the measured thermochronometers using variable shortening velocities rather than a constant rate of 19 mm/yr. Predicted MAr ages in the Kathmandu synform are set by the initiation of the RMT, rather than the MCT, and an initiation age of 17 Ma produces a best fit. However, because the hanging wall cutoffs for these thrust sheets are eroded, and the internal strain in these rocks suggest some additional component of displacement via transport parallel stretching (Law et al., 2013; Long et al., 2016), it is possible that they have travelled a greater distance than that modeled here. Although our model is consistent with both the MCT and the RMT moving close to the long-term average shortening rate of ~20 mm/yr, we have no constraints on the age and rate of the MCT, and any additional, unobserved motion on the RMT means that it would have to start earlier (than 17 Ma) and move faster than modern shortening rates. In the hinterland-dipping models, the MAr ages north of the MCT, along with the ZHe ages 40 km from the MFT are both set by the initiation age of the Trishuli thrust. The youngest MAr ages predicted at the MCT are in turn set by the initiation of the duplex (D1, Figure 2.10a, Table

2.4). The measured ages at these locations constrain the time of this deformation to 9.8 Ma and 6.50-5 Ma, respectively setting the rate of the Trishuli thrust to ~15 mm/yr and the rate of duplex formation to ~40 mm/yr between 6.5 and ~5 Ma. The measured ZHe age (~4.94 Ma) ~60 km north of the MFT is set by the initiation age of the last horse of the duplex, as it moves the assembled duplex over the active mid-crustal ramp, placing it in its modern position. For our best-fit model, this translation is fast (~40 mm/yr) to match the flat pattern of young measured ZHe and AFT ages between 60-120 km north of the MFT. Finally, displacement of the Subhimalayan thrust sheets (MDT and MFT) are maintained at ~20 mm/yr, consistent with modern-day measurements of convergence of the central Himalaya (Grandin *et al.*, 2015).

2.5.4 Out-of-sequence thrusting

Whipple et al. (2016) propose that an out-of-sequence thrust produced an uplift anomaly seen in geodetic data north of PT2 following the Gorkha earthquake and that this thrust fault maintains the increased elevation, steep slopes and intensified erosion north of PT2 as documented in cosmogenic nuclide data. The existence of such a young thrust, important enough in both size and displacement to significantly modify the landscape, should also be revealed in its effect on thermochronological cooling ages (Wobus, Whipple and Hodges, 2006).

We evaluated the predicted cooling ages due to an out-of-sequence thrust that breaks the surface ~80 km north of the MFT with 5 km of displacement, using the hinterland-dipping model based on the Whipple et al. (2016) geometry (Figure 2.3a). The displacement on the thrust is limited by the requirement that only the Kuncha Formation may be exposed at the surface. The out-of-sequence thrust lifts the rocks of the hinterland, focusing exhumation north of 80 km. This extra exhumation creates a break in the trend of the predicted ages, with younger predicted ages to

the north (Figures 2.10 and 2.25). The change in the predicted ages is small (~1 Ma), but distinct in the ZHe and AFT systems. Adding the out-of-sequence thrust to the end of our best-fit velocity profile increases the fit compared to the best-fit velocity profile without the thrust (p-value: 0.62 to 0.7; RMSE: 0.974 to 0.852). The increase in p-values and decrease in RMSE are sufficiently small to unequivocally determine the existence of an out-of-sequence fault based solely on the existing thermochronologic ages. It also suggests that the fault is perhaps best identified by a discrete change in cosmogenic nuclide derived erosion rates and geomorphic indices across the proposed structure (Whipple *et al.*, 2016). The geomorphic markers and erosion rates in the region continue to increase north of PT2, and their highest values are located ~110 km north of the MFT (Wobus, Whipple and Hodges, 2006), coincident with the top of the mid-crustal ramp in our best-fit model geometry.

2.6 Conclusions

Measurements of stratigraphy, surface structural geometries, and cooling ages collected from central Nepal, along with seismic and geodetic data collected during and after the Gorkha earthquake are utilized in various combinations to determine the subsurface geometry of the Main Himalayan thrust. We find that integrating all of these elements with balanced cross sections and thermokinematic models, which predict cooling ages, is necessary to distinguish between proposed geometries of the MHT and to determine the viability of proposed duplex architectures and out-of-sequence thrusting. Of those we considered, the model that best reproduces the observed MAr, ZHe, and AFT data is a hinterland-dipping duplex that has been translated entirely over the MHT mid-crustal ramp, located ~110 km north of the MFT (i.e., Whipple et al., 2016). Comparison

between the measured and predicted cooling ages helps to determine the timing and rates at which structures formed. A long-term constant shortening rate of ~19 mm/yr produces a good fit to the measured data (p-value = 0.32, RMSE = 2.221), and a significantly better fit is produced with variable rates of shortening. Modeled AFT and ZHe ages in the Kathmandu synform are set by the emplacement of the Trishuli thrust at ~10 Ma while the youngest MAr age near the MCT combined with ZHe ages located 50 km north of the MFT are best reproduced with duplex formation initiating at ~6.5 Ma. The youngest ZHe age marks the transition from the MBT to structures that deform the Siwalik Group at ~0.75 Ma (MDT and MFT) These rates require that the assembly and translation of the duplex occurs at ~40 mm/yr., while the rest of the system proceeds at <25 mm/yr. The existence of an out-of-sequence thrust in the hinterland is thought to be responsible for the creation of the linear geomorphic feature known as the Physiographic Transition 2 (PT2) and produces a ~1 Myr change in predicted ZHe and AFT ages. This suggests that the total amount of displacement on this structure is small (<5 km) and that thermochronologic data are limited in their ability to prove or disprove its existence. Finally, this method discriminates between the different duplex geometries and décollement geometries proposed for the central Himalaya, provides confidence in our approach, and highlights the utility of linking balanced cross sections and thermokinematic modeling to evaluate the subsurface geometry of fold-and-thrust belts.

2.7 Acknowledgements

We thank Willi Kappler (Univ. Tübingen) for support in modifying the PECUBE software and cluster computing. This work was supported by an Andrew Mellon Predoctoral Fellowship from the University of Pittsburgh to SG, National Science Foundation (NSF) Grants EAR-1524277

and EAR-1524320 to NM and DR, respectively, and a European Research Council (ERC) Consolidator grant (615703) to TAE. We thank J. Braun, P. Copeland, P. DeCelles, R. Ketcham, and J. R. Thigpen for their comments on earlier versions of the manuscript.

The previously published data used in this article can be found in Hubbard and Harrison (1989), Copeland et al. (1991), Wobus et al. (2003), Herman et al. (2010), and Robert et al. (2011). The new MAr data presented in this manuscript can be found online via sciencebase.gov at https://doi.org/10.5066/ P9FA0HI0, while the new ZHe data are available online via PANGAEA at https://doi.org/10.1594/ PANGAEA.918178. Any use of trade, firm, or product names is for descriptive purposes only and does not imply endorsement by the U.S. Government.

2.8 Supplementary information

The supplementary videos can be accessed online at https://www.youtube.com/ playlist?list¼PLttn6LSpDKTFtINJfTftEOT90-Lq8j9xc.

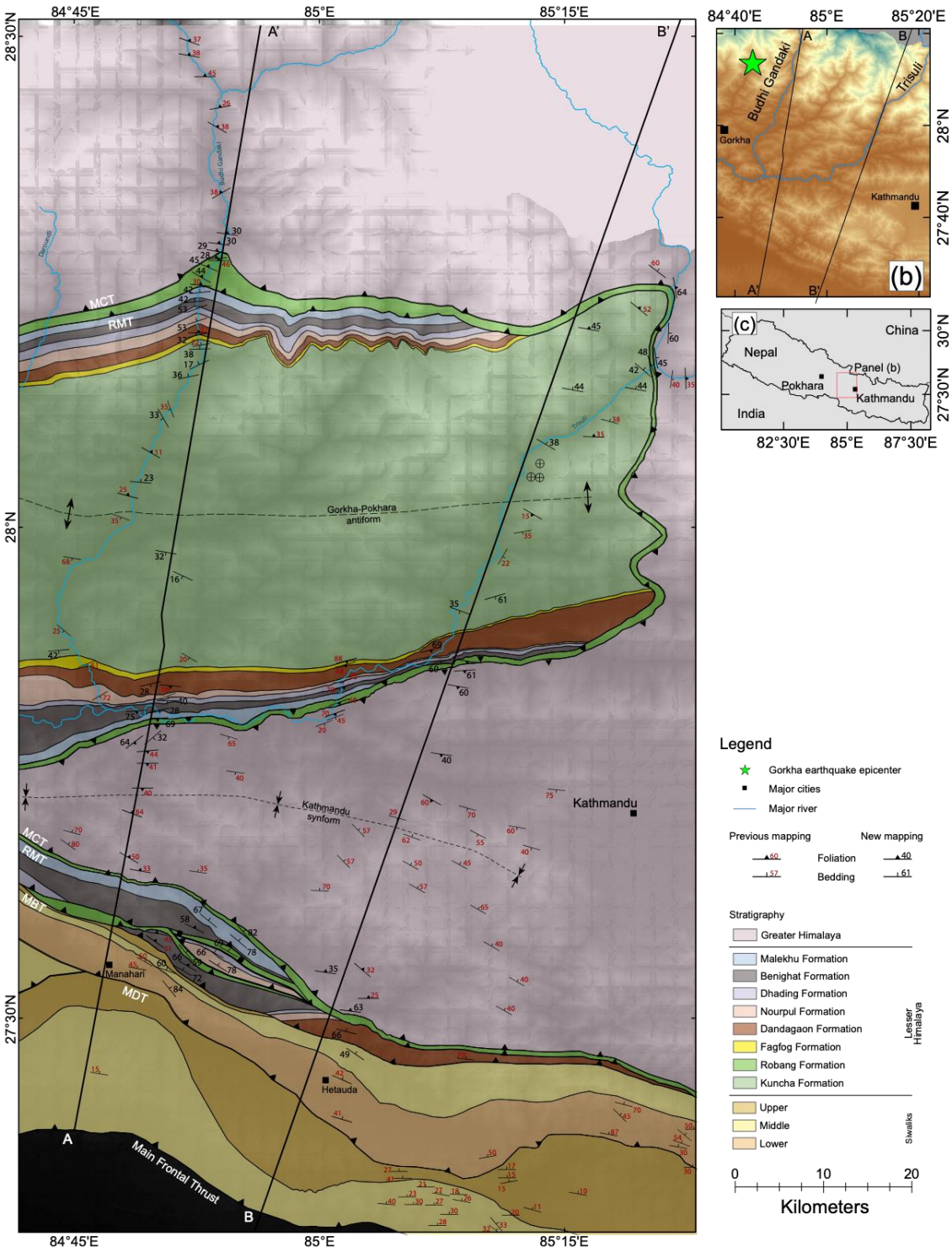

Figure 2.13: Geological map of central Nepal, showing detailed mapping from the region. Black dip values indicate new mapping, while red values indicate past mapping (Lavé and Avouac, 2001; Pearson, 2002; Khanal and Robinson, 2013;).

2.8.1 Geologic mapping

New mapping (Figure 2.13) was concentrated along the Budhi Gandaki and Trishuli valleys north of Kathmandu and in the regions of Hetauda and Manahari from the southern edge of the Kathmandu synform into the Siwaliks. We combine this new mapping with published maps of the region (Lavé and Avouac, 2000; Pearson, 2002; Khanal and Robinson, 2013) for added insight into the lateral continuity of the mapped lithologic units. In this section, we describe the lithologic characteristics of the different formations, focusing on how these units are best recognized in the field, emphasizing similarities to previous mapping.

Figure 2.14: Outcrop photographs from mapping along Budhi Gandaki and Trishuli valleys in central Nepal.

(a) Cobbles and angular clasts from the conglomerates of the Upper Siwalik member. (b) Location of the Main Central Thrust, placing the rocks of the GH on top of the lower Lesser Himalayan Robang Formation in the Trishuli valley. (c) Fresh surface of the phyllites in the Kuncha Formation. (d) Quartz blebs and ribbons in Robang metamorphosed to greenschist facies. (e) Fresh samples of the Robang Formation, showing amphibolite facies metamorphism. (f) Mapped contact of the Ramgarh-Munsiari Thrust (RMT) in the Budhi Gandaki valley, placing the Robang Formation on top of marble and dolostone of the Malekhu Formation. (g) Ripple marks in the Fagfog quartzites. (h) Weathered, wavy layers of the Dandagaon phyllites. (i) Freshly broken outcrop of the Dandagaon Formation with interstitial garnets. (j) Multiple colors of the quartzitic Nourpul Formation. (k) 'Butcher-block' weathering of dolostone/marble in the Dhading Formation. (l) Black slates of the Benighat Formation. (m) Quartz ribbons and partial melt textures in the Greater Himalayan rocks of the northern limb of the Kathmandu synform. (n) Massive quartzites interbedded with schists from the southern limb of the Kathmandu synform. (o-p) Polymineralic leucosomes from the Greater Himalayan rocks north of the MCT, in the Budhi Gandaki valley.

2.8.1.1 Siwalik Group/Subhimalaya

In central Nepal, the middle Miocene to Pliocene Siwalik Group is a 5 km thick coarsening upwards section with mudstone and siltstone at the bottom, to sandstone and conglomerate towards the top (Tokuoka *et al.*, 1986; Harrison *et al.*, 1993; Quade *et al.*, 1995; Ojha *et al.*, 2009). The sequence is divided up informally into three members (lower, middle, and upper). The lower Siwalik Group consist of siltstone and shale, interbedded with fine-grained sandstone. These sandstone interbeds become thicker towards the top. The middle Siwalik Group is made up of medium- to coarse-grained sandstones, with more siltstone interbeds towards the base (Quade *et al.*, 1995). The high mica content and the presence of Greater Himalayan derived feldspars gives the sandstone a "salt and pepper" appearance. Crossbeds are abundant, as are erosional, non-planar basal surfaces indicating channel deposits. The upper Siwalik Group consists of poorly sorted, massive, pebble-supported conglomerate interbedded with tan, coarse-grained sandstone (Pearson,

2002). Upper Siwalik Group pebble to cobble-sized clasts are subangular to rounded and are primarily composed of Lesser Himalayan material (Figure 2.14a). The Siwalik Group are synorogenic deposits derived from the growing Himalayan mountains (Gansser, 1964; Burbank, Beck and Mulder, 1996; DeCelles *et al.*, 1998; Lavé and Avouac, 2000). The dominantly fluvial deposits grade into proximal alluvial fan deposits in the upper Siwalik Group. This coarsening sequence is a result of the southward approaching deformation front and consequent southward migration of the foreland basin (Gansser, 1964; Lyon-Caen and Molnar, 1985; DeCelles *et al.*, 1998).

2.8.1.2 Lesser Himalaya

The Lesser Himalayan sequence is bound in the south by the Main Boundary Thrust (MBT), and the Main Central Thrust (MCT) in the north (Figure 2.14b). The 8-13 km thick sequence can be further divided into a Paleoproterozoic lower LH sequence containing the Robang and Kuncha Formations, and a Mesoproterozoic upper LH sequence containing the Malekhu, Benighat, Dhading, Nourpul, Dandagaon, and Fagfog Formations (Pearson, 2002; Khanal, 2009).

Lower Lesser Himalaya

The Kuncha Formation is an ~3 km thick unit of mainly quartzite with minor phyllite that comprises ~30% of the rocks exposed along the two transects (Figure 2.13) and forms the core of the Gorkha-Pokhara antiform. It makes up the basal unit for the Lesser Himalayas, with a depositional age of ~1900 Ma (Martin *et al.*, 2011). The rocks of the Kuncha Formation are dark yellow-green to light grey-green in color on fresh surfaces (dark grey-green on weathered) (Pearson, 2002). The phyllites are composed primarily of muscovite, with subordinate chlorite, quartz, and feldspar. Abundant detrital quartz and feldspars cause the phyllite to be gritty (Pearson,

2002). The phyllites also contain abundant fine-grained quartz exsolution textures (blebs and ribbons), which have then been deformed. Towards the core of the antiform, the quartzites become significantly impure, containing a large lithic component (Pearson, 2002). The degree of metamorphism of the rocks increases to the north on the northern limb of the Gorkha-Pokhara antiform, increasing the size of muscovite and imparting a silver-grey schistose sheen to fresh rock surfaces (Figure 2.14c). The phyllite also become more graphitic towards the north, especially near the trace of the RMT (Pearson, 2002). The Robang Formation is characterized by chloritic phyllite/schist that often contains exsolution blebs and ribbons of quartz and sparse, thin calcareous beds. The Robang Formation commonly includes a distinctively white to light green, medium- to coarse- grained (sugary) quartzitic arenite with 15 cm – 1 m thick beds termed the Dunga quartzite (Khanal, 2009). In the south, the Robang Formation is metamorphosed to greenschist facies (Figure 2.14d) and contains abundant chlorite and epidote. In the north, metamorphism reaches amphibolite facies (Figure 2.14e) as evidenced by the increasing abundance of large pyrope garnets and uncommon kyanite. Intrusions of thick (~20 m) green-black hornblende-bearing amphibolite intrusions are common (Pearson, 2002). The thickness varies ranging from ~0.5 km thick in the south to ~2.5 km in the northern Budhi Gandaki valley. Structurally, in the northern Budhi Gandaki valley, the Robang Formation is in the footwall of the MCT and in the hanging wall of the Ramgarh-Munsiari Thrust (RMT; Figure 2.14f). In the Trishuli and Langtang valleys the RMT places the Robang directly on top of the Kuncha Formation (Figure 2.13). The Robang (including the Dunga quartzite) was intruded by a Paleoproterozoic augen gneiss (Robinson and Martin, 2014). These intrusions have been dated in the correlative Ranimata Formation in far-west Nepal to suggest that deposition must have occurred prior to ~1831 Ma (DeCelles *et al.*, 2001).

Upper Lesser Himalaya

The Fagfog Formation marks the base of the upper LH, resting on top of the Robang Formation (prior to its emplacement by the RMT). It is a white/tan, medium-grained quartzite, and is ~350 m thick across the field area. Crossbedding and ripple marks (Figure 2.14g) are common, with interbedded extremely thin chloritic phyllites (Pearson, 2002; Khanal, 2009). Bedding in the Fagfog is defined by small grains of muscovite in between the larger quartz grains, and numerous ilmenite and magnetite grains. The Dandagaon Formation lies conformably on top of the Fagfog Formation. It is 1 km thick dominated by shiny, undulating, dark grey to black phyllite, which weathers brown (Figure 2.14h). Rare interbeds of dolostone can be seen near the top of the unit (Pearson, 2002). The undulating foliation surfaces are highly micaceous, producing a characteristic sheen that is distinctive in the field. Upper greenschist-grade Dandagaon is a green-silver colored schist with quartzite interbeds that can range from mm to 10's of cm. These schist-rich layers contain numerous garnets (Figure 2.14i). The Nourpul Formation is a 1.5 km thick unit made up of a mix of thinly bedded calcareous slate, phyllite and quartzite. The quartzite beds are fine-grained, and range in color from pink and white, to purple (Figure 2.14j). The grain size increases with increasing metamorphism, developing a micaceous foliation. At upper greenschist facies, the quartzite commonly retains the distinctive pink color. Quartzite beds are interbedded with thinly foliated, green-black, purple and green slate and phyllite, that become metamorphosed towards the north into dark green, garnet-rich schists and biotite schist. The unit becomes largely dolomitic towards the top, where it is in gradational contact with the Dhading Formation (Pearson, 2002). The Dhading Formation is ~1 km thick and is comprised of extremely fine-grained blue – dark grey dolostone layers, which are uncommonly interbedded with grey cherts. In the north, the Dhading Formation is composed of weak calcite-rich marble and calc-silicate rocks, caused by the

higher degree of metamorphism. There is a large proportion of biotite and muscovite, along with quartz, and trace amounts of alteration-related epidote. Both the dolostone and marble have a distinctive 'butcher-block' weathering pattern (Figure 2.14k). The dolostones of the Dhading show an abrupt lithologic change upwards into the Benighat Formation. The Benighat Formation is composed of a ~1 km thick friable black slate with a dull sheen (unlike the Dandagaon) (Figure 2.14l). The grade of metamorphism of the pelitic protolith increases towards the north, where the Benighat becomes increasingly phyllitic (black). Up-section, the Benighat has a gradational contact with the overlying Malekhu Formation, which is the uppermost unit of the LH. The Malekhu Formation is comprised of ~500 m thick massive, bluish-grey limestones with a buff-colored butcher block textured weathering surface. it is commonly interbedded with dolomite and very thin phyllitic layers (Khanal, 2009). The proximity of these rocks to the RMT, and overlying Robang Formation, has metamorphosed the limestone into marble and dolomite close to the RMT contact (Figure 2.14f). In the north, at amphibolite grade metamorphism, the Malekhu Formation is a white dolomite or white to variegated (common light pinks and purple) calcsilicate containing phlogopite.

2.8.1.3 Greater Himalaya

In our study area, we observed Greater Himalayan rocks in three locations: in the northern Budhi Gandaki valley, the Trishuli valley in Langtang National Park, and in the Kathmandu synform.

Kathmandu synform

The Kathmandu synform is predominantly made up of paragneiss, garnet-rich schist, and massive quartzite. The metamorphic grade decreases upsection towards the middle of the synform,

from amphibolite facies at the base (immediately above the Main Central Thrust) to dominantly greenschist facies in the middle of the synform (Johnson *et al.*, 2001; Pearson, 2002). Greater Himalayan rocks along the northern limb of the synform are paragneiss-rich and contain partial melt textures and quartz ribbons (Figure 2.14m). Kyanite is also present in the basal 1 km, associated with the garnet schist (Johnson *et al.*, 2001). In the southern portion of the synform, garnet schist and paragneiss are interbedded with quartzites (Figure 2.14n) and coarse-grained dolomitic marble (Pearson, 2002).

North of the Main Central thrust

The Greater Himalayan rocks mapped in the Budhi Gandaki and Trishuli valleys are primarily high grade (amphibolite) biotite-muscovite gneiss. Garnet is extremely common within the gneissic foliations, along with kyanite, which gives way to fibrous clusters of sillimanites closer to the MCT (Pearson, 2002; Kohn *et al.*, 2004; Khanal, 2009). Paragneiss in the hanging wall of the MCT show abundant concentrations of partial melt in the form of polymineralic leucosomes, which have also been highly deformed (Figures 2.14o, 2.14p). Calc-silicate rocks become more prevalent towards the north (Kohn, 2008). Farther north, the banded gneiss and calc-silicate schists are intruded by large, foliated leucogranite bodies (Khanal, 2009). The foliations are defined by large muscovite and biotite crystals, wrapping around quartz, large garnet and potassium feldspar porphyroblasts.

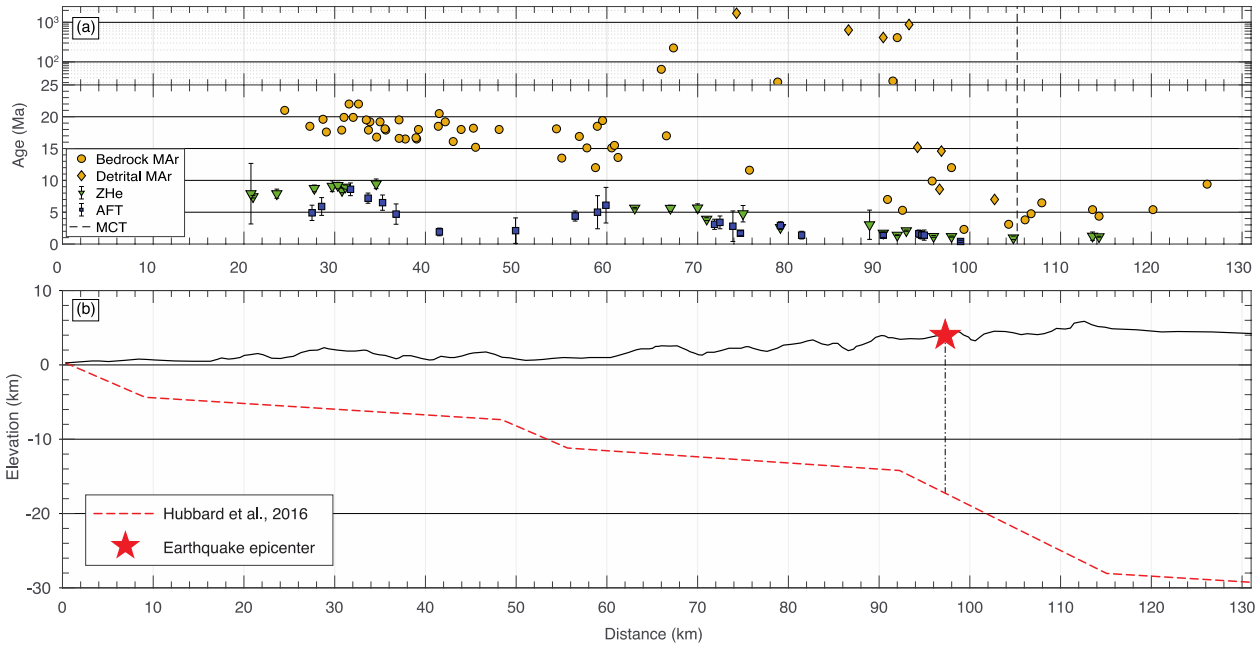

Figure 2.15: Data projected along the Trishuli section line.

Combined MAr (yellow), ZHe (green), and AFT (blue) thermochronometer data plotted along the Trishuli section line (B-B'), parallel to the direction of transport. The location of the MCT is marked by a black, dashed line, while the origin is the location of the MFT. (b) MHT geometry proposed by Hubbard et al., along the Trishuli valley. Distances based on the WGS84 datum.

2.8.2 Thermochronology

2.8.2.1 $^{40}Ar/^{39}Ar$ analysis

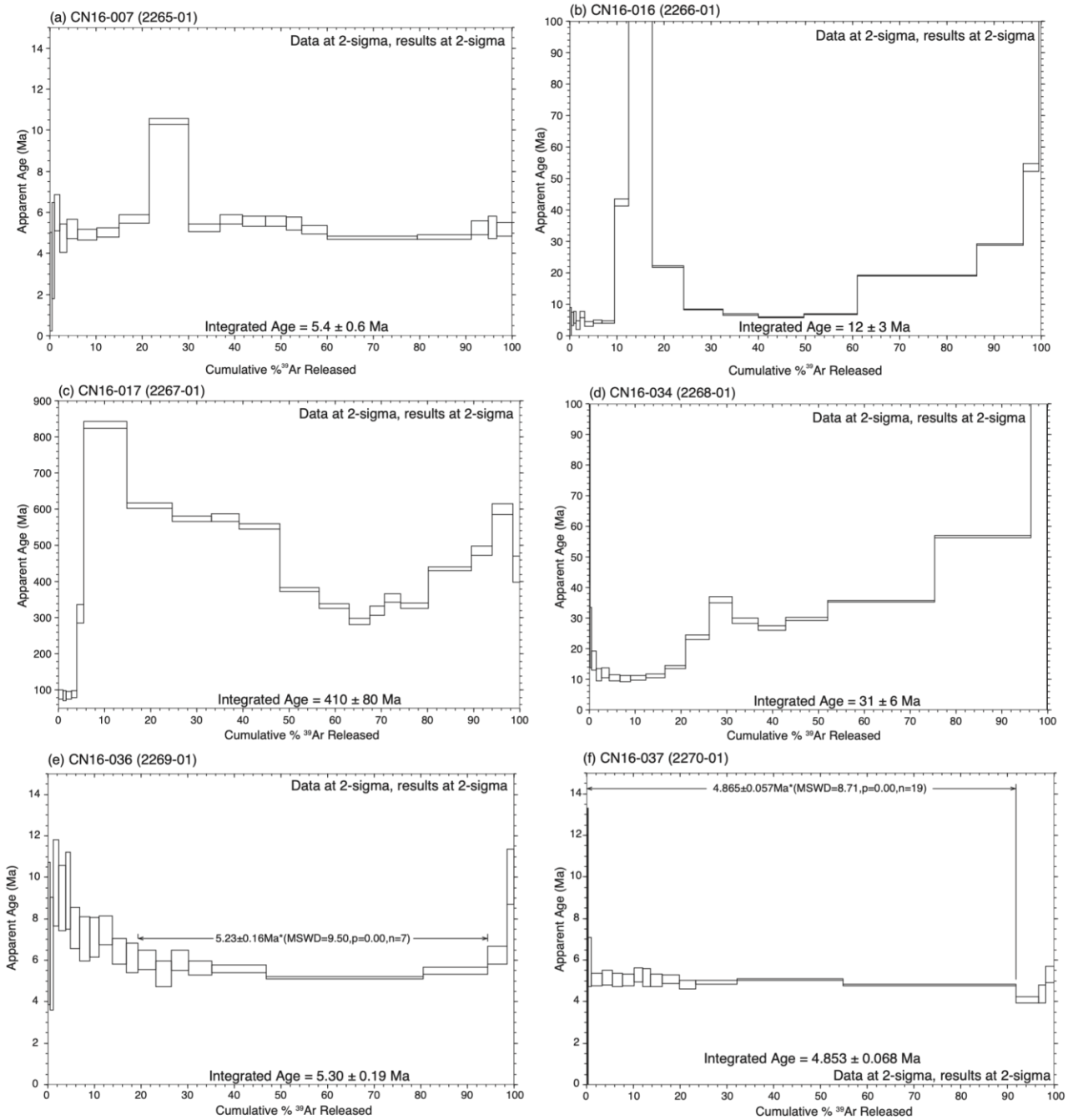

Figure 2.16: $^{40}Ar/^{39}Ar$ age spectra

The $^{40}Ar/^{39}Ar$ analyses were performed at the U.S. Geological Survey in Denver, CO. High purity mineral grains of sample and standard were irradiated for five hours, in the central thimble position of the 1 MW U.S. Geological Survey TRIGA reactor using cadmium lining to prevent nucleogenic production of ^{40}Ar. The neutron flux was monitored using Fish Canyon sanidine, with an age of 28.20 Ma ± 0.08 Ma (Kuiper *et al.*, 2008). The irradiated samples and standards were loaded into 3 mm wells within a stainless steel planchette and placed into a fully automated ultra-high vacuum extraction line constructed of stainless steel. Samples were incrementally heated until fusion using a 20W CO_2 laser equipped with a beam homogenizing lens. The gas was expanded and purified by exposure to a cryotrap maintained at −135°C and two SAES GP50 getters. Following purification, the gas was expanded into a Thermo Scientific ARGUS VI noble gas mass spectrometer, and argon isotopes were measured by multi-collection, using Faraday cup detectors for all Ar isotopes apart from ^{36}Ar, which was measured on a compact discrete dynode. Time-zero intercepts were determined by best-fit regressions to the data. Ages were calculated from data corrected for mass discrimination, blanks, radioactive decay subsequent to irradiation, and interfering nucleogenic reactions (Figure 2.16, Appendix B). Full analytical details and argon geochronology data are available in Morgan (2020).

Correction factors used: For DT-38, correction factors are equal to those of Renne et al. (2005) for $(^{38}Ar/^{39}Ar)K$, $(^{37}Ar/^{39}Ar)K$, and $(^{38}Ar/^{37}Ar)Ca$. Other values are determined from co-irradiated K glass and CaF_2: $(^{36}Ar/^{37}Ar)Ca = 2.673e^{-4} \pm 8.139e^{-7}$; $(^{39}Ar/^{37}Ar)Ca = 7.54e^{-4} \pm 3.75e^{-5}$; $(^{40}Ar/^{39}Ar)K = 1.5105e^{-3} \pm 6.117e^{-4}$. For DT-40, correction factors are equal to those of Renne et al. (2005) for $(^{38}Ar/^{39}Ar)K$, $(^{37}Ar/^{39}Ar)K$, and $(^{38}Ar/^{37}Ar)Ca$. Other values are determined from co-irradiated K glass and CaF_2: $(^{36}Ar/^{37}Ar)Ca = 2.712e^{-4} \pm 8.71657e^{-7}$; $(^{39}Ar/^{37}Ar)Ca = 7.54e^{-4} \pm 3.75e^{-5}$; $(^{40}Ar/^{39}Ar)K = 1.5503e^{-3} \pm 6.474e^{-4}$.

2.8.2.2 Zircon (U-Th)/He analysis

Zircon (U-Th)/He analyses followed the general procedures outlined in Reiners, (2005) and Reiners et al., (2004). Individual zircon grains were selected from separates based on size, morphology, and lack of inclusions. Grains lacking obvious fractures and with a minimum radius of 60 μm, with minimal to no inclusions, were selected. However, due to a lack of unbroken zircon grains with radii above 60 μm in certain samples, smaller unbroken grains with radii as close to 60 μm as possible were selected. The dimensions of individual grains were measured from digital photomicrographs, using the approach outlined in Hourigan et al., (2005) for alpha-ejection corrections. Single grains were then packed into 1 mm Nb foil envelopes. Multiple foil packets were then placed in individual holes in a 30-hole planchette inside a ~7 cm laser cell pumped to <10-9 torr. Individual packets were then heated for 15 minutes by a focused beam of a 1-2 W laser, to extract ^{4}He. The packets were then re-heated for 15 minutes, often multiple times, until ^{4}He yields were less than 1% of total. Standards of Fish Canyon Tuff (FCT) zircon (28.48 ± 0.06 Ma [2σ], Schmitz and Bowring, 2001) were analyzed between every 5 unknowns. Gas released from heated samples was spiked with 0.1-0.2 pmol ^{3}He and condensed onto activated charcoal at the cold head of a cryogenic trap at 16 K. Helium was then released from the cold head at 37 K into a small volume (~50 cc) with an activated Zr-Ti alloy getter and the source of a Balzers quadrupole mass spectrometer (QMS) with a Channeltron electron multiplier. Peak-centered masses at approximately m/z of 1, 3, 4, and 5.2 were measured. Mass 5.2 establishes background, and mass 1 is used to correct mass 3 for HD and H^{3+}. Corrected ratios of masses 4 to 3 were regressed through ten measurement cycles over ~15 s to derive an intercept value, which has an uncertainty of 0.05-0.5% over a ^{4}He/^{3}He range of ~103 and compared with the mean corrected ratio to check for significant anomalous changes in the ratio during analysis. Helium contents of unknown

samples were calculated by first subtracting the average mass-1-corrected $^{4}He/^{3}He$ measured on multiple procedural blanks analyzed by the same method, from the mass-1-corrected $^{4}He/^{3}He$ measured on the unknown. This was then ratioed to the mass-1-corrected $^{4}He/^{3}He$ measured on a shot of an online reference ^{4}He standard analyzed with the same procedure. The resulting ratio of measured $^{4}He/^{3}He$ values was then multiplied by the moles of ^{4}He delivered in the reference shot. After He extraction and measurement, foil packets were retrieved, transferred to Teflon vials, and spiked with 0.5-1.0 ng of ^{233}U and ^{229}Th. High-pressure digestion vessels were used for dissolution of the zircon and Nb foil packet. Natural-to-spike isotope ratios of U and Th were then measured on a high-resolution (single-collector) Element2 ICP-MS with all-PFA Teflon sample introduction equipment and sample preparation/analytical equipment. Blanks for zircon analyses were 2.6 ± 0.5 pg U and 5.5 ± 1.0 pg Th. Precision on measured U-Th ratios is typically better than 0.5% for zircon analyses. Propagated analytical uncertainties for typical zircon samples led to an estimated analytical uncertainty on (U-Th)/He ages of approximately 1-3% (1σ). In some cases, reproducibility of multiple aliquots approaches analytical uncertainty. However, in general, reproducibility of repeat analyses of (U-Th)/He ages is significantly worse than analytical precision. Thus (U-Th)/He ages typically show a much greater scatter and higher MSWD than expected based on analytical precision alone, and multiple replicate analyses of (U-Th)/He ages on several aliquots is necessary for confidence in a particular sample age.

For further information on the methods of (U-Th)/He dating at the Arizona Radiogenic Helium Dating Laboratory, refer to Reiners, 2005, or to the laboratory's website: http://www.geo.arizona.edu/~reiners/arhdl/arhdl.htm. Single-grain ZHe ages and supporting data are available online via PANGAEA at https://doi.org/10.1594/PANGAEA.918178. Mean ZHe ages for each sample are shown in Table 2.1 in the text.

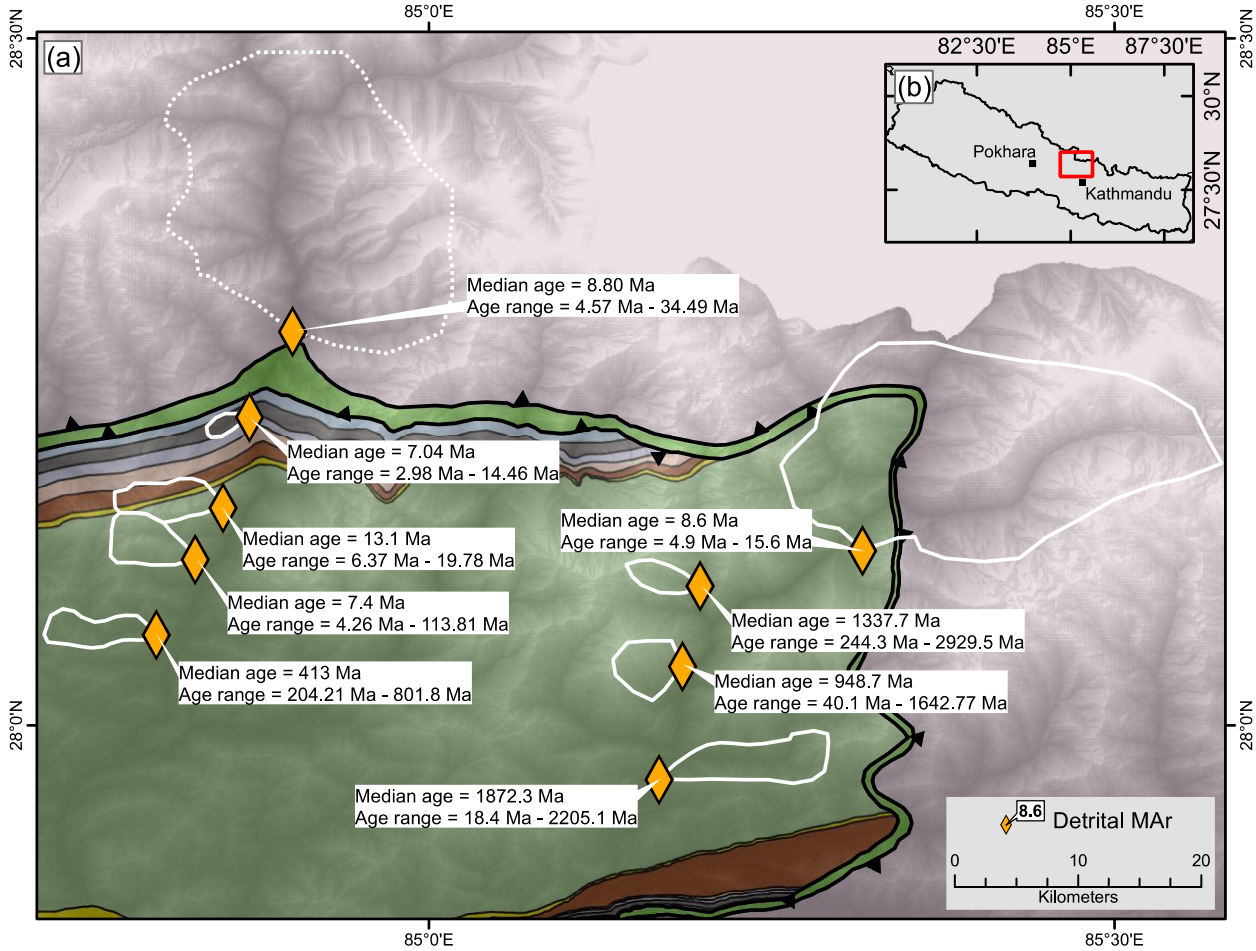

Figure 2.17: Map of estimated drainage basins for detrital MAr samples (yellow diamonds) from Wobus et al. (2006).

The median ages and the total age ranges for each sample is provided. Latitudes and longitudes are based on the (WGS84) datum.

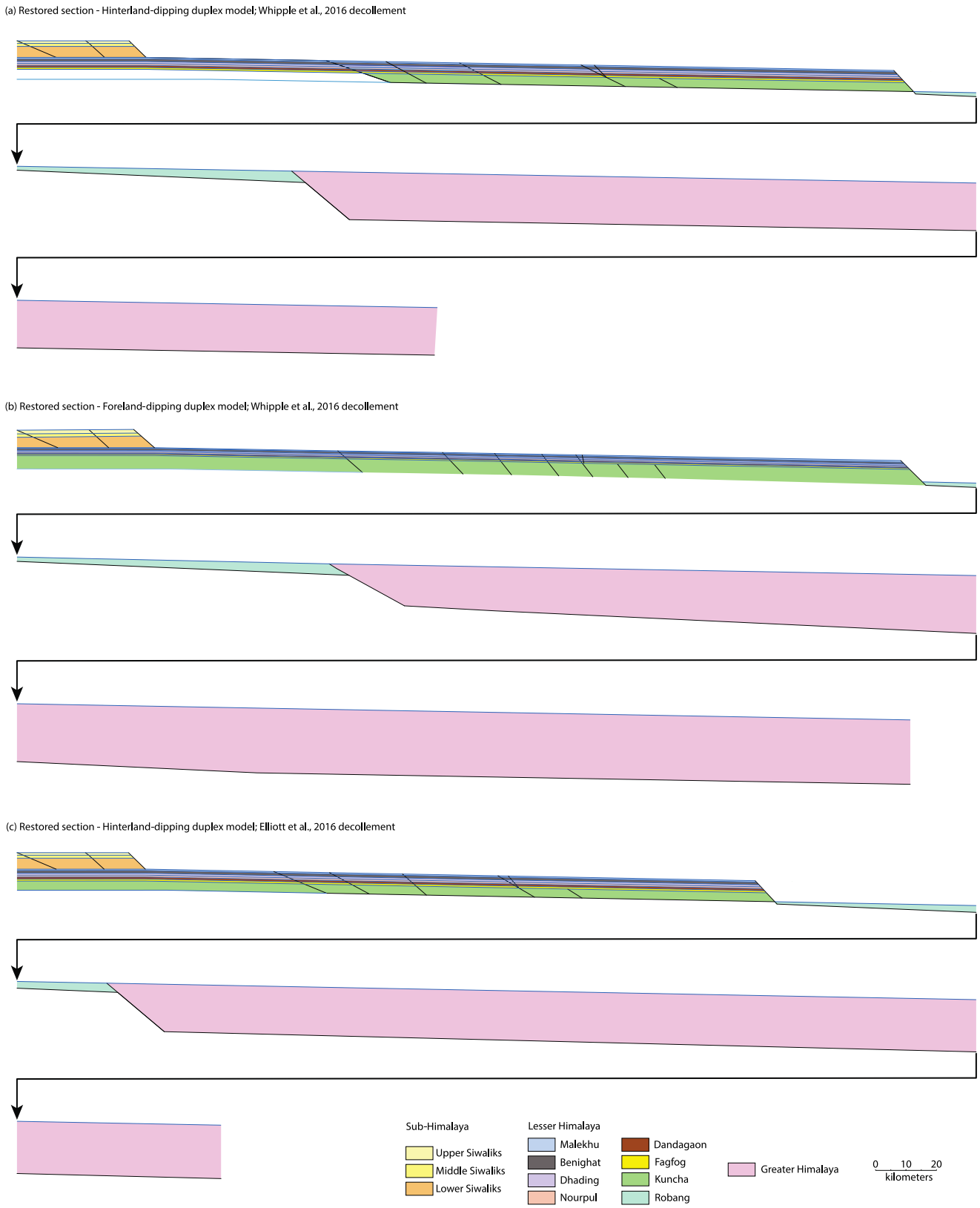

Figure 2.18: Restored cross-sectional geometries.

(a) Restored section geometry for the Hinterland-dipping duplex geometry, based on Whipple et al., 2016; (b) Restored section geometry for the Foreland-dipping duplex geometry, based on Whipple et al., 2016; (c) Restored section geometry for the Hinterland-dipping duplex geometry, based on Elliott et al., 2016.

2.8.3 Sensitivity of ages to ramp location, ramp angle, heat production and velocity

To help visualize the sensitivity of model results (predicted ages) to parameters such as changing ramp angle, radiogenic heat production and velocity, we conducted a series of experiments where we systematically changed one of the above three parameters to highlight the effects of these parameters on the predicted cooling ages. These experiments emphasize the primary control of ramp location on the position of young, reset cooling ages and allow us to examine potential errors associated with the ramp location, taking into account uncertainties in ramp geometry, thrust velocity or heat production values.

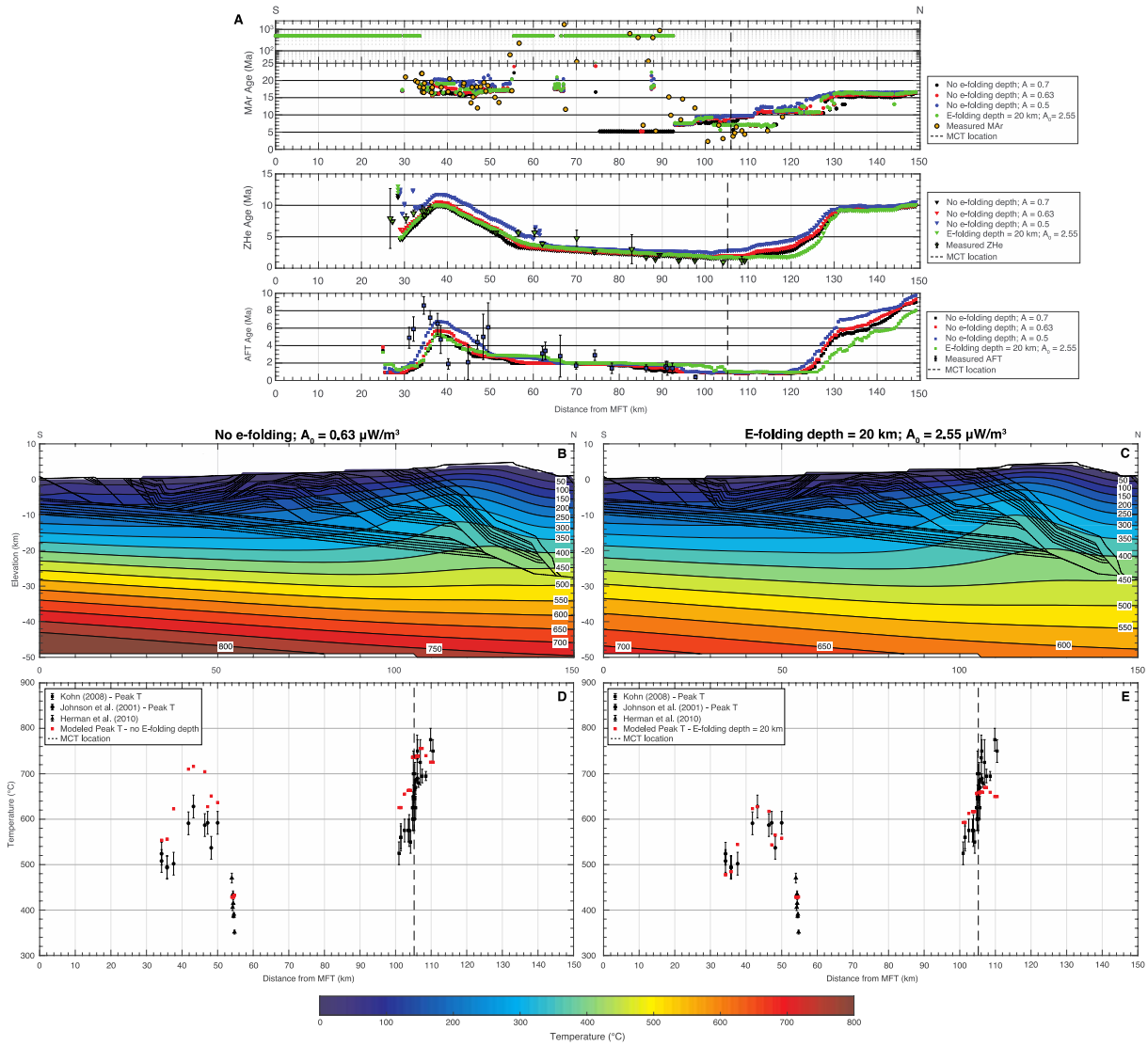

Figure 2.19: Comparison between a constant crustal heat production and an e-folding depth. (A) Plots comparing the predicted MAr, ZHe and AFT cooling ages with measured ages for: No e-folding; A = 0.7 (Black); No e-folding, A = 0.63 (Red); No e-folding, A = 0.5 (Blue); E-folding depth = 20 km, A_0= 2.55 (Green). (B) Plot of the thermal field at the final step of the model for a constant heat production value of 0.63 (best-fit). Isotherm values (white boxes) are shown in steps of 50°C. (C) Plot of the thermal field at the final step of the model for a heat production value of 2.55, using an e-folding depth of 20 km (overall best-fit). Isotherm values (white boxes) are shown in steps of 50° (D) Comparison between peak measured temperatures with those predicted by the model (Constant crustal heat production value = 0.63). (E) Comparison between peak measured temperatures with those predicted by the model (E-folding depth = 20 km, crustal heat production value = 2.55). Distances based on the WGS84 datum.

2.8.3.1 Effect of geometry vs. heat production and velocity

We devised a simplified ramp model experiment to show and discuss the effect of changing the ramp angle, and to compare this effect to that of changing the heat production, or velocity on predicted cooling ages. This simplified model is made up of a single ramp that is 18 km high accommodating 30 km of shortening towards the south. We tested 4 ramp angles that increase from 25° to 50°, while keeping the location of the top of the ramp and the depth of the base constant. Therefore, changing the angle also changes the length of the ramp surface. Figure 2.20A shows the predicted cooling ages (MAr, ZHe and AFT) for this experiment, for angles of 25°, 30°, 35° and 50°, while keeping heat production and velocity constant at 2.55 and 21 mm/yr. respectively. The youngest cooling ages for all three systems are located approximately in the same place (~470 ± 2 km), set by the location of the upper 5 km of the ramp, which stays constant. As the ramp angle becomes shallower (i.e., from 50° to 25°), the component of shortening that goes into uplift decreases, leading to less exhumation, and the zone of reset MAr ages narrows. The lower temperature thermochronometers (ZHe and AFT), have a different effect. Decreasing the angle of the ramp does shift the zone of reset ZHe ages (both in front of and behind the ramp) towards the north (opposite the direction of transport). Since a lower ramp angle means a longer ramp, the shifting of reset ages to the north is a direct result of initiating ramp uplift farther to the north with decreasing ramp angles. For the southern extent of reset ages, the response is similar to the reset MAr ages. Decreasing ramp angles lowers the vertical component of uplift and decreases exhumation, thus the transition from reset to unreset shifts to the north for decreasing ramp angles. The significantly lower closure temperature for the AFT system narrows the zone (less than 2 km) over which a changing ramp angle shift the location that the predicted ages change from unreset to reset (~445 km) at the southern extent. A larger effect of the change in ramp angle is seen in the

northward shift of reset AFT and ZHe ages with decreasing ramp angle at the base of the ramp in the north. In this location it would be challenging to discern a change in ramp angle from a 2-8 km shift in the location of the ramp. However, including MAr ages allows us to differentiate between a different ramp location (which would shift all 3 chronometers to the north or a decrease in ramp angle (which would shift AFT and ZHe to the north, but shift predicted MAr ages to the south).

To highlight the effect of changing radiogenic surface heat production, we varied heat production from $A_0 = 3.00$ to $A_0 = 2.00$ with a ramp angle of 30°, and velocity at 21 mm/yr. (Figure 2.20B). As the heat production is decreased from $A_0 = 3.00$ (black), the zone of reset MAr ages declines from being 25 km wide, to < 2 km wide (green; $A_0 = 2.00$), where reset ages are located at ~468 km, (~5 km vertical distance from the top of the ramp) and exhumation is the greatest after 30 km of displacement. The zone of reset ages also narrows with decreasing heat production (although not as dramatically) for predicted ZHe and AFT ages. Importantly, the effect of changing heat production is different than that of changing ramp angle. Only the predicted MAr ages show a similar magnitude and direction of lateral shift (in the x direction) with increasing ramp angle and higher heat production widening the zone over which reset ages are produced. While the magnitude in the shift of reset ZHe ages is similar between changing ramp angles and changing heat production (~2-8 km) the direction of the shift is different. Lower ramp angles and lower heat production both limit the extent of reset ZHe ages south of the ramp (in the direction of transport). However, decreasing the ramp angle shifts the zone of reset ages northward on the northern side of the ramp, while decreasing the heat production shifts the reset ages to the south. In addition, the magnitude of the shift in predicted AFT ages caused by decreasing the ramp angle is notably larger (2- 10 km) than the shift in predicted ages (~3 km) caused by changing the heat production.

Changes in ramp angle and heat production values produce cooling age patterns that are distinct from changing the rates of thrusting. Since the amount of shortening is kept constant in our models, changing the rate of thrusting means modifying the time over which thrusting occurs, with the end point (0 Ma) remaining constant. Figure 2.20C shows the effect of changing the rate of thrusting on the cooling ages, at a constant surface heat production value of 2.55 over a ramp angle of 30°. Unlike changing the heat production, changing the velocity has a very minimal effect on the width of the zone of reset ages (<2 km), rather it distinctly changes the age at which different chronometers become reset. With slower thrusting (5 mm/yr.; orange-colored lines), deformation initiates at 6 Ma. The cooling ages for all 3 chronometers are the oldest, with the reset MAr ages indicating the age of fault initiation (in this model set up). We show the effect of steadily increasing the rate of thrusting from a very slow 5 mm/yr. to 40 mm/yr. Increasing the rate of thrusting means making the thrusting initiate at a later time, which is shown in the progressively younger reset MAr ages. Of note, the location of highest exhumation is maintained at the same place (i.e., the upper third of the ramp).

Finally, we compare the effects of changing heat production, with changing the angle of the ramp, to show that the resulting effects of shifting the location of reset ages (upper limit of 10-14 km) are distinct enough from each other, and from the location of the ramp to be able to differentiate the patterns of reset ages between those expected from changing the ramp location, the ramp angle or heat production values. Figure 2.20D compares similar magnitude shifts in predicted ages between the effects of changing heat production values and ramp angles.

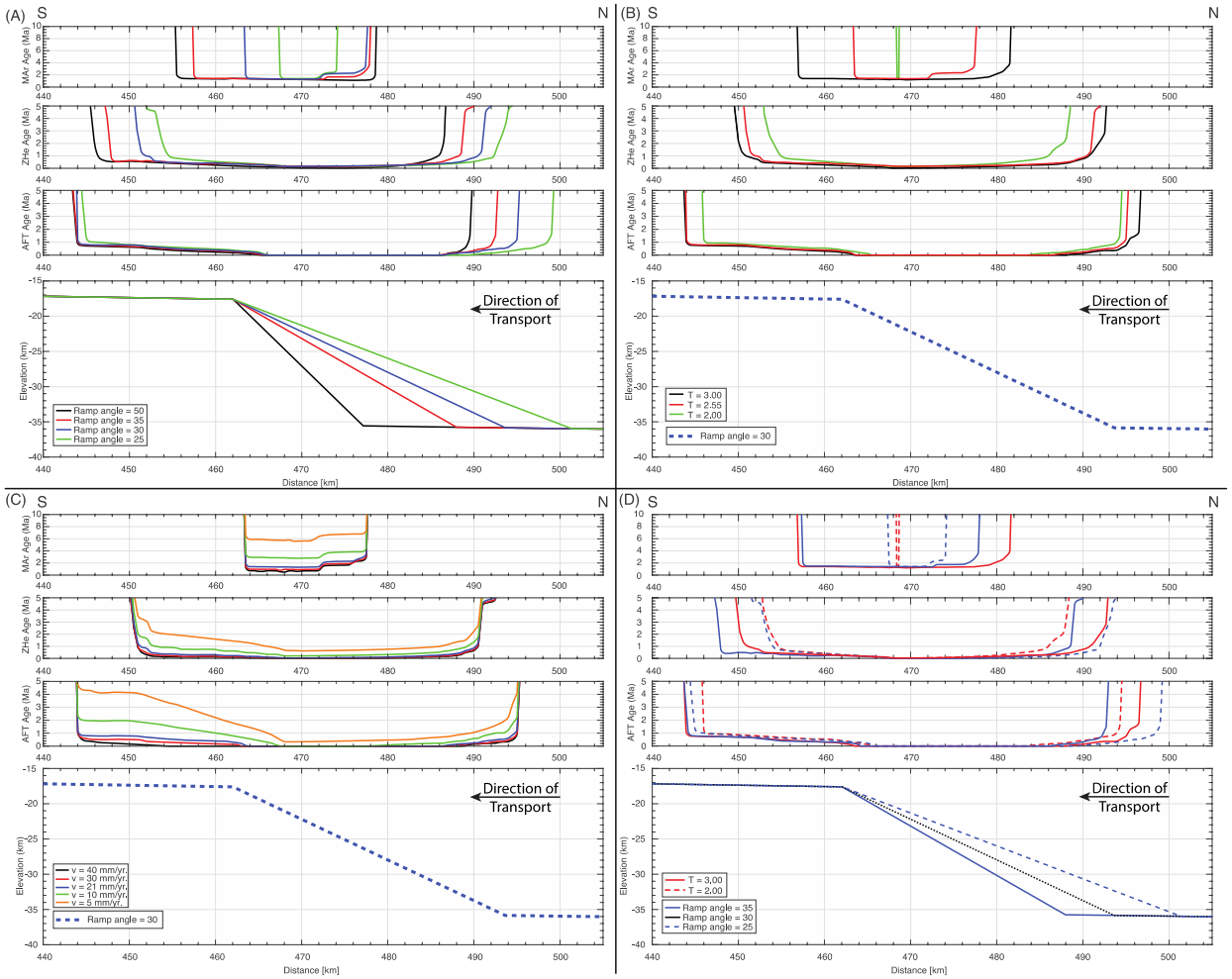

Figure 2.20: Effect of changing ramp angle, crustal heat production and velocity on cooling ages. (A) Comparison between cooling ages (MAr, ZHe and AFT) predicted by variable ramp angles (Black: 50°; Red: 35°; Blue: 30°; Green: 25°). (B) Effect of varying heat production on predicted cooling ages (MAr, ZHe and AFT), with a constant ramp angle (30°; Blue-dashed); Black: A_0 = 3.00; Red: A_0 = 2.50; Green: A_0 = 2.00. (C) Effect of varying velocity on predicted cooling ages (MAr, ZHe and AFT), with a constant ramp angle (30°; Blue-dashed). Heat production is kept constant at 2.55; Black: v = 40 mm/yr.; Red: v = 30 mm/yr.; Blue: v = 21 mm/yr.; Green: v = 10 mm/yr.; Orange: v = 5 mm/yr. (D) Comparison between the effects of changing heat production (Red-solid: A_0 = 3.00; Red-dashed: A_0 = 2.00), and that of changing ramp angle (Blue-solid: 35°; Blue-dashed: 25°). The ramp angle is kept constant at 30° to show the effect of changing heat production (Black-dotted).

2.8.3.2 Effects of e-folding depth

There are two ways of estimating how radiogenic heat changes with depth. One is to assume that radiogenic heat production is constant through the crust. A challenge to this assumption is that surface sampling has shown that heat production declines non-linearly with crustal depth (Ketcham, 1996; Brady *et al.*, 2006). Instead of assuming a constant radiogenic heat production, assigning an e-folding depth can mimic this decay, by setting the depth range over which the radiogenic heat production value decays to 1/e of its original (surface) value (McQuarrie and Ehlers, 2017), and therefore, we have assigned an e-folding depth of 20 km to all the models presented in this study. This approach allows us to honor measured surface values of heat production in the Himalaya (0.8 μWm^{-3} for the Indian Shield, to 1.5- 6.0 μWm^{-3} in the Greater Himalaya, e.g., England et al., 1992; Menon et al., 2003; Whipp et al., 2007) while also producing reasonable temperatures in the middle and lower crust that would not produce partial melts. An important caveat is that these material properties are not transported along thrusts or exhumed in the model. While not all modeled strata originate above the 20 km e-folding depth, following emplacement of the MCT on Lesser Himalayan strata, most of the thrust duplication occurs above a depth of 20 km. In this section, we highlight the differences between modeled results using an e-folding depth, and the application of a constant surface heat production value to the entire thickness of the crust on both the predicted cooling ages, and the resulting temperature distribution in the crust.

To compare the two situations, we show the results from modeling our best-fit geometry (i.e., based on the Whipple et al., 2016 ramp geometry and hinterland-dipping duplex) using a constant velocity (21 mm/yr.) and a constant radiogenic heat production (Figures 2.19A, 2.19B). A constant radiogenic heat production means that heat producing elements are present at the same

concentration throughout the modeled domain of 110 km. This approach is problematic in that it requires notably lower heat production values (e.g., 0.5-0.7 μWm^{-3}) than seen in crustal rocks (e.g., 1.5- 6.0 μWm^{-3}; England et al., 1992; Menon et al., 2003; Whipp et al., 2007) to match the measured ages at the surface. In addition, mantle rocks are assigned values that are significantly higher than mantle values (< 0.03 μWm^{-3}). We tested constant radiogenic heat production values between 0.5 – 1.0 μWm^{-3} and found that values between 0.5 and 0.7 μWm^{-3} created a thermal field that produced modeled ages that more closely matched the measured ages. Figure 2.19A shows the differences between the cooling ages predicted by models with no e-folding depth (Black = 0.7 μWm^{-3}; Red = 0.63 μWm^{-3}; Blue = 0.5 μWm^{-3}), and the best-fit, e-folding model (Green = 2.55 μWm^{-3}) at the same constant velocities. As discussed in the manuscript, viable models must be able to reproduce the zone of partially reset/unreset MAr cooling ages between 60 and 90 km from the MFT in the region above the duplex. A constant radiogenic heat production value of 0.7 μWm^{-3} (Figure 2.19A; black) is too warm and produces young, reset MAr ages between 75 and 90 km from the MFT. A heat production value of 0.5 μWm^{-3} (Figure 2.19A; blue) can reproduce the required zone of unreset MAr ages, however the predicted MAr ages are 3-6 Ma too old compared to the measured ages. In addition, it fails to reproduce the young ZHe ages that are located 2-4 km from the trace of the MCT. A value of 0.63 μWm^{-3} is able to appropriately reproduce the zone of unreset MAr ages between 60 and 90 km and is a much better fit to the young (~1 Ma) ZHe ages located at the MCT. However, this value still produces MAr ages that are 3-6 Ma older than the measured ages, and ~3 Ma older than the best-fit model (green). This important difference is a function of how heat is distributed through the crust. The model using a constant radiogenic heat production value of 0.63 μWm^{-3} produces a geothermal gradient of 20°C/ km at the deformation front (MFT), while the model using a radiogenic heat production value of 2.55 μWm^{-3} and an e-

folding depth of 20 km produces a cooler geothermal gradient of 15°C/km consistent with heat flow measurements from the Indian shield (Roy and Rao, 2000). Conversely, where heat is being advected upward due to exhumation over the ramp, a constant radiogenic heat production value of 0.63 μWm^{-3} produces a geothermal gradient of 29°C/km while the model using a radiogenic heat production value of 2.55 μWm^{-3} and an e-folding depth of 20 km produces a significantly higher geothermal gradient of 35°C/km. The higher gradient in the hinterland is due to the upward advection of material with a higher radiogenic heat production (Figures 2.19B and 2.19C). The higher gradient is needed to match the young MAr and ZHe ages at and immediately north of the MCT (Figure 2.19A). A surface radiogenic heat production value combined with an e-folding depth also limits extreme temperatures in the mid to lower crust (Figures 2.19B and 2.19C).

In addition to comparing the effect on the predicted cooling ages, we can also compare the effect on the peak temperatures that the rocks encounter as they are transported to the surface. Comparisons between our modeled peak temperatures and those measured in the region provides independent constraints on the thermal field that our models generate (Figures 2.19D, 2.19E). Measured data from rocks in the GH shows that the highest temperatures were reached north of the MCT (> 650°-750°C), while the rocks preserved in the Kathmandu synform range between 500°C - 640°C (Johnson *et al.*, 2001; Kohn, 2008). South of the MCT, the LH rocks of the RMT reach lower temperatures, between 500°C - 600°C (Kohn, 2008). There is very little published temperature data for the rocks that make up the Gorkha- Pokhara antiform, with six samples located in the Benighat of the southern limb that recorded temperatures of ~380-480°C (Herman *et al.*, 2010).

Assigning a constant heat production value produces a significantly hotter thermal field, which in turn results in the prediction of peak temperatures for the GH in excess of 700°C. North

of the MCT, the range in the measured peak temperatures (650°C-750°C) matches the higher modeled peak temperatures resulting from a constant heat production value. However, immediately south of the MCT, the predicted temperatures (620°C – 660°C) are notably hotter than the measured values (500°C – 600°C). The rocks of the synform also have a significant mismatch between measured and modeled temperatures with the model predicting peak temperatures ~100°C higher than those measured. The lower peak temperatures predicted with the model that uses an e-folding depth of 20 km means that the peak temperatures in the hinterland (north of the MCT) are lower, only matching the lower range of temperatures (650-700°C) measured there. South of the MCT, the lower predicted peak temperatures mean that, while they are warmer than those measured, the mismatch is much smaller (~20°C). Within the rocks of the synform, the modeled peak temperatures using a e-folding depth of 20 km match the range of measured peak temperatures.

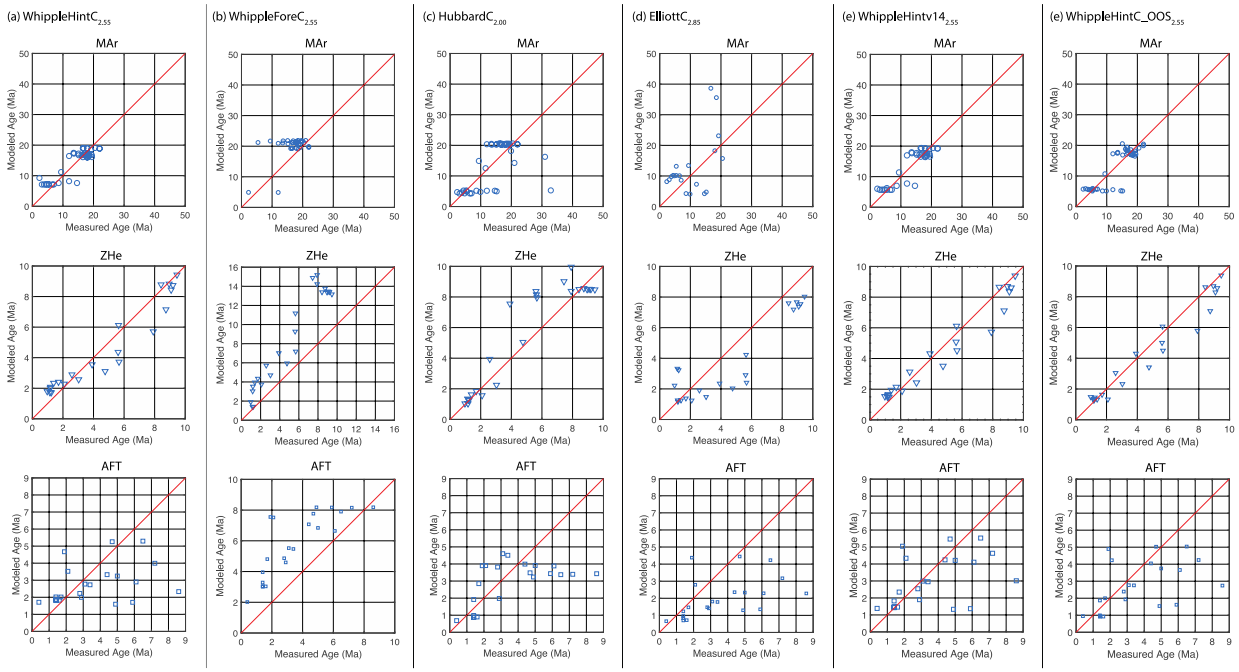

Figure 2.21: Statistical comparisons between modeled and measured MAr, ZHe and AFT ages respectively. (a) Whipple et al. decollement – Hinterland- dipping duplex, Constant rate, A_0 = 2.55; (b) Whipple et al. decollement – Foreland-dipping duplex, Constant rate, A_0 = 2.55; (c) Hubbard et al. decollement, Antiformal

stack, Constant rate, $A_0 = 2.00$; (d) Elliott et al. decollement, Hinterland-dipping duplex, Constant rate, $A_0 = 2.85$; (e) Whipple et al. decollement, Hinterland-dipping duplex, Best-fit velocities, $A_0 = 2.55$; (f) Whipple et al. decollement, Hinterland-dipping duplex, Out-of-sequence motion, Constant rate, $A_0 = 2.55$.

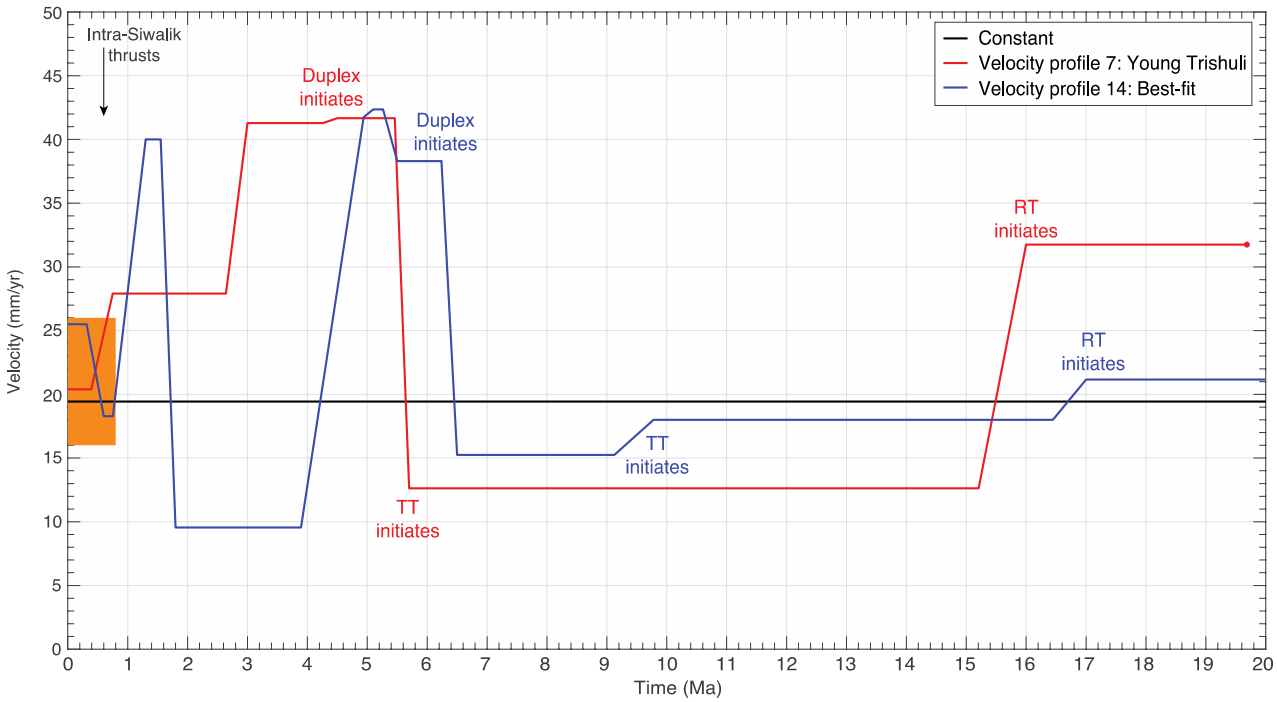

Figure 2.22: Changes in shortening rate with time for models shown in Figure 2.10A. Black = Constant velocity, Red = v7: Young Trishuli, Blue = v14: Best-fit. Orange box indicates measured values of recent convergence in the Subhimalayas (Bilham et al., 1997; Lavé and Avouac, 2000; Jouanne et al., 2004; Bettinelli et al., 2006; Ader et al., 2012).

2.8.4 Data fitting

To quantify the fit between the modeled and measured ages, we used a simple data fitting algorithm in MATLAB. Although the predicted cooling ages have a high resolution (0.5 km), the ages are not always co-located with the measured ages. Therefore, we calculated cooling ages that are co-located with each of the measured data points by averaging predicted ages over a window

that extends 1 km on each side of the measured age. This also takes into account a potential 0.5 km error in the spatial location of measured ages. The average predicted age over the 1 km window is directly compared to the associated measured data point and the age difference between them calculated. Figure 2.21 shows the measured vs. the predicted ages for each of our models. We define the difference between the measured age and the modeled age as the Residual (R). These are classical residuals (i.e., not normalized), since they are meant to show the absolute distance of the modeled value of age from the measured cooling age. Therefore, when the model predicts ages that are younger than the measured age, the Residual is taken to be positive, and vice versa. The differences in the entire model are quantified by calculating the Root Mean Square Error (RMSE) for each individual system, which is calculated using the formula below. Since the calculation of the RMSE treats both negative and positive residuals in the same manner, retaining the direction of the residual (positive/negative) allows us to understand whether the model is overpredicting, or underpredicting cooling ages in individual segments of the model. A combined RMSE value is calculated for each model by taking the mean of the individual RMSE values.

$$RMSE = \sqrt{\frac{\sum_{i=1}^{n} R_i^2}{n}}$$

In addition, we also use a 2-sample Kolmogorov-Smirnov Test (K-S test) (Massey, 1951) to select the model that minimizes the difference between the cumulative distribution functions (CDFs) of the measured and predicted age distributions. We generate cumulative distribution functions (CDFs) for the modeled and measured ages for each of the three thermochronometer systems. The difference between the CDFs for the modeled and measured ages for each system is calculated and the average for all three systems is reported as a combined p-value. To calculate the p-value, if a predicted age is within the 2σ error range associated with the measured data, this is

considered a match. If the predicted age is within a 4s error range we attach a weight to its contribution to the CDF based on how close it is to the 2s boundary, with the fit increasing the closer it is to the measured error. Regarding the measured MAr ages in the partially-reset/unreset zone, we consider any predicted age between 50 and 500 Ma, a match to measured ages between 100 - 2.0 Ga. Finally, the combined p-value is compared with a minimum value ($\alpha = 0.05$). If the p- value for the model is lower than α, the model is deemed to be incorrect. The best-fit model is determined based on a combination of RMSE and p-value. The model with the lowest RMSE has the lowest cumulative difference between the measured and predicted cooling ages. A higher p-value means that there is a better fit between the measured and predicted cooling age distributions. Table 2.5 shows the respective values for our models, and the best-fit.

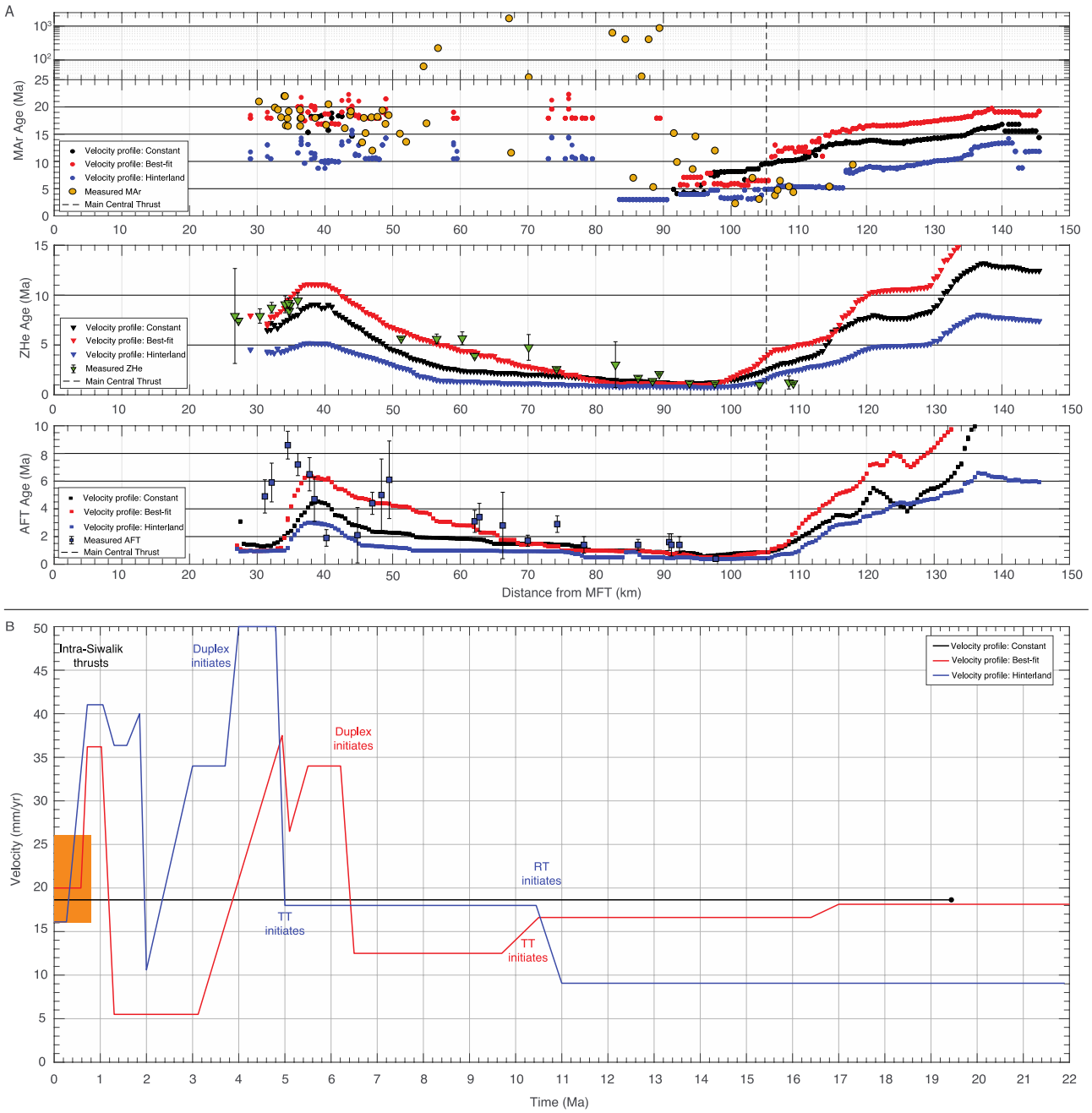

Figure 2.23: Comparison between different velocity profiles tested for the Hinterland-dipping duplex based on the Elliott et al., 2016 decollement geometry.

(a-c) Comparison between predicted and measured cooling ages for different velocity profiles, Black: vConstant; Red: Best-fit; Blue: Hinterland- match. (d) Comparison between shortening rate vs. Time for the velocity profiles shown in parts a-c.

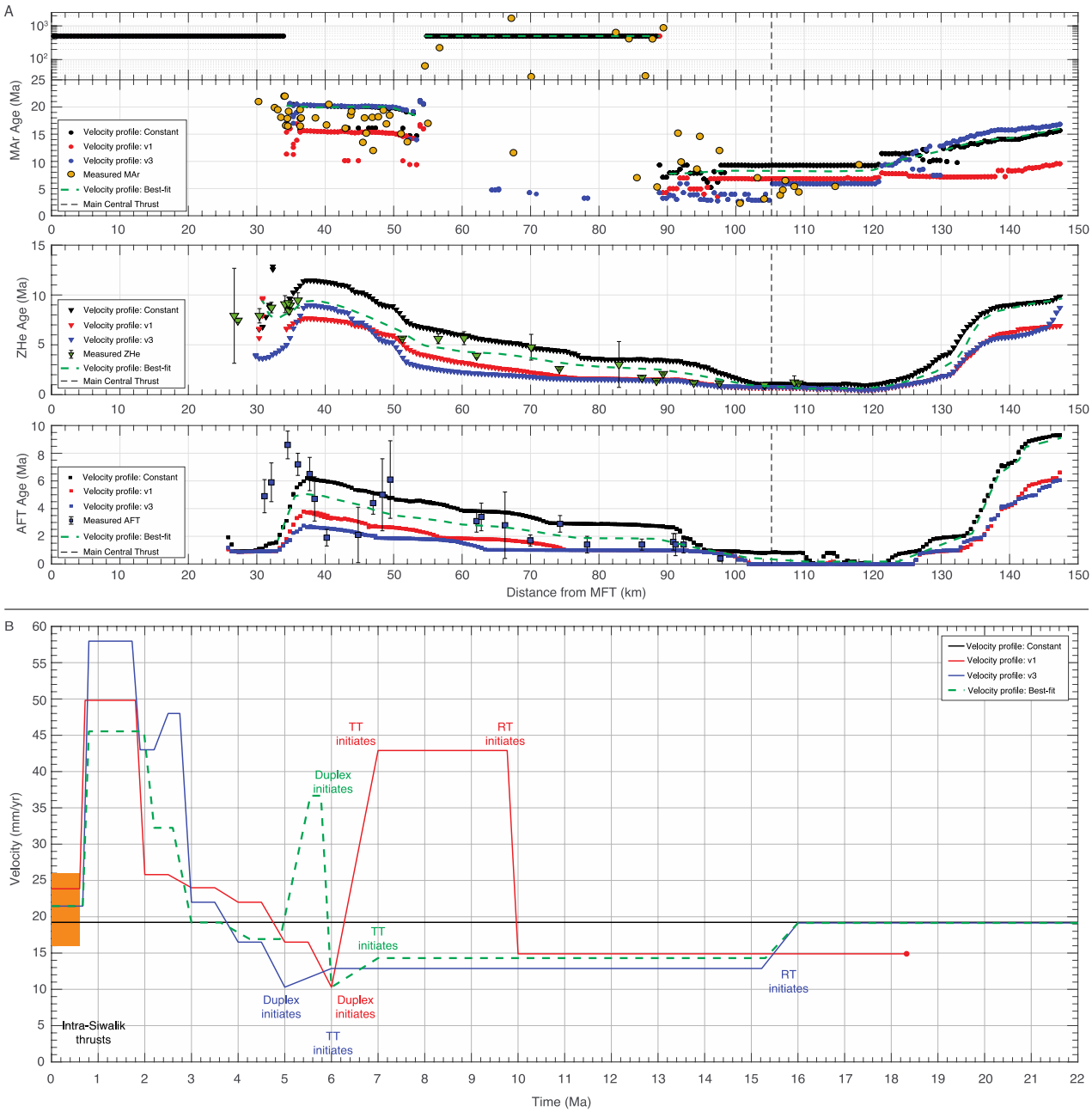

Figure 2.24: Comparison between different velocity profiles tested for the Foreland-dipping duplex based on the Whipple et al., 2016 decollement geometry.

(a-c) Comparison between predicted and measured cooling ages for different velocity profiles, Black: Constant; Red: v1; Blue: v3; Green-dashed: Best-fit. (d) Comparison between shortening rate vs. Time for the velocity profiles shown in parts a-c.

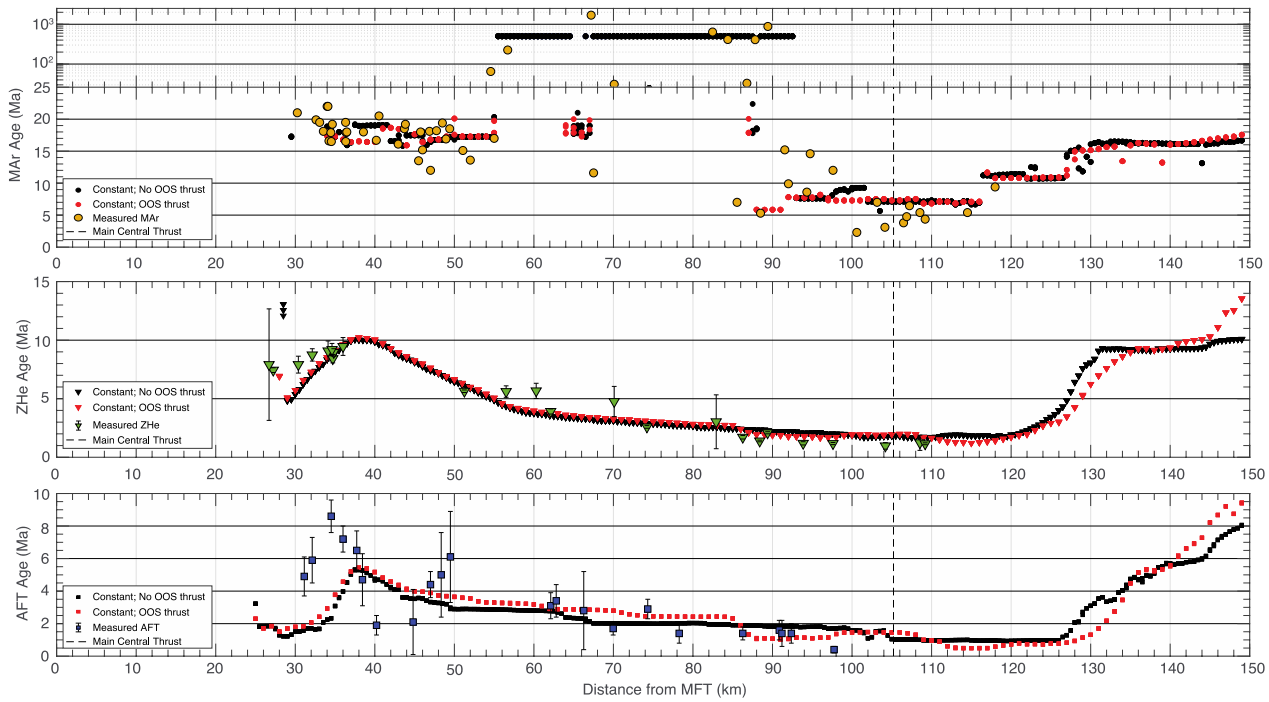

Figure 2.25: Effect of OOS thrusting on cooling ages using a constant velocity (red).

Shown here compared to cooling ages predicted by the constant rate model sans OOS thrusting (black), and measured cooling ages.

Decollement geometry	Duplex geometry	Thermal parameter ($\mu W\ m^{-3}$)	Velocity profile	P-value	RMSE
Whipple et al. (2016)	Hinterland-dipping	2.55	Constant	0.32	2.22
Whipple et al. (2016)	Foreland-dipping	2.00	Constant	0.2	2.59
Hubbard et al. (2016)	Antiformal stack	2	Constant	0.11	6.52
Elliott et al. (2016)	Hinterland-dipping	2.85	Constant	0.27	2.5
Whipple et al. (2016)	Hinterland-dipping	2.55	Constant	0.41	1.98
	Out-of-sequence thrusting				
Whipple et al. (2016)	Hinterland-dipping	2.55	Best-fit	0.62	0.97
Whipple et al. (2016)	Hinterland-dipping	2.55	Best-fit	0.7	0.85
	Out-of-sequence thrusting				

Table 2.5: Model statistics

2.9 References

Ader, T. *et al.* (2012) 'Convergence rate across the Nepal Himalaya and interseismic coupling on the Main Himalayan Thrust: Implications for seismic hazard', *Journal of Geophysical Research: Solid Earth*, 117, p. B04403. doi: 10.1029/2011JB009071.

Argand, E. (1916) 'Sur l'arc des Alpes Occidentales', *Eclogae geol. Helv.*, 14(1), pp. 145–191.

Avouac, J.-P. (2003) 'Mountain building, erosion, and the seismic cycle in the Nepal Himalaya', in *Treatise on Geophysics*. 2nd edn, pp. 1–80. doi: 10.1016/S0065-2687(03)46001-9.

Avouac, J.-P. *et al.* (2015) 'Lower edge of locked Main Himalayan Thrust unzipped by the 2015 Gorkha earthquake', *Nature Geoscience*, 8(9), pp. 708–711. doi: 10.1038/ngeo2518.

Bally, A. W. (1984) 'Tectogenèse et sismique reflexion', *Societe Geologiqne de France Bulletin*, pp. 279–285.

Bally, A. W., Gordy, P. L. and Stewart, G. A. (1966) 'Structure, seismic data, and orogenic evolution of Southern Canadian Rocky Mountains', *Bulletin of Canadian Petroleum Geology*, 14(3), pp. 337–381.

Beaumont, C. *et al.* (2001) 'Himalayan tectonics explained by extrusion of a low-viscosity crustal channel coupled to focused surface denudation', *Nature*, 414(6865), pp. 738–742. doi: 10.1038/414738a.

Bettinelli, P. *et al.* (2006) 'Plate motion of India and interseismic strain in the Nepal Himalaya from GPS and DORIS measurements', *Journal of Geodesy*, 80(8–11), pp. 567–589. doi: 10.1007/s00190-006-0030-3.

Bilham, R. *et al.* (1997) 'GPS measurements of present-day convergence across the Nepal Himalaya', *Nature*, 386, pp. 61–64.

Blanpied, M. L., Lockner, D. A. and Byerlee, J. D. (1995) 'Frictional slip of granite at hydrothermal conditions', *Journal of Geophysical Research: Solid Earth*, 100(B7), pp. 13045–13064. doi: 10.1029/95JB00862.

Bollinger, L. *et al.* (2004) 'Thermal structure and exhumation history of the Lesser Himalaya in central Nepal', *Tectonics*, 23(5), p. n/a-n/a. doi: 10.1029/2003TC001564.

Bollinger, L., Henry, P. and Avouac, J.-P. (2006) 'Mountain building in the Nepal Himalaya: Thermal and kinematic model', *Earth and Planetary Science Letters*, 244(1–2), pp. 58–71. doi: 10.1016/j.epsl.2006.01.045.

Boyer, S. E. and Elliott, D. (1982) 'Thrust systems', *American Association of Petroleum Geologists Bulletin*, 66(9), pp. 1196–1230.

Brady, R. J. *et al.* (2006) 'The distribution of radiogenic heat production as a function of depth in the Sierra Nevada batholith, California', *Lithos*. doi: 10.1016/j.lithos.2005.06.003.

Braun, J. (2003) 'Pecube: A new finite-element code to solve the 3D heat transport equation including the effects of a time-varying, finite amplitude surface topography', *Computers and Geosciences*, 29(6), pp. 787–794. doi: 10.1016/S0098-3004(03)00052-9.

Brewer, I. D., Burbank, D. W. and Hodges, K. V. (2003) 'Modelling detrital cooling-age populations: Insights from two Himalayan catchments', *Basin Research*, 15(3), pp. 305–320. doi: 10.1046/j.1365-2117.2003.00211.x.

Brookfield, M. E. (1993) 'The Himalayan passive margin from Precambrian to Cretaceous times', *Sedimentary Geology*, 84, pp. 1–35.

Burbank, D. W., Beck, R. A. and Mulder, T. (1996) 'The Himalayan foreland', in Lin, A. and Harrison, T. M. (eds) *The Tectonic Evolution of Asia*. United Kingdom: Cambridge University Press, pp. 149–188.

Copeland, P. *et al.* (1991) 'An early Pliocene thermal disturbance of the main central thrust, central Nepal: Implications for Himalayan tectonics', *Journal of Geophysical Research*, 96(B5), p. 8475. doi: 10.1029/91JB00178.

Corrie, S. L. *et al.* (2012) 'Flattening the Bhutan Himalaya', *Earth and Planetary Science Letters*. Elsevier, 349–350, pp. 67–74. doi: 10.1016/j.epsl.2012.07.001.

Coutand, I. *et al.* (2014) 'Geometry and kinematics of the MHT and Neogene crustal exhumation in the Bhutanese Himalaya derived from inversion of multithermochronologic data', *Journal of Geophysical Research: Solid Earth*, (119), pp. 1446–1481. doi: 10.1002/2013JB010891.Received.

Crowley, K. d., Cameron, M. and Schaefer, R. l. (1991) 'Experimental studies of annealing of etched fission tracks in fluorapatite', *Geochimica et Cosmochimica Acta*, 55(5), pp. 1449–1465. doi: 10.1016/0016-7037(91)90320-5.

Dahlstrom, C. D. A. (1969) 'Balanced cross-sections', *Canadian Journal of Earth Sciences*, 6(743), pp. 743–757. Available at: papers2://publication/uuid/66E6734E-BBF3-42E7-9CA3-6E44B6908D7C.

DeCelles, P. G. *et al.* (1998) 'Eocene-early Miocene foreland basin development and the history of Himalayan thrusting, western and central Nepal', *Tectonics*, 17(5), pp. 741–765. doi: 10.1029/98TC02598.

DeCelles, P. G. *et al.* (2001) 'Stratigraphy, structure, and tectonic evolution of the Himalayan fold-thrust belt in western Nepal', *Tectonics*, 20(4), pp. 487–509. doi: 10.1029/2000TC001226.

DeCelles, P. G. *et al.* (2014) 'Paleocene-Eocene foreland basin evolution in the Himalaya of southern Tibet and Nepal: Implications for the age of initial India-Asia collision', *Tectonics*,

33(5), pp. 824–849. doi: 10.1002/2014TC003522.

Dodson, M. H. (1973) ‘Closure temperature in cooling geochronological and petrological systems’, *Contributions to Mineralogy and Petrology*, 40, pp. 259–274. Available at: http://www.raco.cat/index.php/Dovella/article/view/20118.

Duputel, Z. *et al.* (2016) ‘The 2015 Gorkha earthquake: A large event illuminating the Main Himalayan thrust fault’, *Geophysical Research Letters*, 43(6), pp. 2517–2525. doi: 10.1002/2016GL068083.

Ehlers, T. A. *et al.* (2005) ‘Computational tools for low-temperature Thermochronometer Interpretation’, *Reviews in Mineralogy and Geochemistry*, 58(1), pp. 589–622. doi: 10.2138/rmg.2005.58.22.

Ehlers, T. A. (2005) ‘Crustal thermal processes and the interpretation of Thermochronometer data’, *Reviews in Mineralogy and Geochemistry*, 58(1), pp. 315–350. doi: 10.2138/rmg.2005.58.12.

Elliott, D. (1983) ‘The construction of balanced cross-sections’, *Journal of Structural Geology*, 5(2), p. 101. doi: https://doi.org/10.1016/0191-8141(83)90035-4.

Elliott, J. R. *et al.* (2016) ‘Himalayan megathrust geometry and relation to topography revealed by the Gorkha earthquake’, *Nature Geoscience*, 9(2), pp. 174–180. doi: 10.1038/ngeo2623.

England, P. *et al.* (1992) ‘Heat sources for tertiary metamorphism and anatexis in the Annapurna-Manaslu region central Nepal’, *Journal of Geophysical Research*, 97(B2), pp. 2107–2128. doi: 10.1029/91JB02272.

Fuchs, G. (1980) ‘The Lesser Himalayan geology of the West Nepal and its regional importance’, in Valdiya, K. S. and Bhatia, S. B. (eds) *Stratigraphy and Correlation of the Lesser*

Himalayan Formations. Delhi: Hindustan Publishing Corp., pp. 163–173.

Gansser, A. (1964) *Geology of the Himalayas*. New York: Wiley-Interscience.

Garzanti, E., Baud, A. and Mascle, G. (1987) 'Sedimentary record of the northward flight of India and its collision with Eurasia (Ladakh Himalaya, India)', *Geodinamica Acta*. Taylor & Francis, 1(4–5), pp. 297–312. doi: 10.1080/09853111.1987.11105147.

Gautam, P. and Rösler, W. (1999) 'Depositional chronology and fabric of Siwalik Group sediments in central Nepal from magnetostratigraphy and magnetic anisotropy', *Journal of Asian Earth Sciences*, 17(5–6), pp. 659–682. doi: 10.1016/S1367-9120(99)00021-8.

Gilmore, M. E. *et al.* (2018) 'Testing the effects of topography, geometry, and kinematics on modeled thermochronometer cooling ages in the eastern Bhutan Himalaya', *Solid Earth*, 9(3), pp. 599–627. doi: 10.5194/se-9-599-2018.

Grandin, R. *et al.* (2015) 'Rupture process of the M w = 7.9 2015 Gorkha earthquake (Nepal): Insights into Himalayan megathrust segmentation', *Geophysical Research Letters*, 42(20), pp. 8373–8382. doi: 10.1002/2015GL066044.

Gwinn, V. E. (1970) 'Kinematic patterns and estimates of lateral shortening, Valley and Ridge and Great Valley Provinces, central Appalachian, south-central Pennsylvania', in Fisher, G. W. (ed.) *Studies of Appalachian Geology: Central and Southern New York*. New York: Interscience Publishers, pp. 127–146.

Hames, W. E. and Bowring, S. A. (1994) 'An empirical evaluation of the argon diffusion geometry in muscovite', *Earth and Planetary Science Letters*, 124(1–4), pp. 161–169. doi: 10.1016/0012-821X(94)00079-4.

Harrison, T. M. *et al.* (1993) 'Isotopic preservation of Himalayan/Tibetan uplift, denudation, and climatic histories of two molasse deposits', *The Journal of Geology*, 101, pp. 157–

175.

Harrison, T. M. *et al.* (2009) 'Diffusion of 40Ar in muscovite', *Geochimica et Cosmochimica Acta*, 73(4), pp. 1039–1051. doi: 10.1016/j.gca.2008.09.038.

Herman, F. *et al.* (2010) 'Exhumation, crustal deformation, and thermal structure of the Nepal Himalaya derived from the inversion of thermochronological and thermobarometric data and modeling of the topography', *Journal of Geophysical Research: Solid Earth*, 115(6). doi: 10.1029/2008JB006126.

Hodges, K. V. *et al.* (2004) 'Quaternary deformation, river steepening, and heavy precipitation at the front of the Higher Himalayan ranges', *Earth and Planetary Science Letters*, 220(3–4), pp. 379–389. doi: 10.1016/S0012-821X(04)00063-9.

Hodges, K. V. *et al.* (2005) '40Ar/39Ar thermochronology of detrital minerals', *Reviews in Mineralogy and Geochemistry*, 58(1), pp. 239–257. doi: 10.2138/rmg.2005.58.9.

Hodges, K. V. (2014) 'Thermochronology in Orogenic Systems', in Holland, H. D. and Turekian, K. K. (eds) *Treatise on Geochemistry*. Amsterdam: Elsevier, pp. 281–308. doi: 10.1016/B978-0-08-095975-7.00308-9.

Hodges, K. V., Hurtado, J. M. and Whipple, K. X. (2001) 'Southward extrusion of Tibetan crust and its effect on Himalayan tectonics', *Tectonics*, 20(6), pp. 799–809. doi: 10.1029/2001TC001281.

Hodges, K. V., Parrish, R. R. and Searle, M. P. (1996) 'Tectonic evolution of the central Annapurna Range, Nepalese Himalayas', *Tectonics*, 15(6), pp. 1264–1291. doi: 10.1029/96TC01791.

Hourigan, J. K., Reiners, P. W. and Brandon, M. T. (2005) 'U-Th zonation-dependent alpha-ejection in (U-Th)/He chronometry', *Geochimica et Cosmochimica Acta*, 69(13), pp. 3349–

3365. doi: 10.1016/j.gca.2005.01.024.

Hsu, Y. J. *et al.* (2009) 'Spatio-temporal slip, and stress level on the faults within the western foothills of Taiwan: Implications for fault frictional properties', *Pure and Applied Geophysics*, 166(10–11), pp. 1853–1884. doi: 10.1007/s00024-009-0510-5.

Hu, X. *et al.* (2016) 'The timing of India-Asia collision onset – Facts, theories, controversies', *Earth-Science Reviews*. Elsevier B.V., 160, pp. 264–299. doi: 10.1016/j.earscirev.2016.07.014.

Hubbard, J. *et al.* (2016) 'Structural segmentation controlled the 2015 M w 7.8 Gorkha earthquake rupture in Nepal', *Geology*, 44(8), pp. 639–642. doi: 10.1130/G38077.1.

Hubbard, M. S. and Harrison, T. M. (1989) '40Ar/39Ar age constraints on deformation and metamorphism in the main central thrust zone and Tibetan slab, eastern Nepal Himalaya', *Tectonics*, 8(4), pp. 865–880. doi: 10.1029/TC008i004p00865.

Huntington, K. W. *et al.* (2007) 'Topography, exhumation pathway, age uncertainties, and the interpretation of thermochronometer data', *Tectonics*, 26(4), pp. 1–23. doi: 10.1029/2007TC002108.

Jamieson, R. A. *et al.* (2004) 'Crustal channel flows: 2. Numerical models with implications for metamorphism in the Himalayan-Tibetan orogen', *Journal of Geophysical Research: Solid Earth*, 109(6), pp. 1–24. doi: 10.1029/2003JB002811.

Johnson, M. R. W. *et al.* (2001) 'Synthrusting metamorphism, cooling, and erosion of the Himalayan Kathmandu Complex, Nepal', *Tectonics*, 20(3), pp. 394–415. doi: 10.1029/2001TC900005.

Jouanne, F. *et al.* (2004) 'Current shortening across the Himalayas of Nepal', *Geophysical Journal International*, 157(1), pp. 1–14. doi: 10.1111/j.1365-246X.2004.02180.x.

Ketcham, R. A. (1996) 'Distribution of heat-producing elements in the upper and middle crust of southern and west central Arizona: Evidence from the core complexes', *Journal of Geophysical Research: Solid Earth*. doi: 10.1029/96jb00664.

Khanal, S. (2009) *Upper crustal shortening and forward modeling of the Himalayan fold-thrust belt along the Budhi-Gandaki River, central Nepal*. The University of Alabama.

Khanal, S. and Robinson, D. M. (2013) 'Upper crustal shortening and forward modeling of the Himalayan thrust belt along the Budhi-Gandaki River, central Nepal', *International Journal of Earth Sciences*, 102(7), pp. 1871–1891. doi: 10.1007/s00531-013-0889-1.

Kohn, M. J. *et al.* (2004) 'Miocene faulting at plate tectonic velocity in the Himalaya of central Nepal', *Earth and Planetary Science Letters*, 228(3–4), pp. 299–310. doi: 10.1016/j.epsl.2004.10.007.

Kohn, M. J. (2008) 'P-T-t data from central Nepal support critical taper and repudiate large-scale channel flow of the Greater Himalayan Sequence', *Bulletin of the Geological Society of America*, 120(3–4), pp. 259–273. doi: 10.1130/B26252.1.

Kuiper, K. F. *et al.* (2008) 'Synchronizing rock clocks of Earth history', *Science*, 320(5875), pp. 500–504. doi: 10.1126/science.1154339.

Larson, K. P. and Cottle, J. M. (2014) 'Midcrustal discontinuities and the assembly of the Himalayan midcrust', *Tectonics*, 33(5), pp. 718–740. doi: 10.1002/2013TC003452.

Larson, K. P. and Godin, L. (2009) 'Kinematics of the Greater Himalayan sequence, Dhaulagiri Himal: Implications for the structural framework of central Nepal', *Journal of the Geological Society*, 166(1), pp. 25–43. doi: 10.1144/0016-76492007-180.

Larson, K. P., Godin, L. and Price, R. A. (2010) 'Relationships between displacement and distortion in orogens: Linking the Himalayan foreland and hinterland in central Nepal', *Geological*

Society of America Bulletin, 122(7–8), pp. 1116–1134. doi: 10.1130/B30073.1.

Lavé, J. and Avouac, J.-P. (2000) 'Active folding of fluvial terraces across the Siwaliks Hills, Himalayas of central Nepal', *Journal of Geophysical Research: Solid Earth*, 105(B3), pp. 5735–5770. doi: 10.1029/1999JB900292.

Lavé, J. and Avouac, J.-P. (2001) 'Fluvial incision and tectonic uplift across the Himalayas of central Nepal', *Journal of Geophysical Research: Solid Earth*, 106(B11), pp. 26561–26591. doi: 10.1029/2001JB000359.

Law, R. D. *et al.* (2013) 'Deformation temperatures and flow vorticities near the base of the Greater Himalayan Series, Sutlej Valley and Shimla Klippe, NW India', *Journal of Structural Geology*. Elsevier Ltd, 54, pp. 21–53. doi: 10.1016/j.jsg.2013.05.009.

Lay, T. *et al.* (2012) 'Depth-varying rupture properties of subduction zone megathrust faults', *Journal of Geophysical Research: Solid Earth*, 117(4), pp. 1–21. doi: 10.1029/2011JB009133.

Lemonnier, C. *et al.* (1999) 'Electrical structure of the Himalaya of central Nepal: High conductivity around the mid-crustal ramp along the MHT', *Geophysical Research Letters*, 26(21), pp. 3261–3264. doi: 10.1029/1999GL008363.

Lock, J. and Willett, S. (2008) 'Low-temperature thermochronometric ages in fold-and-thrust belts', *Tectonophysics*, 456(3–4), pp. 147–162. doi: 10.1016/j.tecto.2008.03.007.

Long, S. *et al.* (2011) 'Quantifying internal strain and deformation temperature in the eastern Himalaya, Bhutan: Implications for the evolution of strain in thrust sheets', *Journal of Structural Geology*. Elsevier Ltd, 33(4), pp. 579–608. doi: 10.1016/j.jsg.2010.12.011.

Long, S. P. *et al.* (2012) 'Variable shortening rates in the eastern Himalayan thrust belt, Bhutan: Insights from multiple thermochronologic and geochronologic data sets tied to kinematic

reconstructions', *Tectonics*, 31(5). doi: 10.1029/2012TC003155.

Long, S. P. *et al.* (2016) 'Temperature and strain gradients through Lesser Himalayan rocks and across the Main Central thrust, south central Bhutan: Implications for transport-parallel stretching and inverted metamorphism', *Tectonics*, 35(8), pp. 1863–1891. doi: 10.1002/2016TC004242.

Lyon-Caen, H. and Molnar, P. (1985) 'Gravity anomalies, flexure of the Indian Plate, and the structure, support and evolution of the Himalaya and Ganga Basin', *Tectonics*, 4(6), pp. 513–538. doi: 10.1029/TC004i006p00513.

Macfarlane, A. M., Hodges, K. V. and Lux, D. (1992) 'A structural analysis of the Main Central thrust zone, Langtang National Park, central Nepal Himalaya', *Geological Society of America Bulletin*, 104(11), pp. 1389–1402. doi: 10.1130/0016-7606(1992)104<1389:ASAOTM>2.3.CO;2.

Marchant, R. (1993) *The Underground of the Western Alps*. Université de Lausanne, Lausanne.

Marone, C. (1998) 'Laboratory-derived friction laws and their application to seismic faulting', *Annual Review of Earth and Planetary Sciences*, 26(1), pp. 643–696. doi: 10.1146/annurev.earth.26.1.643.

Martin, A. J. *et al.* (2011) 'Stratigraphic and tectonic implications of field and isotopic constraints on depositional ages of Proterozoic Lesser Himalayan rocks in central Nepal', *Precambrian Research*. Elsevier B.V., 185(1–2), pp. 1–17. doi: 10.1016/j.precamres.2010.11.003.

Massey, F. J. (1951) 'The Kolmogorov-Smirnov test for goodness of fit', *Journal of the American Statistical Association*. Taylor & Francis, 46(253), pp. 68–78. doi: 10.1080/01621459.1951.10500769.

McQuarrie, N. *et al.* (2019) 'The influence of foreland structures on hinterland cooling: Evaluating the drivers of exhumation in the eastern Bhutan Himalaya', *Tectonics*, pp. 1–29. doi: 10.1029/2018tc005340.

McQuarrie, N. and Ehlers, T. A. (2015) 'Influence of thrust belt geometry and shortening rate on thermochronometer cooling ages: Insights from thermokinematic and erosion modeling of the Bhutan Himalaya', *Tectonics*, 34(6), pp. 1055–1079. doi: 10.1002/2014TC003783.

McQuarrie, N. and Ehlers, T. A. (2017) 'Techniques for understanding fold-and-thrust belt kinematics and thermal evolution', in Law, R. D. et al. (eds) *Linkages and Feedbacks in Orogenic Systems*. Boulder: Geological Society of America, pp. 25–54. doi: 10.1130/2017.1213(02).

Menon, R. *et al.* (2003) 'Radiogenic heat production of Late Archaean Bundelkhand granite and some Proterozoic gneisses and granitoids of central India', *Current Science*, 85(5), pp. 634–638.

Mitra, S. (1986) 'Duplex structures and imbricate thrust systems: Geometry, structural position, and hydrocarbon potential', *AAPG Bulletin*. doi: 10.1306/94886A7E-1704-11D7-8645000102C1865D.

Morgan, L. E. (2020) 'Argon data for Nepal', *U.S. Geological Survey*. doi: 10.5066/P9FA0HI0.

Mugnier, J. L. *et al.* (1998) 'The break-back thrust splay of the Main Dun thrust (Himalayas of western Nepal): Evidence of an intermediate displacement scale between earthquake slip and finite geometry of thrust systems', *Journal of Structural Geology*, 20(7), pp. 857–864. doi: 10.1016/S0191-8141(98)00024-8.

Ni, J. and Barazangi, M. (1984) 'Seismotectonics of the Himalayan collision zone: Geometry of the underthrusting Indian plate beneath the Himalaya.', *Journal of Geophysical*

Research, 89(B2), pp. 1147–1163. doi: 10.1029/JB089iB02p01147.

Ojha, T. P. *et al.* (2000) 'Magnetic polarity stratigraphy of the Neogene Siwalik Group at Khutia Khola, far western Nepal', *Bulletin of the Geological Society of America*, 112(3), pp. 424–434. doi: 10.1130/0016-7606(2000)112<424:MPSOTN>2.0.CO;2.

Ojha, T. P. *et al.* (2009) 'Magnetic polarity stratigraphy of the Neogene foreland basin deposits of Nepal', *Basin Research*, 21(1), pp. 61–90. doi: 10.1111/j.1365-2117.2008.00374.x.

Orme, D. A., Carrapa, B. and Kapp, P. (2015) 'Sedimentology, provenance and geochronology of the upper Cretaceous-lower Eocene western Xigaze forearc basin, southern Tibet', *Basin Research*, 27(4), pp. 387–411. doi: 10.1111/bre.12080.

Pandey, M. R. *et al.* (1995) 'Interseismic strain accumulation on the Himalayan crustal ramp (Nepal)', *Geophysical Research Letters*, 22(7), pp. 751–754. doi: 10.1029/94GL02971.

Parsons, A. J., Ferré, E. C., *et al.* (2016) 'Orogen-parallel deformation of the Himalayan midcrust: Insights from structural and magnetic fabric analyses of the Greater Himalayan Sequence, Annapurna-Dhaulagiri Himalaya, central Nepal', *Tectonics*, 35(11), pp. 2515–2537. doi: 10.1002/2016TC004244.

Parsons, A. J., Law, R. D., *et al.* (2016) 'Thermo-kinematic evolution of the Annapurna-Dhaulagiri Himalaya, central Nepal: The composite orogenic system', *Geochemistry, Geophysics, Geosystems*, 17(4), pp. 1511–1539. doi: 10.1002/2015GC006184.

Pearson, O. N. (2002) *Structural evolution of the central Nepal fold-thrust belt and regional tectonic and structural significance of the Ramgarh thrust*. The University of Arizona, Tucson.

Pearson, O. N. and DeCelles, P. G. (2005) 'Structural geology and regional tectonic significance of the Ramgarh thrust, Himalayan fold-thrust belt of Nepal', *Tectonics*, 24(4), pp. 1–

26. doi: 10.1029/2003TC001617.

Pêcher, A. (1977) ‘Geology of the Nepal Himalaya: Deformation and petrography in the Main Central thrust zone’, in *Colloques Internationaux du Centre National de la Recherche Scientifique*, pp. 301–318.

Price, R. A. (1981) ‘The Cordilleran thrust and fold belt in the southern Canadian Rocky Mountains’, in McClay, K. R. and Price, N. J. (eds) *Thrust and nappe tectonics*. London: Geological Society of London, pp. 427–448.

Quade, J. *et al.* (1995) ‘Late Miocene environmental change in Nepal and the northern Indian subcontinent: Stable isotopic evidence from paleosols’, *Geological Society of America Bulletin*, 107(12), pp. 1381–1397. doi: 10.1130/0016-7606(1995)107<1381:LMECIN>2.3.CO;2.

Rahn, M. K. and Grasemann, B. (1999) ‘Fission track and numerical thermal modeling of differential exhumation of the Glarus thrust plane (Switzerland)’, *Earth and Planetary Science Letters*, 169(3–4), pp. 245–259. doi: 10.1016/S0012-821X(99)00078-3.

Rak, A. J., McQuarrie, N. and Ehlers, T. A. (2017) ‘Kinematics, exhumation, and sedimentation of the north central Andes (Bolivia): An integrated thermochronometer and thermokinematic modeling approach’, *Tectonics*, 36(11), pp. 2524–2554. doi: 10.1002/2016TC004440.

Ratschbacher, L. *et al.* (1994) ‘Distributed deformation in southern and western Tibet during and after the India-Asia collision’, *Journal of Geophysical Research*, 99(B10), pp. 19,917-19,645.

Ray, L., Bhattacharya, A. and Roy, S. (2007) ‘Thermal conductivity of Higher Himalayan crystallines from Garhwal Himalaya, India’, *Tectonophysics*, 434(1–4), pp. 71–79. doi: 10.1016/j.tecto.2007.02.003.

Reiners, P. W. *et al.* (2004) 'Zircon (U-Th)/He thermochronometry: He diffusion and comparisons with 40Ar/39Ar dating', *Geochimica et Cosmochimica Acta*, 68(8), pp. 1857–1887. doi: 10.1016/j.gca.2003.10.021.

Reiners, P. W. (2005) 'Zircon (U-Th)/He thermochronometry', *Reviews in Mineralogy and Geochemistry*, 58(1), pp. 151–179. doi: 10.2138/rmg.2005.58.6.

Renne, P. R. *et al.* (2005) 'Application of deuteron-deuteron (D-D) fusion neutrons to 40Ar/39Ar geochronology', *Applied Radiation and Isotopes*, 62(1), pp. 25–32. doi: 10.1016/j.apradiso.2004.06.004.

Rich, J. L. (1934) 'Mechanics of low-angle overthrust faulting as illustrated by Cumberland thrust block, Virginia, Kentucky, and Tennessee', *Bulletin of the American Association of Petroleum Geologists*, 18(12), pp. 1584–1596.

Riesner, M. *et al.* (2019) 'Himalayan Main Boundary thrust reactivation as a normal fault: Constraints and implications for the seismic cycle in western Nepal', in *EGU General Assembly Conference Abstracts*, p. 16418. Available at: https://ui.adsabs.harvard.edu/abs/2019EGUGA..2116418R.

Robert, X. *et al.* (2011) 'Control of detachment geometry on lateral variations in exhumation rates in the Himalaya: Insights from low-temperature thermochronology and numerical modeling', *Journal of Geophysical Research: Solid Earth*, 116(5), pp. 1–22. doi: 10.1029/2010JB007893.

Robinson, D. M. *et al.* (2003) 'Kinematic model for the Main Central thrust in Nepal', *Geology*, 31(4), p. 359. doi: 10.1130/0091-7613(2003)031<0359:KMFTMC>2.0.CO;2.

Robinson, D. M., DeCelles, P. G. and Copeland, P. (2006) 'Tectonic evolution of the Himalayan thrust belt in western Nepal: Implications for channel flow models', *Bulletin of the*

Geological Society of America, 118(7–8), pp. 865–885. doi: 10.1130/B25911.1.

Robinson, D. M. and Martin, A. J. (2014) 'Reconstructing the greater Indian margin: A balanced cross section in central Nepal focusing on the Lesser Himalayan duplex', *Tectonics*, 33(11), pp. 2143–2168. doi: 10.1002/2014TC003564.

Robinson, D. M. and Pearson, O. N. (2013) 'Was Himalayan normal faulting triggered by initiation of the Ramgarh-Munsiari thrust and development of the Lesser Himalayan duplex?', *International Journal of Earth Sciences*, 102(7), pp. 1773–1790. doi: 10.1007/s00531-013-0895-3.

Rodgers, J. (1950) 'Mechanics of Appalachian folding as illustrated by Sequatchie anticline Tennessee and Alabama', *AAPG Bulletin*, 34, pp. 672–681.

Roy, S. and Rao, R. U. M. (2000) 'Heat flow in the Indian shield', *Journal of Geophysical Research: Solid Earth*, 105(B11), pp. 25587–25604. doi: 10.1029/2000JB900257.

Ruppel, C. and Hodges, K. V. (1994) 'Role of horizontal thermal conduction and finite time thrust emplacement in simulation of pressure-temperature-time paths', *Earth and Planetary Science Letters*, 123(1–3), pp. 49–60. doi: 10.1016/0012-821X(94)90256-9.

Sakai, H. (1983) 'Geology of the Tansen Group of the Lesser Himalaya in Nepal', *Memoirs of the Faculty of Science, Kyushu University*, pp. 27–74.

Sakai, H. (1985) 'Rifting of the Gondwanaland and uplifting of the Himalayas recorded in Mesozoic and Tertiary fluvial sediments in the Nepal Himalayas', in Taira, A. and Masuda, F. (eds) *Sedimentary Facies in the Active Plate Margin*. Tokyo: Terra Sci., pp. 723–732.

Sambridge, M. (1999) 'Geophysical inversion with a neighbourhood algorithm-I', *Searching a parameter space: Geophysical Journal International*, 138, pp. 479–494.

Schmitz, M. D. and Bowring, S. A. (2001) 'U-Pb zircon and titanite systematics of the Fish

Canyon Tuff: An assessment of high-precision U-Pb geochronology and its application to young volcanic rocks', *Geochimica et Cosmochimica Acta*, 65(15), pp. 2571–2587. doi: 10.1016/S0016-7037(01)00616-0.

Seeber, L. and Armbruster, J. G. (1981) 'Great detachment earthquakes along the Himalayan arc and long-term forecasting', in *Earthquake Prediction: An International Review*, pp. 259–277. doi: 10.1029/ME004p0259.

Shi, Y. and Wang, C. Y. (1987) 'Two-dimensional modeling of the P-T-t paths of regional metamorphism in simple overthrust terrains', *Geology*, 15(11), pp. 1048–1051. doi: 10.1130/0091-7613(1987)15<1048:TMOTPP>2.0.CO;2.

Stöcklin, J. (1980) *Geology of Nepal and its regional frame*, *Journal of the Geological Society*. Geological Society of London. doi: 10.1144/gsjgs.137.1.0001.

Tokuoka, T. *et al.* (1986) 'The Churia (Siwalik) Group of the Arung Khola area, west central Nepal', *Memoirs of the Faculty of Science, Shimane University*, 20, pp. 135–210.

Trümpy, R. (1980) *Geology of Switzerland: A Guide-Book*. Basel and New York: Wepf & Co. doi: 10.1180/minmag.1981.044.335.28.

Upreti, B. N. (1996) 'Stratigraphy of the western Nepal Lesser Himalaya', *Journal of the Nepal Geological Society*, 13, pp. 11–28.

USGS (2015) *M7.8 - 36km E of Khudi, Nepal*. Available at: http://earthquake.usgs.gov/earthquakes/eventpage/us20002926#general_summary.

Whipp, D. M. *et al.* (2007) 'Plio-Quaternary exhumation history of the central Nepalese Himalaya: 2. Thermokinematic and thermochronometer age prediction model', *Tectonics*, 26(3). doi: 10.1029/2006TC001991.

Whipp, D. M. *et al.* (2009) 'Effects of exhumation kinematics and topographic evolution

on detrital thermochronometer data', *Journal of Geophysical Research: Earth Surface*, 114(4), pp. 1–20. doi: 10.1029/2008JF001195.

Whipple, K. X. *et al.* (2016) 'Active shortening within the Himalayan orogenic wedge implied by the 2015 Gorkha earthquake', *Nature Geoscience*, 9(9), pp. 711–716. doi: 10.1038/ngeo2797.

Wobus, C. *et al.* (2005) 'Active out-of-sequence thrust faulting in the central Nepalese Himalaya', *Nature*, 434(7036), pp. 1008–1011. doi: 10.1038/nature03499.

Wobus, C. W., Hodges, K. V. and Whipple, K. X. (2003) 'Has focused denudation sustained active thrusting at the Himalayan topographic front?', *Geology*, 31(10), p. 861. doi: 10.1130/G19730.1.

Wobus, C. W., Whipple, K. X. and Hodges, K. V. (2006) 'Neotectonics of the central Nepalese Himalaya: Constraints from geomorphology, detrital 40 Ar/ 39 Ar thermochronology, and thermal modeling', *Tectonics*, 25(4), p. n/a-n/a. doi: 10.1029/2005TC001935.

Woodward, N. B., Boyer, S. E. and Suppe, J. (1989) *Balanced geological cross-sections: An essential technique in geological research and exploration*, *Balanced Geological Cross-Sections: An Essential Technique in Geological Research and Exploration*. doi: 10.1029/sc006.

Yagi, Y. and Okuwaki, R. (2015) 'Integrated seismic source model of the 2015 Gorkha, Nepal, earthquake', *Geophysical Research Letters*, 42(15), pp. 6229–6235. doi: 10.1002/2015GL064995.

Zhang, J. and Guo, L. (2007) 'Structure and geochronology of the southern Xainza-Dinggye rift and its relationship to the south Tibetan detachment system', *Journal of Asian Earth Sciences*, 29(5–6), pp. 722–736. doi: 10.1016/j.jseaes.2006.05.003.

Ziesch, J., Tanner, D. C. and Krawczyk, C. M. (2014) 'Strain associated with the fault-

parallel flow algorithm during kinematic fault displacement', *Mathematical Geosciences*, 46(1), pp. 59–73. doi: 10.1007/s11004-013-9464-3.

3.0 Erosional controls on the architecture and kinematics of the Himalaya: Insights from thermokinematic modeling

3.1 Introduction

Mountain ranges are the result of the interplay between tectonically-driven uplift, and climatically-driven erosion. Sandbox experiments and numerical modeling suggest that changes in the location and magnitude of uplift occur as direct responses to the location and magnitude of erosion within a convergent, critically-tapered system (Willett, 1999; Konstantinovskaia and Malavieille, 2005; Malavieille, 2010). Erosion reduces the taper of the system by redistributing mass at the surface, inducing further deformation and uplift in order to restore it (Willett, 1999; Konstantinovskaia and Malavieille, 2005; Whipple, 2009). However, attempts to detect this response in active mountain ranges have so far failed to reach a consensus, with some concluding that the location and magnitude of uplift and exhumation are strongly linked to changes in precipitation (Horton, 1999; Montgomery, Balco and Willett, 2001; Hodges *et al.*, 2004; Thiede *et al.*, 2004), while others contend that no such coupling exists (Burbank *et al.*, 2003; Roe and Brandon, 2011; Godard *et al.*, 2014). This debate has been particularly noteworthy in the central Himalaya, where the south Asian monsoon focuses rainfall and erosion at the high Himalayan topographic front and facilitates exhumation. The large amounts of material removed by this focused erosional exhumation is expected to induce tectonic uplift at this location in the form of duplexing (Konstantinovskaia and Malavieille, 2005), or out-of-sequence thrusting (Hodges *et al.*, 2004; Wobus *et al.*, 2005; Huntington, Blythe and Hodges, 2006). This debate, however, hinges on the supposed positive correlation between precipitation and erosion, and global studies have

thus far failed to show a clear dependance of erosion on precipitation (Harel *et al.*, 2019; Hilley *et al.*, 2019). However, recent work from the Nepal and Bhutan Himalaya showing that erosion is modulated by mean rainfall (Adams *et al.*, 2020) provides us with an opportunity to identify and highlight the relationship between monsoon-driven precipitation and tectonic uplift.

While the precise origin of the monsoon is under considerable debate, a large body of evidence suggests that its strength has not remained static through time but rather that it has undergone numerous phases of strengthening and weakening between ~13 Ma and present (Clift *et al.*, 2008; Sanyal *et al.*, 2010; Gupta *et al.*, 2015; Clift, 2017). These changes in the strength of the monsoon are inferred through proxy data collected from Himalaya-derived sedimentary rocks in the foreland basin, and the Indus and Bengal fans. In particular, the concentration of the foraminifer *G. bulloides* in the sediment of the Indus fans is commonly used as a proxy for the strength of the oceanic upwellings associated with the arrival of the monsoon (Kroon, Steens and Troelstra, 1991; Curry *et al.*, 1992; Overpeck *et al.*, 1996; Gupta, Anderson and Overpeck, 2003). Measurements made of the concentration of these foraminifera have been used to infer a series of pulses in the strength of these upwellings, starting between ~13 – 10 Ma, followed by a stronger pulse between 7 – 4 Ma, and a final strengthening starting at ~3 Ma that continues till the present (Figure 3.1A). A shift towards positive $\boldsymbol{\delta}^{13}$C measurements in carbonates in the Siwalik Group and the Bengal fan indicates a significant drying of the climate at ~7 Ma, and thought to either be due to the establishment of a seasonal monsoon (Quade, Cerling and Bowman, 1989; France-Lanord, Derry and Michard, 1993; Quade *et al.*, 1995; Freeman and Colarusso, 2001), or as a result of global cooling during the Northern Hemisphere Glaciation (NHG) (Clift, 2017; Roy, Ghosh and Sanyal, 2020) (Figure 3.1B) .

Potential responses to the increased erosion and exhumation driven by the monsoon include reset mineral cooling ages, high cosmogenic nuclide-derived erosion rates, and higher measured sedimentation rates in the foreland basin and the Bengal and Indus fans. On regional scales, mineral cooling ages are the result of erosional exhumation, with the ages interpreted as reflecting times of focused exhumation (e.g., Willett and Brandon, 2002; Reiners and Brandon, 2006). Therefore, the focused exhumation brought by the monsoon should increase the probability of finding reset cooling ages that are similar to the estimated ages for increased monsoon strength in the Himalayas. Clift et al. (2008) interpreted reset Muscovite $^{40}Ar/^{39}Ar$ ages ranging between ~10 – 14 Ma (mean age ≅ 12 Ma) from Bhutan to NW India to suggest a possible correlation between high exhumation and a strong monsoon over that window of time, along with the prevalence of young (< 3.5 Ma) Apatite Fission Track (AFT) ages to reflect accelerated monsoon-driven erosion since the late Pliocene (Thiede *et al.*, 2004; Huntington, Blythe and Hodges, 2006; Clift *et al.*, 2008). A more localized dataset of MAr, monazite and AFT ages collected from the high peaks of central Nepal (Catlos *et al.*, 2001; Kohn *et al.*, 2001; Huntington, Blythe and Hodges, 2006; Blythe *et al.*, 2007) help highlight potential periods of pronounced cooling, with the MAr ages concentrated between 5 – 4 Ma (Figure 3.1D). The monazite ages (a higher temperature thermochronometer) suggest a period of intense exhumation occurring around 7 Ma, coinciding with the mid-Miocene strengthening of the monsoon. Measured AFT ages from central Nepal are overwhelmingly younger than 3 Ma, similar to the dataset compiled by Clift et al. (2008), where they were interpreted as signifying young, monsoon-driven exhumation since the late Pliocene (Figure 3.1D). These correlations between the distribution of bedrock cooling ages, and periods of high monsoon activity suggest the possibility of a genetic relationship. This relationship also implies that during periods of high monsoon activity, the increased precipitation that drives heavy

erosion and exhumation at the mountain front significantly increases the amount of sediment deposited in the foreland basin and abyssal fans. Detrital AFT ages collected from the Indus fan suggest an acceleration of exhumation rates after ~7 Ma (Zhou, Carter and Clift, 2019). In contrast, detrital AFT ages from the central Nepal Siwalik Group do not record a similar increase in exhumation rates, suggesting instead that exhumation rates have remained unchanged over the last ~7 Ma (van der Beek *et al.*, 2006), with measurements from the Bengal fan extending this to over the last 13 Ma (Huyghe *et al.*, 2020). Similarly, reconstructed erosion rates calculated from ^{10}Be measurements made in the Bengal fan have remained constant over the last 6 Ma (Lenard *et al.*, 2020), while sedimentation rates calculated in the Indus fan steadily decline from 13 Ma to ~2.5 Ma, followed by a sharp increase to reach modern rates (Clift *et al.*, 2008) (Figure 1C). More localized models in the Marsyangdi valley have also been unable to agree on the drivers of exhumation, with one study suggesting a climate-driven increase in exhumation rates at ~2.5 Ma (Huntington, Blythe and Hodges, 2006), while others have found no decrease in exhumation rates corresponding to an approximately fourfold decrease in modern rainfall (Burbank *et al.*, 2003; Blythe *et al.*, 2007).

In compressional systems like the Himalayas, exhumation occurs by uplift over ramps, and out-of-sequence thrusts (Wobus, Hodges and Whipple, 2003; Hodges *et al.*, 2004; Wobus *et al.*, 2005; Huntington, Blythe and Hodges, 2006; Whipp *et al.*, 2007; Lock and Willett, 2008; Herman *et al.*, 2010; Robert *et al.*, 2011; Adlakha *et al.*, 2013; McQuarrie and Ehlers, 2015; McQuarrie *et al.*, 2019; Ghoshal *et al.*, 2020). As these compressional systems evolve, both the location and size of the ramps are expected to change with time. We simulate this development of structures over time in the Marsyangdi valley, using a detailed kinematic model based on a balanced cross-section. Unlike past modeling efforts for this region, this systematic development of structures and ramps

with time allows us to distinguish between changes in exhumation rates caused by structural changes, height of ramps, duplexing, out-of-sequence thrusting, or changes in the rates of thrusting. Combining this kinematic model with a thermal model (e.g., PECUBE) allows us to recreate detailed exhumation and cooling histories for the rocks at the surface. We can tightly constrain these cooling histories and eliminate invalid models by comparing the modeled cooling ages with a large dataset of multi-system cooling ages compiled from the Marsyangdi valley. If the Himalayas are responding to an increase in erosional exhumation due to the strengthening of the south Asian monsoon, we hypothesize that there will be a concurrent change in the behavior of faulting, such as: (1) an increase in the rates of shortening, accelerating uplift and exhumation over active ramps, and/or (2) out-of-sequence faulting in the hinterland. We quantify how the location and magnitude of exhumation in the Himalaya have changed in response to different structural drivers of uplift (e.g., mid-crustal ramps, duplexing, and out-of-sequence thrusts), and evaluate whether changes in shortening rates over time are required to reproduce the distribution of cooling ages at the surface. Finally, if marked changes in location, geometry or rates of shortening are required, are these changes (i.e., rates of thrusting and/or out-of-sequence thrusting) coeval with significant shifts in the strength of the monsoon?

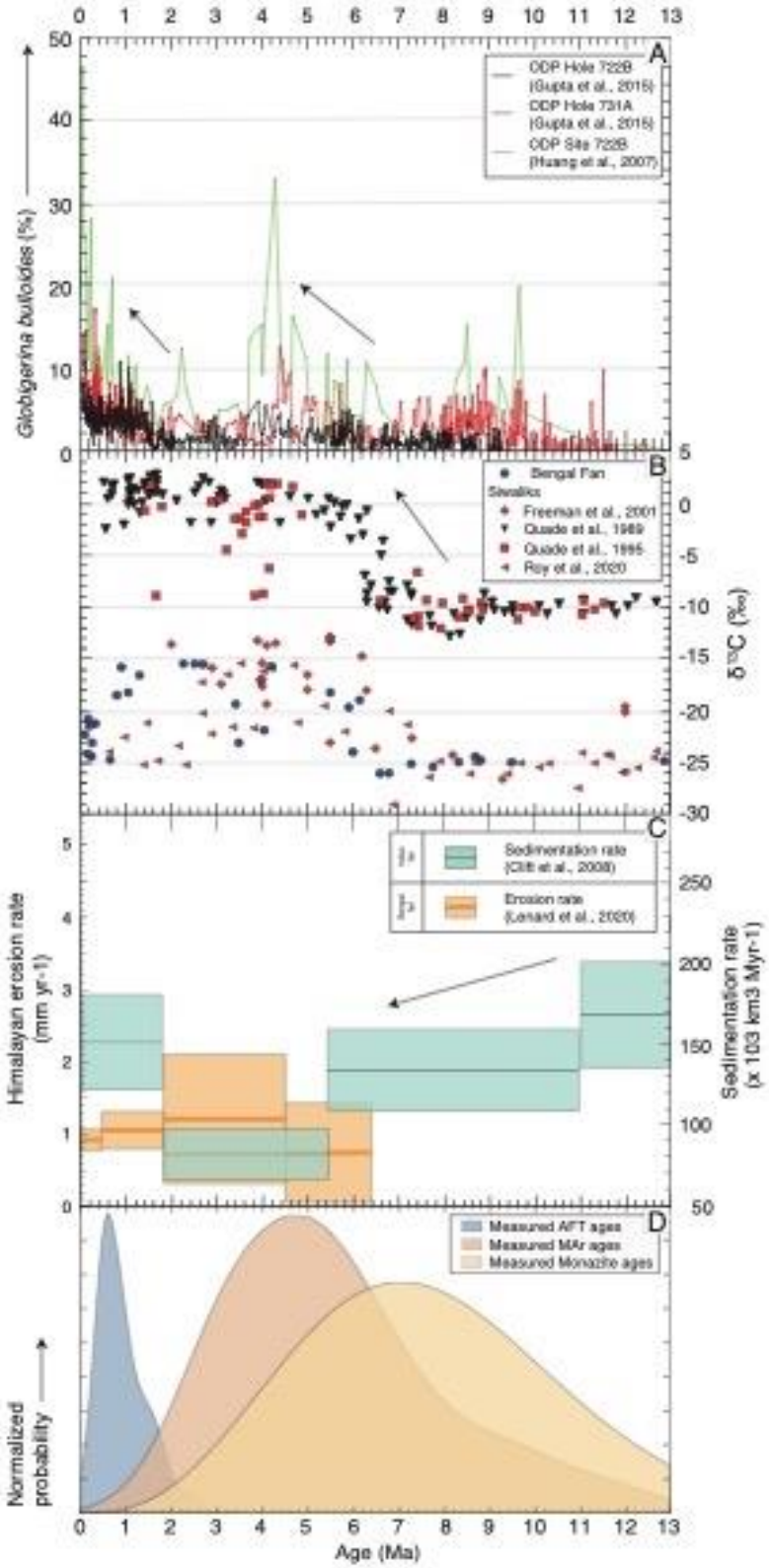

Figure 3.1: Plots of monsoon proxies through time.

(A) Concentration of G. bulloides in Indus fan sediments (modified from Gupta et al., 2015); (B) δ13C measurements from Bengal fan and foreland basin sediments (Quade, Cerling and Bowman, 1989; France-Lanord, Derry and Michard, 1993; Quade et al., 1995; Freeman and Colarusso, 2001; Roy, Ghosh and Sanyal, 2020); (C) Measured sedimentation rates from the Indus fan (Clift et al., 2008), and reconstructed 10Be erosion rates from the Bengal fan (Lenard et al., 2020) for the last 13 Ma; (D) Normalized probability distributions of measured AFT, MAr, and Monazite ages from central Nepal (Catlos et al., 2001; Kohn et al., 2001; Burbank et al., 2003; Huntington, Blythe and Hodges, 2006; Blythe et al., 2007).

3.2 Geologic background

The Himalaya were formed when the Indian and Eurasian plates collided at around ~58 Ma (Garzanti, Baud and Mascle, 1987; DeCelles *et al.*, 2014; Orme, Carrapa and Kapp, 2015; Hu *et al.*, 2016). India is moving towards the Tibetan Plateau at around ~20 mm/yr, with most motion being accommodated on the Main Himalayan thrust (MHT), the primary décollement of the Himalayas (Bilham *et al.*, 1997; Lavé and Avouac, 2000; Jouanne *et al.*, 2004; Bettinelli *et al.*, 2006; Ader *et al.*, 2012). Motion due to the collision translates Greater India-derived sedimentary and metasedimentary rocks southwards along major thrust faults and shear zones. These faults and shear zones divide the Himalayas into four major tectonostratigraphic zones: the Subhimalaya, Lesser Himalaya, Greater Himalaya, and the Tethyan Himalaya.

3.2.1 Tectonostratigraphy

3.2.1.1 Subhimalayas

The Siwalik Group is made up of foreland basin sedimentary rock that was eroded from the rising Himalayas in the north (Gansser, 1964; Tokuoka *et al.*, 1986; Harrison *et al.*, 1993; Quade *et al.*, 1995; Burbank, Beck and Mulder, 1996; DeCelles *et al.*, 1998; Gautam and Rösler, 1999; Ojha *et al.*, 2000, 2009). The rocks that make up the Siwalik Group coarsen upwards from siltstones and mudstones at the bottom, to sandstones and conglomerates at the top, and are divided into informal lower, middle and upper members (Tokuoka *et al.*, 1986; Harrison *et al.*, 1993; Quade *et al.*, 1995; Ojha *et al.*, 2009). In central Nepal, all three members are exposed, and have a total measured thickness of ~5 km (Tokuoka *et al.*, 1986; Harrison *et al.*, 1993) (Figure 3.2). The Siwalik Group is bounded in the south by the Main Frontal thrust (MFT), which is the present surface expression of the Himalayan décollement, the MHT, and in the north by the Main Boundary thrust (MBT).

3.2.1.2 Lesser Himalayas

The Lesser Himalaya (LH) is made up of eight mappable formations in central Nepal, which can be grouped into Paleoproterozoic lower and Mesoproterozoic upper units, with a total thickness of ~8 – 13 km (Sakai, 1983; Harutaka Sakai, 1985; Upreti, 1996; Khanal and Robinson, 2013; Robinson *et al.*, 2021). The lower LH is made up of two distinct units, the Kuncha and Robang formations, both of which have been metamorphosed to greenschist (south) and amphibolite (north) facies (Stöcklin, 1980; Martin *et al.*, 2011; Robinson and Martin, 2014). The basal Kuncha formation is made up of grey-green quartz- and chlorite-rich phyllite, green quarzitic schists, and micaceous quartzite, forming a layer ~3 – 3.6 km thick. Detrital zircons place the

maximum depositional age of the Kuncha Formation at ~1900 Ma (Martin *et al.*, 2011). The Robang formation was deposited at some point prior to 1850 Ma and is interpreted as an older and more distal facies of the Kuncha (Martin *et al.*, 2011). It is made up of chloritic schists, often interbedded with a distinctive, white-light green quartzite known as the Dunga quartzite. In the Marsyangdi valley, the Robang has been mapped structurally above the rocks of the upper LH, with its base interpreted as the Ramgarh-Munsiari thrust (RMT) (Pearson and DeCelles, 2005; Robinson and Pearson, 2013) (Figure 3.2).

In central Nepal, the upper LH stratigraphy overlies the Kuncha Formation, and is made up of six Paleoproterozoic – Mesoproterozoic units: the Fagfog, Dandagaon, Nourpul, Dhading, Benighat, and Malekhu formations (Upreti, 1996; Martin *et al.*, 2011) (Figure 3.2). The degree of metamorphism of the units increases from the lower greenschist facies in the south to upper greenschist – amphibolite in the footwall of the Main Central thrust (MCT) in the north (e.g., Martin et al., 2011). Overlying the Kuncha, the Fagfog formation is a thin (~300 m) unit made up of a tan/white, coarse- to fine-grained quartzite, with individual beds often separated by green, chloritic phyllite. The maximum depositional age for the Fagfog is ~1770 Ma (Martin *et al.*, 2011). Sitting conformably on top of the Fagfog, the ~650 m thick Dandagaon formation is primarily made up of dark brown to grey-green phyllite interbedded with thin beds of slate and dolomite in the southern Marsyangdi transect (Olree, 2018). With the higher degrees of metamorphism in the north, the formation is dominantly made up of grey-green garnetiferous schist. The ~450 m thick Nourpul formation is primarily made up of thinly bedded variegated quartzite (pink, purple, green and white) interbedded with blue-grey dolomite, and dark purple and green phyllite, with a silicic dolostone dominating the upper portion of the unit (Pearson, 2002; Olree, 2018). In the north, the Nourpul is metamorphosed into dark green garnetiferous schist. Detrital zircon measurements

suggest a maximum depositional age for the Nourpul at ~1750 Ma (Cross III, 2014). The Dhading formation is made up of massive blue-grey dolomite, with a distinctive 'butcher-block' weathering pattern. Exposures in the Marsyangdi transect suggest that it is ~150 m thick, with an abrupt contact with the overlying Benighat formation. The Benighat formation is primarily made up of dull, dark grey-black slate and thin limestone beds, with a measured thickness of ~950 m in the Marsyangdi transect. In the north, the Benighat slate becomes increasingly phyllitic, but retain their dark, dull color, distinguishing them from the Dandagaon. The ~500 m thick Malekhu formation lies conformably on top of the Benighat, and consists of blue-grey limestone and dolostone, interbedded with grey-black and brown phyllite, and is proposed to have been deposited prior to ~1300 Ma (Martin *et al.*, 2011). In the north of the transect, the high temperatures in the footwall of the RMT have metamorphosed the limestone and dolostone into white dolomitic marble. The uppermost unit of the LH in the Marsyangdi transect is a ~1.6 km thick sequence from the late Paleozoic – Mesozoic Gondwana Tansen group (Sakai, 1983; Harutaka Sakai, 1985), commonly referred to as the Gondwana Sequence. The sequence sits disconformably on top of the upper LH (Sakai, 1983; Robinson and Martin, 2014; DeCelles *et al.*, 2020), and is made up of interbedded mudstone, shale, limestone, and diamictite.

3.2.1.3 Greater Himalaya

In the Marsyangdi valley, the Greater Himalayan (GH) sequence is mapped as a 23 km thick unit of metasedimentary rocks dated to between 1000 – 600 Ma, intruded by early Paleozoic granites, both of which have been metamorphosed to amphibolite – granulite grade (Martin *et al.*, 2005; Gehrels *et al.*, 2011) (Figure 3.2). Near the MCT, GH rock is predominantly made up of kyanite- and garnet-bearing pelitic schist and paragneiss, along with lenses of orthogneiss (Coleman, 1996; Walters and Kohn, 2017). The rocks in the immediate hanging wall of the MCT

are characterized by abundant deformed polymineralic leucosomes, suggesting widespread partial melting and migmatization. Farther north, the degree of metamorphism is sillimanite-grade, with layered calc-silicate and marble, and minor schist and paragneiss, crosscut by abundant leucogranite intrusions (Coleman, 1996; Kohn, 2008; Walters and Kohn, 2017). Above these units is a distinctive coarse-grained augen gneiss that can be up to 1 km thick in the Marsyangdi valley. The top of the GH is marked by a sequence of high-grade interbedded calc-silicate and paragneiss (Coleman, 1996).

3.2.1.4 Tethyan Himalaya

Exposed Tethyan rocks in the Marsyangdi transect show a complete sequence from the Cambrian to Jurassic (Fuchs, Widder and Tuladhar, 1988), of metamorphosed limestone, sandstone and shale. The basal unit, known as the Annapurna Yellow Formation, is a highly deformed, greenschist-amphibolite grade marble, with phlogopite-rich foliations (Coleman, 1996). A top-to-the-north shear zone known as the South Tibetan Detachment (STD) separates the Greater Himalayan sequence from the Tethyan sequence above (Burg *et al.*, 1984; Burchfiel *et al.*, 1992). Motion on the detachment in the Marsyangdi Valley is proposed to have ended between 18 – 24 Ma (Guillot *et al.*, 1993; Harrison, McKeegan and LeFort, 1995; Harrison *et al.*, 1999).

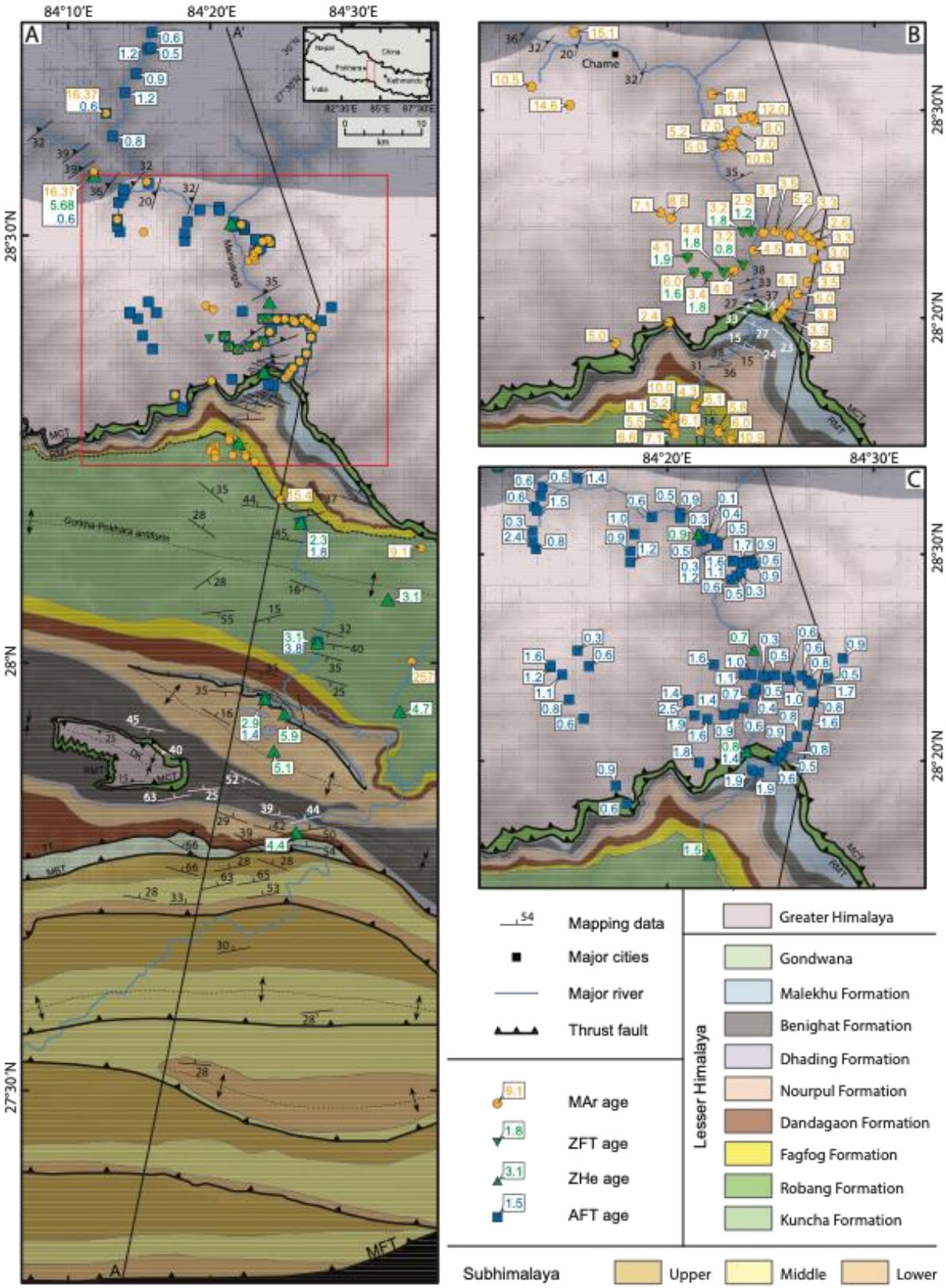

Figure 3.2: Geological map along the Marsyangdi transect of central Nepal.

(A) Detailed geologic map of the Marsyangdi transect in central Nepal, showing the distribution of measured MAr, ZHe, ZFT and AFT thermochronological ages. Geology shown is based on new mapping in the region, combined with past mapping from Kimura (1999), Cross III (2014), Khanal (2014), and Dhital (2015). Red outline highlights area shown in B and C. (B) Measured MAr (yellow text), and ZFT (green text) ages, and mapping in the northern Marsyangdi. (C) Measured ZHe (green text) and AFT (blue text) ages in the northern Marsyangdi.

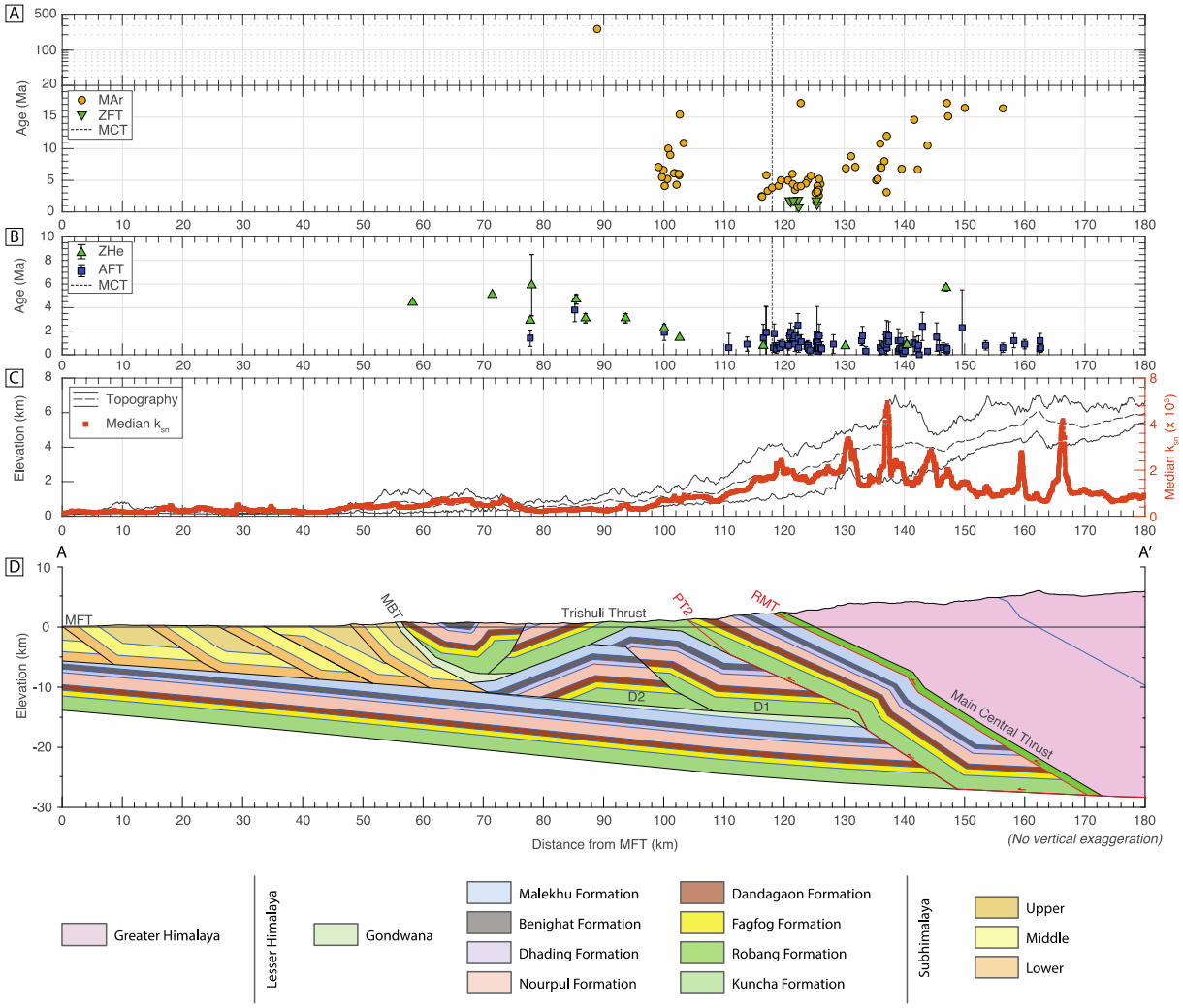

Figure 3.3: Plots of projected data along the Marsyangdi transect.

(A) Combined measured MAr (yellow) and ZFT (green, downward-pointing triangles) thermochronometer data plotted along the Marsyangdi section line; (B) Combined measured ZHe (green, upward-pointing triangles) and AFT (blue). The location of the MCT is marked by a black, dashed line, while the origin is the

location of the MFT. (C) Max, min, and median swath topography along the Marsyangdi cross-section line. The mean topography is shown as a solid, black line. Median k_{sn} values calculated along the swath are shown in orange. (D) Balanced cross-section along the Marsyangdi transect. Locations of major OOS thrusts are marked in red. There is no vertical exaggeration on the figure, and the topography shown is the mean topographic profile for the transect.

3.3 Thermochronology

We constrain our thermokinematic model using a set of published thermochronometer cooling ages from central Nepal (Figure 3.2), made up of 60 muscovite $^{40}Ar/^{39}Ar$ (MAr) (Copeland et al., 1991; Arita et al., 1997; Catlos et al., 2001; Burbank et al., 2003; Bollinger et al., 2004; Huntington et al., 2006; Huntington et al, 2021), 7 zircon fission track (ZFT) (Blythe *et al.*, 2007), 13 zircon (U-Th)/He (ZHe) (Cross III, 2014; Robinson *et al.*, 2021), and 84 apatite fission track (AFT) (Burbank *et al.*, 2003; Huntington, Blythe and Hodges, 2006; Blythe *et al.*, 2007; Robinson *et al.*, 2021) ages (see Appendices B, C, D and E for complete list). The uncertainties in the MAr and ZFT ages are represented by 2σ analytical errors. We present the ZHe ages as a mean, calculated from the spread of individual grain ages (typically three) with an error that encompasses both the spread in ages from individual grains, and their 2σ analytical errors. The AFT data used here are all reported with 2σ errors to maintain consistency. We project these cooling ages onto the cross-section line along-strike, maintaining their relative structural positions (Figure 3.3). This projection is limited to ~20 km from the cross-section to avoid the effect of any lateral variations in structure on the cooling ages. These projected ages are shown in the age-distance plots with respect to their distance from the surface trace of the MFT.

The MAr ages range from very young (2.4 Ma) to unreset (247 Ma), with the majority of samples located north of 118 km from the MFT. The youngest ages (between 2.4 – 6 Ma) are predominantly concentrated between 118 – 126 km. The ages are older towards the north, reaching the regional maximum for reset MAr ages (~17.2 Ma) between 148 – 157 km from the MFT. Another cluster of reset MAr ages is located within LH rocks, immediately south of the MCT (between 98 – 105 km from the MFT), displaying a broad range in ages (between ~4 – 16 Ma). The single unreset MAr age (247 Ma) in the Marsyangdi region is located ~89 km from the MFT. The seven ZFT ages measured in the region were all sampled immediately to the north of the MCT (121 – 125 km from the MFT) and display a very narrow range in ages (between 0.8 – 1.9 Ma). Measured ZHe ages range between 0.74 – 5.9 Ma and extend from 58 – 148 km from the MFT. The youngest ZHe ages (0.74 – 0.85 Ma) are located north of the RMT (i.e., between 118 – 140 km from the MFT). The northernmost sample, located 148 km from the MFT, shows a notably older age of 5.5 Ma. While the AFT ages are the most numerous of the thermochronometers measured in the Marsyangdi transect, they are focused in both their spatial extent and age range. Most of the AFT ages are located between 111 – 163 km from the MFT and range in age between 0.1 – 2.5 Ma. Three additional samples are located between 76 – 100 km, collected from the Nourpul and Kuncha formations, and range in age between 1.4 – 3.8 Ma.

3.4 Methods

3.4.1 Balanced cross-section

We present a new balanced cross-section along the Marsyangdi valley, using both newly acquired, and existing map data as surface constraints. We concentrated our new mapping along the Marsyangdi trunk channel, and along a number of tributary valleys; integrating it with published maps from the region (Kimura, 1999; Cross III, 2014; Khanal, 2014; Dhital, 2015) (Figure 3.2). The southern portion of the section line is oriented ~10° from N, perpendicular to the front of the Himalayan arc as defined by mapping, and parallel to measured lineation orientations. At 128 km from the MFT, the cross-section line is oriented 18°NW to keep the cross-section perpendicular to the broad orientation of the mapped structures. Map orientations were projected onto the line of section, maintaining their structural position, and used to limit permissible geometries. The line lengths of each of the units in the deformed section were measured and balanced in the restored section (Figure 3.11). Small-scale internal deformation (brittle or ductile) within the units is not accounted for in our modeling.

The base of the cross-section is defined by the MHT, which can be divided into three main parts: the ramp of the MFT, a mid-crustal ramp, and a broad flat in between (Pandey *et al.*, 1995; Lavé and Avouac, 2001). The height of the MFT ramp is primarily defined by the required thickness and orientation of the Siwalik sedimentary rocks exposed at the surface. A further constraint is provided by extrapolating the depth of the Siwalik Group and the dip of its base (4.5°N) measured from the Raxaul drill hole to the southeast (Sastri *et al.*, 1971; Lavé and Avouac, 2000). Inversion of seismic data from the Gorkha earthquake suggests a narrow range in the permissible angles (4° – 8°) for the flat of the MHT (Whipple *et al.*, 2016). To construct our cross-

section, we explored décollement angles within this range to find the one that fits the geophysical constraints, the required thickness of LH units mapped at the surface and viable repetition of units between the surface geology and décollement. Finally, thermokinematic modeling (Lock and Willett, 2008; McQuarrie and Ehlers, 2015; Ghoshal *et al.*, 2020) shows predictive relationships between the location of ramps and the resulting pattern of predicted cooling ages. Resetting higher temperature thermochronometers like MAr and ZFT require almost a complete translation over a mid-crustal ramp, with the top of the ramp located at or north of the youngest reset ages (Ghoshal *et al.*, 2020). The base of the ramp is indicated by the transition from younger reset MAr and ZHe ages to older, background ages. We used the distribution of cooling ages to estimate the location of the mid-crustal ramp and tested the sensitivity of predicted cooling ages to variations in ramp location and identified a solution that best matches the distribution of all the available cooling ages.

3.4.2 Kinematic and Flexural modeling

Our restored cross-section was kinematically and flexurally forward modeled using the structural modeling software Move 2019.1 (Midland Valley/Petex) to recreate the final deformed cross-sectional geometry. The kinematic model is divided into displacement increments of ~10 km and modeled using the fault-parallel flow algorithm. This algorithm best replicates displacement along discrete compressional structures, where the fault bends do not exceed 45° (Ziesch, Tanner and Krawczyk, 2014). Each of these kinematic increments were followed by flexural loading and erosional unloading. The magnitude of flexural loading for each step is calculated using the difference between the deformed topography resulting from each ~10 km increment of displacement, and the estimated topography from the previous step. We use a ‘responsive

topography' method to calculate the amount of erosion at each step, where the new eroded topography is defined by a taper angle (2°) that increases in elevation towards the north (McQuarrie and Ehlers, 2015; Gilmore *et al.*, 2018). This angle is based on the taper angle of modern topography in central Nepal and accommodates erosion where active uplift has exceeded the 2° slope. In locations where no uplift has occurred, the new topography follows the existing, isostatically-loaded topography. The initial topography for the model is represented by a steady increase (2°) in elevation towards the north, reaching a maximum elevation of 5 km above the southern limit of the GH. This simplified topography reproduces the elevation of the Tibetan Plateau, which is thought to have reached its modern elevation by the late Oligocene (DeCelles *et al.*, 2007). Prior to any deformation in our models, we use our best-fit estimate for the initial geometry of the Indian margin to define the taper of the décollement. We use an angle of 1.5° as this starting taper, applied from the foreland to the northern extent of the model. This angle allows us to reproduce the ~15 km section of Tethyan rocks exposed in southern Tibet (Brookfield, 1993; Ratschbacher *et al.*, 1994; Zhang and Guo, 2007), and facilitates the burial of the initial base of the GH section to ~45 km in order to match measured values of peak pressure and temperature (Catlos *et al.*, 2001, 2018; Kohn *et al.*, 2001, 2004; Kohn, 2008). The building of topography and subsequent erosion occurring at each increment in the models flexurally steepens the décollement and increases the depth of the foreland basin. The final dip and depth of the décollement is dependent upon three parameters (effective elastic thickness, crustal density, and the initial dip of the decollement) that are systematically varied until the surface geology and expected foreland basin depth is replicated. The best-fit values for these parameters are listed in Table 3.1.

The kinematic and flexural forward model is tracked using a 2D grid of points with a resolution of 0.5 km that is deformed sequentially at each increment. Assigning an age to each step

of the model converts the displacement field into a velocity field, which is then input into a modified version of PECUBE. In addition to testing a constant rate of shortening, varying the ages at which faults are initiated allows us to assign variable rates of thrusting, and quantify their effects on the predicted cooling ages. Finally, comparing the magnitude of erosion that occurs over each timestep in the model allows us to quantify changes in erosion/exhumation rates through time.

3.4.3 Thermokinematic modeling

PECUBE solves the three-dimensional heat transport equation to simulate the evolution of a transient thermal field (defined by input thermal parameters for the crust) as it is affected by the imported velocity grids and erosion at the topographic surface, calculating time-temperature (t-T) paths for the rocks at the surface. Finally, age-prediction algorithms use these t-T paths to predict the surface cooling ages for each of the tracked points when they are brought to the surface (Braun, 2003; Ehlers *et al.*, 2005). These algorithms calculate the respective closure temperatures for each of the thermochronometer systems based on the rate of cooling and published models for mineral kinetics. The MAr kinetics are based on the thermally-activated diffusion model as set out in Dodson (1973), using the parameters defined in Hames and Bowring (1994) for cylindrical geometries (Hodges, 2014). The ZFT ages are calculated based on the parameters outlined in Brandon et al. (1998), while the ZHe kinetic model is defined in Reiners et al. (2004). Finally, AFT ages are calculated using the Durango apatite parameters given in Crowley et al. (1991).

Prior to the accommodation of any motion, PECUBE simulates the thermal state of the crust using the input values of heat flow from the mantle, and the material properties of the crust (thermal conductivity, density, heat capacity, and radiogenic heat production). The amount of heat generated in the crust is determined by a surface heat production value (A_0), which is applied over

a distance known as the 'e-folding depth', over which the heat production decays exponentially to 1/e of the assigned surface value (McQuarrie and Ehlers, 2017). Using an e-folding depth allows us to match both the non-linear decline of heat production in the crust with depth (Ketcham, 1996; Menon *et al.*, 2003; Brady *et al.*, 2006) and measured heat production values for the Himalayas (England *et al.*, 1992; Whipp *et al.*, 2007), while also avoiding the formation of partial melt in the middle and lower crust. We vary A_0 between 1.8 – 2.5 μWm^{-3} to identify the best-fit value, using an e-folding depth of 20 km (see Section 2.8.3.2 for a further treatment of heat production). The values of thermal conductivity and heat capacity used in our models are based on measured values from the Himalayas (Ehlers, 2005; Ray, Bhattacharya and Roy, 2007; Whipp *et al.*, 2007). These crustal properties (e.g., heat production, thermal conductivity, and thermal capacity) are not advected by the imposed displacement fields, remaining static throughout the simulations. The best-fit parameters used to set up the thermal model in PECUBE are listed in Table 3.1.

Parameter	**Input/Best-fit value**
Initial dip of décollement	1.5°
Material properties	
Effective elastic thickness	50 km
Crustal density	2850 kg m-3
Mantle density	3300 kg m-3
Specific heat capacity	800 J kg-1 K
Crustal volumetric heat production	2.0 μW m-3
e-folding depth	20 km
Thermal conductivity	2.5 W m-1 K
Numerical properties	
Temperature at base of model	1300°C
Model thickness	110 km
Surface temperature	20°C
Atmospheric lapse rate	7°C km^{-1}
Kinematic grid spacing	0.5 km
Horizontal node spacing	0.5 km

Vertical node spacing	1 km
Model domain	1000 km x 110 km x 5 km
Model start time	500 Ma

Table 3.1: Mechanical and thermal properties for PECUBE

3.5 Results

3.5.1 Balanced cross-section

3.5.1.1 Structural zones

Subhimalayan faults

The MFT ramp dips at an angle of ~30°N, with an approximate depth of 5 km. This dip is consistent with mapped upper through lower Siwalik Group thicknesses at the MFT, and the depth of the Siwalik basement, as defined by the Raxaul drill hole (Sastri *et al.*, 1971).

Along the Marsyangdi transect, Siwalik Group units have been mapped from the MFT in the south to ~55 km north where the MBT marks the beginning of LH rocks, dipping between 30° and 50°N. Mapping between the MFT and the MBT shows that the three-part sequence of the Siwalik Group goes through four asymmetric repetitions, which in the past have been interpreted as four distinct thrust sheets (Khanal, 2014; Olree, 2018). However, the 10 km wide exposure of the middle Siwaliks between 30 – 40 km is inconsistent with its expected 2 km thickness and measured dips of 28° and 30° in Siwalik Group units to the north and south of the middle Siwalik section respectively (Figure 3.2). To rectify this inconsistency, we divide the middle Siwalik section into two separate thrust sheets, with the structurally lower sheet carrying only the lower

and middle Siwalik members, and the upper sheet carrying all three members (Figure 3.3). The extra shortening required to accommodate motion on this new thrust sheet lends support to the location of the mid-crustal ramp, which is significantly farther north than previously interpreted (Khanal, 2014; Robinson and Martin, 2014; Olree, 2018; DeCelles *et al.*, 2020).

Main Boundary thrust

In the Marsyangdi transect, the MBT is defined as the contact between a ~1.6 km thick sequence of Paleozoic Gondwana Sequence rocks that dip steeply (50° - 65°) towards the north (Figure 3.2). We apply a minimum estimate for the displacement accommodated by the MBT, since its hanging wall cutoff has been eroded away and the total amount of shortening on the fault is unknown.

Gorkha-Pokhara antiform and Trishuli thrust

Immediately north of the MBT, the Trishuli thrust (TT) places the LH Dandagaon formation on top of Gondwana Sequence rocks with the Dandagaon and younger units dipping between 28° - 50°N (Figure 3.2). North of the fault boundary, the Trishuli thrust sheet forms a tightly folded synform with the Benighat formation at its core. The rocks of the northern limb of the synform dip southwards at angles between 15° - 50°. These south dipping upper LH rocks are repeated by a south dipping thrust fault, interpreted as a backthrust, placing the Nourpul formation on top of the significantly younger Malekhu formation.

The upper LH rocks in the northern limb of the synform are separated from the upper LH rocks exposed immediately south of the MCT by the Gorkha-Pokhara antiform, which is a major EW-trending antiformal structure that has been mapped across central Nepal (Figure 3.2). The core of the Gorkha-Pokhara antiform is made up of the lower LH Kuncha formation. While the antiform

is interpreted to be representative of a duplex at depth (Pandey *et al.*, 1995; Lavé and Avouac, 2001; Pearson, 2002; Avouac, 2003; Khanal and Robinson, 2013; Khanal, 2014; Robinson and Martin, 2014; Hubbard *et al.*, 2016; Ghoshal *et al.*, 2020), the rocks at the surface are part of the roof thrust (Trishuli thrust), obscuring the geometry of the duplex (Ghoshal *et al.*, 2020). The horses of the duplex fill the space defined by the map pattern of rocks at the surface and the décollement below. Since the youngest horse carries rocks that are derived from the active ramp, it is required to have a thickness that corresponds to the height of the modern ramp (Figure 3).

In the Marsyangdi valley, the youngest MAr ages are located at, and to the south of 128 km, while the oldest reset MAr and ZHe ages are located at ~150 km (i.e., ~22 km apart). Therefore, we predict that the modern ramp is located between 128 – 150 km from the MFT, a surface width of ~22 km (Figure 3.3). This width of the ramp, combined with reasonable angles of dip (20° - 30°) imply that the height of the proposed ramp is between 8 and 12 km, consistent with the measured thickness of the LH sequence. Using this thickness for the horses, a duplex comprised of two horses that repeat the entire LH stratigraphy (Kuncha to Malekhu) can fill the space between the mapped surface geology and the décollement.

Ramgarh-Munsiari and Main Central thrust sheets

In the Marsyangdi valley, the GH sequence dips between 20° - 39° NNE over a distance of 30 km northwards from the MCT. The Robang Formation, located structurally beneath the MCT, dips towards the north at ~34°. The GH and Robang are also exposed in the south, within the synformal Damauli klippe, with the southern limb dipping 15° - 20°N and the northern limb dipping between 25° - 40°S (Figure 3.2). The consistency in the measured dips in the klippe, and across the northern traces of the TT, RMT and MCT suggest that the RMT carries the entire section of the Robang and GH sequences and emplaces them on top of LH rocks carried by the Trishuli

thrust sheet (Figure 3.3). In addition, the presence of the Robang and GH within the klippe implies that both the RMT and MCT buried the entire length of the Trishuli thrust sheet.

Finally, moderate ~30° dips over a ~50 km distance north of the MCT, through the upper Marsyangdi valley implies that GH rocks in the subsurface must extend down to and maintain a 30° dip to a minimum depth of ~20 km. This requires that the upper ramp edge of the footwall cutoffs of the Trishuli thrust sheet be located at a minimum of ~152 km from the MFT to promote the ~30 ° measured dips (Figure 3.3).

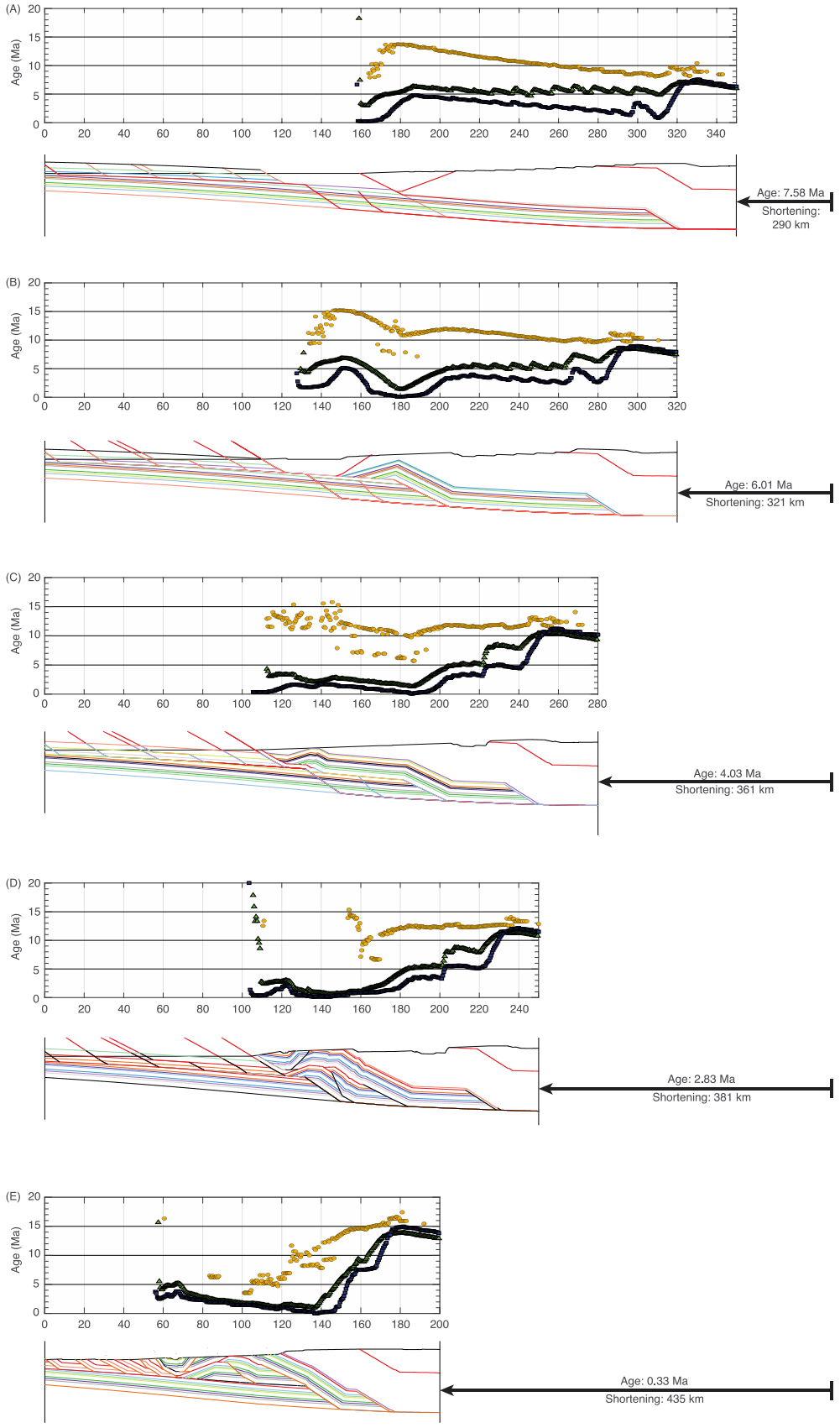
(A)
Age (Ma)
Age: 7.58 Ma
Shortening:
290 km
(B)
Age (Ma)
Age: 6.01 Ma
Shortening: 321 km
(C)
Age (Ma)
Age: 4.03 Ma
Shortening: 361 km
(D)
Age (Ma)
Age: 2.83 Ma
Shortening: 381 km
(E)
Age (Ma)
Age: 0.33 Ma
Shortening: 435 km

Figure 3.4: Structural and thermochronologic evolution of the Marsyangdi cross-section. (A - E) Sequential cross-section reconstructions and associated predicted cooling ages for select model timesteps. The sequence assumes a constant rate of shortening starting at 23 Ma (21 mm/yr.) and an A_0 value of 2.00 μW m^{-3}.

3.5.2 Predicted cooling ages

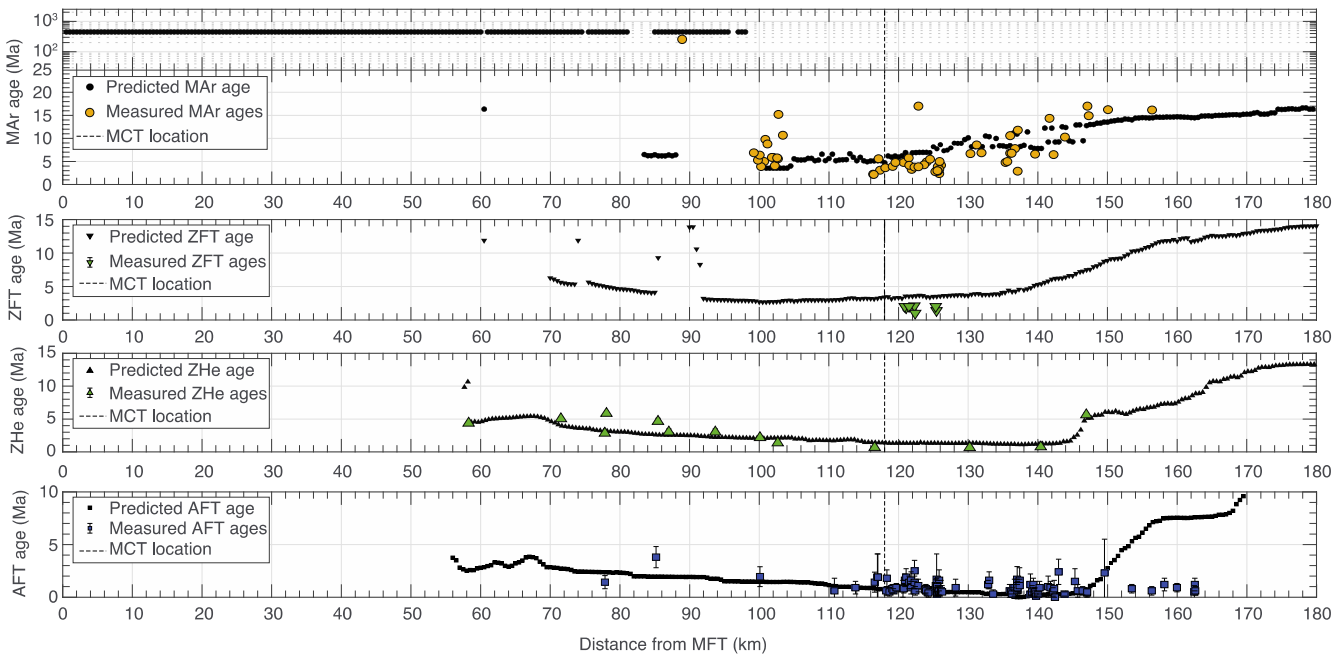

Figure 3.5: Predicted cooling ages using a constant velocity of 21 mm/yr. and an A_0 value of 2.00 μW m^{-3}.

3.5.2.1 Effect of constant shortening rates

In this section, we evaluate the effect of the subsurface geometry on the predicted cooling ages using a constant rate (~21 mm/yr.) of displacement on faults, and a surface heat production (A_0) value of 2.00 μW m^{-3}. This shortening rate is comparable to measured long-term shortening rates in the central Nepal Himalaya (Bilham *et al.*, 1997; Ader *et al.*, 2012).

At the beginning of our sequential model, the MCT is emplaced over the Robang formation by motion over a ~25 km high ramp (**Error! Reference source not found.**: Steps 1 – 16). A

ssociated erosional exhumation produces reset AFT, ZHe and MAr cooling ages, with the youngest ages located at the top of the ramp (~460 km from the MFT) and becoming steadily older towards the south. Emplacement of the RMT over upper LH rocks occurs via a ~10 km high ramp (currently located at ~300 km) defined by the footwall cutoff of what will become the Trishuli thrust sheet. Uplift and exhumation resulting from motion of rocks over this ramp resets AFT ages, with the youngest ages predicted over the ramp, becoming progressively older towards the south (Figure 3.4A, **Error! Reference source not found.**: Steps 17 - 30). While the predicted AFT ages in these time steps record the emplacement of the RMT, the predicted MAr ages still only record the emplacement of the MCT. The predicted ZHe ages partially record both periods of cooling and become ~2 Ma younger due to motion over the ramp (**Error! Reference source not found.**: Steps 1 7 - 30). The Trishuli thrust is then emplaced on top of the Gondwana sequence, moving over a ~12 km high footwall ramp located at 180 km, which cuts across the entire LH and Gondwana sequence. This period of exhumation predicts reset ZHe and AFT ages above the ramp (Figure 3.4B, **Error! Reference source not found.**: Steps 31 – 33). Emplacement of the MBT (Figure 3.4C, Video 3.1: Steps 34 – 37), places the Gondwana sequence over the Siwalik Group, and continues to bring the distal part of the Trishuli thrust sheet over the ramp. This continued exhumation over the ramp starts to partially reset the MAr ages. Development of the duplex promotes exhumation above it, as the overlying GH is removed, and a zone of unreset MAr ages is created (Figure 3.4D, Video 3.1: Steps 38-40). Part of the shortening responsible for the development of the duplex is accommodated by motion on the south-dipping backthrust (Figures 3.2, 3.3, and 3.4D). Finally, deformation steps southwards into the Siwalik Group, translating the duplex over the final active ramp, predicting ZHe and AFT ages that steadily increase in age

towards the south, with the youngest ages located above the ramp (Figure 3.4E, Video 3.1: Steps 41-48).

At the end of the sequential model, the youngest MAr ages (~2 – 3 Ma) are predicted at 100 – 104 km from the MFT. A swath of reset (~5 – 6 Ma) MAr ages are located between 104 – 120 km. Northwards from 120 km, the predicted MAr ages become steadily older, reaching a maximum age of ~15 Ma north of 160 km (Figure 3.5). The model can correctly to reproduce the trend of increasing MAr ages north of the MCT, and the zone of young reset ages between 100 – 125 km from the MFT. It also predicts unreset ages ~99 km from the MFT, at the same location as the oldest measured MAr age (247 Ma) in the region (Figure 3.5). The youngest ZFT ages (~3 Ma) are predicted ~102 km from the MFT, becoming steadily older towards the north. The youngest ZHe ages (~1 Ma) are predicted ~140 km from the MFT, increasing steadily towards the south and successfully matching the overall trend of the measured ages (Figure 3.5). ZHe ages predicted to the north of 145 km increase sharply from 1 Ma to 5 Ma, successfully matching the location of the expected inflection point in the ZHe ages (i.e., from younger to older ages) at ~145 km. The predicted AFT ages follow a similar trend to that of the ZHe ages, with the youngest ages predicted at ~145 km from the MFT and increasing steadily towards the south. North of 148 km, the predicted AFT ages increase sharply from < 1 Ma to ~7 Ma.

While this model can reproduce broad age and location trends in the measured cooling ages, there are some notable misfits. The model currently predicts MAr ages that are ~3 – 5 Ma older than the youngest measured ages around the MCT (between 118 – 126 km; Figure 3.5). In addition, it predicts MAr ages that are 2 – 3 Ma younger than the measured ages located north of 148 km. The predicted ZFT ages between 118 – 126 km are 3 Ma older than the measured ages. While the overall distribution of the measured AFT ages is reproduced well, the cluster of young,

reset ages between 152 – 164 km are completely missed, with the model currently predicting ages of ~7 – 8 Ma, compared to the ~1 Ma measured ages (Figure 3.5).

3.5.2.2 Effect of incision

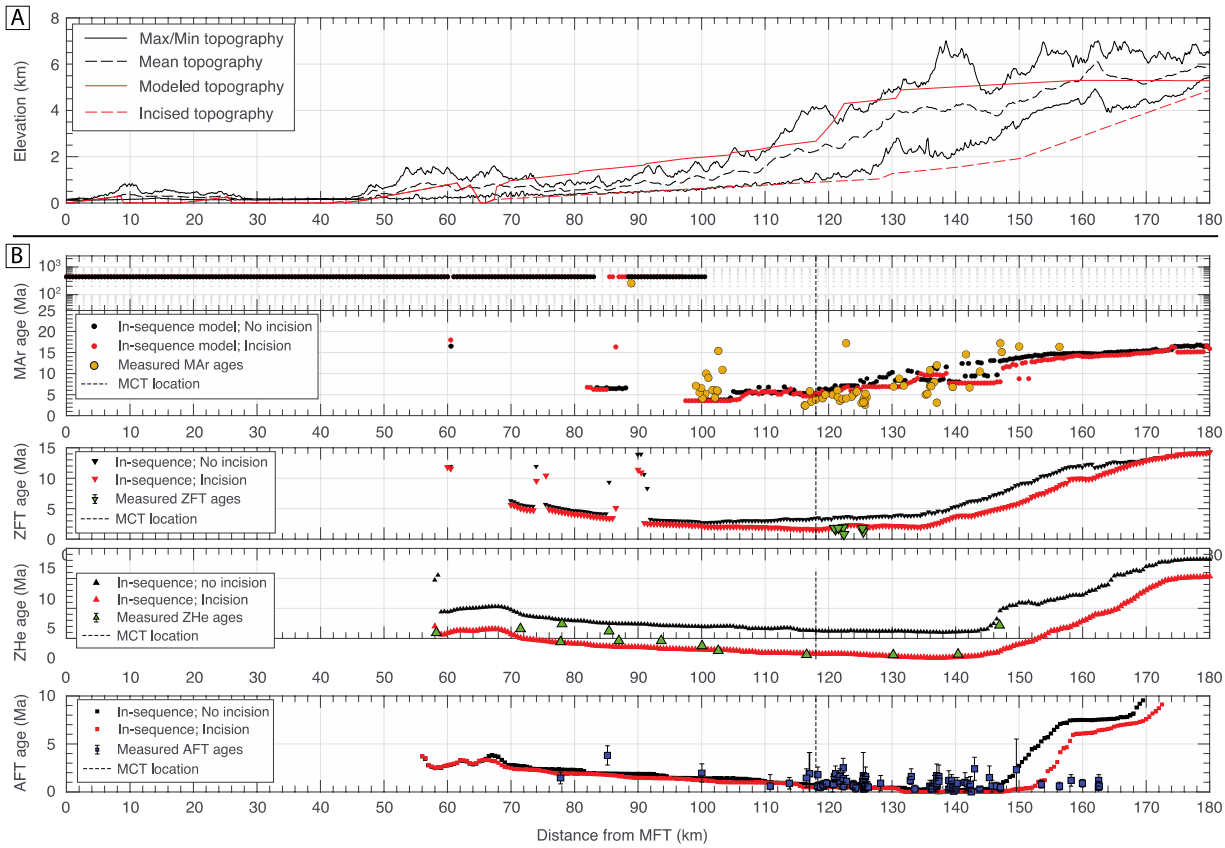

Figure 3.6: Effect of incision on modeled topography and predicted cooling ages.

(A) Comparison between the modeled topographies with (red - dashed) and without (red - solid) incision. Max, min, and mean swath topographies are shown in black; (B) Plots showing the effect of incision on the predicted cooling ages. No incision: Black; Incision: Red. Both models use a constant velocity of 21 mm/yr. and an A_0 value of 2.0 μW m^{-3}.

The canyon carved by the Marsyangdi river places the riverbed approximately 2 – 3 km below the elevations of the ridgelines (Figure 3.6A: dashed black). The result of this extreme topographic relief is that the rocks exposed at the bottom of the canyon have endured a minimum

of 2 km of extra exhumation compared to the rocks at higher elevations. We examine if significant river incision is responsible for the young, measured cooling ages. In particular, the youngest MAr and ZFT ages measured near the MCT, and the cluster of measured AFT ages in the north that our current forward model is unable to reproduce. We test this by simulating extra exhumation with a topographic profile that is ~3.5 km lower (Figure 3.6A: dashed red) than the original modeled topography (Figure 3.6A: solid red). South of 65 km, the incised topography follows the final modeled topography. Between 65 and 120 km from the MFT, the incised topography follows a predicted shape of the river bottom close to modern river elevations. Farther to the north, the incised topography is ~1 km deeper than the modern minimum topography, steadily steepening towards the north, until it reaches the same elevation as the initial modeled topography north of 180 km. The ~1 km deeper modeled incision level (compared to modern) was chosen to best reproduce the maximum relief. The original estimated topographic profile was designed to represent mean topography requiring a deeper incision level to replicate the full topographic relief (Figure 3.6A). The evolution of this incised topography occurs over the final 2 Ma of our forward model.

The simulated incision can successfully predict the young (< 2 Ma) ZFT ages located between 120 – 126 km. The effect of incision on the predicted MAr ages is primarily confined to the cooling ages located between 130 – 148 km from the MFT, predicting ages that are 1 – 2 Ma younger (Figure 3.6B, red) than those predicted by our model with no incision (Figure 3.6B, black). However, incision does not predict younger MAr ages near the MCT (between 118 – 126 km). The extra incision also does not affect the fit of the predicted ZHe and AFT ages to the south of 140 km. However, the increased exhumation north of 145 km leads to the prediction of ZHe ages that are between 1 – 4 Ma younger than our model with no incision between 145 – 158 km from

the MFT (Figure 3.6B), meaning that the model can no longer match the measured 5.5 Ma ZHe age located at 147 km. However, while the incision predicts ~1 Ma AFT ages between 145 – 154 km, reproducing the measured AFT age located 153 km from the MFT, it is still unable to reproduce the ~1 Ma ages farther to the north (Figure 3.6B).

Therefore, while the extra exhumation produced by the incision of the Marsyangdi can reproduce the young ZFT ages near the MCT, it is insufficient to reproduce the youngest MAr ages over the same area. The incision also fails to reproduce the inflection point in the trend of ZHe ages at ~145 km, and the reset AFT ages located between 154 – 164 km. A different mechanism is therefore required to reproduce: (i) the young MAr and ZFT ages between 116 – 127 km, and (ii) ~1 Ma AFT ages between 153 – 163 km, while retaining the inflection point in the ZHe ages (i.e., from ~1 Ma ages to ~6 Ma) located at ~145 km.

3.5.2.3 Effect of out-of-sequence thrusting

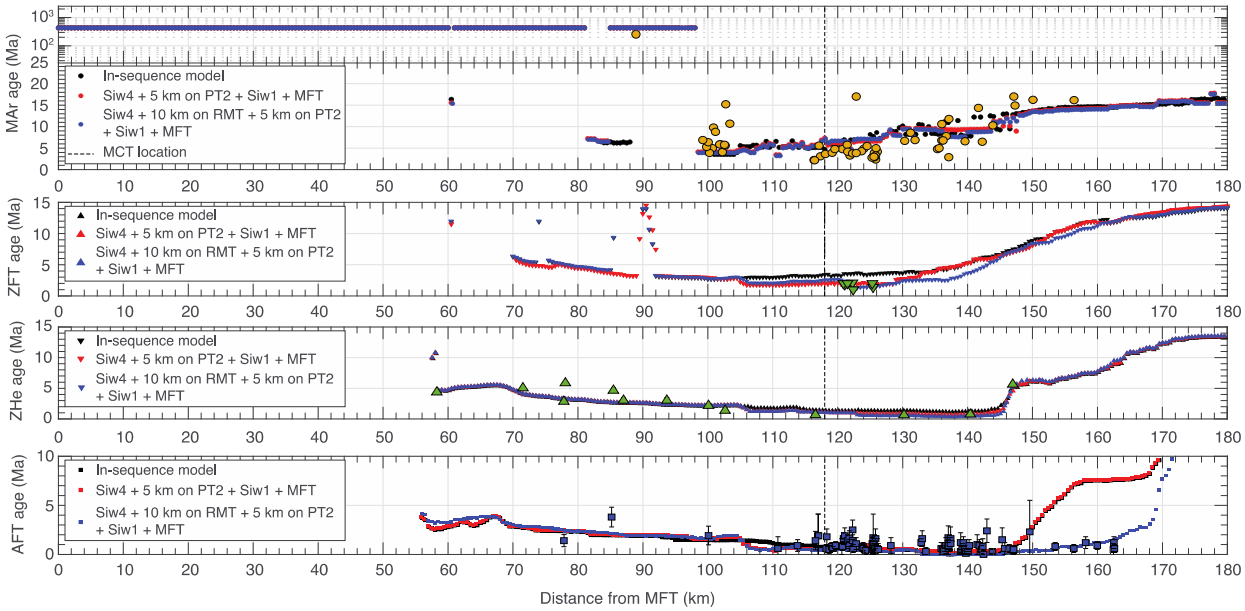

Figure 3.7: Plots showing the effect of out-of-sequence thrusting on the predicted cooling ages.

Black: No OOS; Red: 5 km of OOS thrusting on PT2; Blue: 5 km of OOS thrusting on PT2 + 10 km of OOS thrusting on RMT. Both models use a constant velocity of 21 mm/yr. and an A_0 value of 2.0 μW m^{-3}.

In this section, we test the effect of additional exhumation from young out-of-sequence (OOS) faults that have been proposed as drivers of uplift in the High Himalayas (Wobus, Hodges and Whipple, 2003; Hodges *et al.*, 2004; Wobus *et al.*, 2005; Huntington, Blythe and Hodges, 2006; Wobus, Whipple and Hodges, 2006; Whipple *et al.*, 2016). The first of these OOS thrusts is located ~100 km from the MFT and is proposed to be the mechanism responsible for the active uplift driving the sharp increase in elevations, slopes and steepness indices referred to as Physiographic Transition 2 (PT2) (Wobus, Hodges and Whipple, 2003; Wobus, Whipple and Hodges, 2006; Whipple *et al.*, 2016). OOS thrusting has also been proposed for the RMT – MCT zone, to explain the concentration of young, reset cooling ages north of this zone (Harrison *et al.*, 1997; Catlos *et al.*, 2001, 2018; Hodges *et al.*, 2004; Huntington, Blythe and Hodges, 2006).

We first test the effect of an OOS thrust located at the trace of PT2 (103 km from the MFT; Figures 3.2, 3.3), accommodating 5 km of shortening (Figure 3.7 – red) (e.g., Ghoshal et al., 2020). The effect of this OOS thrusting is particularly visible in the predicted cooling ages to the north of 105 km, where the predicted ZFT are 1 – 2 Ma younger, predicted ZHe ages are younger by ~1 Ma, and predicted AFT ages are similarly 1 Ma younger than the model without OOS thrusting. However, the effect on MAr ages is negligible, and does not reproduce the younger measured MAr ages between 118 – 126 km from the MFT. Finally, while the OOS thrusting increases the fit of the ZFT ages significantly, it does not affect the AFT ages north of 150 km at all (Figure 3.7 – red).

We also evaluated the effect of an additional 5 – 10 km of shortening accommodated by the reactivation of the RMT (~116 km; Figures 3.2, 3.3, 3.7 – blue). A full 10 km of displacement on the RMT is necessary to uplift and exhume rocks north of 150 km to reproduce the ~1 Ma AFT

ages between 153 – 163 km (Figure 3.7 – blue). Modeling 10 km of OOS thrusting on the RMT in addition to 5 km on PT2 reproduces measured cooling ages for the AFT, ZHe and ZFT systems between 100 and 164 km from the MFT but do not appreciably alter the predicted MAr ages. As a result, two main discrepancies between the predicted and measured ages remain: (i) the youngest measured MAr ages between 118 – 128 km, and (ii) the oldest reset MAr ages (> 15 Ma) to the north of 147 km.

3.5.2.4 Effect of variable shortening rates

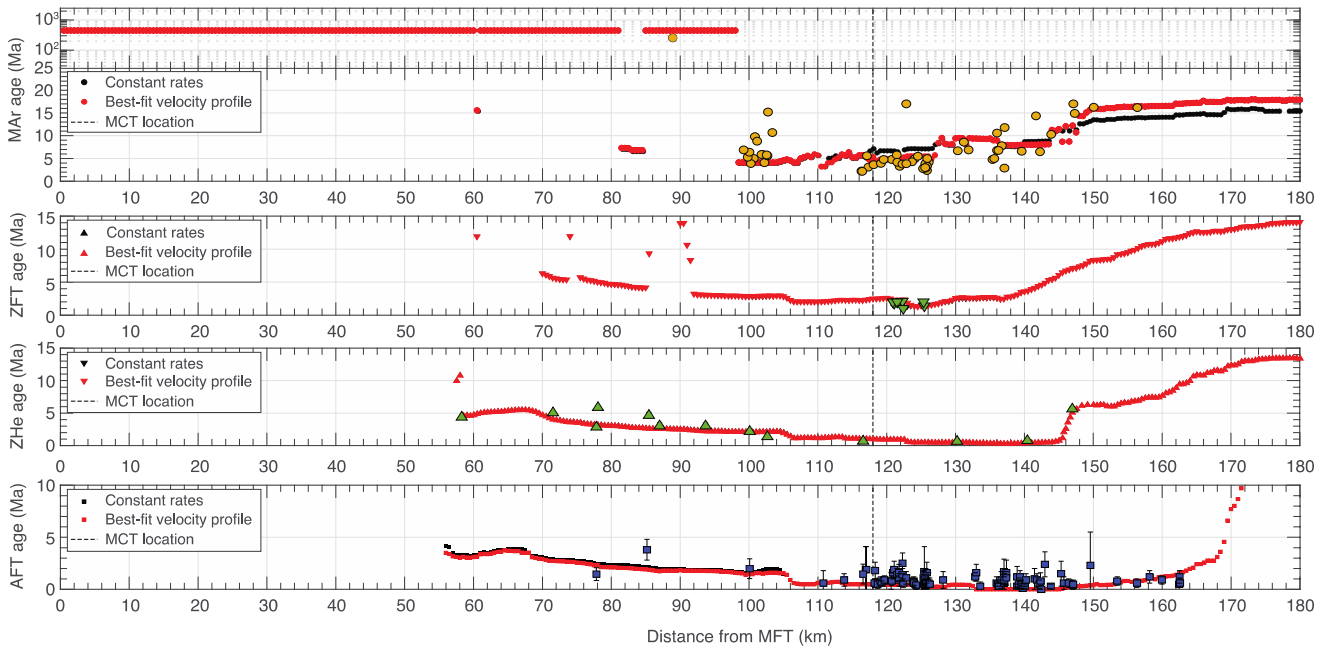

Figure 3.8: Plots showing the effect of variable rates of thrusting on the predicted cooling ages. Black: constant rates of thrusting (21 mm/yr.); Red: best-fit velocity profile. Both models use an A_0 value of 2.0 μW m^{-3}.

To evaluate whether variable rates of shortening can produce a better match between predicted and measured cooling ages we varied when shortening initiates, and the rates at which it occurs on different structures through time (e.g., Ghoshal et al., 2020). Since the MAr ages located north of 148 km are controlled by the age at which motion on the RMT initiates, increasing its

initiation age from ~15 Ma to 16 Ma is sufficient to reproduce the measured MAr ages (Figure 3.8). The youngest MAr ages (located between 118 – 128 km) are set by the initiation of the MBT, which occurs at ~6.5 Ma in our constant-rate model. Decreasing the age at which the MBT initiates to ~5.6 Ma and increasing the rate at which it moves to 40 mm/yr. allows us to match these measured ages (~5 Ma). This higher rate of shortening forces significantly faster exhumation over this period and driving the younger predicted MAr ages. Shortening rates return to the long-term average between 4.9 – 3.2 Ma. In order to reproduce the ZHe ages located between 79 – 94 km from the MFT, shortening rates need to decrease further to 14 mm/yr. between 3 – 2 Ma. This period of slow shortening, combined with the requirement that we match modern shortening rates (~19 – 21 mm/yr.) (Bilham *et al.*, 1997; Lavé and Avouac, 2000, 2001; Ader *et al.*, 2012) between 1.2 Ma and present means that the rates of shortening in the intervening period (2 – 1.2 Ma) need to be notably faster (33 mm/yr.). The best-fit velocity profile is listed in Table 3.2.

Structure	**Shortening (km)**	**Constant rate**		**Best-fit rates**	
		Initiation (Ma)	**Rate (mm/yr.)**	**Initiation (Ma)**	**Rate (mm/yr.)**
MCT	155.6	23.00	19.90	23.00	22.23
RMT	142.5	15.18	19.90	16.00	15.83
TT	31	8.02	19.90	7.00	22.14
MBT	30	6.46	19.90	5.60	40.00
MBT	10	4.95	19.90	4.85	15.38
D1Bt	5	4.45	19.90	4.20	20.00
D2	15	4.20	19.90	3.95	20.00
Siw1	8	3.45	19.90	3.20	20.00
Siw2	13.2	3.04	19.90	2.80	14.67
Siw3	13.9	2.38	19.90	1.90	33.90
Siw4	9.6	1.68	19.90	1.49	33.10
RMTOOS	10	1.20	19.90	1.20	19.23
PT2OOS	5	0.70	19.90	0.68	19.23
Siw1OOS	2	0.45	19.90	0.42	21.19
MFT	6.9	0.35	19.90	0.33	21.19

Table 3.2: Velocity profiles for final OOS models

3.6 Discussion

3.6.1 Out-of-sequence thrusting and topography

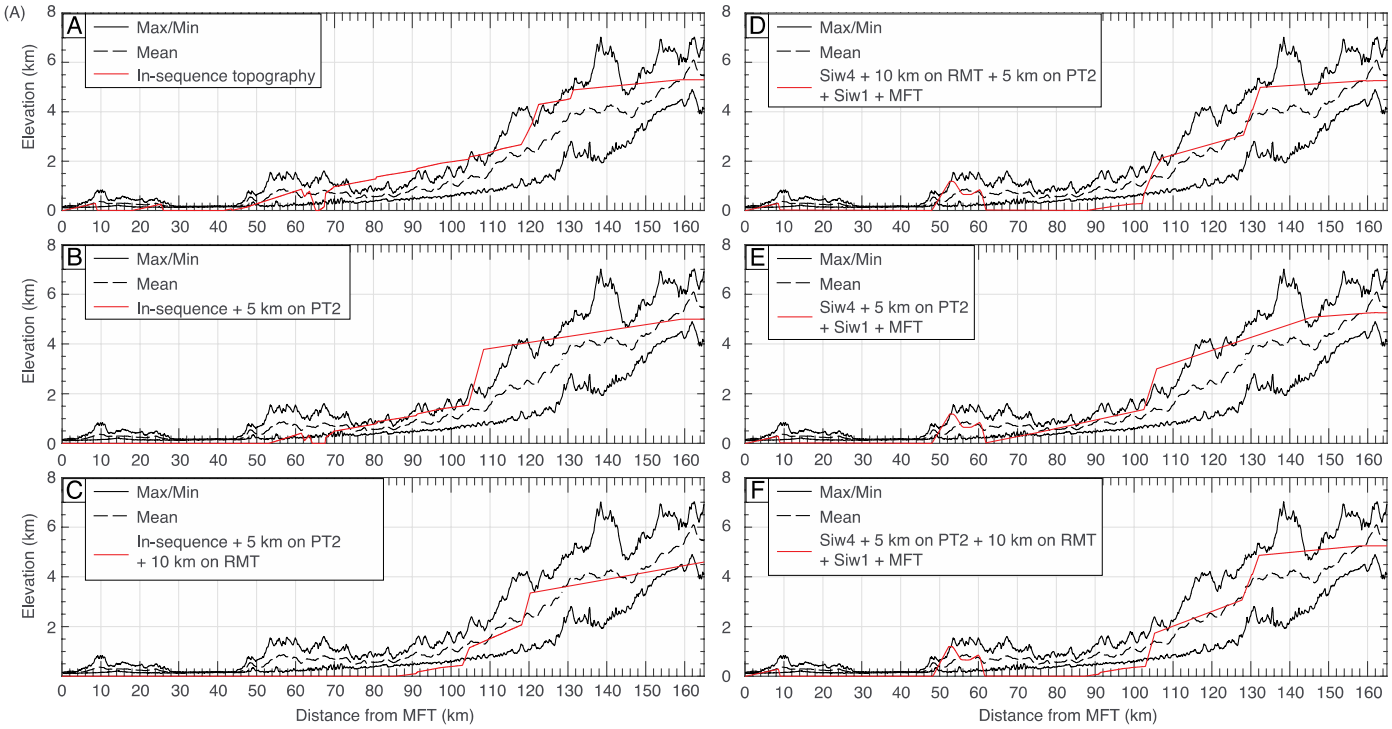

Figure 3.9: Plots showing the effect of out-of-sequence thrusting on modeled topography. (A) Final modeled topography for the in-sequence model; (B) Modeled topography produced by the addition of 5 km of OOS thrusting at PT2 at the end; (C) Modeled topography produced by the addition of 5 km of OOS thrusting at PT2 + 10 km of OOS thrusting on the RMT at the end; (D) Modeled topography produced by 10 km of OOS thrusting on RMTOOS + 5 km on PT2, accommodated prior to final motion on Siw1OOS and MFT (Table 2.); (E) Modeled topography produced by 5 km of OOS thrusting on PT2 accommodated prior to final motion on Siw1OOS, and MFT; (F) Modeled topography produced by 5 km of OOS thrusting on PT2 + 10 km on RMTOOS, accommodated prior to final motion on Siw1OOS and MFT. All figures show max, min and mean swath topographies in black.

Young OOS thrusting has long been proposed as one of the primary drivers of uplift in the Himalayas (Wobus, Hodges and Whipple, 2003; Hodges *et al.*, 2004; Wobus *et al.*, 2005; Wobus, Whipple and Hodges, 2006; Whipple *et al.*, 2016). Previous attempts at modeling the relative

importance of OOS thrusting versus ramp-driven uplift focused on the respective effects of these structures on the distribution of young reset MAr and AFT ages located at the RMT – MCT zone (Wobus, Whipple and Hodges, 2006; Whipp *et al.*, 2007; Herman *et al.*, 2010; Ghoshal *et al.*, 2020). Our model in the Marsyangdi valley shows that OOS thrusting in the hinterland (at PT2 or at the RMT) does not alter the predicted MAr or AFT ages in the region of the MCT. In contrast to previous models, 10 km of OOS faulting on the RMT is required to reproduce the young (~1 Ma), reset AFT ages located within the Tethyan (35 – 45 km north of the MCT) (Figure 7). The consistent ~35° dips mapped at the surface across both Greater Himalayan and Tethyan Himalayan rocks requires that both the MCT and RMT fault planes continue down at this dip to a depth of ~25 km (Figures 3.2, 3.3). The cross-sectional extent of the RMT from its surface location at 118 km to where it joins the MHT at 170 km from the MFT allows reactivation of the RMT to drive uplift and erosional exhumation between 118 – 170 km, providing the only plausible mechanism that can reset AFT ages that far to the north.

During OOS thrusting, the locus of uplift moves from the front of the system to the hinterland, promoting the building of topography there and increasing the overall taper angle. However, the isostatic load imparted by the sharp topographic increase resulting from OOS thrusting suppresses existing topography to the south. With a model that does not include OOS thrusting, uplift and translation of topography over the mid-crustal ramp allows the building of high topography (3 – 5 km elevation) in the hinterland. Simultaneously, in-sequence motion on the MBT and the intra-Siwalik thrusts create and maintain topography in the south (Figure 3.9A). When 5 km of OOS thrusting located at PT2 is introduced at the end of the model, it brings the zone of high hinterland topography southwards by ~20 km, producing a large topographic transition ~105 km from the MFT where modeled topography sharply increases from 1.8 to 4 km,

while the resulting isostatic load suppresses topography to the south, resulting in no topography (0 km elevation) modeled between 0 – 56 km from the MFT (Figure 3.9B). The addition of 10 km of shortening on the reactivated RMT forms a second topographic transition zone farther to the north (120 km from the MFT). The added isostatic load suppresses topography south of the OOS fault, decreasing the size of the topographic transition zone at PT2 from 4 km to between 1 – 1.5 km, and increasing the width of the zone of 0 km elevation to span between the MFT and 90 km north of the MFT (Figure 3.9C).

While OOS thrusting is necessary to match the distribution of cooling ages, the existence of topography south of PT2 means that the full magnitude of OOS faulting cannot occur at the end of the model. Using the simple estimate that links structural uplift to estimates of topographic elevation presented in section 4.2, we tested variations of OOS and in-sequence faulting to identify the order of thrusting that best reproduced the first-order shape of topography. Motion (~7 km) on the MFT is responsible for creating 1 km of topographic elevation between 0 – 20 km, while motion on the northernmost intra-Siwalik thrust (2 km) fault creates a topographic high (1.5 km high) between 50 – 60 km from the MFT. The presence of these topographic highs argues that these faults are the youngest in the sequence, and that motion on the PT2 and RMT must have occurred prior to motion on these two thrusts. The inference that the most recent motion has been on the MFT is also consistent with measured incision rates from Holocene river terraces in central Nepal (Lavé and Avouac, 2000).

Keeping OOS motion confined to 5 km on PT2 reproduces the topographic transition between 100 – 110 km (Wobus, Hodges and Whipple, 2003; Hodges *et al.*, 2004; Whipple *et al.*, 2016) very well and is also able to maintain a significant match to the modeled topography to the south (Figure 3.9E). However, as discussed above, this model is unable to reproduce the measured

cooling ages (Figure 3.7) and is therefore invalid. Introducing OOS thrusting on PT2 and the RMT prior to motion on the northernmost intra-Siwalik thrust and the MFT reproduces the pronounced topographic transition at PT2 while maintaining elevated topography in the foreland. A fault order that has 5 km of motion on PT2 follow the 10 km of motion on the reactivated RMT produces a more pronounced transition in elevation located at PT2 while maintaining the elevation gained at ~130 km during OOS motion of the RMT (Figure 3.9D). The differences imparted to the predicted topography by the order in which motion on PT2 and RMT occur are quite subtle (Figures 3.9D and F) and potentially indistinguishable given the resolution of our models. However, we use PT2 as the most recent OOS fault in our best-fit sequence to better highlight the pronounced topographic transition. The sequential development of cooling ages using this kinematic variant is shown in Video 3.2. Finally, using our best-fit velocity profile, reactivation of the RMT occurs at ~1.2 Ma, followed by motion on PT2 at 0.68 Ma.

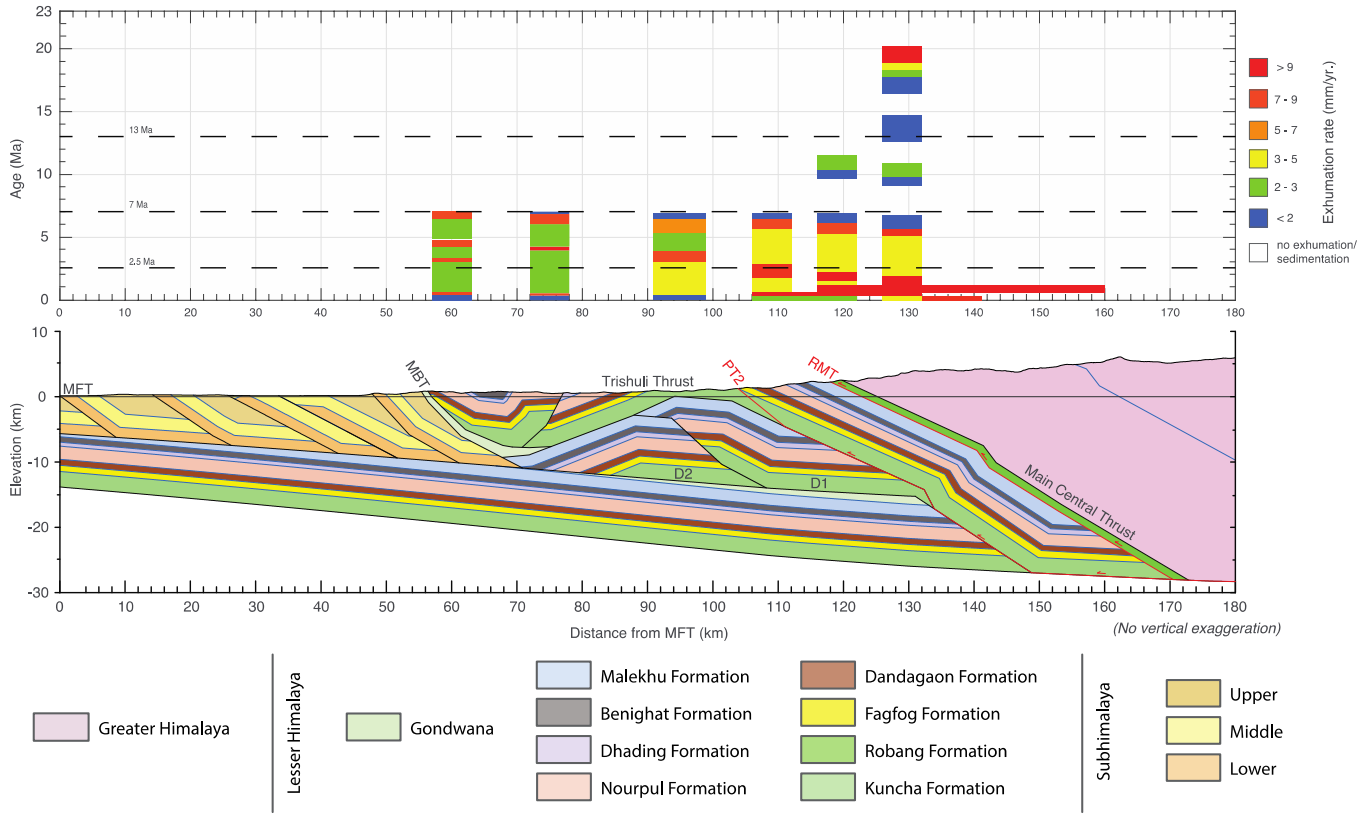

Figure 3.10: Plot of measured exhumation rates through time (starting at 23 Ma) for rocks exposed at the surface in the model.

The color bar indicates the variation in the rate of exhumation in mm/yr. Dashed black lines indicate proposed periods of monsoon strengthening.

3.6.2 Exhumation rates in the Marsyangdi valley

Coupling the amount of material being removed at every 10 km increment of displacement in our final kinematic sequence with the amount of time over which the step occurs allows us to calculate the resulting exhumation rates for each model timestep. Figure 3.10 shows how exhumation rates have changed over time for the rocks that are currently exposed at the surface. The rocks exposed in the hanging wall of the MCT were first exhumed between 20.3 – 18.9 Ma at ~10.5 mm/yr. During the emplacement of the RMT, the Robang Formation and GH rocks are

exhumed between 11.6 – 9.7 Ma at a significantly slower rate of ~3.2 mm/yr. Emplacement of the TT and the MBT begins ~7 Ma, exhuming the frontal portions (between 57 – 98 km) of the TT thrust sheet at ~6 – 7 mm/yr. In the hinterland, emplacement of the TT and the MBT exhumes the portions of the LH, Robang and GH currently exposed between 106 – 132 km from the MFT, at a rate of ~7 – 8 mm/yr. between 6.5 – 5.1 Ma. Formation of the duplex, and motion on the backthrust exhumes the rocks located between 72 – 78 km extremely fast (~11 mm/yr.) from 4.2 – 3.9 Ma. This is followed by exhumation of the rocks exposed at the core of the Gorkha-Pokhara antiform (between 92 – 98 km) at ~7 mm/yr. Motion on the Subhimalayan thrust sheets translates the duplex over the active ramp, exhuming the Trishuli-Robang-GH column (exposed between 106 – 132 km). While the initial motion (between 3.2 – 1.9 Ma) is slow, with shortening rates as low as ~14 mm/yr., exhumation rates remain high at ~9 mm/yr. Exhumation rates between 1.9 – 1.2 Ma are higher (~11 mm/yr.), reflecting the significantly higher rates at which shortening occurs (~34 mm/yr.) over this period. While shortening rates decrease back down to the long-term average of ~20 mm/yr., initiation of OOS thrusting on the RMT (1.2 Ma) and on PT2 (0.68 Ma) drives high rates of exhumation in the hinterland (> 10 mm/yr.), with the final modern-day motion on the MFT exhuming the rocks located over the active ramp at ~9.5 mm/yr.

In contrast to detrital studies that suggest exhumation rates have remained constant over the last 6 - 13 Ma (e.g., van der Beek et al., 2006; Huyghe et al., 2020), our models indicate four periods between which exhumation rates have significant changed over the last 23 Ma. The first change occurred at ~16 Ma, where exhumation rates decreased from 10 mm/yr., during the emplacement of the MCT, to 3 mm/yr. accompanying shortening on the RMT. At 7 Ma, exhumation rates increased more than twofold to an average rate of 7 – 8 mm/yr., driven by the high rates of shortening during the emplacement of the TT (up to 40 mm/yr.), followed by the

formation of the LH duplex. Finally, beginning at 2.5 Ma, translation of the duplex in its entirety over the modern mid-crustal ramp, and the onset of OOS thrusting in the hinterland at 1.2 Ma further increased exhumation rates, reaching rates of up to ~11 mm/yr., with exhumation over the 10 km high mid-crustal ramp maintaining these high rates till the modern day (Figure 3.10).

3.6.3 South Asian monsoon and potential tectonic response

Proxies for the south Asian monsoon suggest that it went through three periods of strengthening over the last 23 Myrs (Clift *et al.*, 2008; Sanyal *et al.*, 2010; Gupta *et al.*, 2015). Sandbox experiments and numerical modeling highlight that the focused erosion driven by these periods of intensified monsoon activity should induce an increase in the magnitude of uplift potentially due to faster rates of shortening, formation of a duplex, translation over higher ramps (Konstantinovskaia and Malavieille, 2005), or out-of-sequence thrusting (Hodges *et al.*, 2004; Wobus *et al.*, 2005; Huntington, Blythe and Hodges, 2006) to re-establish the eroded topography.

Comparing periods of change in the strength of the monsoon with changes in the behaviour of the orogenic system, seen as either a pronounced increase in the rate of shortening (increasing the rate of uplift over ramps), or the initiation of OOS thrusting, both of which drive increases in exhumation rates, should reveal whether a tectonic response exists. We can compare exhumation rates predicted by our best-fit model with periods of monsoon strengthening to identify correlations between high exhumation rates and strong monsoons. The first period where an increase in the strength of the monsoon has been proposed is ~13 Ma (Figure 3.1). This proposed increase in strength is not reflected in our model, as it coincides with the lowest rates of exhumation (~3.2 mm/yr.) (Figure 3.10). However, the second period of proposed monsoonal strengthening (7 Ma; Figure 3.1) coincides with a substantial increase in exhumation, beginning with the initiation of

the TT. The increase in exhumation rates (from 3.2 mm/yr. to 7 – 8 mm/yr.) is driven by a combination of an increase in shortening rates (from 15 mm/yr. to 40 mm/yr.), along with translation over a ~10 km high ramp, followed by the exhumation generated by the construction of the duplex. The most recent period of monsoon strengthening (~2.5 to present), is proposed to be the strongest (e.g., Gupta and Thomas, 2003; Gupta et al., 2015), and coincides with an additional increase in exhumation rates (up to 9 - 10 mm/yr.), driven by the translation of the entire duplex over the modern-day ramp stating at ~3 Ma. A short period of high shortening rates (~34 mm/yr.) beginning at 1.9 Ma drives exhumation rates of up to 11 mm/yr. The onset of OOS thrusting at 1.2 Ma, followed by active uplift over the modern ramp maintains these high exhumation rates through to modern day, despite shortening rates declining to the long-term average (~20 mm/yr.).

Rates at which rocks in the central Nepal Himalaya have been exhumed to the surface increase significantly immediately prior to 7 Ma and at 3 Ma, coinciding with pulses in the strength of the south Asian monsoon. At 7 Ma, the change in exhumation rates is driven by shortening rates increasing from their long-term average of ~20 mm/yr. to a high of 40 mm/yr. At 3 Ma, the architecture of the orogen changes significantly, initially with the translation of the entire duplex over the active ramp, followed by the initiation of OOS thrusting in the hinterland. These correlations suggest that the increase in the rates of shortening, and the changes in the architecture of the central Himalayas represents a systemic response to the increase in erosion brought on by the monsoon.

3.7 Conclusions

We combine new and existing mapping of stratigraphy and structural geometry, and published cooling ages collected from central Nepal with thermokinematic modeling to propose a new subsurface geometry, and kinematic sequence of events for the Marsyangdi valley (Figure 3D). We find that a model where uplift and exhumation are driven entirely by duplexing and motion over a mid-crustal ramp is not able to reproduce the entire distribution of cooling ages in the Marsyangdi transect. The additional exhumation provided by the incision of the Marsyangdi river is also not sufficient. Rather, major OOS thrusting on the reactivated RMT (10 km), and at PT2 (5 km) is required. In particular, the shortening accommodated on the reactivated RMT advects material from a depth of ~25 km and is the only mechanism capable of resetting AFT ages located between 152 – 160 km from the MFT (i.e., sampled in the Tethyan). While OOS faulting is required for ~1 Ma AFT ages located notably north of the MCT, and 1 - 2 Ma ZFT ages at the MCT, both MAr ages and AFT ages in the region of the MCT are remarkably insensitive to existence and magnitude of OOS faulting. The primary exhumation signature of these proposed OOS thrusts is to the north, where they are the only recent drivers of exhumation. The topographic signature of 15 km of recent OOS thrusting in the hinterland is flexural suppression of all modeled topography in the foreland. The existence of topography in the frontal portions of the central Himalayas means that OOS thrusting cannot be the most recent component of deformation and must predate motion on Siwalik thrusts. Our best-fit model shows OOS faulting between 1.2 Ma, till 0.4 Ma, followed by motion on the MFT from 0.4 Ma to present.

Finally, quantifying the amount of exhumation occurring at every timestep in our model allowed us to track whether exhumation rates have changed with time, and whether pronounced changes in exhumation correlate with proposed climate drivers. We find that exhumation rates in

the central Himalaya increase significantly at 7 Ma, due to an increase in shortening rates from 20 mm/yr. to 40 mm/yr., and again at 3 Ma, where the increase in exhumation rates is a function of a major shift in the architecture of the Himalaya, with the translation of the duplex over the mid-crustal ramp, followed by initiation of OOS thrusting in the hinterland. The correlation between the periods over which the south Asian monsoon is proposed to have strengthened with the periods of enhanced uplift and exhumation, suggest that these increases in the rates of shortening and changes in the internal architecture that drive the faster exhumation rates represent tectonic responses by the orogenic system to the changes in climate.

3.8 Supplementary information

The supplementary videos can be accessed online at https://www.youtube.com/playlist?list=PLttn6LSpDKTHS5i-QCimBnf2oCdZcsj8O

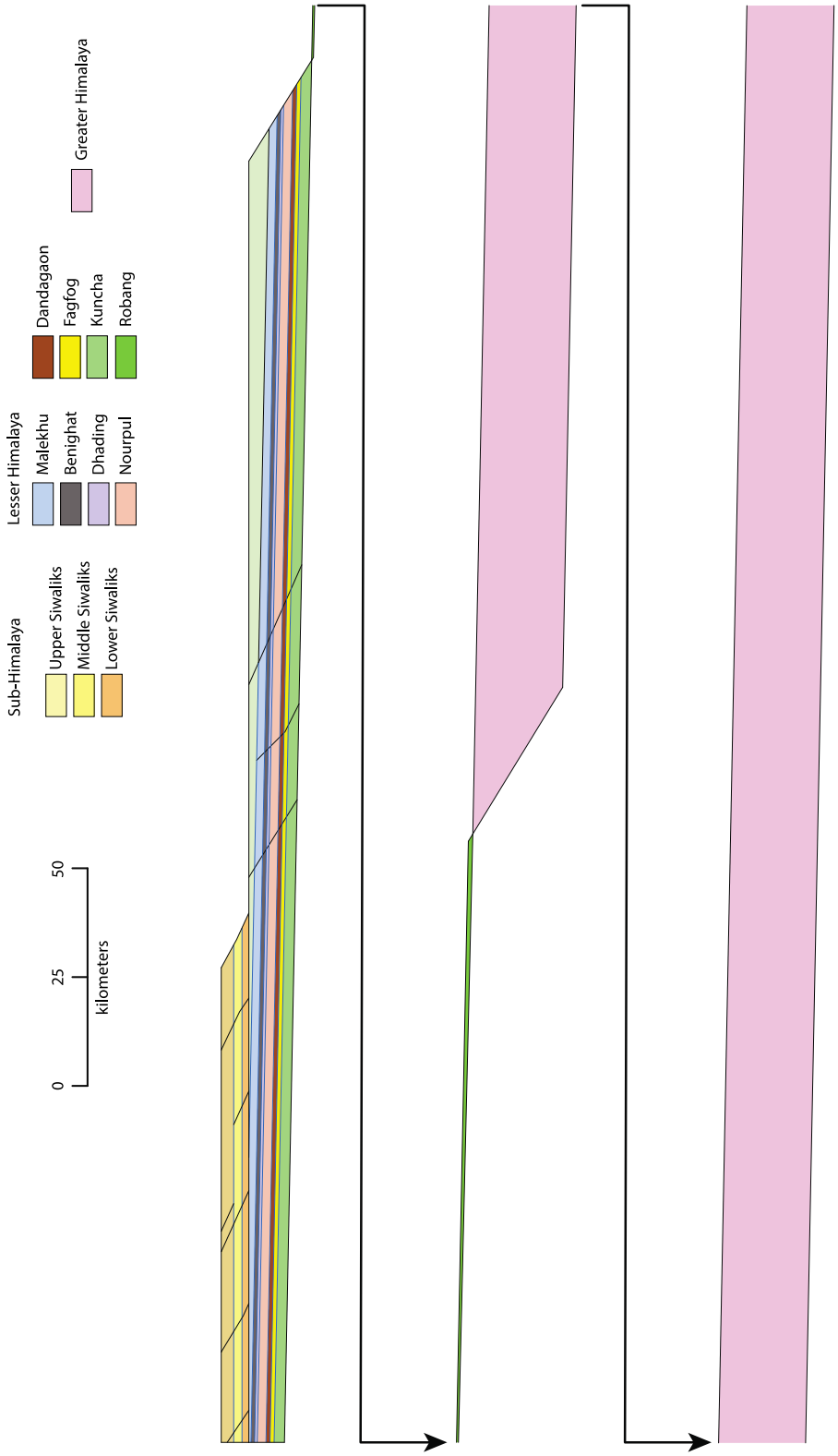

Figure 3.11: Restored cross-section geometry for the Marsyangdi transect

3.9 References

Adams, B. A. *et al.* (2020) 'Climate controls on erosion in tectonically active landscapes', *Science Advances*, 6(42). doi: 10.1126/sciadv.aaz3166.

Ader, T. *et al.* (2012) 'Convergence rate across the Nepal Himalaya and interseismic coupling on the Main Himalayan Thrust: Implications for seismic hazard', *Journal of Geophysical Research: Solid Earth*, 117, p. B04403. doi: 10.1029/2011JB009071.

Adlakha, V. *et al.* (2013) 'Rapid long-term erosion in the rain shadow of the Shillong Plateau, Eastern Himalaya', *Tectonophysics*. Elsevier B.V., 582, pp. 76–83. doi: 10.1016/j.tecto.2012.09.022.

Arita, K., Dallmeyer, R. D. and Takasu, A. (1997) 'Tectonothermal evolution of the Lesser Himalaya, Nepal: Constraints from 40Ar/39Ar ages from the Kathmandu Nappe', *Island Arc*, 6(4), pp. 372–385. doi: 10.1111/j.1440-1738.1997.tb00047.x.

Avouac, J.-P. (2003) 'Mountain building, erosion, and the seismic cycle in the Nepal Himalaya', in *Treatise on Geophysics*. 2nd edn, pp. 1–80. doi: 10.1016/S0065-2687(03)46001-9.

van der Beek, P. *et al.* (2006) 'Late Miocene - Recent exhumation of the central Himalaya and recycling in the foreland basin assessed by apatite fission-track thermochronology of Siwalik sediments, Nepal', *Basin Research*, 18(4), pp. 413–434. doi: 10.1111/j.1365-2117.2006.00305.x.

Bettinelli, P. *et al.* (2006) 'Plate motion of India and interseismic strain in the Nepal Himalaya from GPS and DORIS measurements', *Journal of Geodesy*, 80(8–11), pp. 567–589. doi: 10.1007/s00190-006-0030-3.

Bilham, R. *et al.* (1997) 'GPS measurements of present-day convergence across the Nepal Himalaya', *Nature*, 386, pp. 61–64.

Blythe, A. E. *et al.* (2007) 'Plio-Quaternary exhumation history of the central Nepalese

Himalaya: 1. Apatite and zircon fission track and apatite [U-Th]/He analyses', *Tectonics*, 26(3), pp. 1–16. doi: 10.1029/2006TC001990.

Bollinger, L. *et al.* (2004) 'Thermal structure and exhumation history of the Lesser Himalaya in central Nepal', *Tectonics*, 23(5), p. n/a-n/a. doi: 10.1029/2003TC001564.

Brady, R. J. *et al.* (2006) 'The distribution of radiogenic heat production as a function of depth in the Sierra Nevada batholith, California', *Lithos*. doi: 10.1016/j.lithos.2005.06.003.

Brandon, M. T., Roden-Tice, M. K. and Carver, J. I. (1998) 'Late Cenozoic exhumation of the Cascadia accretionary wedge in the Olympic Mountains, northwest Washington State', *Bulletin of the Geological Society of America*, 110(8), pp. 985–1009. doi: 10.1130/0016-7606(1998)110<0985:LCEOTC>2.3.CO;2.

Braun, J. (2003) 'Pecube: A new finite-element code to solve the 3D heat transport equation including the effects of a time-varying, finite amplitude surface topography', *Computers and Geosciences*, 29(6), pp. 787–794. doi: 10.1016/S0098-3004(03)00052-9.

Brookfield, M. E. (1993) 'The Himalayan passive margin from Precambrian to Cretaceous times', *Sedimentary Geology*, 84, pp. 1–35.

Burbank, D. W. *et al.* (2003) 'Decoupling of erosion and precipitation in the Himalayas', *Nature*, 426(6967), pp. 652–655. doi: 10.1038/nature02187.

Burbank, D. W., Beck, R. A. and Mulder, T. (1996) 'The Himalayan foreland', in Lin, A. and Harrison, T. M. (eds) *The Tectonic Evolution of Asia*. United Kingdom: Cambridge University Press, pp. 149–188.

Burchfiel, B. C. *et al.* (1992) *The South Tibetan Detachment System, Himalayan Orogen: Extension Contemporaneous With and Parallel to Shortening in a Collisional Mountain Belt, Geological Society of America Special Paper 269*. doi: 10.1130/spe269-p1.

Burg, J. P. *et al.* (1984) ‘Deformation of leucogranites of the crystalline Main Central Sheet in southern Tibet (China)’, *Journal of Structural Geology*, 6(5), pp. 535–542. doi: 10.1016/0191-8141(84)90063-4.

Catlos, E. J. *et al.* (2001) ‘Geochronologic and thermobarometric constraints on the evolution of the Main Central Thrust, central Nepal Himalaya’, *Journal of Geophysical Research: Solid Earth*, 106(B8), pp. 16177–16204. doi: 10.1029/2000JB900375.

Catlos, E. J. *et al.* (2018) ‘Modeling High-Resolution Pressure-Temperature Paths Across the Himalayan Main Central Thrust (Central Nepal): Implications for the Dynamics of Collision’, *Tectonics*, 37(8), pp. 2363–2388. doi: 10.1029/2018TC005144.

Clift, P. D. *et al.* (2008) ‘Correlation of Himalayan exhumation rates and Asian monsoon intensity’, *Nature Geoscience*, 1(12), pp. 875–880. doi: 10.1038/ngeo351.

Clift, P. D. (2017) ‘Cenozoic sedimentary records of climate-tectonic coupling in the Western Himalaya’, *Progress in Earth and Planetary Science*. Progress in Earth and Planetary Science, 4(1), p. 39. doi: 10.1186/s40645-017-0151-8.

Coleman, M. E. (1996) ‘Orogen-parallel and orogen-perpendicular extension in the central Nepalese Himalayas’, *Bulletin of the Geological Society of America*, 108(12), pp. 1594–1607. doi: 10.1130/0016-7606(1996)108<1594:OPAOPE>2.3.CO;2.

Copeland, P. *et al.* (1991) ‘An early Pliocene thermal disturbance of the main central thrust, central Nepal: Implications for Himalayan tectonics’, *Journal of Geophysical Research*, 96(B5), p. 8475. doi: 10.1029/91JB00178.

Cross III, E. A. (2014) *The structure, stratigraphy, and evolution of the Lesser Himalaya of central Nepal*. The University of Arizona.

Crowley, K. d., Cameron, M. and Schaefer, R. l. (1991) ‘Experimental studies of annealing

of etched fission tracks in fluorapatite', *Geochimica et Cosmochimica Acta*, 55(5), pp. 1449–1465. doi: 10.1016/0016-7037(91)90320-5.

Curry, W. B. *et al.* (1992) 'Foraminiferal production and monsoonal upwelling in the Arabian Sea: evidence from sediment traps', *Geological Society, London, Special Publications*, 64(1), pp. 93–106. doi: 10.1144/GSL.SP.1992.064.01.06.

DeCelles, P. G. *et al.* (1998) 'Eocene-early Miocene foreland basin development and the history of Himalayan thrusting, western and central Nepal', *Tectonics*, 17(5), pp. 741–765. doi: 10.1029/98TC02598.

DeCelles, P. G. *et al.* (2007) 'High and dry in central Tibet during the Late Oligocene', *Earth and Planetary Science Letters*, 253(3–4), pp. 389–401. doi: 10.1016/j.epsl.2006.11.001.

DeCelles, P. G. *et al.* (2014) 'Paleocene-Eocene foreland basin evolution in the Himalaya of southern Tibet and Nepal: Implications for the age of initial India-Asia collision', *Tectonics*, 33(5), pp. 824–849. doi: 10.1002/2014TC003522.

DeCelles, P. G. *et al.* (2020) *Structural and Thermal Evolution of the Himalayan Thrust Belt in Midwestern Nepal*, *Geological Society of America*. Boulder, Colorado: Geological Society of America. doi: 10.1130/SPE547.

Dhital, M. R. (2015) *Geology of the Nepal Himalaya*. Cham: Springer International Publishing (Regional Geology Reviews). doi: 10.1007/978-3-319-02496-7.

Dodson, M. H. (1973) 'Closure temperature in cooling geochronological and petrological systems', *Contributions to Mineralogy and Petrology*, 40, pp. 259–274. Available at: http://www.raco.cat/index.php/Dovella/article/view/20118.

Ehlers, T. A. *et al.* (2005) 'Computational tools for low-temperature Thermochronometer Interpretation', *Reviews in Mineralogy and Geochemistry*, 58(1), pp. 589–622. doi:

10.2138/rmg.2005.58.22.

Ehlers, T. A. (2005) 'Crustal thermal processes and the interpretation of Thermochronometer data', *Reviews in Mineralogy and Geochemistry*, 58(1), pp. 315–350. doi: 10.2138/rmg.2005.58.12.

England, P. *et al.* (1992) 'Heat sources for tertiary metamorphism and anatexis in the Annapurna-Manaslu region central Nepal', *Journal of Geophysical Research*, 97(B2), pp. 2107–2128. doi: 10.1029/91JB02272.

France-Lanord, C., Derry, L. and Michard, A. (1993) 'Evolution of the Himalaya since Miocene time: Isotopic and sedimentological evidence from the Bengal Fan', *Geological Society Special Publication*, 74(74), pp. 603–621. doi: 10.1144/GSL.SP.1993.074.01.40.

Freeman, K. H. and Colarusso, L. A. (2001) 'Molecular and isotopic records of C4 grassland expansion in the late miocene', *Geochimica et Cosmochimica Acta*, 65(9), pp. 1439–1454. doi: 10.1016/S0016-7037(00)00573-1.

Fuchs, G., Widder, R. and Tuladhar, R. (1988) 'Contributions to the Geology of the Annapurna Range (Manang Area, Nepal)', *Jahrbuch der Geologischen Bundesanstalt*, 131(4), pp. 593–607.

Gansser, A. (1964) *Geology of the Himalayas*. New York: Wiley-Interscience.

Garzanti, E., Baud, A. and Mascle, G. (1987) 'Sedimentary record of the northward flight of India and its collision with Eurasia (Ladakh Himalaya, India)', *Geodinamica Acta*. Taylor & Francis, 1(4–5), pp. 297–312. doi: 10.1080/09853111.1987.11105147.

Gautam, P. and Rösler, W. (1999) 'Depositional chronology and fabric of Siwalik Group sediments in central Nepal from magnetostratigraphy and magnetic anisotropy', *Journal of Asian Earth Sciences*, 17(5–6), pp. 659–682. doi: 10.1016/S1367-9120(99)00021-8.

Gehrels, G. *et al.* (2011) 'Detrital zircon geochronology of pre-Tertiary strata in the Tibetan-Himalayan orogen', *Tectonics*, 30(5). doi: 10.1029/2011TC002868.

Ghoshal, S. *et al.* (2020) 'Constraining Central Himalayan (Nepal) Fault Geometry Through Integrated Thermochronology and Thermokinematic Modeling', *Tectonics*, 39(9), pp. 1–33. doi: 10.1029/2020TC006399.

Gilmore, M. E. *et al.* (2018) 'Testing the effects of topography, geometry, and kinematics on modeled thermochronometer cooling ages in the eastern Bhutan Himalaya', *Solid Earth*, 9(3), pp. 599–627. doi: 10.5194/se-9-599-2018.

Godard, V. *et al.* (2014) 'Dominance of tectonics over climate in himalayan denudation', *Geology*, 42(3), pp. 243–246. doi: 10.1130/G35342.1.

Guillot, S. *et al.* (1993) 'The emplacement of the Manaslu granite of Central Nepal: Field and magnetic susceptibility constraints', *Geological Society Special Publication*, 74(April 2017), pp. 413–428. doi: 10.1144/GSL.SP.1993.074.01.28.

Gupta, A. K. *et al.* (2015) 'Evolution of the South Asian monsoon wind system since the late Middle Miocene', *Palaeogeography, Palaeoclimatology, Palaeoecology*. Elsevier B.V., 438, pp. 160–167. doi: 10.1016/j.palaeo.2015.08.006.

Gupta, A. K., Anderson, D. M. and Overpeck, J. T. (2003) 'Abrupt changes in the Asian southwest monsoon during the holocene and their links to the North Alantic Ocean', *Nature*, 421(6921), pp. 354–357. doi: 10.1038/nature01340.

Gupta, A. K. and Thomas, E. (2003) 'Initiation of Northern Hemisphere glaciation and strengthening of the northeast Indian monsoon: Ocean Drilling Program Site 758, eastern equatorial Indian Ocean', *Geology*, 31(1), pp. 47–50. doi: 10.1130/0091-7613(2003)031<0047:IONHGA>2.0.CO;2.

Hames, W. E. and Bowring, S. A. (1994) 'An empirical evaluation of the argon diffusion geometry in muscovite', *Earth and Planetary Science Letters*, 124(1–4), pp. 161–169. doi: 10.1016/0012-821X(94)00079-4.

Harel, E. *et al.* (2019) 'Drainage reversal toward cliffs induced by lateral lithologic differences', *Geology*, 47(10), pp. 928–932. doi: 10.1130/G46353.1.

Harrison, T. M. *et al.* (1993) 'Isotopic preservation of Himalayan/Tibetan uplift, denudation, and climatic histories of two molasse deposits', *The Journal of Geology*, 101, pp. 157–175.

Harrison, T. M. *et al.* (1997) 'A Late Miocene-Pliocene origin for the Central Himalayan inverted metamorphism', *Earth and Planetary Science Letters*, 146, pp. E1–E7.

Harrison, T. M. *et al.* (1999) 'Origin and episodic emplacement of the Manaslu intrusive complex, Central Himalaya', *Journal of Petrology*, 40(1), pp. 3–19. doi: 10.1093/petroj/40.1.3.

Harrison, T. M., McKeegan, K. D. and LeFort, P. (1995) 'Detection of inherited monazite in the Manaslu leucogranite by 208Pb232Th ion microprobe dating: Crystallization age and tectonic implications', *Earth and Planetary Science Letters*, 133(3–4), pp. 271–282. doi: 10.1016/0012-821X(95)00091-P.

Herman, F. *et al.* (2010) 'Exhumation, crustal deformation, and thermal structure of the Nepal Himalaya derived from the inversion of thermochronological and thermobarometric data and modeling of the topography', *Journal of Geophysical Research: Solid Earth*, 115(6). doi: 10.1029/2008JB006126.

Hilley, G. E. *et al.* (2019) 'Earth's topographic relief potentially limited by an upper bound on channel steepness', *Nature Geoscience*. Springer US, 12(October), pp. 828–833. doi: 10.1038/s41561-019-0442-3.

Hodges, K. V. *et al.* (2004) 'Quaternary deformation, river steepening, and heavy precipitation at the front of the Higher Himalayan ranges', *Earth and Planetary Science Letters*, 220(3–4), pp. 379–389. doi: 10.1016/S0012-821X(04)00063-9.

Hodges, K. V. (2014) 'Thermochronology in Orogenic Systems', in Holland, H. D. and Turekian, K. K. (eds) *Treatise on Geochemistry*. Amsterdam: Elsevier, pp. 281–308. doi: 10.1016/B978-0-08-095975-7.00308-9.

Horton, B. K. (1999) 'Erosional control on the geometry and kinematics of thrust belt development in the central Andes', *Tectonics*, 18(6), pp. 1292–1304. doi: 10.1029/1999TC900051.

Hu, X. *et al.* (2016) 'The timing of India-Asia collision onset – Facts, theories, controversies', *Earth-Science Reviews*. Elsevier B.V., 160, pp. 264–299. doi: 10.1016/j.earscirev.2016.07.014.

Hubbard, J. *et al.* (2016) 'Structural segmentation controlled the 2015 M w 7.8 Gorkha earthquake rupture in Nepal', *Geology*, 44(8), pp. 639–642. doi: 10.1130/G38077.1.

Huntington, K. W., Blythe, A. E. and Hodges, K. V. (2006) 'Climate change and Late Pliocene acceleration of erosion in the Himalaya', *Earth and Planetary Science Letters*, 252(1–2), pp. 107–118. doi: 10.1016/j.epsl.2006.09.031.

Huyghe, P. *et al.* (2020) 'Rapid exhumation since at least 13 Ma in the Himalaya recorded by detrital apatite fission-track dating of Bengal fan (IODP Expedition 354) and modern Himalayan river sediments', *Earth and Planetary Science Letters*. Elsevier B.V., 534, p. 116078. doi: 10.1016/j.epsl.2020.116078.

Jouanne, F. *et al.* (2004) 'Current shortening across the Himalayas of Nepal', *Geophysical Journal International*, 157(1), pp. 1–14. doi: 10.1111/j.1365-246X.2004.02180.x.

Ketcham, R. A. (1996) 'Distribution of heat-producing elements in the upper and middle crust of southern and west central Arizona: Evidence from the core complexes', *Journal of Geophysical Research: Solid Earth*. doi: 10.1029/96jb00664.

Khanal, S. (2014) *Structural and Kinematic Evolution of the Himalayan Thrust Belt, central Nepal*. The University of Alabama.

Khanal, S. and Robinson, D. M. (2013) 'Upper crustal shortening and forward modeling of the Himalayan thrust belt along the Budhi-Gandaki River, central Nepal', *International Journal of Earth Sciences*, 102(7), pp. 1871–1891. doi: 10.1007/s00531-013-0889-1.

Kimura, K. (1999) 'Diachronous evolution of sub-Himalayan piggyback basins, Nepal', *Island Arc*, 8(1), pp. 99–113. doi: 10.1046/j.1440-1738.1999.00224.x.

Kohn, M. J. *et al.* (2001) 'Pressure-temperature-time path discontinuity in the Main Central thrust zone, central Nepal', *Geology*, 29(7), pp. 571–574. doi: 10.1130/0091-7613(2001)029<0571:PTTPDI>2.0.CO;2.

Kohn, M. J. *et al.* (2004) 'Miocene faulting at plate tectonic velocity in the Himalaya of central Nepal', *Earth and Planetary Science Letters*, 228(3–4), pp. 299–310. doi: 10.1016/j.epsl.2004.10.007.

Kohn, M. J. (2008) 'P-T-t data from central Nepal support critical taper and repudiate large-scale channel flow of the Greater Himalayan Sequence', *Bulletin of the Geological Society of America*, 120(3–4), pp. 259–273. doi: 10.1130/B26252.1.

Konstantinovskaia, E. and Malavieille, J. (2005) 'Erosion and exhumation in accretionary orogens: Experimental and geological approaches', *Geochemistry, Geophysics, Geosystems*, 6(2). doi: 10.1029/2004GC000794.

Kroon, D., Steens, T. and Troelstra, S. R. (1991) 'Onset of monsoonal related upwelling in

the western Arabian Sea as revealed by planktonic foraminifers', *Proc., scientific results, ODP, Leg 117, Oman Margin/Neogene package*. doi: 10.2973/odp.proc.sr.117.126.1991.

Lavé, J. and Avouac, J.-P. (2000) 'Active folding of fluvial terraces across the Siwaliks Hills, Himalayas of central Nepal', *Journal of Geophysical Research: Solid Earth*, 105(B3), pp. 5735–5770. doi: 10.1029/1999JB900292.

Lavé, J. and Avouac, J.-P. (2001) 'Fluvial incision and tectonic uplift across the Himalayas of central Nepal', *Journal of Geophysical Research: Solid Earth*, 106(B11), pp. 26561–26591. doi: 10.1029/2001JB000359.

Lenard, S. J. P. *et al.* (2020) 'Steady erosion rates in the Himalayas through late Cenozoic climatic changes', *Nature Geoscience*. Springer US, 13(6), pp. 448–452. doi: 10.1038/s41561-020-0585-2.

Lock, J. and Willett, S. (2008) 'Low-temperature thermochronometric ages in fold-and-thrust belts', *Tectonophysics*, 456(3–4), pp. 147–162. doi: 10.1016/j.tecto.2008.03.007.

Malavieille, J. (2010) 'Impact of erosion, sedimentation, and structural heritage on the structure and kinematics of orogenic wedges: Analog models and case studies', *GSA Today*, 20(1), pp. 4–10. doi: 10.1130/GSATG48A.1.

Martin, A. J. *et al.* (2005) 'Isotopic and structural constraints on the location of the Main Central thrust in the Annapurna Range, central Nepal Himalaya', *Bulletin of the Geological Society of America*, 117(7–8), pp. 926–944. doi: 10.1130/B25646.1.

Martin, A. J. *et al.* (2011) 'Stratigraphic and tectonic implications of field and isotopic constraints on depositional ages of Proterozoic Lesser Himalayan rocks in central Nepal', *Precambrian Research*. Elsevier B.V., 185(1–2), pp. 1–17. doi: 10.1016/j.precamres.2010.11.003.

McQuarrie, N. *et al.* (2019) 'The influence of foreland structures on hinterland cooling:

Evaluating the drivers of exhumation in the eastern Bhutan Himalaya', *Tectonics*, pp. 1–29. doi: 10.1029/2018tc005340.

McQuarrie, N. and Ehlers, T. A. (2015) 'Influence of thrust belt geometry and shortening rate on thermochronometer cooling ages: Insights from thermokinematic and erosion modeling of the Bhutan Himalaya', *Tectonics*, 34(6), pp. 1055–1079. doi: 10.1002/2014TC003783.

McQuarrie, N. and Ehlers, T. A. (2017) 'Techniques for understanding fold-and-thrust belt kinematics and thermal evolution', in Law, R. D. et al. (eds) *Linkages and Feedbacks in Orogenic Systems*. Boulder: Geological Society of America, pp. 25–54. doi: 10.1130/2017.1213(02).

Menon, R. *et al.* (2003) 'Radiogenic heat production of Late Archaean Bundelkhand granite and some Proterozoic gneisses and granitoids of central India', *Current Science*, 85(5), pp. 634–638.

Montgomery, D. R., Balco, G. and Willett, S. D. (2001) 'Climate, tectonics, and the morphology of the Andes', *Geology*, 29(7), pp. 579–582. doi: 10.1130/0091-7613(2001)029<0579:CTATMO>2.0.CO;2.

Ojha, T. P. *et al.* (2000) 'Magnetic polarity stratigraphy of the Neogene Siwalik Group at Khutia Khola, far western Nepal', *Bulletin of the Geological Society of America*, 112(3), pp. 424–434. doi: 10.1130/0016-7606(2000)112<424:MPSOTN>2.0.CO;2.

Ojha, T. P. *et al.* (2009) 'Magnetic polarity stratigraphy of the Neogene foreland basin deposits of Nepal', *Basin Research*, 21(1), pp. 61–90. doi: 10.1111/j.1365-2117.2008.00374.x.

Olree, E. C. (2018) *Kinematic and Flexural Isostasy Modeling in Central Nepal: Using erosional, depositional, and cooling histories to validate a balanced cross-section*. The University of Alabama.

Orme, D. A., Carrapa, B. and Kapp, P. (2015) 'Sedimentology, provenance and

geochronology of the upper Cretaceous-lower Eocene western Xigaze forearc basin, southern Tibet', *Basin Research*, 27(4), pp. 387–411. doi: 10.1111/bre.12080.

Overpeck, J. *et al.* (1996) 'The southwest Indian Monsoon over the last 18000 years', *Climate Dynamics*. doi: 10.1007/BF00211619.

Pandey, M. R. *et al.* (1995) 'Interseismic strain accumulation on the Himalayan crustal ramp (Nepal)', *Geophysical Research Letters*, 22(7), pp. 751–754. doi: 10.1029/94GL02971.

Pearson, O. N. (2002) *Structural evolution of the central Nepal fold-thrust belt and regional tectonic and structural significance of the Ramgarh thrust*. The University of Arizona, Tucson.

Pearson, O. N. and DeCelles, P. G. (2005) 'Structural geology and regional tectonic significance of the Ramgarh thrust, Himalayan fold-thrust belt of Nepal', *Tectonics*, 24(4), pp. 1–26. doi: 10.1029/2003TC001617.

Quade, J. *et al.* (1995) 'Late Miocene environmental change in Nepal and the northern Indian subcontinent: Stable isotopic evidence from paleosols', *Geological Society of America Bulletin*, 107(12), pp. 1381–1397. doi: 10.1130/0016-7606(1995)107<1381:LMECIN>2.3.CO;2.

Quade, J., Cerling, T. E. and Bowman, J. R. (1989) 'Development of Asian monsoon revealed by marked ecological shift during the latest Miocene in northern Pakistan', *Nature*, 342(6246), pp. 163–166. doi: 10.1038/342163a0.

Ratschbacher, L. *et al.* (1994) 'Distributed deformation in southern and western Tibet during and after the India-Asia collision', *Journal of Geophysical Research*, 99(B10), pp. 19,917-19,645.

Ray, L., Bhattacharya, A. and Roy, S. (2007) 'Thermal conductivity of Higher Himalayan crystallines from Garhwal Himalaya, India', *Tectonophysics*, 434(1–4), pp. 71–79. doi:

10.1016/j.tecto.2007.02.003.

Reiners, P. W. *et al.* (2004) 'Zircon (U-Th)/He thermochronometry: He diffusion and comparisons with 40Ar/39Ar dating', *Geochimica et Cosmochimica Acta*, 68(8), pp. 1857–1887. doi: 10.1016/j.gca.2003.10.021.

Reiners, P. W. and Brandon, M. T. (2006) 'Using Thermochronology to Understand Orogenic Erosion', *Annual Review of Earth and Planetary Sciences*, 34(1), pp. 419–466. doi: 10.1146/annurev.earth.34.031405.125202.

Robert, X. *et al.* (2011) 'Control of detachment geometry on lateral variations in exhumation rates in the Himalaya: Insights from low-temperature thermochronology and numerical modeling', *Journal of Geophysical Research: Solid Earth*, 116(5), pp. 1–22. doi: 10.1029/2010JB007893.

Robinson, D. M. *et al.* (2021) 'Controls of Stratigraphic Architecture on Along Strike Cooling Age Patterns', *Terra Nova*, 33(2), pp. 129–136. doi: 10.1111/ter.12498.

Robinson, D. M. and Martin, A. J. (2014) 'Reconstructing the greater Indian margin: A balanced cross section in central Nepal focusing on the Lesser Himalayan duplex', *Tectonics*, 33(11), pp. 2143–2168. doi: 10.1002/2014TC003564.

Robinson, D. M. and Pearson, O. N. (2013) 'Was Himalayan normal faulting triggered by initiation of the Ramgarh-Munsiari thrust and development of the Lesser Himalayan duplex?', *International Journal of Earth Sciences*, 102(7), pp. 1773–1790. doi: 10.1007/s00531-013-0895-3.

Roe, G. H. and Brandon, M. T. (2011) 'Critical form and feedbacks in mountain-belt dynamics: Role of rheology as a tectonic governor', *Journal of Geophysical Research: Solid Earth*, 116(2), pp. 1–17. doi: 10.1029/2009JB006571.

Roy, B., Ghosh, S. and Sanyal, P. (2020) 'Morpho-tectonic control on the distribution of C3-C4 plants in the central Himalayan Siwaliks during Late Plio-Pleistocene', *Earth and Planetary Science Letters*. Elsevier B.V., 535, p. 116119. doi: 10.1016/j.epsl.2020.116119.

Sakai, H. (1983) 'Geology of the Tansen Group of the Lesser Himalaya in Nepal', *Memoirs of the Faculty of Science, Kyushu University*, pp. 27–74.

Sakai, H. (1985) 'Rifting of the Gondwanaland and uplifting of the Himalayas recorded in Mesozoic and Tertiary fluvial sediments in the Nepal Himalayas', in Taira, A. and Masuda, F. (eds) *Sedimentary Facies in the Active Plate Margin*. Tokyo: Terra Sci., pp. 723–732.

Sanyal, P. *et al.* (2010) 'Intensification of monsoon, microclimate and asynchronous C4 appearance: Isotopic evidence from the Indian Siwalik sediments', *Palaeogeography, Palaeoclimatology, Palaeoecology*. Elsevier B.V., 296(1–2), pp. 165–173. doi: 10.1016/j.palaeo.2010.07.003.

Sastri, V. *et al.* (1971) 'Tectonic framework and subsurface stratigraphy of the Ganga basin', *Journal of the Geological Society of India*, 12, pp. 222–233.

Stöcklin, J. (1980) *Geology of Nepal and its regional frame, Journal of the Geological Society*. Geological Society of London. doi: 10.1144/gsjgs.137.1.0001.

Thiede, R. C. *et al.* (2004) 'Climatic control on rapid exhumation along the Southern Himalayan Front', *Earth and Planetary Science Letters*, 222(3–4), pp. 791–806. doi: 10.1016/j.epsl.2004.03.015.

Tokuoka, T. *et al.* (1986) 'The Churia (Siwalik) Group of the Arung Khola area, west central Nepal', *Memoirs of the Faculty of Science, Shimane University*, 20, pp. 135–210.

Upreti, B. N. (1996) 'Stratigraphy of the western Nepal Lesser Himalaya', *Journal of the Nepal Geological Society*, 13, pp. 11–28.

Walters, J. B. and Kohn, M. J. (2017) 'Protracted thrusting followed by late rapid cooling of the Greater Himalayan Sequence, Annapurna Himalaya, Central Nepal: Insights from titanite petrochronology', *Journal of Metamorphic Geology*, 35(8), pp. 897–917. doi: 10.1111/jmg.12260.

Whipp, D. M. *et al.* (2007) 'Plio-Quaternary exhumation history of the central Nepalese Himalaya: 2. Thermokinematic and thermochronometer age prediction model', *Tectonics*, 26(3). doi: 10.1029/2006TC001991.

Whipple, K. X. (2009) 'The influence of climate on the tectonic evolution of mountain belts', *Nature Geoscience*, 2(2), pp. 97–104. doi: 10.1038/ngeo413.

Whipple, K. X. *et al.* (2016) 'Active shortening within the Himalayan orogenic wedge implied by the 2015 Gorkha earthquake', *Nature Geoscience*, 9(9), pp. 711–716. doi: 10.1038/ngeo2797.

Willett, S. D. (1999) 'Orogeny and orography: The effects of erosion on the structure of mountain belts', *Journal of Geophysical Research: Solid Earth*, 104(B12), pp. 28957–28981. doi: 10.1029/1999jb900248.

Willett, S. D. and Brandon, M. T. (2002) 'On steady states in mountain belts', *Geology*, 30(2), pp. 175–178. doi: 10.1130/0091-7613(2002)030<0175:OSSIMB>2.0.CO;2.

Wobus, C. *et al.* (2005) 'Active out-of-sequence thrust faulting in the central Nepalese Himalaya', *Nature*, 434(7036), pp. 1008–1011. doi: 10.1038/nature03499.

Wobus, C. W., Hodges, K. V. and Whipple, K. X. (2003) 'Has focused denudation sustained active thrusting at the Himalayan topographic front?', *Geology*, 31(10), p. 861. doi: 10.1130/G19730.1.

Wobus, C. W., Whipple, K. X. and Hodges, K. V. (2006) 'Neotectonics of the central Nepalese Himalaya: Constraints from geomorphology, detrital 40 Ar/ 39 Ar thermochronology,

and thermal modeling', *Tectonics*, 25(4), p. n/a-n/a. doi: 10.1029/2005TC001935.

Zhang, J. and Guo, L. (2007) 'Structure and geochronology of the southern Xainza-Dinggye rift and its relationship to the south Tibetan detachment system', *Journal of Asian Earth Sciences*, 29(5–6), pp. 722–736. doi: 10.1016/j.jseaes.2006.05.003.

Zhou, P., Carter, A. and Clift, P. D. (2019) 'Slowing rates of regional exhumation in the western Himalaya: fission track evidence from the Indus Fan', *Geological Magazine*.

Ziesch, J., Tanner, D. C. and Krawczyk, C. M. (2014) 'Strain associated with the fault-parallel flow algorithm during kinematic fault displacement', *Mathematical Geosciences*, 46(1), pp. 59–73. doi: 10.1007/s11004-013-9464-3.

4.0 Assessing the geometry of the Main Himalayan thrust in central Nepal: Insights from thermokinematic modeling

4.1 Introduction

In 2015, the Gorkha EQ occurred on the Main Himalayan thrust (MHT) in central Nepal (Avouac *et al.*, 2015; USGS, 2015; Yagi and Okuwaki, 2015), the primary décollement accommodating the convergence between India and Asia at ~20 mm/yr. (Bilham *et al.*, 1997; Lavé and Avouac, 2000; Jouanne *et al.*, 2004; Bettinelli *et al.*, 2006; Ader *et al.*, 2012). Geodetic and seismic studies of the MHT prior to the EQ suggest that it was uniformly locked along its length (Ader *et al.*, 2012; Stevens and Avouac, 2015), implying that any EQ ruptures occurring on it should be able to easily propagate in any direction. However, the Gorkha EQ rupture was limited to a 150 km-long, ~50 km-wide segment of the MHT, propagating exclusively eastwards from its epicenter (Avouac *et al.*, 2015; Grandin *et al.*, 2015). Notably, this segment was located within the zone affected by the 1833 EQ (Mw 7.3), and appears to share its western extent (Mugnier *et al.*, 2013, 2017). This raises the question, is there a change in the geometry of the MHT that inhibited the propagation of these ruptures towards the west? Since the magnitude of energy released by an EQ is directly proportional to the area of the rupture (Scholz, 1998), the locations of these barriers to the propagation of EQ ruptures, and the isolated zones of slip that they delineate, can provide insight into the amount of energy that can potentially be released in future Himalayan earthquakes.

Following the Gorkha EQ, models for the geometry of the MHT were proposed as a mechanism to explain the eastern and western boundaries of the rupture (Hubbard *et al.*, 2016; Mugnier *et al.*, 2017). Mugnier et al. (2017) suggested that the boundaries are the result of lateral

ramps in the MHT, formed due to offsets in the pre-Himalayan basement that lowered the depth of the décollement in the region of the rupture. These proposed deep-seated structures are thought to be expressed at the surface as lineaments formed by aligned offsets of lithologic boundaries and topographic features. (e.g. the Judi and Gaurishankar lineaments (Kayal, 2009; Mugnier *et al.*, 2011). Hubbard et al. (2016) suggested that the ruptured MHT surface in central Nepal is contained between two ramps that are separated by 50 km in the center of the ruptured patch and merge together towards both the eastern extent of the rupture and towards the Gorkha EQ epicenter in the west (Hubbard *et al.*, 2016; Qiu *et al.*, 2016). Although the details of how the MHT is compartmentalized are different, both of these models suggest that the extent of the Gorkha rupture, as well as the propagation extent of historical earthquakes were controlled by the locations of ramps in the MHT (Hubbard *et al.*, 2016; Mugnier *et al.*, 2017). Ramps in the decollement control the location and magnitude of uplift and associated erosional exhumation of rocks, exerting a first-order control on measured thermochronometers at the surface (Shi and Wang, 1987; Ruppel and Hodges, 1994; Rahn and Grasemann, 1999; Huntington *et al.*, 2007; Lock and Willett, 2008; Robert *et al.*, 2011; McQuarrie and Ehlers, 2017). Since measured thermochronological cooling ages are the result of the cumulative thermal history of rocks, from their burial to exhumation at the surface, the distribution of cooling ages at the surface can be used to identify marked changes in the MHT geometry or depth across the western boundary of the Gorkha rupture extent.

The existence of a pronounced lateral boundary to the west of the EQ epicenter is supported by both an offset in the surface trace of the Main Central thrust (MCT), as well as an offset in the distribution of young (< 5 Ma) Muscovite $^{40}Ar/^{39}Ar$ (MAr) ages. New mapping in the Daraundi valley, proximal to the proposed Judi lineament (Kayal, 2009; Mugnier *et al.*, 2017), shows that the traces of the MCT and RMT step ~30 km southwards from their locations to the east (Budhi

Gandaki valley) (Figure 4.1). Intriguingly, there is a marked southward step in the distribution of young MAr ages in the region, closely following the mapped expression of the MCT (Figure 4.2A). In contrast, the distributions of Zircon (U-Th)/He (ZHe) and Apatite Fission Track (AFT) ages show a much more linear distribution of ages across central Nepal (Figures 4.2B, 4.2C). There are two main ways in which these offset features may have formed: (i) a lateral ramp in the modern MHT (e.g., Hubbard et al., 2016; Mugnier et al., 2017), or (ii) a change in the cumulative history of uplift and exhumation experienced by the rocks being translated over the MHT. For the first of these options to be true, we would expect the modern MHT ramp to exhibit a similar southward offset. This offset in the ramp of the MHT would allow the Greater Himalayan sequence (GH) to be exposed farther to the south and advect cooling ages towards the south. The second option requires that the difference in mapped lithology and cooling ages seen at the surface is the result of one or more changes in the geometry of the MHT in the past and the resulting thermal history of the rocks it carries. Lateral changes in the geometry of deformation and exhumation in the past do not require any lateral variations in the geometry of the modern MHT to explain the southward step in the GH rocks, or the young MAr cooling ages.

In this paper, we use the relationship between the location of ramps and cooling ages to assess the modern geometry of the Main Himalayan thrust in central Nepal and test these two hypotheses; 1) the MHT changes laterally from east to west, or 2) the changes that we see at the surface are due to changes in the geometry of the MHT in the past. We present a new balanced cross-section, and detailed kinematic model through the Daraundi valley of central Nepal, intersecting the southward step in the surface trace of the MCT. We combine this new section with cross-sections from the Marsyangdi and BG valleys to assess the geometry of the modern MHT across western portion of the Gorkha earthquake rupture. Combining the sequential kinematics

from each of these three sections with a thermokinematic model (PECUBE) allows us to reproduce the exhumation and cooling histories for the rocks exposed at the surface and predict the resulting cooling ages. We constrain the models by comparing these predicted cooling ages to measured ones from the region, allowing us to invalidate and discard models that do not reproduce the distribution of cooling ages. This approach allows us to disentangle the effects of changes in the modern décollement from the effects of changes in the upper plate history on the surface geology and thermochronology and highlight which of these changes are required to match the pronounced lateral variations at the surface.

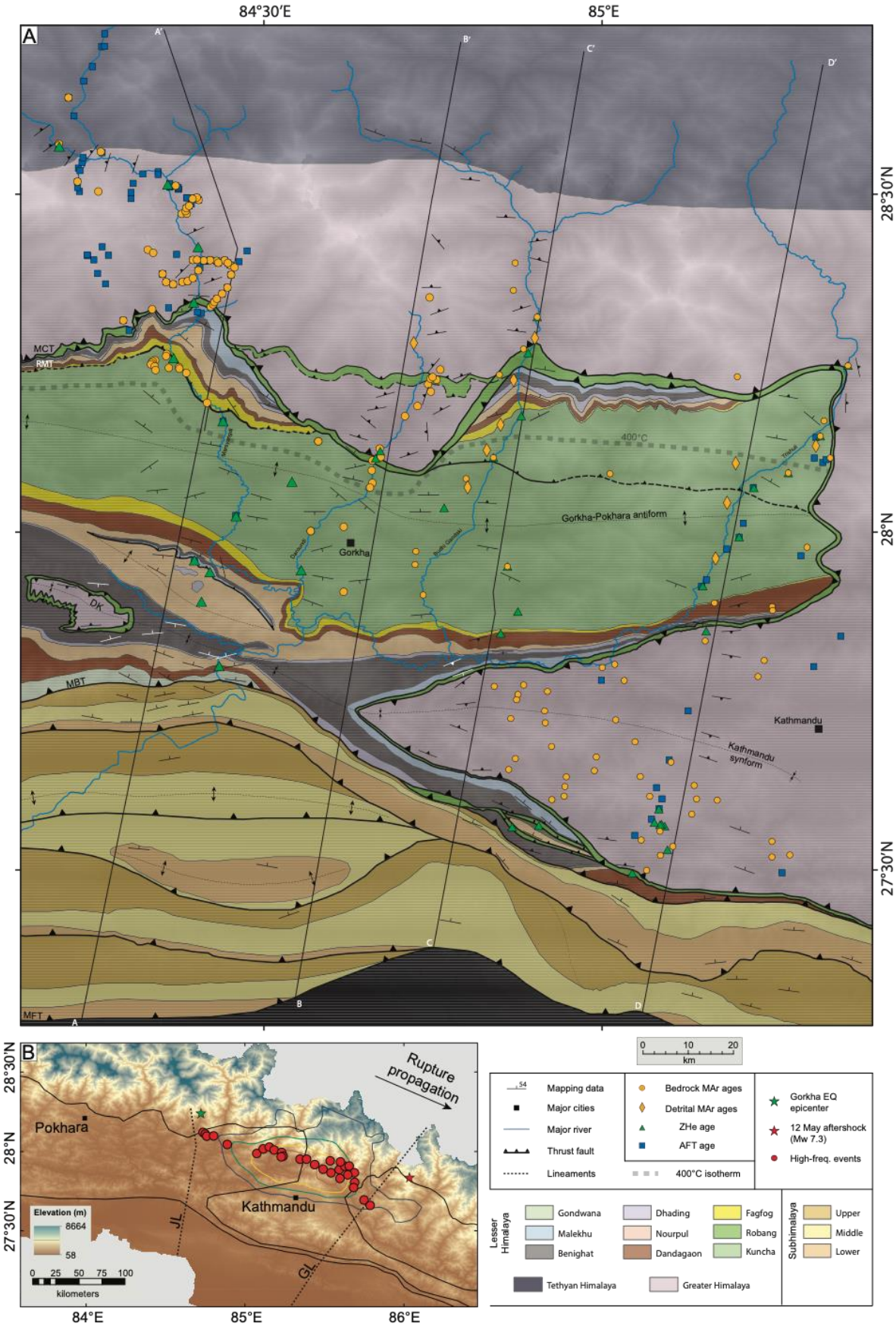
84°30′E
85°E
28°30′N
28°N
27°30′N
A
A′
B′
C′
D′
MCT
RMT
400°C
Gorkha-Pokhara antiform
Gorkha
DK
MBT
Kathmandu
Kathmandu synform
MFT
B
Rupture propagation
Pokhara
Kathmandu
JL
GL
Elevation (m)
8664
58
0 25 50 75 100
kilometers
84°E
85°E
86°E
0 10 20
km
Mapping data
Major cities
Major river
Thrust fault
Lineaments
Bedrock MAr ages
Detrital MAr ages
ZHe age
AFT age
400°C isotherm
Gorkha EQ epicenter
12 May aftershock (Mw 7.3)
High-freq. events
Lesser Himalaya
Gondwana
Malekhu
Benighat
Dhading
Nourpul
Dandagaon
Fagfog
Robang
Kuncha
Subhimalaya
Upper
Middle
Lower
Tethyan Himalaya
Greater Himalaya

Figure 4.1: Geologic map of central Nepal.

(A) Detailed geologic map of central Nepal, showing the distribution of measured MAr, ZHe, ZFT and AFT thermochronological ages. Geology shown is based on new mapping in the region, combined with past mapping from Kimura (1999), Cross III (2014), Khanal (2014), Dhital (2015), Lavé and Avouac (2000), Pearson (2002), Khanal and Robinson (2013), Olree (2018) and Larson et al. (2010). Inset map shows location of Panel A in Nepal. (B) Regional elevation map with the complete rupture length of the earthquake delineated by red circles moving from west to east (Avouac et al., 2015) (propagation direction indicated by black arrow), relative to a generalized surface trace of the Main Central Thrust (MCT). Slip distance (m) is shown in colored contours (Avouac et al., 2015). The EQ epicenter is marked by a green star, while the major Mw 7.3 aftershock (May 23rd) is indicated by a red star.

4.2 Geologic setting

4.2.1 Tectonostratigraphy of the Daraundi valley

4.2.1.1 Subhimalayas

The Subhimalaya are made up of foreland basin sediments eroded from the rising Himalayas in the north, deposited as the Siwalik Group (Gansser, 1964; Tokuoka *et al.*, 1986; Harrison *et al.*, 1993; Quade *et al.*, 1995; Burbank, Beck and Mulder, 1996; DeCelles *et al.*, 1998; Gautam and Rösler, 1999; Ojha *et al.*, 2000, 2009). The Siwalik Group coarsens upwards from the siltstones and mudstones at the bottom to sandstones and conglomerates at the top, and are informally divided into three members, the lower, middle and upper (Tokuoka *et al.*, 1986; Harrison *et al.*, 1993; Quade *et al.*, 1995; Ojha *et al.*, 2009). In central Nepal, all three members are exposed at the surface with a total measured thickness of ~5 km (Tokuoka *et al.*, 1986; Harrison *et al.*, 1993) (Figure 4.1). In the south, the Siwaliks are bound by the Main Frontal thrust (MFT),

which is the present surface expression of the MHT, and to the north by the Main Boundary thrust (MBT).

4.2.1.2 Lesser Himalayas

In central Nepal, the Lesser Himalaya (LH) is made up of eight mappable formations, which can be divided into Paleoproterozoic lower, and Mesoproterozoic upper units, with a total thickness of ~8 – 13 km (Sakai, 1983; Harutaka Sakai, 1985; Upreti, 1996; Khanal and Robinson, 2013; Robinson *et al.*, 2021). The lower LH is made up of two distinct units, the Kuncha and Robang formations, both of which have been metamorphosed to greenschist (south) and amphibolite (north) facies (Martin *et al.*, 2011). The basal Kuncha formation is made up of grey-green quartz- and chlorite-rich phyllite, green quarzitic schist, and micaceous quartzite, forming a layer ~3 – 3.6 km thick. Detrital zircons place the maximum depositional age of the Kuncha Formation at ~1900 Ma (Martin *et al.*, 2011). The Robang formation was deposited at some point prior to 1850 Ma and is interpreted as an older and more distal facies of the Kuncha (Martin *et al.*, 2011). It is made up of chloritic schist, often interbedded with a distinctive, white-light green quartzite known as the Dunga quartzite. The base of the Robang is interpreted in central Nepal as the Ramgarh-Munsiari thrust (RMT) (Pearson and DeCelles, 2005; Robinson and Pearson, 2013). The Kuncha Formation is exposed in a broad antiform between the RMT and MCT in the north and the MBT in the south. On the southern limb of the antiform, the Kuncha formation is overlain by a full section of upper LH stratigraphy composed of six Paleoproterozoic – Mesoproterozoic units: the Fagfog, Dandagaon, Nourpul, Dhading, Benighat, and Malekhu formations (Upreti, 1996; Martin *et al.*, 2011) (Figure 4.1). The Fagfog formation, a thin (~300 m) unit made up of a tan/white, coarse- to fine-grained quartzite, with individual beds often separated by green, chloritic phyllite has a maximum depositional age of ~1770 Ma (Martin *et al.*, 2011), and is mapped

uncomformably over the Kuncha Formation. Overlying the Fagfog, the ~650 m thick Dandagaon formation is primarily made up of dark brown to grey-green phyllite interbedded with thin beds of slate and dolomite. The ~450 m thick Nourpul formation is primarily made up of thinly bedded variegated quartzite (pink, purple, green and white) interbedded with blue-grey dolomite, and dark purple and green phyllite, with a silicic dolostone dominating the upper portion of the unit (Pearson, 2002; Olree, 2018). Detrital zircon measurements suggest a maximum depositional age for the Nourpul at ~1750 Ma (Cross III, 2014). The ~150 m thick Dhading formation is made up of massive blue-grey dolomite, with a distinctive 'butcher-block' weathering pattern. The contact between the Dhading and the Benighat formations is abrupt, with the dolomite changing into dull, dark grey-black slate and thin limestone beds. In the Daraundi transect, the Benighat has a measured thickness of ~1 km. The ~500 m thick Malekhu formation lies conformably on top of the Benighat and consists of blue-grey limestone and dolostone, interbedded with grey-black and brown phyllite. It is proposed to have been deposited prior to ~1300 Ma (Martin *et al.*, 2011).

4.2.2 Greater Himalayas

In central Nepal, the metasedimentary GH sequence is mapped as being between ~15 – 23 km thick and metamorphosed to the amphibolite – granulite grade (Colchen, Le Fort and Pecher, 1986; Coleman, 1996; Kohn, 2008; Corrie and Kohn, 2011; Ghoshal *et al.*, 2020, 2021). In the neighboring Marsyangdi valley, the GH sequence has been dated to between 1000 – 600 Ma, with early Paleozoic granitic intrusions (Martin *et al.*, 2005; Gehrels *et al.*, 2011). The base of the GH is defined as the Main Central thrust, which places the GH onto the rocks of the LH. In the Daraundi valley, the upper portion of the GH sequence is made up of high-grade, diopside-bearing calc-silicate schist, below which are granitic orthogneisses that are also mapped in the Budhi

Gandaki valley (Larson, Godin and Price, 2010). Below the orthogneisses are sillimanite-bearing paragneisses, and quartzite intercalated with pelitic gneiss (Colchen, Le Fort and Pecher, 1986; Kohn *et al.*, 2001; Larson, Godin and Price, 2010). Below these quartzites, we mapped interlayered biotite schist, biotite-rich quartzite and a two mica (biotite, muscovite) orthogneiss with feldspar augen, along with a flat-lying sequence of calc-silicate and marble. Within the immediate hanging wall of the MCT, we also noted the presence of polymineralic leucosomes (i.e., partial melt textures) in the biotite schist, indicating temperatures high enough to produce melt, and supporting the southern location of the MCT.

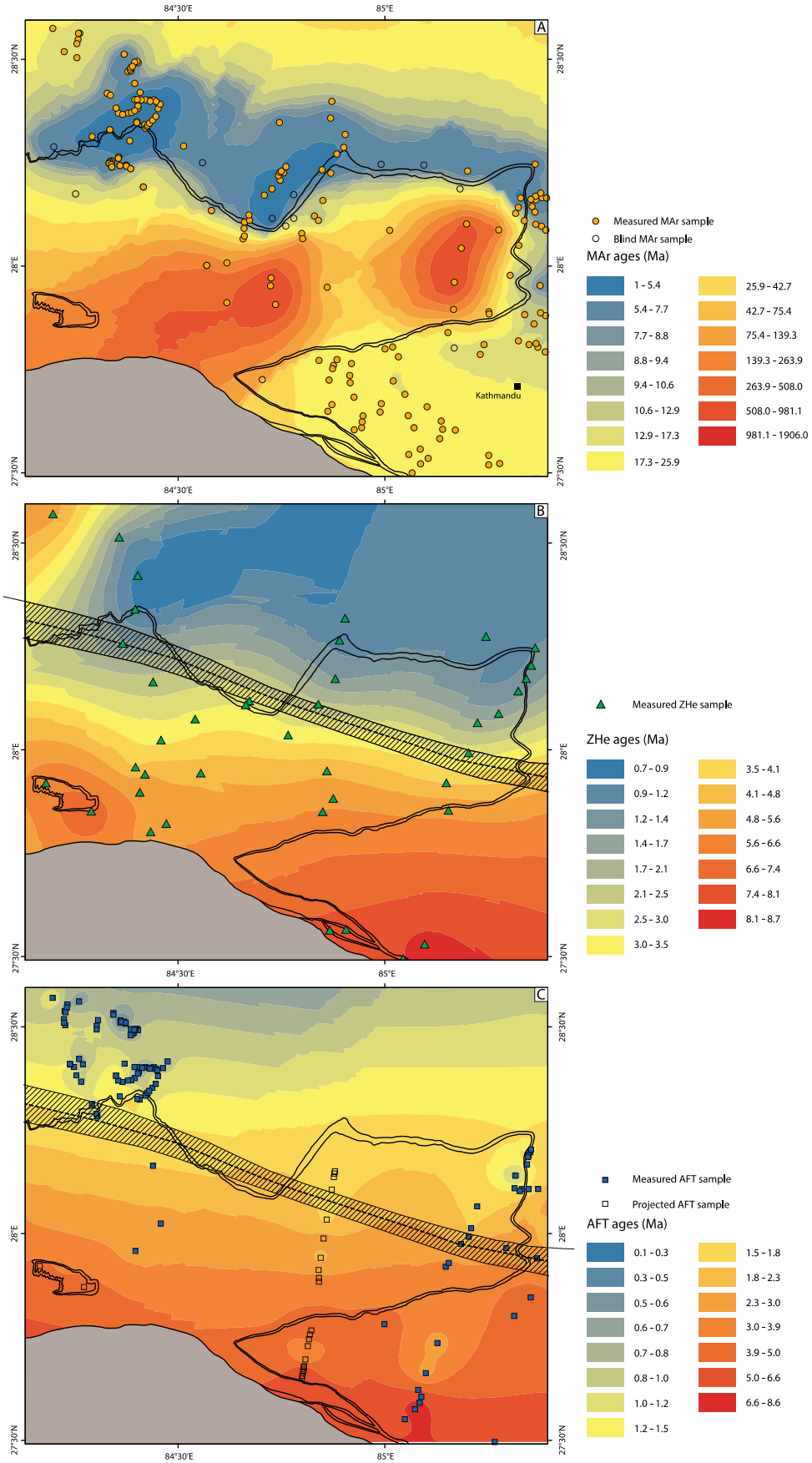
A
84°30'E
85°E
28°30'N
28°E
27°30'N
Kathmandu
Measured MAr sample
Blind MAr sample
MAr ages (Ma)
1 - 5.4
5.4 - 7.7
7.7 - 8.8
8.8 - 9.4
9.4 - 10.6
10.6 - 12.9
12.9 - 17.3
17.3 - 25.9
25.9 - 42.7
42.7 - 75.4
75.4 - 139.3
139.3 - 263.9
263.9 - 508.0
508.0 - 981.1
981.1 - 1906.0
B
Measured ZHe sample
ZHe ages (Ma)
0.7 - 0.9
0.9 - 1.2
1.2 - 1.4
1.4 - 1.7
1.7 - 2.1
2.1 - 2.5
2.5 - 3.0
3.0 - 3.5
3.5 - 4.1
4.1 - 4.8
4.8 - 5.6
5.6 - 6.6
6.6 - 7.4
7.4 - 8.1
8.1 - 8.7
C
Measured AFT sample
Projected AFT sample
AFT ages (Ma)
0.1 - 0.3
0.3 - 0.5
0.5 - 0.6
0.6 - 0.7
0.7 - 0.8
0.8 - 1.0
1.0 - 1.2
1.2 - 1.5
1.5 - 1.8
1.8 - 2.3
2.3 - 3.0
3.0 - 3.9
3.9 - 5.0
5.0 - 6.6
6.6 - 8.6

Figure 4.2: Predictive cooling age maps of central Nepal.

(A) MAr, (B) ZHe, (C) AFT. Interpolations use a kriging process that produces a narrower contour interval where data density is high and age variation is small.

4.3 Thermochronology

In this paper, we have compiled a dataset of 148 MAr (135 bedrock and 13 detrital) ages, 39 ZHe ages, and 83 AFT ages collected from the Marsyangdi, Daraundi, Budhi Gandaki and Trishuli valleys of central Nepal (see Appendices B, C, D, and E for complete list). To this existing dataset of cooling ages, we add two new ZHe ages, collected from the Daraundi valley, with one collected from the GH (CN16 - 162), and the other from the Robang (CN16 - 168). These analyses were performed at the University of Arizona Radiogenic Helium Dating Laboratory (Schmitz and Bowring, 2001; Reiners *et al.*, 2004; Hourigan, Reiners and Brandon, 2005; Reiners, 2005; Renne *et al.*, 2005; Kuiper *et al.*, 2008). The sample collected from the GH is located ~90 km from the MFT, and is dated to 3.18 ± 0.5 Ma, while the sample collected from the Robang is located immediately to south (~87 km from the MFT), with an age of 2.94 ± 0.1 Ma. In addition to these bedrock ages, we also include a group of ten detrital MAr ages collected from modern river sediments in tributaries to the Budhi Gandaki, Trishuli and Daraundi rivers (Figure 4.1; yellow diamonds). The uncertainties in the MAr and AFT ages are represented by 2σ analytical errors, with those AFT ages that were initially reported with 1σ errors shown here as 2σ to maintain consistency. We present the ZHe ages as a mean calculated from the spread of the ages for individual grains (typically three), and their respective 2σ analytical errors.

4.3.1 Spatial distribution of cooling ages

To highlight the first-order distribution of cooling ages in the region, we applied an Empirical Bayesian kriging approach to each dataset (Figure 4.2). The resulting distributions are binned and contoured such that the intervals are narrowest between samples that are similar in age, and spatially closer to each other. The measured MAr ages in central Nepal are the most numerous and are spatially well distributed, primarily clustered within the rocks of the GH (i.e., the northern Marsyangdi and Daraundi valleys, and the Kathmandu synform). While there are significantly fewer measured ZHe ages in central Nepal, the ones that exist are well distributed along the four river valleys. The AFT ages in the central Nepal are the least well-distributed of the thermochronometers systems, with a significant majority clustered to the north of the MCT in the Marsyangdi, distributed along the Trisuli river valley and across the Kathmandu Syncline (Figure 4.1, 4.2). The low spatial resolution of the AFT ages in central Nepal biases a kriged contour map. Due to the along-strike similarities between the Budhi Gandaki and Trisuli regions, and measured MAr and ZHe ages, we increase the resolution of the data by projected distribution of AFT ages along the Budhi Gandaki transect (e.g., Ghoshal et al., 2020) and use these projected ages in the calculation of the kriging contours (Figure 4.2C – open squares).

4.3.2 Thermochronology of the Daraundi valley

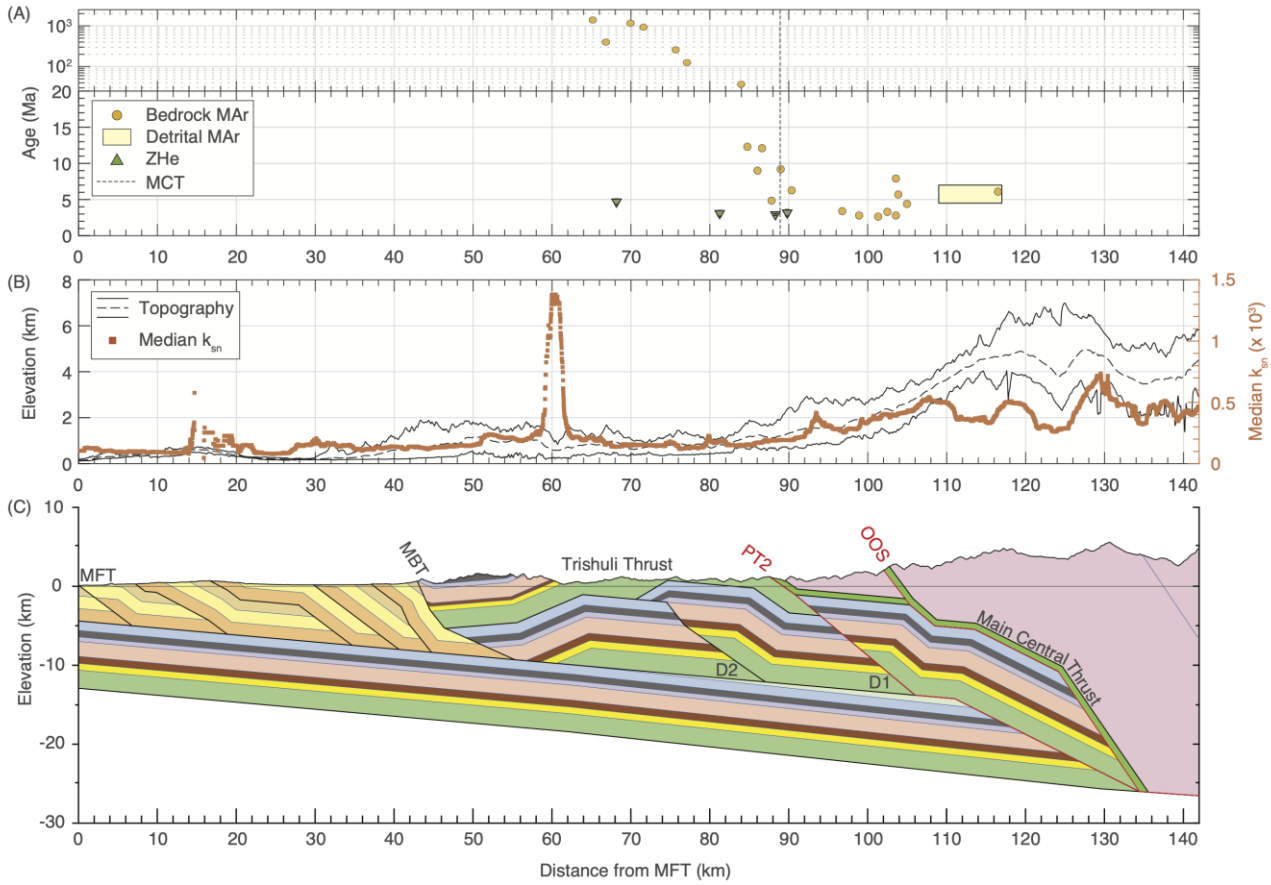

Figure 4.3: Plots of projected data along the Daraundi transect.

(A) Combined measured MAr (yellow) and ZHe (green, downward-pointing triangles) thermochronometer data plotted along the Daraundi section line. The location of the MCT is marked by a black, dashed line, while the origin is the location of the MFT. (B) Max, min, and mean swath topography along the Daraundi cross-section line. The mean topography is shown as a dashed, black line. Median k_{sn} values calculated along the swath are shown in orange. (C) Balanced cross-section along the Daraundi transect. Locations of major OOS thrusts are marked in red. There is no vertical exaggeration on the figure, and the topography shown is the mean topographic profile for the transect.

We constrain our cross-section along the Daraundi valley with a smaller subset (22 MAr and four ZHe) of cooling ages that are within ~15 km of the cross-section, to eliminate the effect of lateral structures. These cooling ages were then projected onto the cross-section line along-

strike, maintaining their relative structural positions (Figure 4.3A), and plotted with respect to their distance from the trace of the MFT. In order to add more constraints to our model, we show the age distribution found within the drainage basin for a detrital MAr sample collected from the headwaters of the Daraundi river (S40; Brewer et al., 2006). We also include three detrital samples collected from the Kuncha formation, which show the distribution of unreset ages of rocks above the Gorkha-Pokhara antiform. The bedrock MAr ages in the Daraundi valley range between very young (2.64 Ma) to unreset (398 Ma), with the majority of reset ages located north of the MCT (89 km from the MFT), with the youngest cluster of ages located between 98 – 104 km from the MFT. The northernmost measured MAr age (dated to ~6.5 Ma) is located 117 km from the MFT. This sample is located within the range of ages sampled from a detrital sample collected at a similar location within the headwaters of the Daraundi valley. Projected onto the section, the drainage basin for these detrital ages extends from 109 km to 117 km, with a 2σ range of ages between 4.5 – 7 Ma. There are three unreset/partially reset bedrock MAr ages, all of which have been collected from south of the MCT. The southernmost age, dated to 398 Ma, is located 66 km from the MFT. Farther north, the ages are dated to 257 Ma, and 125 Ma, respectively. These ages are located ~75 km and 77 km from the MFT, respectively. Finally, the four measured ZHe ages in the transect range between 2.5 – 4.9 Ma, extending 68 – 90 km from the MFT. The youngest ZHe age (~2.5 Ma) is located to the north of the MCT (88.5 km from the MFT).

4.4 Methods

4.4.1 Balanced cross-section

We present a new balanced cross-section along the Daraundi valley, using newly acquired mapping (Section 4.5.1), integrated with existing published mapping (Colchen, Le Fort and Pecher, 1986; Catlos *et al.*, 2001; Larson, Godin and Price, 2010). Measured map orientations were projected onto the line of section, maintaining their structural position, and used to limit permissible geometries. The line lengths of each of the units in the deformed section were measured and balanced in the restored section (Figure 4.9). Small-scale internal deformation (brittle or ductile) within the units is not accounted for in our modeling.

The base of the cross-section is defined by the MHT, and is divided into three parts: the ramp of the MFT, a mid-crustal ramp and a broad flat in between (Pandey *et al.*, 1995; Lavé and Avouac, 2001). The height of the MFT ramp is primarily defined by the thickness and orientation of the exposed Siwaliks at the surface. In addition, extrapolating the depth and dip of the base of the Siwalik Group measured at the Raxaul drill-hole (located to the southeast) provides an additional constraint for the ~5 km depth. Inversion of seismic data from the Gorkha EQ provides a narrow range of permissible angles for the MHT flat (4° – 8°) (Avouac *et al.*, 2015; Elliott *et al.*, 2016; Whipple *et al.*, 2016). To construct our cross-section, we explored décollement angles within this range to find the one that fits the geophysical constraints, the required thickness of LH units mapped at the surface and viable repetition of units between the surface geology and décollement. Finally, thermokinematic modeling (Lock and Willett, 2008; McQuarrie and Ehlers, 2015; McQuarrie *et al.*, 2019; Ghoshal *et al.*, 2020) shows predictive relationships between the location of ramps and the resulting pattern of predicted cooling ages. Producing young, reset higher

temperature thermochronometers (e.g., MAr) requires the overlying rocks to be completely translated over a mid-crustal ramp. Therefore, the top of the ramp must be located to the north of the youngest reset ages (Ghoshal *et al.*, 2020). However, due to a lack of measured thermochronometer ages in the north of the Daraundi valley, we tested a variety of different geometries and locations of the ramp and identified a solution that best matches the distribution of all the available cooling ages.

4.4.2 Kinematic and flexural modeling

Our restored cross-section was kinematically and flexurally forward modeled using the structural modeling software, Move 2019.1 (Midland Valley/Petex). The kinematic model is divided into displacement increments of ~10 km and modeled using the fault-parallel flow algorithm. Each of these kinematic increments were followed by flexural loading and erosional unloading. The magnitude of flexural loading for each step is calculated using the difference between the deformed topography resulting from each ~10 km increment of displacement, and the estimated topography from the previous step. We use a 'responsive topography' method to calculate the amount of erosion at each step, where the new eroded topography is defined by a taper angle (2°) that increases in elevation towards the north (McQuarrie and Ehlers, 2015; Gilmore *et al.*, 2018). This angle is based on the taper angle of modern topography in central Nepal and accommodates erosion where active uplift has exceeded the 2° slope. In locations where no uplift has occurred, the new topography follows the existing, isostatically-loaded topography. The initial topography for the model is represented by a steady increase (2°) in elevation towards the north, reaching a maximum elevation of 5 km above the southern limit of the GH. This simplified

topography reproduces the elevation of the Tibetan Plateau, which is thought to have reached its modern elevation by the late Oligocene (DeCelles *et al.*, 2007).

Prior to any deformation in our models, we use our best-fit estimate for the initial geometry of the Indian margin to define the original dip of the décollement. We use an angle of 1.5° as this original sedimentary taper, applied from the foreland to the northern extent of the model. This angle allows us to reproduce the ~15 km section of Tethyan rocks exposed in southern Tibet (Brookfield, 1993; Ratschbacher *et al.*, 1994; Zhang and Guo, 2007), and facilitates the burial of the initial base of the GH section to ~45 km in order to match measured values of peak pressure and temperature (Catlos *et al.*, 2001, 2018; Kohn *et al.*, 2001, 2004; Kohn, 2008). The building of topography and subsequent erosion occurring at each increment in the models flexurally steepens the décollement and increases the depth of the foreland basin. The final dip and depth of the décollement is dependent upon three parameters (i.e., effective elastic thickness, crustal density, and the initial dip of the decollement) that are systematically varied until the surface geology and expected foreland basin depth is replicated. The best-fit values for these parameters are listed in Table 4.1.

The kinematic and flexural forward model is tracked using a 2D grid of points with a resolution of 0.5 km that is deformed sequentially at each increment. Assigning an age to each step of the model converts the displacement field into a velocity field, which is then input into a modified version of PECUBE. While we initially test the model with a constant rate of shortening (20 mm/yr.), varying the ages at which faults are initiated allows us to assign variable rates of thrusting, and quantify their effects on the predicted cooling ages. We show the results for the best-fit velocity profile, which is consistent with the velocities identified for the kinematic models along the Budhi Gandaki, and Marsyangdi transects (Ghoshal *et al.*, 2020, 2021).

Parameter	Input/Best-fit value
Initial dip of décollement	1.5°
Material properties	
Effective elastic thickness	70 km
Crustal density	2950 kg m^{-3}
Mantle density	3300 kg m^{-3}
Specific heat capacity	800 J kg^{-1} K
Crustal volumetric heat production	2.35 μW m^{-3}
e-folding depth	20 km
Thermal conductivity	2.5 W m^{-1} K
Numerical properties	
Temperature at base of model	1300°C
Model thickness	110 km
Surface temperature	20°C
Atmospheric lapse rate	7°C km^{-1}
Kinematic grid spacing	0.5 km
Horizontal node spacing	0.5 km
Vertical node spacing	1 km
Model domain	1000 km x 110 km x 5 km
Model start time	500 Ma

Table 4.1: Mechanical and thermal parameters for PECUBE

4.4.3 Thermokinematic modeling

PECUBE solves the three-dimensional heat transport equation to simulate the evolution of a transient thermal field (defined by input thermal parameters for the crust) as it is affected by the imported velocity grids and erosion at the topographic surface, calculating time-temperature (t-T)

paths for the rocks at the surface. Age-prediction algorithms use these t-T paths to predict the surface cooling ages for each of the tracked points at the surface (Braun, 2003; Ehlers *et al.*, 2005). Instead of estimated closure temperatures, PECUBE calculates closure temperature for each system based on the rate of cooling, and published models for mineral kinetics. The MAr kinetics are based on the thermally-activated diffusion model as set out in Dodson (1973), using the parameters defined in Hames and Bowring (1994) for cylindrical geometries (Hodges, 2014). The ZHe kinetic model is defined in Reiners et al. (2004), while the AFT ages are calculated using the Durango apatite parameters given in Crowley et al. (1991).

Prior to the start of deformation, PECUBE simulates the thermal state of the crust using the input values of heat flow from the mantle, and the material properties of the crust (thermal conductivity, density, heat capacity, and radiogenic heat production). The amount of heat generated in the crust is determined by a surface heat production value (A_0), which is applied over a distance known as the 'e-folding depth', over which the heat production decays exponentially to 1/e of the assigned surface value (McQuarrie and Ehlers, 2017). Using an e-folding depth allows us to match both the non-linear decline of heat production in the crust with depth (Ketcham, 1996; Menon *et al.*, 2003; Brady *et al.*, 2006) and measured heat production values for the Himalayas (England *et al.*, 1992; Whipp *et al.*, 2007), while also avoiding the formation of partial melt in the middle and lower crust. The values of thermal conductivity and heat capacity used in our models are consistent with measured values from the Himalayas (Ehlers, 2005; Ray, Bhattacharya and Roy, 2007; Whipp *et al.*, 2007). Finally, these crustal properties (e.g., heat production, thermal conductivity, and thermal capacity) are not advected by the imposed displacement fields, remaining static throughout the simulations. The best-fit parameters used to set up the thermal model in PECUBE are listed in Table 4.1.

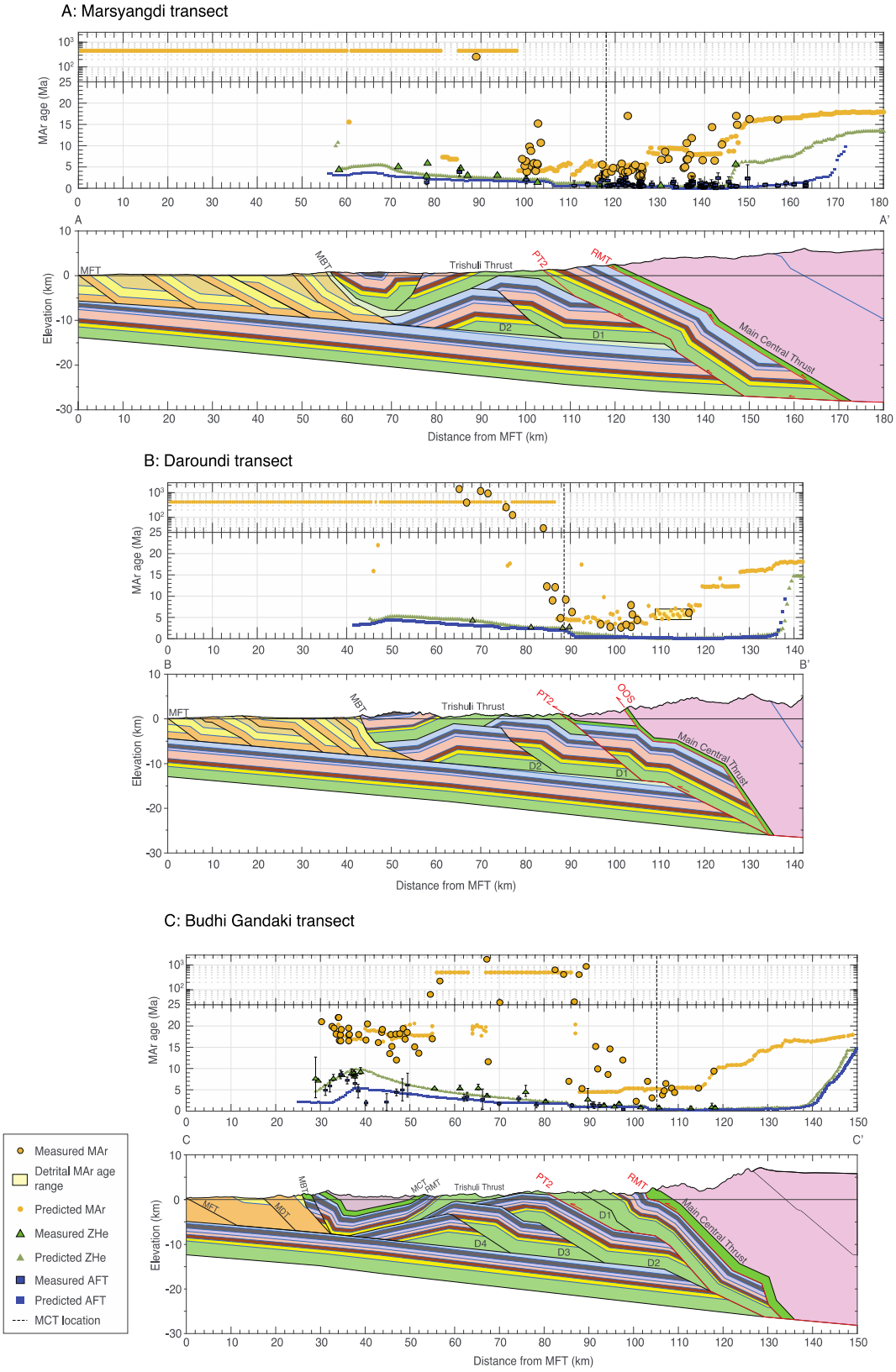

Figure 4.4: Plots comparing best-fit predicted cooling ages to measured data.

(A) Marsyangdi transect; (B) Daraundi transect; and (C) Budhi Gandaki transect. MAr: Yellow; ZHe: Green; AFT: Blue.

4.5 Results

4.5.1 Along-strike variations in surface geology

Fieldwork along the Daraundi valley reveals a marked change in the latitude of the Main Central thrust (MCT) between the Daraundi and Budhi Gandaki river valleys. In the Budhi Gandaki and Marsyangdi valleys, mapping shows that the RMT and MCT thrust sheets are located on top of the entire upper LH sequence, which in turn rests on top of the lower LH Kuncha formation (Khanal and Robinson, 2013; Ghoshal *et al.*, 2020, 2021) (Figure 4.1). However, new mapping in the Daraundi valley diverges from this. The visually distinct chlorite-garnet-rich schists and white quartzites of the Paleoproterozoic (DeCelles et al., 2000) Robang formation (Pearson and DeCelles, 2005) are located structurally above Kuncha Fm, separated by the RMT. North of the Robang, we observed interlayered biotite schist, biotite rich quartzite and a two mica (biotite, muscovite) orthogneiss with feldspar augen. Traces of partial melt can be found within the biotite schist, located approximately 800 m to the north of the Robang, suggesting that this is within the hanging wall of the MCT. This new location of the MCT is ~30 km farther south than that mapped in the Budhi Gandaki and Marsyangdi valleys (Ghoshal et al., 2020; 2021). It is also ~10 km farther south along the Daraundi river than mapped in the past (Colchen, Le Fort and Pecher, 1986; Catlos *et al.*, 2001), coinciding with the trace of MCT – 1 from Catlos et al. (2001).

In the Marsyangdi valley to the west, out-of-sequence thrusting been proposed for the RMT – MCT zone, to explain the concentration of young, reset cooling ages north of this zone (Harrison et al., 1997; Catlos et al., 2001, 2018; Hodges et al., 2004; Huntington et al., 2006; Ghoshal et al., 2021). Integrating cross section geometry and thermokinematic modelling highlights that ~ 10 km of OOS faulting along the RMT-MCT zone is required to reproduce young AFT cooling ages in ~ 150 -160 km north of the MFT (Ghoshal et al., 2021). Faulting of this magnitude in the Marsyandi is expected to be present in the Daraundi valley as well. Approximately 10 km north of the newly mapped trace of the MCT are clean white quartzites, which were mapped by Colchen et al. (1986) as part of the LH, contiguous with the Robang Formation in the Budhi Gandaki valley (Figure 4.1; Figure 4.10). These quartzites and their along-strike extension align with the proposed OOS fault in the Marsyangdi valley and support additional OOS faulting in the RMT- MCT zone along the Budhi Gandaki valley. We suggest these quartzites are a repetition of the Robang Fm., due to an OOS thrust connecting the traces of the RMT in the Budhi Gandaki and Marsyangdi transects and closely following the trace of the Chomrong thrust (as shown in Parsons et al. 2016) (Figure 4.1). Motion on this OOS thrust is responsible for steepening the dips farther north, from horizontal to between 25° - 54°N (Figure 1). Farther north, undisputed Greater Himalayan paragneisses lie above a sequence of marble and calcsilicates (Colchen, Le Fort and Pecher, 1986; Catlos *et al.*, 2001; Larson, Godin and Price, 2010).

Since field mapping is mostly confined to the valleys, we use satellite imagery to project the surface trace of the MCT and RMT between the Budhi Gandaki and Marsyangdi valleys, and the Daraundi. We processed multiple ASTER images to highlight specific units, relying on the different reflectance of a variety of minerals in the IR region of the EM spectrum. While vegetation and snow cover complicate this analysis, we were able to identify high concentrations of chlorite

(Figure 4.10), which we interpret to be indicative of the Robang formation. Further analyzing these images in the thermal IR bands allowed us to distinguish between distinctly carbonaceous rocks and silicic rocks, highlighting the southwestern extent of the LH carbonates that have been observed in the Budhi Gandaki valley (Figure 4.10).

4.5.2 Balanced cross-section along the Daraundi valley

4.5.2.1 Structural zones

Subhimalayan faults

The MFT ramp is proposed to dip at an angle of ~30°N, with an approximate depth of 5 km. This depth and dip is consistent with mapped upper through lower Siwalik thicknesses at the MFT (Figure 4.3), and the depth of the Siwalik basement, as defined by the Raxaul drill hole (Sastri *et al.*, 1971).

Along the Daraundi transect, Siwalik units are exposed over an ~43 km distance from the Main Frontal thrust to the MBT. The area over which the Siwaliks are exposed increases systematically from the Budhi Gandaki valley to the west. This area gain is primarily a combination of two factors: (i) the MFT surfacing ~15 km farther to the south in the Daraundi valley, and ~20 km farther south in the Marsyangdi valley, respectively, and (ii) the recessional in the MBT within the Daraundi and Marsyangdi valley is ~7 km and ~10 km farther north (respectively) than in the Budhi Gandaki (Figure 1). Along the Marsyangdi and Daraundi transects, the three-part sequence of the Siwaliks goes through four asymmetric repetitions of lower to upper Siwaliks (Figure 4.1). However, in the Marsyangdi section, Ghoshal et al., 2021 found that this interpretation was inconsistent with the ~2 km thick middle Siwalik unit exposed over a ~10 km

distance between 30 – 40 km from the MFT with dips of 28°N and 30°N measured to the north and south of the unit, respectively (Figures 4.1, 4.4). They interpreted the mapped middle Siwalik unit as two separate thrust sheets, with the structurally lower sheet carrying only the lower and middle Siwalik members, and the upper sheet carrying all three members (Figure 4.4A). Along the Daraundi, the ~10 km exposure of the middle Siwaliks between 19 – 35 km from the MFT, combined with ~20°N - 25°N dips support this interpretation of five intra-Siwalik thrust sheets.

Main Boundary thrust

In the Daraundi transect, the Main Boundary thrust places the Dhading formation and the underlying rocks of the LH against the Siwaliks to the south (Figures 4.1, 4.3). In the Marsyangdi and Budhi Gandaki valleys, Siwalik rocks south of the MBT and LH rocks immediately north of the MBT dip 40° - 66° towards the north. Using the mapping in these two valleys, and published mapping from the Siwaliks of the Bagmati region (Dhital, 2015), we estimate the approximate dip of the rocks to the immediate north of the MBT to be ~45°N.

Trishuli thrust and the Gorkha-Pokhara antiform

In the hanging wall of the MBT, rocks of the Trishuli thrust sheet are deformed into a tightly folded synform, with the Benighat Formation at its core (Figure 4.1). To create the geometry of the synform in the Daraundi, we project dips measured along the Marsyangdi and Budhi Gandaki valleys along-strike on to the line of section while remaining consistent with the mapped changes in geology. Projecting these measurements onto the section suggests that the 54° – 25°N mapped dips to the west are expressed in the Daraundi section as a 25-40° dip for the southern limb of the synform. The rocks exposed in the broader northern limb of the synform dip southwards between 18° – 23°S. The northern limb of the synform exposes the Dhading and lower LH section

down to the Kuncha formation. The Kuncha formation forms the core of the Gorkha-Pokhara antiform, which is a major EW-trending antiformal structure that has been mapped across central Nepal (Figure 1). In the Daraundi valley (Section 4.5.1), and the RMT and MCT are directly on top of the Kuncha formation, with the trace of the RMT cutting across the upper LH units 9.5 km to the east and 6 km to the west of the Daraundi River (Figure 4.1). We argue that this represents a lateral ramp system that offset upper Lesser Himalayan rocks from lower Lesser Himalayan rocks (i.e., Kuncha) during the emplacement of the Ramgarh-Munsiari thrust (Figure 4.3, Figure 4.10).

Across central Nepal, the antiform is interpreted to represent a subsurface duplex (Pandey et al., 1995; Lavé and Avouac, 2001; Pearson, 2002; Avouac, 2003; Khanal and Robinson, 2013; Robinson and Martin, 2014; Hubbard et al., 2016; Ghoshal et al., 2020), whose geometry is obscured by the rocks at the surface, which are part of its roof thrust (Trishuli thrust). Along the Budhi Gandaki transect and Marsyangdi transects, sequential thermokinematic modeling of the cross section geometries shows that the duplex is comprised of hinterland-dipping horses that repeats the entire LH sequence that is then translated over the modern MHT ramp (Ghoshal et al., 2020; 2021). In both of these transects, the youngest horse of the duplex must carry rocks that are derived from the active ramp, and therefore has a thickness that corresponds to its height (Ghoshal et al., 2020; 2021). Along the Daraundi valley, the height of the modern ramp, and the architecture of the duplex are both unknown. However, the geometry of the duplex is limited by the space created between the rocks at the surface and viable décollement depths below.

The youngest MAr ages (2-3 Ma) along the Daraundi valley are located between 98 – 104 km (Figure 4.3), suggesting that the top of the modern MHT ramp must be located farther to the north. Although limited in their northern extent, an isolated MAr bedrock age of 6.1 Ma and detrital

MAr ages that range from 4.5 – 7 Ma suggest a location for the top of the ramp between 104 and 114 km from the MFT. The lack of cooling ages farther north prevents us from directly predicting the location of the bottom of the ramp, and therefore, its height. However, evaluation locations for top of the ramp between 104 and 114 km from the MFT and duplex geometries capable of filling the available space above the décollement, allows us to evaluate potential decollement and duplex geometries. The resulting duplex geometry capable of filling the available space is made up of two horses, both carrying a thickness of ~9 km of LH material (upper LH + Kuncha). Since the rocks making up the youngest horse of the duplex are derived from the active ramp, this suggests that the modern ramp is ~9 km high. Combining the estimated height of the ramp (~9 km) with reasonable angles of dip (20° – 30°N), allows us to predict a ramp width of ~20 km.

Ramgarh-Munsiari and Main Central thrust sheets

In the Daraundi valley, rocks within the RMT (i.e., Robang) dip north at ~39°, with the structurally higher GH rocks within the immediate hanging wall of the MCT similarly dipping ~40°N. However, these moderately steep dips are limited to within 3-4 km of the RMT before apparent dips becomes largely horizontal until ~100 km from the MFT. These near-horizontal dips strongly suggest a footwall flat in the décollement, as well as within the underlying LH stratigraphy. North of 100 km, we interpret the repetition of a clean, white quartzite (Colchen, Le Fort and Pecher, 1986), and a change to steeper dips as indicating a structural repetition of the RMT and MCT by a steeply-dipping OOS thrust similar to that proposed for the Marsyangdi valley (Ghoshal *et al.*, 2021). Finally, rocks in the upper Daraundi valley (> 130 km from the MFT) become significantly steeper, with dips increasing from 24°N to between 45 – 52°N. These steeper dips cannot be generated by the dip of the modern ramp (20°), suggesting that the rocks have been

steepened by the stacking of two ramps. We interpret this as the footwall ramp of the second horse of the duplex, with the top edge of the ramp located ~125 km from the MFT.

While the Robang and GH are not exposed south of the Pokhara antiform in the Daraundi valley, they are exposed in the Kathmandu synform to the east, and the Damauli klippe to the west. Similar to the cross-sections in the Marsyangdi and Budhi Gandaki, the RMT carried the entire section of the Robang and GH sequences, emplacing them on top of lesser Himalayan rocks carried by the Trishuli thrust sheet, completely burying them.

Structure	**Shortening (km)**	**Constant rate**		**Best-fit rates**	
		Initiation (Ma)	Rate (mm/yr.)	Initiation (Ma)	Rate (mm/yr.)
MCT	171	23.00	19.79	23.00	24.43
RMT	104	14.36	19.79	16.00	11.56
TT	90.5	9.10	19.79	7.00	37.51
D1	11.8	4.53	19.79	4.60	15.71
D2	10	3.93	19.79	3.85	15.38
Siw1	8	3.43	19.79	3.20	20.00
Siw2	10.5	3.02	19.79	2.90	11.67
Siw3	17.4	2.49	19.79	1.90	32.83
Siw4	11.9	1.61	19.79	1.37	32.16
RMT OOS	10	1.01	19.79	1.00	20.00
PT2 OOS	5	0.51	19.79	0.50	20.00
Siw1 OOS	2	0.25	19.79	0.25	20.00
MFT	3	0.15	19.79	0.15	20.00

Table 4.2: Velocity profiles for final models along the Daraundi

4.5.3 Predicted cooling ages

In this section, we evaluate the effect of the subsurface geometry along the Daraundi valley on the predicted cooling ages using a surface heat production (A_0) value of 2.35 μW m^{-3}, and a best-fit velocity profile that is consistent with the best-fit models for the Budhi Gandaki and Marsyangdi transects. Our models start at 500 Ma, allowing an equilibrated thermal field to be created before kinematic deformation begins at 23 Ma with motion on the MCT. The MCT is first emplaced onto the Robang formation, moving over a ~25 km high ramp (Video 4.1: Steps 1 - 16). The resulting erosional exhumation produces reset AFT, ZHe, and MAr cooling ages, with the youngest ages located at the top of the ramp (~420 km), becoming progressively older towards the south. Beginning at 16 Ma, the RMT is emplaced over the rocks that will become the Trishuli thrust sheet. The footwall cutoff of the Trishuli thrust sheet is divided into two smaller ramps that are connected by a ~6 km flat. The lower ramp is 4 km high, with the RMT being emplaced over the lower LH Kuncha formation (currently located at ~240 km). After moving over the flat, the RMT is then translated onto the upper LH over a ~7 km high ramp. This uplift and exhumation resets AFT ages, with the youngest ages predicted over the ramp through upper LH strata, with the predicted ages becoming progressively older towards the south. While the predicted AFT ages record the emplacement of the RMT, the predicted MAr still only record the emplacement of the MCT. The predicted ZHe ages at the former surface partially record both periods of cooling and become ~2 Ma younger due to motion over the upper LH ramp. Beginning at 7 Ma, the Trishuli thrust is emplaced on top of the LH rocks that become the horses of the LH duplex, moving over a ~9 km high ramp (located at ~190 km from the MFT) that cuts across the entire lesser Himalayan sequence. This exhumation predicts reset ZHe and AFT ages above the ramp, continuing till 4.6 Ma, with the hanging wall cutoff of the Trishuli thrust being emplaced onto the rocks that become

the Siwaliks at the MBT. This translation also results in the footwall edge of the Trishuli thrust sheet (i.e., the active ramp during the emplacement of the RMT) being brought over the new ramp. Continued exhumation associated with this translation resets MAr ages above the Trishuli thrust. The duplex starts to form at 4.6 Ma, promoting exhumation at the surface, steadily removing the GH overlying it as the duplex is translated southward over the ramp. This exhumation results in the formation of a zone of unreset MAr ages in LH rocks that are now exposed in the core of the Gorkha-Pokhara antiform above the duplex. Translation of the duplex over the modern MHT ramp begins at 3.2 Ma, when deformation steps into the Siwaliks, predicting ZHe and AFT ages that steadily increase in age towards the south, with the youngest ages located at the ramp. Deformation in the Siwaliks is interrupted at ~1 Ma, by 10 km of OOS thrusting located ~105 km from the MFT that repeats the Robang formation and MCT. Exhumation associated with this thrusting exposes younger predicted MAr ages, and resets ZHe and AFT ages immediately to the north, creating an inflection point in the predicted ages at 105 km from the MFT (Video 4.1: Step 46). This OOS thrusting is immediately followed by reactivation along the original trace of the RMT, which surfaces 90 km from the MFT, co-located with PT2 in the Daraundi valley. Erosional exhumation associated with this motion produces ZHe and AFT ages that are ~1 Ma younger than prior. Active deformation jumps southward to deform the MFT and translate the duplex over the modern ramp as suggested by river incision rates derived from Holocene terraces in central Nepal (Lavé and Avouac, 2001).

At the end of the sequential model, the youngest MAr ages (~2 – 3 Ma) are predicted between 97 – 106 km from the MFT, correctly reproducing the youngest measured MAr ages in the Daraundi valley. Farther north, the model predicts a swath of reset MAr ages (~4.5 – 7 Ma) between 108 – 119 km from the MFT, consistent with the range of ages measured within the

detrital sample collected from the headwaters of the Daraundi river and matching the single measured bedrock age located ~116 km from the MFT. The model also successfully reproduces the zone of partially-reset/unreset ages located to the south of ~88 km, predicting unreset ages in locations where the measured MAr ages are between 1903 – 247 Ma. Finally, while predicting young ZHe ages (~1 Ma) between 102 – 130 km, the model is also able to successfully reproduce the steady southward increase in the measured ages (between 68 and 90 km) south of the trace of the MCT.

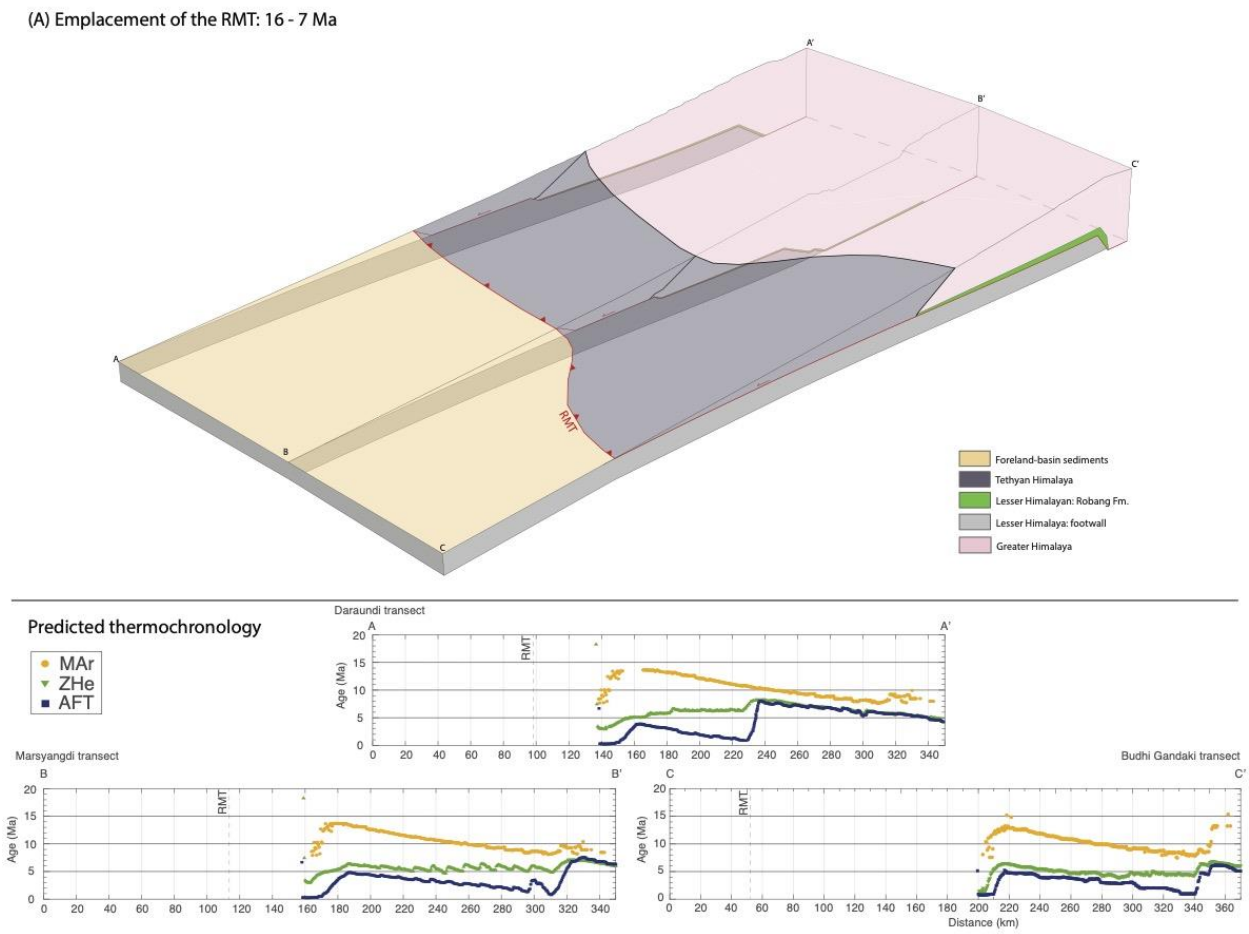

(B) Translation of the TT: 7 - 6 Ma

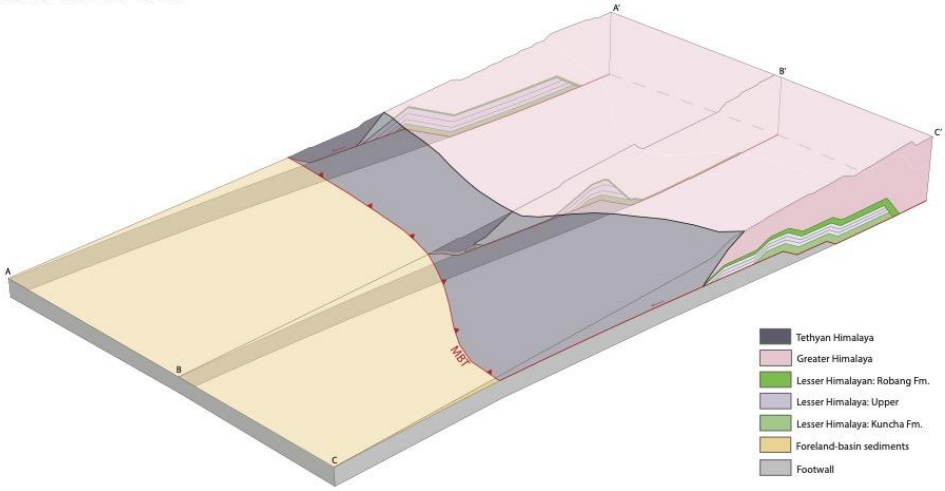

Predicted thermochronology

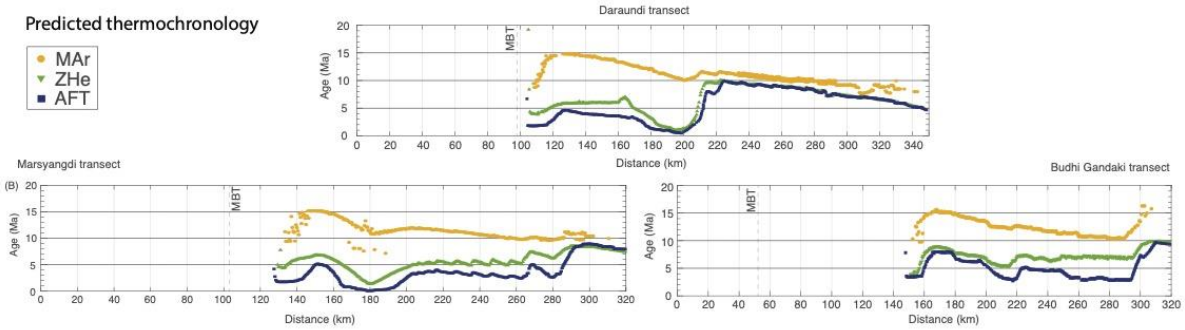

(C) Inititation of the duplex: ~4.5 Ma

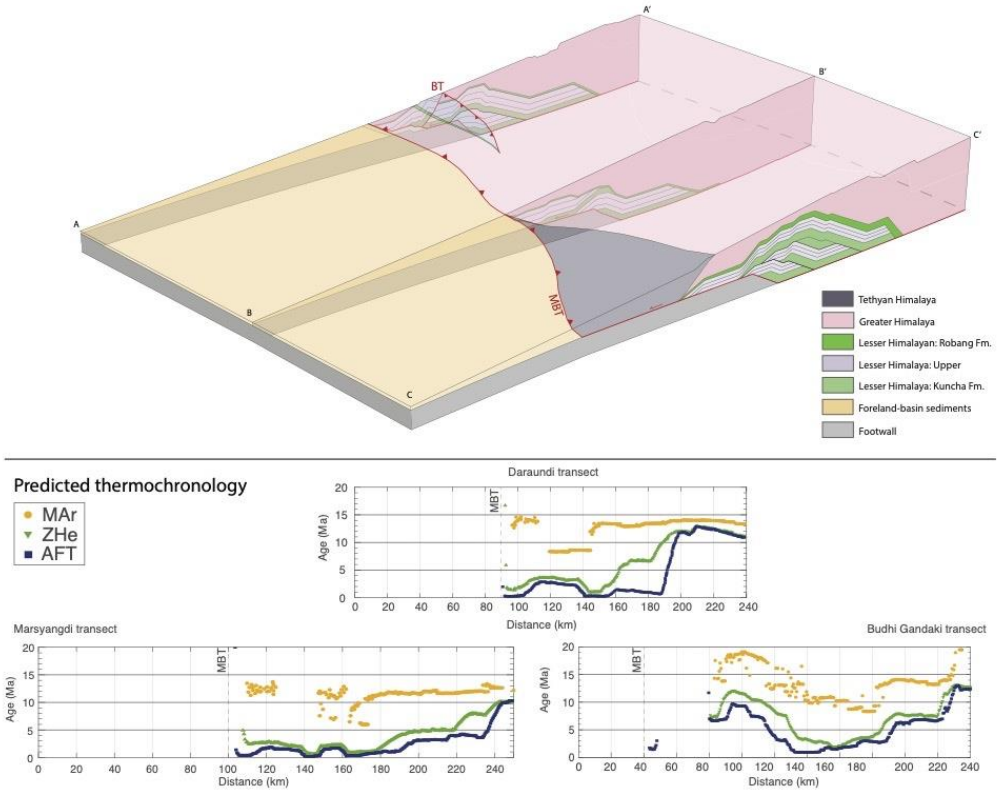

(D) Translation of duplex over modern ramp: ~3.2 Ma

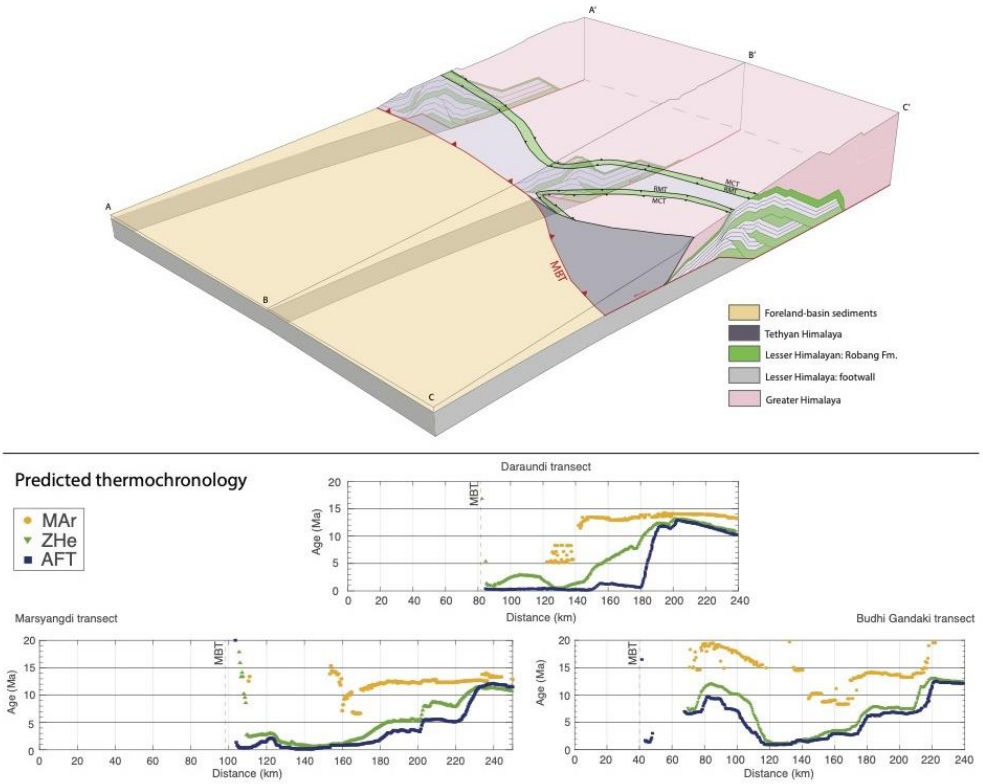

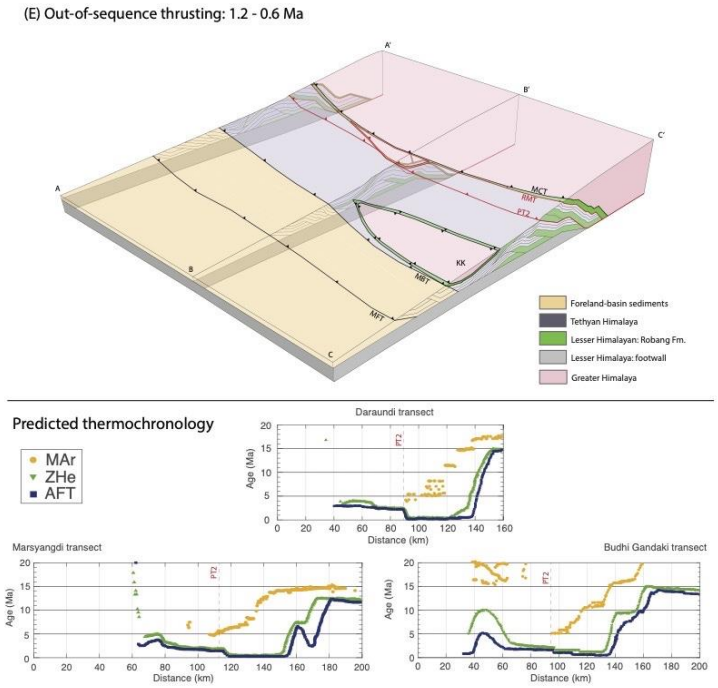

Figure 4.5: Evolution of the central Nepal Himalayas through time, showing predicted cooling ages for each transect.

A-A': Marsyangdi; B-B': Daraundi; C-C': Budhi Gandaki. In order to show greater detail in the surface geology, the Budhi Gandaki transect is shown at a greater relative distance from the Daraundi and plotted along D-D' (Figure 4.1).

(A) Emplacement of the RMT: ~16-7 Ma; (B) Initiation and emplacement of the TT: ~7-6 Ma; (C) Initiation of the duplex: ~4.6 Ma; (D) Completion of duplex construction: ~3.2 Ma; (E) OOS thrusting in the hinterland: ~1.2 Ma.

4.6 Discussion

4.6.1 Kinematic evolution of the central Nepal Himalayas

Combining the kinematic models for the Marsyangdi, Daraundi and Budhi Gandaki allows us to evaluate how the geometry of the MHT has changed with time in central Nepal, and how these changes have affected the development of the surface geology and cooling ages of minerals that we see at the surface today. Figure 4.5 shows the kinematic evolution of the central Nepal Himalayas over five important stages of development and highlights the effects of the resulting geometry and kinematics on the predicted cooling ages.

The models begin with motion on the MCT, at approximately 23 Ma, followed by the RMT at ~16 Ma. Emplacement of the RMT ends around 7 Ma, completely burying the rocks that will later become the Trishuli thrust and exposing rocks of the GH at the surface (Figure 4.5A). Along the Daraundi transect, the footwall ramp over which the RMT is emplaced offsets the upper LH from the lower LH, allowing the Robang Formation to be placed directly over the Kuncha. The footwall ramp itself is located 80 - 100 km farther south than in the neighboring Budhi Gandaki and Marsyangdi transects, implying that the uplift and exhumation associated with the emplacement of the RMT is concentrated farther to the south within the Daraundi transect, predicting young AFT ages ~220 km from the southern end of the transect, compared to ~300 km and ~340 km for the Marsyangdi and Budhi Gandaki transects, respectively. Emplacement of the Trishuli thrust sheet occurs between ~7 – 5 Ma, which shifts the locus of exhumation ~120 km southwards along the Marsyangdi, and Budhi Gandaki transects and begins to passively fold the GH above it (Figure 4.5B). The exhumation generated by the translation over the ramp completely resets the AFT and ZHe ages but is insufficient to completely reset the MAr ages, predicting ages

at the former surface that are 1 – 2 Ma younger. While the Trishuli thrust accommodates ~70 km and 90 km of motion in the Marsyangdi and Daraundi transects respectively, it only accommodates 50 km in the Budhi Gandaki transect. Further southward translation of the Trishuli thrust in the Budhi Gandaki is achieved by the initiation of duplex motion, with ~40 km of shortening being transferred to the first two horses of the LH duplex (Figure 4C: D1, D2). In the Marsyangdi and Daraundi transects, construction of the duplex begins at ~4.2 Ma, coinciding with the initiation of the third horse of the duplex in the Budhi Gandaki transect (Figure 4.5C). Motion on a backthrust in the Marsyangdi transect exposes LH rocks (i.e., part of the Trishuli thrust sheet) at the surface (Figure 5C). As the duplex develops (in all three sections), the southward migration of the active ramp creates a southward younging pattern of predicted ZHe and AFT ages. In addition, erosional exhumation occurring above the duplex produces a pattern of reset MAr ages that recorded earlier exhumation during the emplacement of the Trishuli thrust. The horses of the LH duplex begin to move over the modern ramp at ~3.2 Ma, lifting the overlying rocks of the Trishuli, Ramgarh-Munsiari and Main Central thrust sheets (Figure 4.5D). In the Marsyangdi and Daraundi transects, this translation places LH rocks over the footwall of the Siwaliks (i.e., along the MBT), erosionally removing all GH rocks in the south. In the Budhi Gandaki transect, the trace of the active MBT is located ~50 km farther to the south, creating a zone of translation and limited exhumation between the duplex and the MBT. This region of low structural elevation between the duplex and MBT facilitates the formation of the Kathmandu synform and the associated erosional preservation of GH rocks in the south (Figures 4-4C, 4-5D). The erosional removal of GH rocks over the duplex and the resulting exhumation of the underlying Trishuli thrust sheet creates a zone of unreset MAr ages. In the Daraundi and Marsyangdi transects, this zone is largely continuous towards the south due to the lack of GH rocks exposed south of the duplex. However, the isolated klippe of GH rocks

in the southern Budhi Gandaki show reset MAr ages that record the age of the emplacement of the RMT (Figure 4.4C). Following the translation of the duplex over the modern ramp via slip on the intra-Siwalik thrust sheets, hinterland OOS faulting initiates between 1.2 – 1 Ma with the reactivation of the RMT (Figure 4.5E).

In the Marsyangdi and Budhi Gandaki transects, the alignment of the northern edge of the translated duplex and active ramp impart an advantageous northward dip to the weak and contiguous RMT fault plane. In the Daraundi, the surface trace of the RMT is located ~25 km farther to the south and the RMT exhibits a ramp/flat shape at the time of OOS faulting. We suggest that the length (~42 km), and alignment of the deeper steeply dipping portion of the RMT in the Daraundi, with the contiguous RMT OOS fault in the Marsyangdi and BG facilitated the continuation of the steep fault angle and the repetition of the Robang and GH rocks in the Daraundi due to reactivation of the RMT. When reactivated, the cross-sectional extent of the RMT from where it surfaces to where it meets the MHT between 135 – 170 km (depending on the cross section; Figure 4.3) and, when combined with the final motion over the ramp due to the most recent activity at the MFT, results in uplift and erosional exhumation occurring over this entire region, predicting reset AFT ages. The northward limit of the associated young (~1 Ma) reset ZHe is the base of the active ramp (Figure 4.3).

Following the reactivation of the RMT in the Marsyangdi and BG transects, OOS faulting steps southward, and is accommodated on pre-existing fault zones that connect the active MHT ramp to the surface between 80 – 100 km from the MFT. Uplift along this out-of-sequence thrust creates the topographic transition zone known as Physiographic Transition 2 (PT2) (Wobus, Hodges and Whipple, 2003; Hodges *et al.*, 2004; Wobus, Whipple and Hodges, 2006; Whipple *et al.*, 2016). In the Daraundi transect, the trace of PT2 is co-located with the surface trace of the

original RMT (~86 km from the MFT). However, the complexity of the required path that the shortening would have to travel means that reactivation of the original RMT is unlikely. We suggest instead that the alignment of the footwall ramp of the TT in the Daraundi with the path of the OOS thrust in the Marsyangdi and Budhi Gandaki allowed the fault to seek out a more direct route to the surface (Figure 4.5E). Motion on this new fault breaks the first horse of the duplex into two parts, offsetting the northern segment, and exhuming a ~30 km wide region to the north of the trace of PT2. This additional exhumation results in a swath of reset AFT ages (~0.5 Ma) extending 50 km, from PT2 (~86 km) to the bottom of the MHT ramp (~136 km), along with reset ZHe ages (~0.5 – 1 Ma), extending from PT2 to ~125 km from the MFT (Figure 4.5E; Video 4.1: Step 46). This cumulative effect of the motion on the RMT and PT2 is also visible in the Marsyangdi and Budhi Gandaki transects, with motion on PT2 resulting in reset AFT ages between the surface trace of PT2 and the bottom of the ramp (Figure 4.5E; Videos 4.2, 4.3). Finally, motion steps southwards again into the Siwaliks, with motion on the intra-Siwalik thrust faults bringing the duplex over the active ramp into its final position.

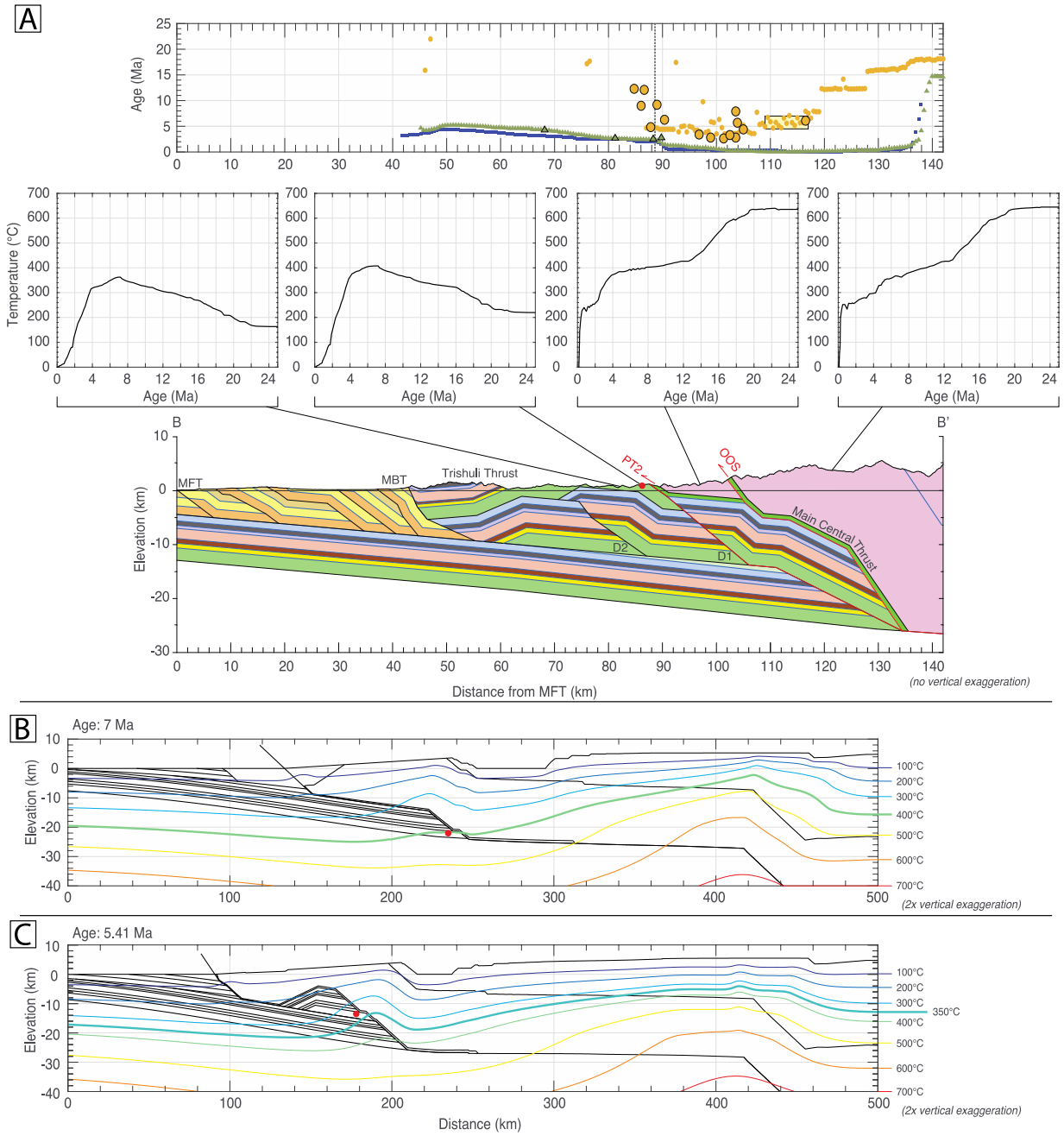

Figure 4.6: Thermal evolution of the Daraundi transect.

(A) Time-temperature paths of representative portions along the Daraundi transect. Predicted vs. measured cooling ages, along with the final cross-section are provided as reference. There is no vertical exaggeration in the cross-section. (B - C) Distance vs. Elevation plots showing the thermal fields at 7 and 5.41 Ma, respectively. The 400° and 350°C isotherms are highlighted. The plots have a 2x vertical exaggeration.

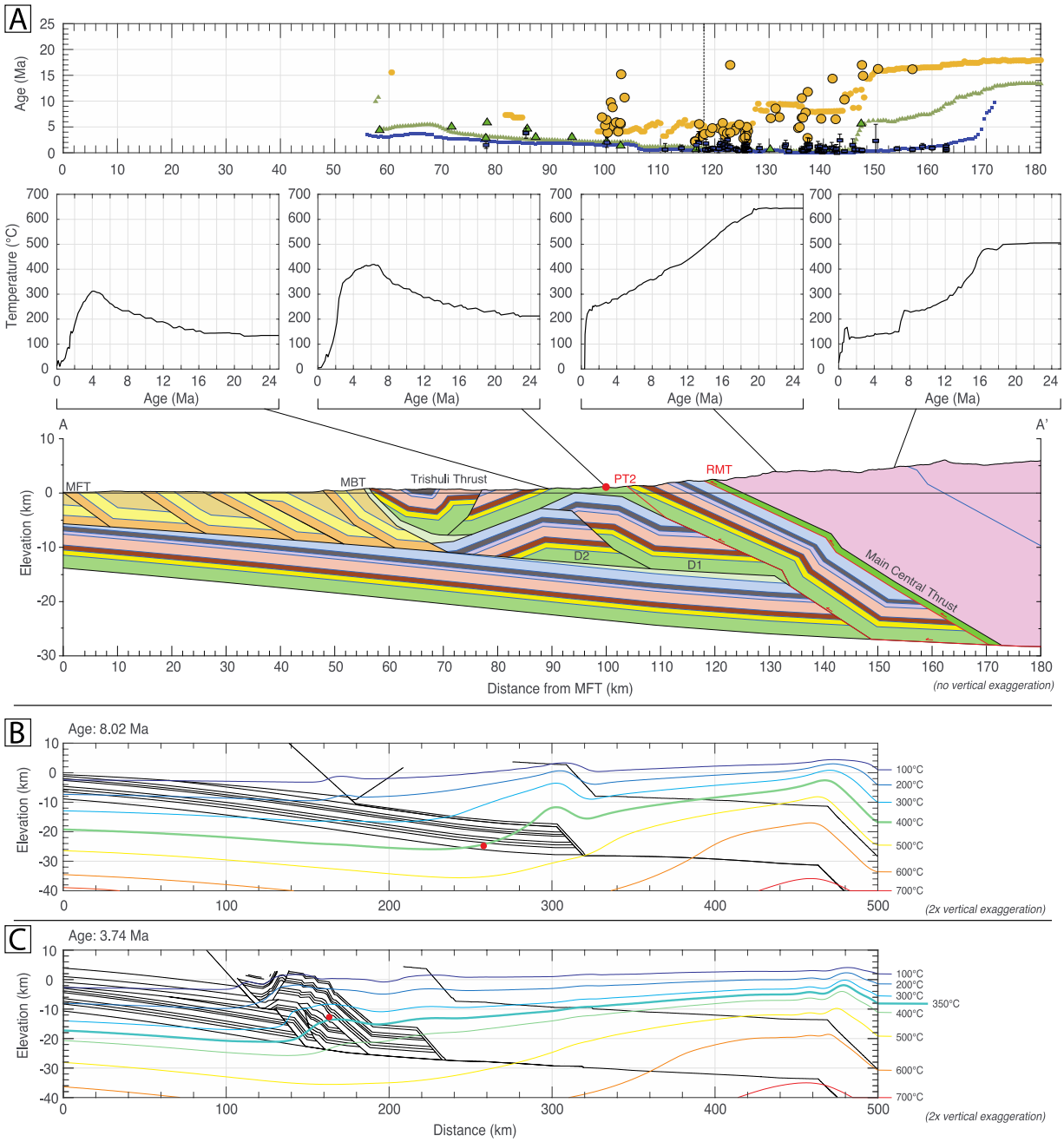

Figure 4.7: Thermal evolution of the Marsyangdi transect.

(A) Time-temperature paths of representative portions along the Marsyangdi transect. Predicted vs. measured cooling ages, along with the final cross-section are provided as reference. There is no vertical exaggeration in the cross-section. (B - C) Distance vs. Elevation plots showing the thermal fields at 8.02 and 3.74 Ma, respectively. The 400° and 350°C isotherms are highlighted. The plots have a 2x vertical exaggeration.

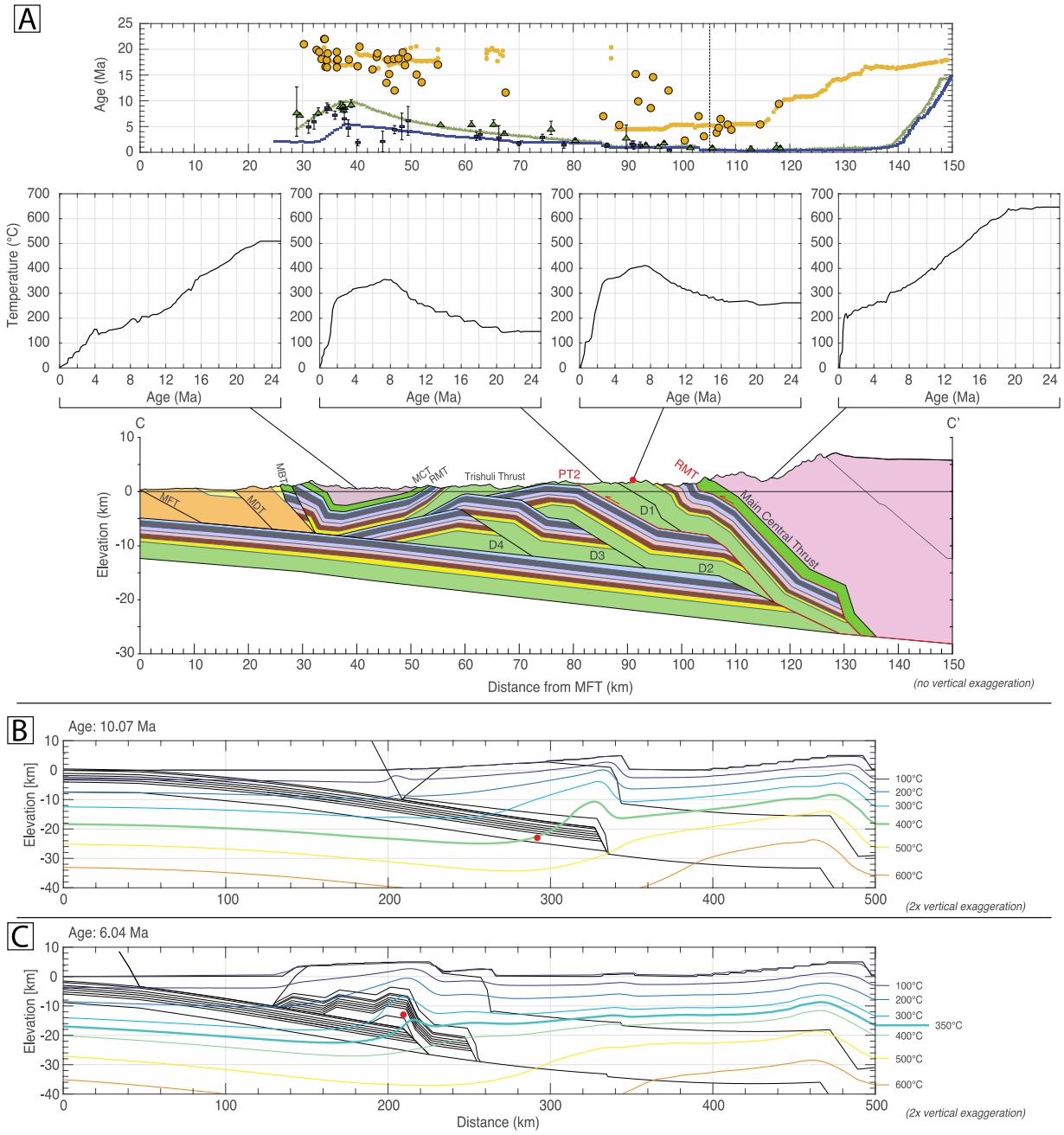

Figure 4.8: Thermal evolution of the Budhi Gandaki transect.

(A) Time-temperature paths of representative portions along the Marsyangdi transect. Predicted vs. measured cooling ages, along with the final cross-section are provided as reference. There is no vertical exaggeration in the cross-section. (B - C) Distance vs. Elevation plots showing the thermal fields at 10.07 and 6.04 Ma, respectively. The 400° and 350°C isotherms are highlighted. The plots have a 2x vertical exaggeration.

4.6.2 Controls/drivers of along-strike changes of upper plate geometry

Thermokinematic modeling of the Daraundi transect reveals how lateral changes in the upper plate that are visible today at the surface began life as critical changes to the geometry of the MHT in the mid- to late-Miocene. The most pronounced geometric change between the three sections is in the length of the Trishuli thrust sheet and the southern location of its trailing footwall. Along the Daraundi transect, the Trishuli thrust sheet is only 35 km long, compared to 120 km and 105 km in the Marsyangdi and Budhi Gandaki transects, respectively. (Figure 4.5A). Mostly due to this shorter length, the footwall ramp that facilitates the emplacement of the RMT over the rocks that make up the Trishuli thrust sheet along the Daraundi transect is ~100 – 110 km farther to the south than in the other transects. The northern edge of the Trishuli thrust sheet, and the transition to the Robang Formation marks the distal edge of the Kuncha Formation (Pearson and DeCelles, 2005; Martin *et al.*, 2011; Khanal and Robinson, 2013; Robinson and Pearson, 2013), and potentially the northern limit of the upper LH. If so, the southern limit of the RMT footwall ramp would be a function of the geometry of the northern Indian margin, and this abrupt lateral step in the Indian margin (between the RMT footwall ramp in the Budhi Gandaki and Daraundi sections) may be related to features ascribed to the Judi Lineament (Mugnier *et al.*, 2011).

While the Trishuli thrust sheet is significantly shorter in the Daraundi transect than in its neighbors, the total amount of shortening that it accommodates (90 km) remains comparable to those in the neighboring Marsyangdi and Budhi Gandaki transects. This magnitude of shortening, combined with its significantly shorter length means that the thrust sheet has been translated entirely over, and is currently south of, the modern ramp. Immediately prior to the initiation of the duplex, the trailing end of the Trishuli thrust sheet is ~50 km farther to the south in the Daraundi compared to adjacent sections and is located over the first horse in the duplex (Figure 4.5C; Video

4.1). In contrast, the first horse in the duplex initiates in the middle or near the southern, leading edge of the Trishuli thrust sheet in the neighboring Budhi Gandaki and Marsyangdi transects respectively (Figure 4.5C, D). Because of the limited length, magnitude of displacement and southern location, Trishuli thrust motion also places a flat portion of the RMT and overlying GH rocks directly on top of the long northernmost horse of the duplex (Figure 4.5C). This flat portion of the RMT and MCT directly over a flat portion of the LH rocks in the duplex (Figure 4.5D) is maintained following translation of the duplex over the modern ramp (Figure 4.4, 4.5E). The combination of a short Trishuli thrust sheet, comparatively high displacement, and the long length of the northernmost horse of the duplex produces the southern step in the trace of the RMT and MCT in the Daraundi compared to the neighboring two transects (Figure 4.5E).

In addition to this southward step in the surface geology along the Daraundi transect, there is also a corresponding southward step in the distribution of young MAr ages (Figure 4.2). While the active MHT ramp is located ~110 km from the MFT, the southernmost young MAr age is located 88 km from the MFT (Figure 4.4B). In contrast to the southward step in the trace of the MCT and RMT unique to the Daraundi transect, the southward extent of young MAr ages continues west to the Marsyangdi (Figure 4.2). Analyzing and comparing how key differences in the geometry of each transect has affected the resulting cooling histories highlights how this present-day distribution of reset MAr ages was formed. The southernmost of these reset MAr ages are located within the rocks of the Kuncha Formation, within the Trishuli thrust sheet along each transect. However, Kuncha Formation samples also from the Trishuli thrust, but located farther to the south, are partially to fully unreset requiring a difference in their cooling histories (Figure 4.4). Examining the time-temperature histories of the Trishuli thrust sheet shows that the rocks along the northern edge of the Trishuli thrust subside and slowly warm due to adjacent emplacement of

the MCT over the RMT (Figures 4.6, 4.7, 4.8; Videos 3.2, 4.1, 4.2; 23-16 Ma). The emplacement of the RMT over its footwall ramp (i.e., the trailing edge of the Trishuli thrust sheet) accelerates this heating by both increasing burial and advecting heat at the ramp. By the time that the RMT has been completely emplaced (7 Ma), the rocks that show reset ages have been heated to over 400°C (Figures 4.6, 4.7, 4.8 – red circle).Advection of heat at the ramp creates a pattern of southward dipping isotherms, which place rocks located at the northern edge of the Trishuli thrust above the 400°C isotherm while rocks located immediately to the south are never heated to above 370°C (Figures 4.6, 4.7, 4.8). Complete translation of the Trishuli thrust over its footwall ramp is required for the rocks to subsequently cool through below 350°C, occurring at ~5.4 Ma along the Daraundi section, ~3.7 Ma along the Marsyangdi and ~6 Ma in the Budhi Gandaki, setting the MAr ages (Figures 4.6, 4.7, 4.8 – red circle). Since Trishuli thrust rocks located immediately to the south were never heated above 370°C, they were never fully reset, and therefore show partially-unreset to unreset ages. We find that the southern extent of reset MAr ages is controlled by the relationship between horses of the duplex that define the antiform, and the modern MHT ramp. In the Marsyangdi, the horses of the duplex have been almost entirely translated over the ramp. In the Daraundi, the horse that is part of the footwall ramp of PT2, has been entirely translated over the ramp. This allows rocks that have been heated above 400°C to be exposed further south. However, in the Budhi Gandaki, the northernmost horse of the duplex (D2) has not been entirely translated over the MHT ramp. Therefore, the combination of the MHT ramp, and the footwall ramp of the horse steepens the overlying TT sheet and forces it to be exposed farther to the north, resulting in an offset in the distribution of cooling ages at the surface between the Budhi Gandaki and the Daraundi.

4.6.3 Lateral changes in the geometry of the MHT

While mapping in central Nepal shows that the surface traces of the MCT, RMT and exposed LH strata have significant along-strike variations in location and exposure along the northern limb of the Gorkha-Pokhara antiform, the geometry of the MHT and the recent OOS thrusts remain remarkably consistent between the Budhi Gandaki and Marsyangdi transects (Figure 4.5E). The along-strike continuity of MHT isseen in the distribution of the youngest reset ZHe and AFT ages (Figure 4.2), which are the most sensitive to the location of the active ramp (McQuarrie *et al.*, 2019; Ghoshal *et al.*, 2020, 2021; Robinson *et al.*, 2021). This continuity is particularly notable in the linearity of the distribution of the ZHe ages (Figure 4.2B). Unlike the measured MAr ages, the youngest ZHe ages are located ~10 km to the north of the trace of the MCT in both the Marsyangdi and Budhi Gandaki and stay young at least 25 km north of the MCT (Figure 4.3; Marsyangdi transect). The linearity of the modern MHT ramp and the OOS faults suggests a relationship between the two, particularly between the modern ramp and PT2 (e.g., Whipple et al., 2016). The OOS fault at PT2 soles directly into the modern ramp, transferring motion on the ramp directly to the surface (Figure 4.4). This direct link between the fault and the ramp has meant that the surface trace of PT2 is highly linear (e.g., Wobus et al., 2003, 2006; Hodges et al., 2004; Whipple et al., 2016), and runs distinctly parallel to the trace of the modern ramp. The reactivated RMT also owes its alignment largely to the linearity of the modern ramp. The fault plane soles into the MHT to the north of the ramp, with its orientation determined by the relationship of the TT sheet (in the Marsyangdi and Budhi Gandaki transects) and the northernmost horse of the duplex (in the Daraundi transect) with the modern ramp.

4.7 Conclusions

We combine detailed mapping and published MAr, ZHe and AFT ages, with thermokinematic modeling to propose a new subsurface geometry and kinematic sequence for the Daraundi valley in central Nepal. Integrating this new geometry with previously proposed fault geometries for the neighboring Budhi Gandaki and Marsyangdi valleys allows us to develop an integrated kinematic evolution for central Nepal capable of predicting the distribution of cooling ages measured at the surface. We use this regional kinematic model to assess how the subsurface geometry of the region varies from east to west, and evaluate the continuity of active structures over 100 km.While the southward step in the trace of the MCT, and the coincident step in the distribution of reset MAr ages suggests that the geometry of the Main Himalayan thrust changes between the Budhi Gandaki and Marsyangdi valleys, our modeling shows that these variations at the surface are caused by critical changes in the upper plate geometry. In particular, we find that the Trishuli thrust sheet is only ~35 km long in the Daraundi, compared to 105 - 120 km in the Budhi Gandaki and Marsyangdi, meaning that with similar magnitudes of displacement (~90-100 km) the footwall of the Trishuli is translated 80 – 100 km farther to the south. The combination of this amount of displacement and short length of the Trishuli with the long northern horse of the LH duplex results in the formation of the southward step in the surface geology. In addition, we find that the corresponding step in the reset MAr ages is controlled by the relationship between the modern MHT ramp, and the geometry of the LH duplex. Finally, a total of 10 – 15 km of out-of-sequence thrusting occurs across central Nepal, with the shortening split between two discrete fault zones that are aligned with the modern MHT ramp, and therefore show a distinct linearity across central Nepal. This out-of-sequence motion is not the most recent component of deformation, with OOS motion occurring between ~1.2 Ma to 0.25 Ma.

While the Daraundi is a zone of pronounced lateral variations in surface geology and measured MAr ages, these changes are not the result of variations in the geometry of the modern Main Himalayan thrust, rather resulting from a change in the geometry of the rocks being translated over the ramp. Therefore, we find no evidence for a significant lateral boundary in the MHT in the region that may have restricted the propagation of the 2015 Gorkha EQ.

4.8 Supplementary information

The supplementary videos can be accessed online at https://www.youtube.com/playlist?list=PLttn6LSpDKTFIzYV8UyL_Cw3WdbFgblLv

4.8.1 Geologic mapping

Along the Daraundi section, the lower Lesser Himalayan Kuncha Formation is overlain by ~5 km of upper Lesser Himalayan rocks consisting of alternating aluminum rich schist, quartzite, marble and dolostone (Khanal and Robinson, 2013). Although strongly metamorphosed, distinctive formations such as the pink and green quartzite and intervening variegated phyllite/schist of the Nourpul Formation (Stöcklin, 1980; H. Sakai, 1985), exhibit the same identifying characteristics as their less metamorphosed equivalents farther south. Structurally above the upper Lesser Himalayan rocks, the Paleoproterozoic (DeCelles *et al.*, 2000; Kohn, Paul and Corrie, 2010) Robang Formation is carried by the Ramgarh-Munsiari thrust (Pearson and DeCelles, 2005; Robinson and Pearson, 2013). This formation is ~2 km thick with chlorite and garnet-rich schist interbedded with a clean, white, fine- to medium- grained quartzite (Dunga

quartzite ~ 10-50 m) that is visually distinct (Stöcklin, 1980; Pearson and DeCelles, 2005). The schist has a deep green color, wavy foliation and contains abundant white quartz augen, lenticles, and veins. North of the Robang Formation is Greater Himalayan biotite garnet gneiss with partial melt textures (e.g., polymineralic leucosomes), which require that the rocks were once hot enough to produce melt (Kohn and Malloy, 2004; Kohn, 2008; Long and McQuarrie, 2010). The structure that places these high-grade metamorphic gneisses over the Lesser Himalayan Robang Formation is the Main Central Thrust (MCT).

Southward along the Daraundi River, our mapping diverges from prior mapping (Colchen, Le Fort and Pecher, 1981) (Figure 4.10). The green biotite schist and white quartzite of the Robang Formation directly overlies the grey, lithic and micaceous rich Kuncha Formation. Structurally above and north of the 1.5 km thick Robang Formation, we mapped interlayered biotite schist with garnet and muscovite, biotite rich quartzite and a two mica (biotite, muscovite) orthogneiss with feldspar augen. Problematically, augen gneiss is present in both Lesser and Greater Himalayan rocks. It has been mapped in the Kuncha Formation, the Robang Formation and in Greater Himalayan rocks above the Main Central Thrust (Pearson and DeCelles, 2005), but has never been identified in upper Lesser Himalayan stratigraphy. North of the interbedded schist, quartzite and orthogneiss is a flat to north striking (10°-20° dips to the east and west) section of marble and calcsilicate (~750 m thick) overlain by biotite rich quartzite and schist (~600 m thick) before reaching undisputed Greater Himalayan paragneiss with kyanite and sillimanite (Colchen, Le Fort and Pecher, 1981; Kohn *et al.*, 2001). Although previous authors placed the Main Central Thrust immediately below the paragneiss, and argued that the calcsilicate rocks were the carbonate rich upper Lesser Himalayan section (Colchen, Le Fort and Pecher, 1981; Kohn *et al.*, 2001), this

proposed relationship would be missing 3.5 km of the 5 thick section upper Lesser Himalayan rocks as mapped in the Budhi Gandaki (Khanal and Robinson, 2013).

We argue that both the Robang Formation and the presence of partial melt textures in the biotite schist located ~800 m to the north of the Robang Formation, support a southern MCT location as shown in Figure 4.1. The original mapping (Colchen, Le Fort and Pecher, 1981) of the region (Figure 4.10A) shows a 30-km southward step in contiguous mapped geology and an abrupt change in the strike of Lesser Himalayan rocks from broadly east-west to north-northeast, south-southwest. Thus, even if the calcsilicate rocks exposed along the Daraundi River valley are upper Lesser Himalayan in origin, the same 30 km offset is still expressed by both the upper LH rocks and the MCT. The flat dip (Colchen, Le Fort and Pecher, 1981; Kohn *et al.*, 2001) and limited thickness (1.3 km) of these rocks, also requires that Greater Himalayan rocks would be exposed on the unmapped ridge between the Daraundi and Budhi Gandaki Rivers (Figure 4.10A).

4.8.2 Satellite-assisted mapping

To assist in tracing the stratigraphic units in the region, we primarily concentrate on three overlapping ASTER (L2) scenes. Each of the scenes used were first stacked to create images containing the VNIR, SWIR and TIR spectral bands in single files, and then processed to highlight the presence of quartz, carbonates, muscovite, biotite and chlorite (Rockwell and Hofstra, 2008; Bertoldi *et al.*, 2011).

Each of the images were first pre-processed to remove the effects of vegetation and snow/ice using NDVI and band ratio methodologies. These masked images were then processed using ratios of ASTER bands to highlight specific minerals based on mineralogical spectral profiles (Rockwell and Hofstra, 2008; Bertoldi *et al.*, 2011).

We used these ratios to create several false-color composites and used them to trace out the units identified in the field. In the image created from the RGB couplet 7/5-7/6-5/6, high 7/5-7/6 ratios (orange-red) indicates the presence of chlorite and calcite, while a high 5/6 (blue) indicates the presence of muscovite. A second composite, created from RGB 4/5-6/8-7/6 was used to distinguish between calcite, chlorite, and other micas. High red values indicate calcite, while greens indicate the presence of metamorphic chlorite (Bertoldi *et al.*, 2011). Finally, a 12/10 ratio was used to highlight the differences between silicic and carbonatic rocks (Rockwell and Hofstra, 2008; Bertoldi *et al.*, 2011) (Figure 4.10C).

A further false color composite was created based on Relative Band Depth (RBD), which is defined as the ratio of the sum of the two bands surrounding the spectral peak of interest, with the band nearest to the peak itself (Crowley, Brickey and Rowan, 1989; Mars and Rowan, 2006). We used three RBD ratios: RBD4, RBD5 and RBD6, in the RGB channels. High reds (high RBD4) indicate the presence of chlorite, while high blue values indicate calcite (high RBD6) (Bertoldi *et al.*, 2011) (Figure 4.10B).

The final map was then created using the presence of highlighted mineralogies and field observations, considering the effect of topography.

4.8.3 Kriging

We used an Empirical Bayesian Kriging approach to create the interpolation for the thermochronological ages. This was performed using the Geostatistical Analyst toolset present in ArcGIS 10.5. The higher concentration of younger cooling ages (<10 Ma) required a Log Empirical transformation to resemble a normal distribution of ages. A simple kriging model was applied to the data using an exponential semivariogram, and the best-fit semivariogram for the

input data was calculated by iteratively to minimize residuals between the semivariance and the model (Krivoruchko, 2012; Krivoruchko and Gribov, 2014).

The calculation is based on both the values of the ages and the distances between pairs of samples; thus the contour intervals do not represent equal ages and are the narrowest between the data that are closely spaced with a smaller age range. We included the detrital MAr ages in the calculation, using ages from the middle quartile, as provided in Wobus et al. (2006).

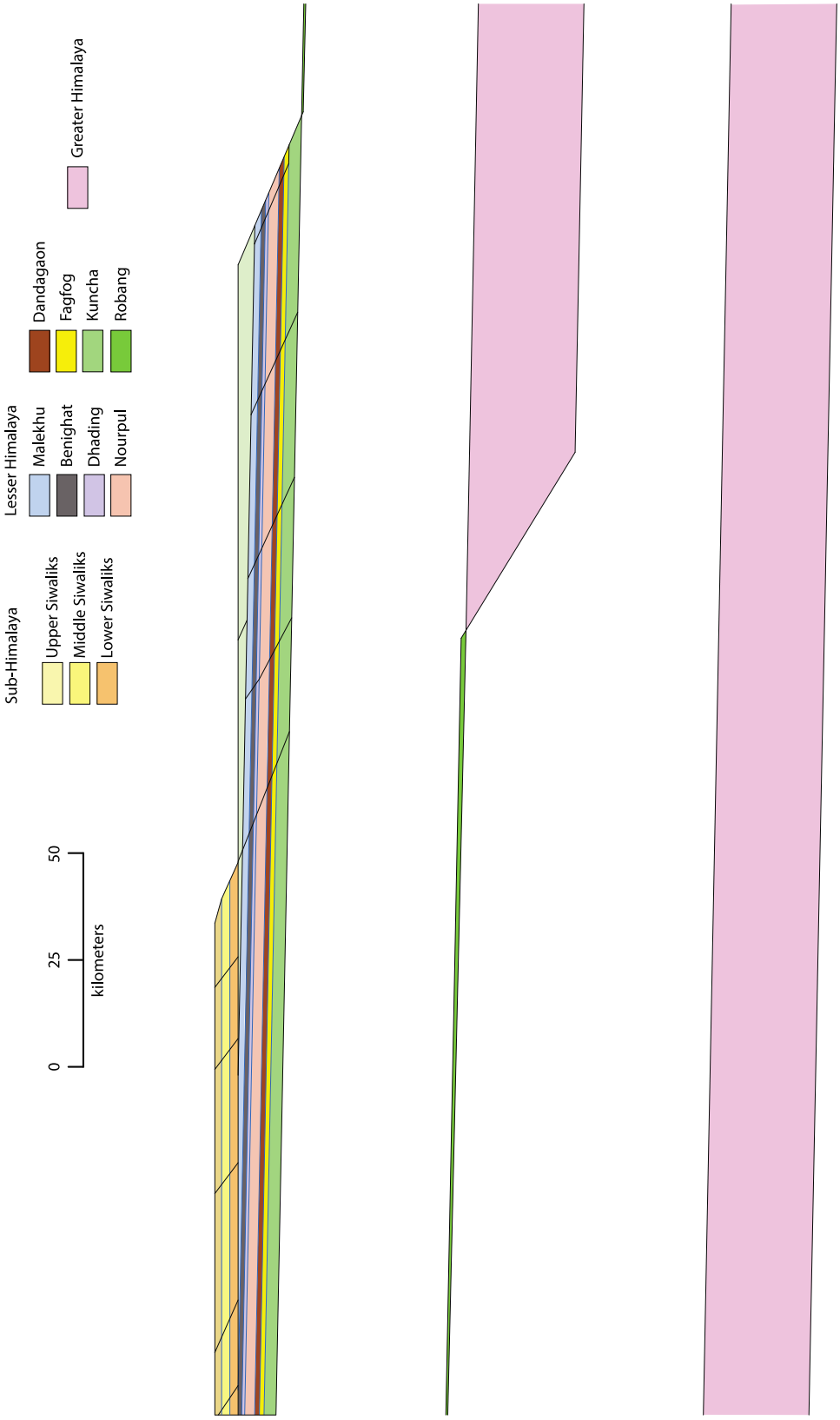

Figure 4.9: Restored cross-section geometry for the Daraundi transect

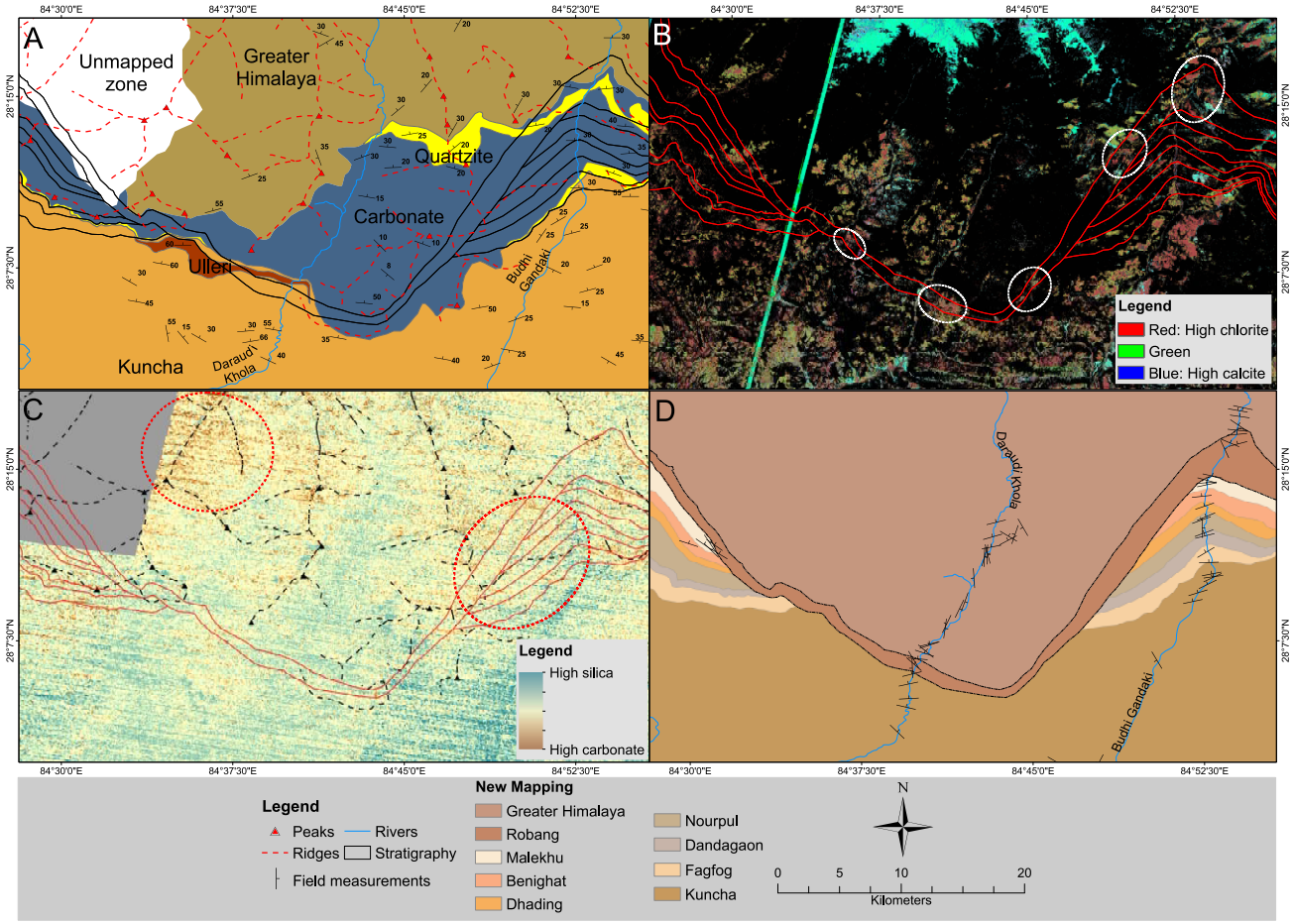

Figure 4.10: Integration of new geologic mapping with remote sensing.

A: Geologic map by Colchen et al. (1981) shows the prior interpretation of the study region. The blue carbonate map pattern includes aluminum rich schist, quartzite, marble and dolostone interpreted as upper lesser Himalayan carbonate rocks. For comparison, our mapping is outlined in black, and detailed in D. Topographic features (peaks and ridges) in the region are shown in red (triangles and dashed lines). B: Processed VNIR-SWIR imagery with the new mapping (D) shown as red lines. Chlorite-rich areas used in identifying the Robang Formation are circled in white. C: Processed TIR imagery highlighting carbonaceous and silica rich units with new mapping (D) shown in red. Carbonaceous units west of the Budhi Gandaki valley used to identify the trend of the Upper Lesser Himalayas are circled in red (left) along with carbonaceous-rich GH region in the north. D: New geologic map of the region around the earthquake

epicenter. The new field measurements are shown in black (Appendix A), while the mapped geologic formations are identified by color in the legend.

4.9 References

Ader, T. *et al.* (2012) 'Convergence rate across the Nepal Himalaya and interseismic coupling on the Main Himalayan Thrust: Implications for seismic hazard', *Journal of Geophysical Research: Solid Earth*, 117, p. B04403. doi: 10.1029/2011JB009071.

Avouac, J.-P. (2003) 'Mountain building, erosion, and the seismic cycle in the Nepal Himalaya', in *Treatise on Geophysics*. 2nd edn, pp. 1–80. doi: 10.1016/S0065-2687(03)46001-9.

Avouac, J.-P. *et al.* (2015) 'Lower edge of locked Main Himalayan Thrust unzipped by the 2015 Gorkha earthquake', *Nature Geoscience*, 8(9), pp. 708–711. doi: 10.1038/ngeo2518.

Bertoldi, L. *et al.* (2011) 'Mapping the Buraburi granite in the Himalaya of Western Nepal: Remote sensing analysis in a collisional belt with vegetation cover and extreme variation of topography', *Remote Sensing of Environment*. Elsevier Inc., 115(5), pp. 1129–1144. doi: 10.1016/j.rse.2010.12.016.

Bettinelli, P. *et al.* (2006) 'Plate motion of India and interseismic strain in the Nepal Himalaya from GPS and DORIS measurements', *Journal of Geodesy*, 80(8–11), pp. 567–589. doi: 10.1007/s00190-006-0030-3.

Bilham, R. *et al.* (1997) 'GPS measurements of present-day convergence across the Nepal Himalaya', *Nature*, 386, pp. 61–64.

Brady, R. J. *et al.* (2006) 'The distribution of radiogenic heat production as a function of depth in the Sierra Nevada batholith, California', *Lithos*. doi: 10.1016/j.lithos.2005.06.003.

Braun, J. (2003) ‘Pecube: A new finite-element code to solve the 3D heat transport equation including the effects of a time-varying, finite amplitude surface topography’, *Computers and Geosciences*, 29(6), pp. 787–794. doi: 10.1016/S0098-3004(03)00052-9.

Brewer, I. D., Burbank, D. W. and Hodges, K. V. (2006) ‘Downstream development of a detrital cooling-age signal: Insights from 40 Ar/ 39 Ar muscovite thermochronology in the Nepalese Himalaya’, *Special Paper of the Geological Society of America*, 398(20), pp. 321–338. doi: 10.1130/2006.2398(20).

Brookfield, M. E. (1993) ‘The Himalayan passive margin from Precambrian to Cretaceous times’, *Sedimentary Geology*, 84, pp. 1–35.

Burbank, D. W., Beck, R. A. and Mulder, T. (1996) ‘The Himalayan foreland’, in Lin, A. and Harrison, T. M. (eds) *The Tectonic Evolution of Asia*. United Kingdom: Cambridge University Press, pp. 149–188.

Catlos, E. J. *et al.* (2001) ‘Geochronologic and thermobarometric constraints on the evolution of the Main Central Thrust, central Nepal Himalaya’, *Journal of Geophysical Research: Solid Earth*, 106(B8), pp. 16177–16204. doi: 10.1029/2000JB900375.

Catlos, E. J. *et al.* (2018) ‘Modeling High-Resolution Pressure-Temperature Paths Across the Himalayan Main Central Thrust (Central Nepal): Implications for the Dynamics of Collision’, *Tectonics*, 37(8), pp. 2363–2388. doi: 10.1029/2018TC005144.

Colchen, M., Le Fort, P. and Pecher, A. (1981) ‘Geological map of Annapurnas-Manaslu-Ganesh Himalaya of Nepal, 1:200,000.’ Washington, DC: American Geophysical Union.

Colchen, M., Le Fort, P. and Pecher, A. (1986) ‘Recherches geologiques dans l’Himalaya du Nepal, Annapurna; Manaslu, Ganesh Himal’, *Centre Nacional de la Recherche Scientifique, Notice de la carte geologique au 1:200,000*, p. 137.

Coleman, M. E. (1996) ‘Orogen-parallel and orogen-perpendicular extension in the central Nepalese Himalayas’, *Bulletin of the Geological Society of America*, 108(12), pp. 1594–1607. doi: 10.1130/0016-7606(1996)108<1594:OPAOPE>2.3.CO;2.

Corrie, S. L. and Kohn, M. J. (2011) ‘Metamorphic history of the central Himalaya, Annapurna region, Nepal, and implications for tectonic models’, *Geological Society of America Bulletin*, 123(9–10), pp. 1863–1879. doi: 10.1130/B30376.1.

Cross III, E. A. (2014) *The structure, stratigraphy, and evolution of the Lesser Himalaya of central Nepal*. The University of Arizona.

Crowley, J. K., Brickey, D. W. and Rowan, L. C. (1989) ‘Airborne imaging spectrometer data of the Ruby Mountains, Montana: Mineral discrimination using relative absorption band-depth images’, *Remote Sensing of Environment*, 29(2), pp. 121–134. doi: 10.1016/0034-4257(89)90021-7.

Crowley, K. d., Cameron, M. and Schaefer, R. l. (1991) ‘Experimental studies of annealing of etched fission tracks in fluorapatite’, *Geochimica et Cosmochimica Acta*, 55(5), pp. 1449–1465. doi: 10.1016/0016-7037(91)90320-5.

DeCelles, P. G. *et al.* (1998) ‘Eocene-early Miocene foreland basin development and the history of Himalayan thrusting, western and central Nepal’, *Tectonics*, 17(5), pp. 741–765. doi: 10.1029/98TC02598.

DeCelles, P. G. *et al.* (2000) ‘Tectonic Implications of U-Pb Zircon Ages of the Himalayan Orogenic Belt in Nepal’, *Science*, pp. 497–499.

DeCelles, P. G. *et al.* (2007) ‘High and dry in central Tibet during the Late Oligocene’, *Earth and Planetary Science Letters*, 253(3–4), pp. 389–401. doi: 10.1016/j.epsl.2006.11.001.

Dhital, M. R. (2015) *Geology of the Nepal Himalaya*. Cham: Springer International

Publishing (Regional Geology Reviews). doi: 10.1007/978-3-319-02496-7.

Dodson, M. H. (1973) ‘Closure temperature in cooling geochronological and petrological systems’, *Contributions to Mineralogy and Petrology*, 40, pp. 259–274. Available at: http://www.raco.cat/index.php/Dovella/article/view/20118.

Ehlers, T. A. *et al.* (2005) ‘Computational tools for low-temperature Thermochronometer Interpretation’, *Reviews in Mineralogy and Geochemistry*, 58(1), pp. 589–622. doi: 10.2138/rmg.2005.58.22.

Ehlers, T. A. (2005) ‘Crustal thermal processes and the interpretation of Thermochronometer data’, *Reviews in Mineralogy and Geochemistry*, 58(1), pp. 315–350. doi: 10.2138/rmg.2005.58.12.

Elliott, J. R. *et al.* (2016) ‘Himalayan megathrust geometry and relation to topography revealed by the Gorkha earthquake’, *Nature Geoscience*, 9(2), pp. 174–180. doi: 10.1038/ngeo2623.

England, P. *et al.* (1992) ‘Heat sources for tertiary metamorphism and anatexis in the Annapurna-Manaslu region central Nepal’, *Journal of Geophysical Research*, 97(B2), pp. 2107–2128. doi: 10.1029/91JB02272.

Gansser, A. (1964) *Geology of the Himalayas*. New York: Wiley-Interscience.

Gautam, P. and Rösler, W. (1999) ‘Depositional chronology and fabric of Siwalik Group sediments in central Nepal from magnetostratigraphy and magnetic anisotropy’, *Journal of Asian Earth Sciences*, 17(5–6), pp. 659–682. doi: 10.1016/S1367-9120(99)00021-8.

Gehrels, G. *et al.* (2011) ‘Detrital zircon geochronology of pre-Tertiary strata in the Tibetan-Himalayan orogen’, *Tectonics*, 30(5). doi: 10.1029/2011TC002868.

Ghoshal, S. *et al.* (2020) ‘Constraining Central Himalayan (Nepal) Fault Geometry

Through Integrated Thermochronology and Thermokinematic Modeling', *Tectonics*, 39(9), pp. 1–33. doi: 10.1029/2020TC006399.

Ghoshal, S. *et al.* (2021) 'Erosional controls on the architecture and kinematics of the Himalayas: Insights from thermokinematic modeling'.

Gilmore, M. E. *et al.* (2018) 'Testing the effects of topography, geometry, and kinematics on modeled thermochronometer cooling ages in the eastern Bhutan Himalaya', *Solid Earth*, 9(3), pp. 599–627. doi: 10.5194/se-9-599-2018.

Grandin, R. *et al.* (2015) 'Rupture process of the M w = 7.9 2015 Gorkha earthquake (Nepal): Insights into Himalayan megathrust segmentation', *Geophysical Research Letters*, 42(20), pp. 8373–8382. doi: 10.1002/2015GL066044.

Hames, W. E. and Bowring, S. A. (1994) 'An empirical evaluation of the argon diffusion geometry in muscovite', *Earth and Planetary Science Letters*, 124(1–4), pp. 161–169. doi: 10.1016/0012-821X(94)00079-4.

Harrison, T. M. *et al.* (1993) 'Isotopic preservation of Himalayan/Tibetan uplift, denudation, and climatic histories of two molasse deposits', *The Journal of Geology*, 101, pp. 157–175.

Harrison, T. M. *et al.* (1997) 'A Late Miocene-Pliocene origin for the Central Himalayan inverted metamorphism', *Earth and Planetary Science Letters*, 146, pp. E1–E7.

Hodges, K. V. *et al.* (2004) 'Quaternary deformation, river steepening, and heavy precipitation at the front of the Higher Himalayan ranges', *Earth and Planetary Science Letters*, 220(3–4), pp. 379–389. doi: 10.1016/S0012-821X(04)00063-9.

Hodges, K. V. (2014) 'Thermochronology in Orogenic Systems', in Holland, H. D. and Turekian, K. K. (eds) *Treatise on Geochemistry*. Amsterdam: Elsevier, pp. 281–308. doi:

10.1016/B978-0-08-095975-7.00308-9.

Hourigan, J. K., Reiners, P. W. and Brandon, M. T. (2005) 'U-Th zonation-dependent alpha-ejection in (U-Th)/He chronometry', *Geochimica et Cosmochimica Acta*, 69(13), pp. 3349–3365. doi: 10.1016/j.gca.2005.01.024.

Hubbard, J. *et al.* (2016) 'Structural segmentation controlled the 2015 M w 7.8 Gorkha earthquake rupture in Nepal', *Geology*, 44(8), pp. 639–642. doi: 10.1130/G38077.1.

Huntington, K. W. *et al.* (2007) 'Topography, exhumation pathway, age uncertainties, and the interpretation of thermochronometer data', *Tectonics*, 26(4), pp. 1–23. doi: 10.1029/2007TC002108.

Huntington, K. W., Blythe, A. E. and Hodges, K. V. (2006) 'Climate change and Late Pliocene acceleration of erosion in the Himalaya', *Earth and Planetary Science Letters*, 252(1–2), pp. 107–118. doi: 10.1016/j.epsl.2006.09.031.

Jouanne, F. *et al.* (2004) 'Current shortening across the Himalayas of Nepal', *Geophysical Journal International*, 157(1), pp. 1–14. doi: 10.1111/j.1365-246X.2004.02180.x.

Kayal, J. R. (2009) *Microearthquake Seismology and Seismotectonics of South Asia*. Springer.

Ketcham, R. A. (1996) 'Distribution of heat-producing elements in the upper and middle crust of southern and west central Arizona: Evidence from the core complexes', *Journal of Geophysical Research: Solid Earth*. doi: 10.1029/96jb00664.

Khanal, S. (2014) *Structural and Kinematic Evolution of the Himalayan Thrust Belt, central Nepal*. The University of Alabama.

Khanal, S. and Robinson, D. M. (2013) 'Upper crustal shortening and forward modeling of the Himalayan thrust belt along the Budhi-Gandaki River, central Nepal', *International Journal*

of Earth Sciences, 102(7), pp. 1871–1891. doi: 10.1007/s00531-013-0889-1.

Kimura, K. (1999) 'Diachronous evolution of sub-Himalayan piggyback basins, Nepal', *Island Arc*, 8(1), pp. 99–113. doi: 10.1046/j.1440-1738.1999.00224.x.

Kohn, M. J. *et al.* (2001) 'Pressure-temperature-time path discontinuity in the Main Central thrust zone, central Nepal', *Geology*, 29(7), pp. 571–574. doi: 10.1130/0091-7613(2001)029<0571:PTTPDI>2.0.CO;2.

Kohn, M. J. *et al.* (2004) 'Miocene faulting at plate tectonic velocity in the Himalaya of central Nepal', *Earth and Planetary Science Letters*, 228(3–4), pp. 299–310. doi: 10.1016/j.epsl.2004.10.007.

Kohn, M. J. (2008) 'P-T-t data from central Nepal support critical taper and repudiate large-scale channel flow of the Greater Himalayan Sequence', *Bulletin of the Geological Society of America*, 120(3–4), pp. 259–273. doi: 10.1130/B26252.1.

Kohn, M. J. and Malloy, M. A. (2004) 'Formation of monazite via prograde metamorphic reactions among common silicates: Implications for age determinations', *Geochimica et Cosmochimica Acta*, 68(1), pp. 101–113. doi: 10.1016/S0016-7037(03)00258-8.

Kohn, M. J., Paul, S. K. and Corrie, S. L. (2010) 'The lower lesser himalayan sequence: A paleoproterozoic arc on the northern margin of the Indian plate', *Bulletin of the Geological Society of America*, 122(3–4), pp. 323–335. doi: 10.1130/B26587.1.

Krivoruchko, K. (2012) 'Empirical Bayesian Kriging', in *ArcUser Fall 2012*.

Krivoruchko, K. and Gribov, A. (2014) 'Pragmatic Bayesian kriging for non-stationary and moderately non-Gaussian data', in *Mathematics of Planet Earth. Proceedings of the 15th Annual Conference of the International Association for Mathematical Geosciences*. Springer, pp. 61–64.

Kuiper, K. F. *et al.* (2008) 'Synchronizing rock clocks of Earth history', *Science*,

320(5875), pp. 500–504. doi: 10.1126/science.1154339.

Larson, K. P., Godin, L. and Price, R. A. (2010) 'Relationships between displacement and distortion in orogens: Linking the Himalayan foreland and hinterland in central Nepal', *Geological Society of America Bulletin*, 122(7–8), pp. 1116–1134. doi: 10.1130/B30073.1.

Lavé, J. and Avouac, J.-P. (2000) 'Active folding of fluvial terraces across the Siwaliks Hills, Himalayas of central Nepal', *Journal of Geophysical Research: Solid Earth*, 105(B3), pp. 5735–5770. doi: 10.1029/1999JB900292.

Lavé, J. and Avouac, J.-P. (2001) 'Fluvial incision and tectonic uplift across the Himalayas of central Nepal', *Journal of Geophysical Research: Solid Earth*, 106(B11), pp. 26561–26591. doi: 10.1029/2001JB000359.

Lock, J. and Willett, S. (2008) 'Low-temperature thermochronometric ages in fold-and-thrust belts', *Tectonophysics*, 456(3–4), pp. 147–162. doi: 10.1016/j.tecto.2008.03.007.

Long, S. and McQuarrie, N. (2010) 'Placing limits on channel flow: Insights from the Bhutan Himalaya', *Earth and Planetary Science Letters*, 290(3–4), pp. 375–390. doi: 10.1016/j.epsl.2009.12.033.

Mars, J. C. and Rowan, L. C. (2006) 'Regional mapping of phyllic- and argillic-altered rocks in the zagros magmatic arc, Iran, using advanced spaceborne thermal emission and reflection radiometer (ASTER) data and logical operator algorithms', *Geosphere*, 2(3), pp. 161–186. doi: 10.1130/GES00044.1.

Martin, A. J. *et al.* (2005) 'Isotopic and structural constraints on the location of the Main Central thrust in the Annapurna Range, central Nepal Himalaya', *Bulletin of the Geological Society of America*, 117(7–8), pp. 926–944. doi: 10.1130/B25646.1.

Martin, A. J. *et al.* (2011) 'Stratigraphic and tectonic implications of field and isotopic

constraints on depositional ages of Proterozoic Lesser Himalayan rocks in central Nepal', *Precambrian Research*. Elsevier B.V., 185(1–2), pp. 1–17. doi: 10.1016/j.precamres.2010.11.003.

McQuarrie, N. *et al.* (2019) 'The influence of foreland structures on hinterland cooling: Evaluating the drivers of exhumation in the eastern Bhutan Himalaya', *Tectonics*, pp. 1–29. doi: 10.1029/2018tc005340.

McQuarrie, N. and Ehlers, T. A. (2015) 'Influence of thrust belt geometry and shortening rate on thermochronometer cooling ages: Insights from thermokinematic and erosion modeling of the Bhutan Himalaya', *Tectonics*, 34(6), pp. 1055–1079. doi: 10.1002/2014TC003783.

McQuarrie, N. and Ehlers, T. A. (2017) 'Techniques for understanding fold-and-thrust belt kinematics and thermal evolution', in Law, R. D. et al. (eds) *Linkages and Feedbacks in Orogenic Systems*. Boulder: Geological Society of America, pp. 25–54. doi: 10.1130/2017.1213(02).

Menon, R. *et al.* (2003) 'Radiogenic heat production of Late Archaean Bundelkhand granite and some Proterozoic gneisses and granitoids of central India', *Current Science*, 85(5), pp. 634–638.

Mugnier, J. L. *et al.* (2011) 'Seismites in the Kathmandu basin and seismic hazard in central Himalaya', *Tectonophysics*. Elsevier B.V., 509(1–2), pp. 33–49. doi: 10.1016/j.tecto.2011.05.012.

Mugnier, J. L. *et al.* (2013) 'Structural interpretation of the great earthquakes of the last millennium in the central Himalaya', *Earth-Science Reviews*. Elsevier B.V., 127, pp. 30–47. doi: 10.1016/j.earscirev.2013.09.003.

Mugnier, J. L. *et al.* (2017) 'Segmentation of the Himalayan megathrust around the Gorkha earthquake (25 April 2015) in Nepal', *Journal of Asian Earth Sciences*. Elsevier Ltd, 141(April 2015), pp. 236–252. doi: 10.1016/j.jseaes.2017.01.015.

Ojha, T. P. *et al.* (2000) 'Magnetic polarity stratigraphy of the Neogene Siwalik Group at

Khutia Khola, far western Nepal', *Bulletin of the Geological Society of America*, 112(3), pp. 424–434. doi: 10.1130/0016-7606(2000)112<424:MPSOTN>2.0.CO;2.

Ojha, T. P. *et al.* (2009) 'Magnetic polarity stratigraphy of the Neogene foreland basin deposits of Nepal', *Basin Research*, 21(1), pp. 61–90. doi: 10.1111/j.1365-2117.2008.00374.x.

Olree, E. C. (2018) *Kinematic and Flexural Isostasy Modeling in Central Nepal: Using erosional, depositional, and cooling histories to validate a balanced cross-section*. The University of Alabama.

Pandey, M. R. *et al.* (1995) 'Interseismic strain accumulation on the Himalayan crustal ramp (Nepal)', *Geophysical Research Letters*, 22(7), pp. 751–754. doi: 10.1029/94GL02971.

Parsons, A. J. *et al.* (2016) 'Geology of the Dhaulagiri-Annapurna-Manaslu Himalaya, Western Region, Nepal. 1:200,000', *Journal of Maps*, 12(1), pp. 100–110. doi: 10.1080/17445647.2014.984784.

Pearson, O. N. (2002) *Structural evolution of the central Nepal fold-thrust belt and regional tectonic and structural significance of the Ramgarh thrust*. The University of Arizona, Tucson.

Pearson, O. N. and DeCelles, P. G. (2005) 'Structural geology and regional tectonic significance of the Ramgarh thrust, Himalayan fold-thrust belt of Nepal', *Tectonics*, 24(4), pp. 1–26. doi: 10.1029/2003TC001617.

Qiu, Q. *et al.* (2016) 'The mechanism of partial rupture of a locked megathrust: The role of fault morphology', *Geology*, 44(10), pp. 875–878. doi: 10.1130/G38178.1.

Quade, J. *et al.* (1995) 'Late Miocene environmental change in Nepal and the northern Indian subcontinent: Stable isotopic evidence from paleosols', *Geological Society of America Bulletin*, 107(12), pp. 1381–1397. doi: 10.1130/0016-7606(1995)107<1381:LMECIN>2.3.CO;2.

Rahn, M. K. and Grasemann, B. (1999) 'Fission track and numerical thermal modeling of differential exhumation of the Glarus thrust plane (Switzerland)', *Earth and Planetary Science Letters*, 169(3–4), pp. 245–259. doi: 10.1016/S0012-821X(99)00078-3.

Ratschbacher, L. *et al.* (1994) 'Distributed deformation in southern and western Tibet during and after the India-Asia collision', *Journal of Geophysical Research*, 99(B10), pp. 19,917-19,645.

Ray, L., Bhattacharya, A. and Roy, S. (2007) 'Thermal conductivity of Higher Himalayan crystallines from Garhwal Himalaya, India', *Tectonophysics*, 434(1–4), pp. 71–79. doi: 10.1016/j.tecto.2007.02.003.

Reiners, P. W. *et al.* (2004) 'Zircon (U-Th)/He thermochronometry: He diffusion and comparisons with 40Ar/39Ar dating', *Geochimica et Cosmochimica Acta*, 68(8), pp. 1857–1887. doi: 10.1016/j.gca.2003.10.021.

Reiners, P. W. (2005) 'Zircon (U-Th)/He thermochronometry', *Reviews in Mineralogy and Geochemistry*, 58(1), pp. 151–179. doi: 10.2138/rmg.2005.58.6.

Renne, P. R. *et al.* (2005) 'Application of deuteron-deuteron (D-D) fusion neutrons to 40Ar/39Ar geochronology', *Applied Radiation and Isotopes*, 62(1), pp. 25–32. doi: 10.1016/j.apradiso.2004.06.004.

Robert, X. *et al.* (2011) 'Control of detachment geometry on lateral variations in exhumation rates in the Himalaya: Insights from low-temperature thermochronology and numerical modeling', *Journal of Geophysical Research: Solid Earth*, 116(5), pp. 1–22. doi: 10.1029/2010JB007893.

Robinson, D. M. *et al.* (2021) 'Controls of Stratigraphic Architecture on Along Strike Cooling Age Patterns', *Terra Nova*, 33(2), pp. 129–136. doi: 10.1111/ter.12498.

Robinson, D. M. and Martin, A. J. (2014) 'Reconstructing the greater Indian margin: A balanced cross section in central Nepal focusing on the Lesser Himalayan duplex', *Tectonics*, 33(11), pp. 2143–2168. doi: 10.1002/2014TC003564.

Robinson, D. M. and Pearson, O. N. (2013) 'Was Himalayan normal faulting triggered by initiation of the Ramgarh-Munsiari thrust and development of the Lesser Himalayan duplex?', *International Journal of Earth Sciences*, 102(7), pp. 1773–1790. doi: 10.1007/s00531-013-0895-3.

Rockwell, B. W. and Hofstra, A. H. (2008) 'Identification of quartz and carbonate minerals across northern Nevada using aster thermal infrared emissivity data-implications for geologic mapping and mineral resource investigations in well-studied and frontier areas', *Geosphere*, 4(1), pp. 218–246. doi: 10.1130/GES00126.1.

Ruppel, C. and Hodges, K. V. (1994) 'Role of horizontal thermal conduction and finite time thrust emplacement in simulation of pressure-temperature-time paths', *Earth and Planetary Science Letters*, 123(1–3), pp. 49–60. doi: 10.1016/0012-821X(94)90256-9.

Sakai, H. (1983) 'Geology of the Tansen Group of the Lesser Himalaya in Nepal', *Memoirs of the Faculty of Science, Kyushu University*, pp. 27–74.

Sakai, H. (1985) 'Geology of the Kali Gandaki Supergroup of the Lesser Himalayas in Nepal: memoirs of the Faculty of Science, Kyushu University, Series D.', *Geology*, 25(3), pp. 337–397.

Sakai, Harutaka (1985) 'Rifting of the Gondwanaland and uplifting of the Himalayas recorded in Mesozoic and Tertiary fluvial sediments in the Nepal Himalayas', in Taira, A. and Masuda, F. (eds) *Sedimentary Facies in the Active Plate Margin*. Tokyo: Terra Sci., pp. 723–732.

Sastri, V. *et al.* (1971) 'Tectonic framework and subsurface stratigraphy of the Ganga

basin', *Journal of the Geological Society of India*, 12, pp. 222–233.

Schmitz, M. D. and Bowring, S. A. (2001) 'U-Pb zircon and titanite systematics of the Fish Canyon Tuff: An assessment of high-precision U-Pb geochronology and its application to young volcanic rocks', *Geochimica et Cosmochimica Acta*, 65(15), pp. 2571–2587. doi: 10.1016/S0016-7037(01)00616-0.

Scholz, C. (1998) 'Earthquakes and friction laws', *Nature*, 391, pp. 37–43.

Shi, Y. and Wang, C. Y. (1987) 'Two-dimensional modeling of the P-T-t paths of regional metamorphism in simple overthrust terrains', *Geology*, 15(11), pp. 1048–1051. doi: 10.1130/0091-7613(1987)15<1048:TMOTPP>2.0.CO;2.

Stevens, V. L. and Avouac, J.-P. (2015) 'Interseismic coupling on the main Himalayan thrust', *Geophysical Research Letters*, 42(14), pp. 5828–5837. doi: 10.1002/2015GL064845.

Stöcklin, J. (1980) *Geology of Nepal and its regional frame, Journal of the Geological Society*. Geological Society of London. doi: 10.1144/gsjgs.137.1.0001.

Tokuoka, T. *et al.* (1986) 'The Churia (Siwalik) Group of the Arung Khola area, west central Nepal', *Memoirs of the Faculty of Science, Shimane University*, 20, pp. 135–210.

Upreti, B. N. (1996) 'Stratigraphy of the western Nepal Lesser Himalaya', *Journal of the Nepal Geological Society*, 13, pp. 11–28.

USGS (2015) *M7.8 - 36km E of Khudi, Nepal*. Available at: http://earthquake.usgs.gov/earthquakes/eventpage/us20002926#general_summary.

Whipp, D. M. *et al.* (2007) 'Plio-Quaternary exhumation history of the central Nepalese Himalaya: 2. Thermokinematic and thermochronometer age prediction model', *Tectonics*, 26(3). doi: 10.1029/2006TC001991.

Whipple, K. X. *et al.* (2016) 'Active shortening within the Himalayan orogenic wedge

implied by the 2015 Gorkha earthquake', *Nature Geoscience*, 9(9), pp. 711–716. doi: 10.1038/ngeo2797.

Wobus, C. W., Hodges, K. V. and Whipple, K. X. (2003) 'Has focused denudation sustained active thrusting at the Himalayan topographic front?', *Geology*, 31(10), p. 861. doi: 10.1130/G19730.1.

Wobus, C. W., Whipple, K. X. and Hodges, K. V. (2006) 'Neotectonics of the central Nepalese Himalaya: Constraints from geomorphology, detrital 40 Ar/ 39 Ar thermochronology, and thermal modeling', *Tectonics*, 25(4), p. n/a-n/a. doi: 10.1029/2005TC001935.

Yagi, Y. and Okuwaki, R. (2015) 'Integrated seismic source model of the 2015 Gorkha, Nepal, earthquake', *Geophysical Research Letters*, 42(15), pp. 6229–6235. doi: 10.1002/2015GL064995.

Zhang, J. and Guo, L. (2007) 'Structure and geochronology of the southern Xainza-Dinggye rift and its relationship to the south Tibetan detachment system', *Journal of Asian Earth Sciences*, 29(5–6), pp. 722–736. doi: 10.1016/j.jseaes.2006.05.003.

Appendix A Mapping data

Waypoint	Latitude	Longitude	Elevation (m)	Strike	Dip
CN16 001	27.83970902	85.167288	1053	-	-
CN16 002	27.83745001	85.15332098	886	100	60
CN16 003	27.85601903	85.15529701	718	91	44
CN16 004	27.85350001	85.153972	759	86	61
CN16 005	27.86251903	85.15523801	647	98	40
CN16 006	27.86265003	85.13627403	525	52	40
CN16 007	28.24641304	85.36366601	1787	344	64
CN16 008	28.20404797	85.35449898	1647	2	60
CN16 009	28.17220001	85.34240498	1441	350	45
CN16 010	28.16525099	85.33985202	1463	338	48
CN16 011	28.16584099	85.34308802	1462	355	55
CN16 012	28.16346598	85.34101501	1468	353	57
CN16 013	28.15869399	85.33800004	1651	335	58
CN16 014	28.16036099	85.33883303	1599	0	0
CN16 015	28.15969102	85.33443698	1420	313	42
CN16 016	28.14202398	85.32276199	1781	280	44
CN16 017	28.08754002	85.27540701	2022	20	30
CN16 018	28.06546301	85.22443104	2041	78	24
CN16 019	27.99269903	85.20261596	1482	-	-
CN16 020	27.92008803	85.14891403	600	110	35
CN16 021	27.85816798	85.10926704	526	75	69
CN16 022	27.83924801	85.02403499	456	74	61
CN16 023	27.83547004	85.02405602	454	74	71
CN16 024	27.79939701	85.00123797	437	0	0
CN16 025	27.81037102	84.83603904	444	82	72
CN16 026	27.81227597	84.83681797	428	77	28
CN16 027	27.80755604	84.83483297	367	284	90
CN16 028	27.80332603	84.83361198	371	85	75
CN16 029	27.80428802	84.83337301	406	-	-
CN16 030	27.805278	84.83288904	379	255	90
CN16 031	27.82155499	84.84497197	437	89	40
CN16 032	27.850118	84.84990598	459	279	31
CN16 033	27.88243904	84.875451	535	284	10

CN16 034	27.949104	84.86009502	1185	117	16
CN16 035	27.97225297	84.84260903	1003	101	27
CN16 036	28.11037098	84.83924001	587	149	33
CN16 037	28.31830597	84.90405601	1208	230	49
CN16 038	28.313423	84.90405299	1083	121	49
CN16 039	28.31380597	84.90580497	1159	243	20
CN16 040	28.29384699	84.90273803	1149	102	22
CN16 041	28.29386098	84.89947203	1226	280	29
CN16 042	28.28949996	84.90080601	1029	278	30
CN16 043	28.28291698	84.90036101	997	304	28
CN16 044	28.27950002	84.89913901	926	276	39
CN16 045	28.26936102	84.89888898	1215	255	47
CN16 046	28.27647197	84.89872201	926	265	28
CN16 047	28.27011103	84.89413904	929	293	45
CN16 048	28.26516696	84.89063901	939	335	44
CN16 049	28.23972202	84.876472	1069	258	34
CN16 050	28.24122196	84.87666696	1043	266	32
CN16 051	28.24288904	84.87711104	992	285	25
CN16 052	28.24613904	84.88086102	984	282	46
CN16 053	28.23133299	84.87286099	842	264	42
CN16 054	28.22413897	84.87472203	948	251	53
CN16 055	28.21644397	84.87569399	814	247	58
CN16 056	28.21394398	84.87244399	1093	250	37
CN16 057	28.20711097	84.87430603	782	-	-
CN16 058	28.20441702	84.87430603	790	250	44
CN16 059	28.202472	84.87502797	781	256	32
CN16 060	28.190333	84.87547204	830	239	62
CN16 061	28.18308298	84.878111	821	268	38
CN16 062	28.17472204	84.87994404	808	259	36
CN16 063	28.17275003	84.881333	748	262	27
CN16 064	28.17197202	84.88041703	763	245	27
CN16 065	28.16708302	84.876861	666	244	17
CN16 066	28.16097203	84.86991702	743	253	30
CN16 067	28.154611	84.86630601	721	258	36
CN16 068	28.03630597	84.79680603	753	208	48
CN16 069	28.03586097	84.76636103	913	120	24
CN16 070	27.98069799	84.75608096	578	130	41
CN16 071	27.94851601	84.73505303	458	282	32
CN16 072	27.38802804	84.85519404	498	315	67

CN16 073	27.54741697	84.85355596	383	321	84
CN16 074	27.54577797	84.85850003	361	122	87
CN16 075	27.54583304	84.86255603	376	290	60
CN16 076	27.59615304	84.91935398	528	122	77
CN16 077	27.582829	84.91647698	520	122	86
CN16 078	27.58159703	84.914726	585	304	82
CN16 079	27.57482504	84.91267101	550	309	67
CN16 080	27.57416002	84.91174104	539	302	78
CN16 081	27.57205096	84.90882497	473	279	57
CN16 082	27.57118	84.90732403	474	305	70
CN16 083	27.56714101	84.90721397	465	296	58
CN16 084	27.56565901	84.90636103	517	321	72
CN16 085	27.56751702	84.89316599	448	299	66
CN16 086	27.56599403	84.89112499	441	132	74
CN16 087	27.56503296	84.89078402	442	302	76
CN16 088	27.56308299	84.88844404	492	134	50
CN16 089	27.56733304	84.88513897	506	302	78
CN16 090	27.57360497	84.88168697	427	305	80
CN16 091	27.56945701	84.88082497	405	28	85
CN16 092	27.56349999	84.86702803	386	152	66
CN16 093	27.55705498	84.862306	366	299	68
CN16 094	27.557778	84.862694	366	114	38
CN16 095	27.56036097	84.865556	371	128	80
CN16 096	27.56169403	84.86638899	375	300	72
CN16 097	27.56444396	84.86791701	379	125	89
CN16 098	27.56608296	84.87169398	390	138	82
CN16 099	27.56744402	84.87563901	410	330	83
CN16 100	27.56816704	84.87697198	455	301	80
CN16 101	27.56058301	84.86675	443	100	74
CN16 102	27.52989904	85.09667398	841	278	35
CN16 103	27.49512998	85.04448197	620	277	63
CN16 104	27.483685	85.04568997	561	284	66
CN16 105	27.47152898	85.041568	516	304	49
CN16 106	27.71801803	84.16788401	458	252	30
CN16 107	27.72236698	84.16423897	634	264	46
CN16 108	27.73375204	84.16241297	900	269	43
CN16 109	27.74024298	84.15064403	915	268	53
CN16 110	27.74725696	84.15322096	1253	249	50
CN16 111	27.75179702	84.15550302	1300	158	55

CN16 112	27.758812	84.14727199	1419	-	-
CN16 113	27.77475103	84.11664502	1366	62	55
CN16 114	27.78409802	84.12146101	1235	263	60
CN16 115	27.81967099	84.12321199	660	287	74
CN16 116	27.83579098	84.12545398	607	265	10
CN16 117	27.84060898	84.136085	426	318	38
CN16 118	27.84167801	84.15354702	272	284	70
CN16 119	27.85199898	84.28633397	668	312	12
CN16 120	27.85169497	84.28828301	632	263	11
CN16 121	27.85164502	84.29018796	513	280	52
CN16 122	27.84890899	84.29443801	392	295	36
CN16 123	27.844739	84.29756404	381	287	62
CN16 124	27.84081602	84.29712902	328	255	63
CN16 125	27.81052801	84.29943698	364	112	85
CN16 126	27.80059696	84.29458503	502	50	57
CN16 127	27.866484	83.96696904	429	86	26
CN16 128	27.86715204	83.93527304	336	301	67
CN16 129	27.87958098	83.93634399	335	310	23
CN16 130	27.89466002	83.99553398	756	56	30
CN16 131	27.89670001	84.02229697	783	332	26
CN16 132	27.91875497	84.085809	945	30	24
CN16 133	27.92766896	84.09171799	873	336	23
CN16 134	27.97196103	84.08691902	446	279	58
CN16 135	27.97451902	84.08440403	469	316	18
CN16 136	27.98751097	84.08601503	455	254	24
CN16 137	27.99660299	84.09265199	482	108	16
CN16 138	28.00369198	84.08699797	515	5	32
CN16 139	28.00628199	84.08742	472	285	28
CN16 140	28.00913301	84.089231	546	337	33
CN16 141	28.02507699	84.10079702	477	55	23
CN16 142	28.02422396	84.10991997	506	323	32
CN16 143	28.02169698	84.11538002	527	338	45
CN16 144	28.18848303	84.71786904	912	345	35
CN16 145	28.18592596	84.71558397	911	16	26
CN16 146	28.17066	84.70585098	791	176	15
CN16 147	28.207246	84.741634	1845	150	12
CN16 148	28.20281499	84.73577497	1728	199	29
CN16 149	28.20210102	84.73263896	1610	301	16
CN16 150	28.199164	84.73129601	1572	242	24

CN16 151	28.19434701	84.71942003	1114	259	20
CN16 152	28.20176901	84.72025202	952	254	25
CN16 153	28.212395	84.72286901	1010	256	30
CN16 154	28.18772203	84.71769403	912	2	10
CN16 155	28.18590802	84.71553401	911	2	20
CN16 156	28.15304602	84.70116802	711	20	63
CN16 157	28.14785996	84.697225	702	26	19
CN16 158	28.13773999	84.68604103	674	206	20
CN16 159	28.13373302	84.68690696	733	8	26
CN16 160	28.12372796	84.67445799	627	257	39
CN16 161	28.12279204	84.673812	642	252	36
CN16 162	28.11817504	84.67247802	678	310	39
CN16 163	28.11695203	84.67111797	645	288	30
CN16 164	28.112877	84.66604197	609	275	40
CN16 165	28.11178803	84.663775	615	329	76
CN16 166	28.10179302	84.66149102	588	256	56
CN16 167	28.10506297	84.66089398	596	178	79
CN16 168	28.10874104	84.66391096	606	311	39
CN16 169	28.09449901	84.658885	563	258	44
CN16 170	28.08389599	84.65943502	540	267	32
CN16 171	28.07759296	84.65763803	542	283	53
CN16 172	28.05938898	84.65164899	520	314	38
CN16 173	27.96483333	84.39983333	493	-	-
CN16 174	27.96245503	84.40249097	539	108	28
CN16 175	27.95800701	84.39490501	673	106	30
CN16 176	27.941625	84.39751002	944	125	8
CN16 177	27.96586001	84.40619401	412	117	53
CN16 178	27.95973896	84.41263701	421	140	40
CN16 179	27.95158999	84.425248	485	122	34
CN16 180	27.94731597	84.43682098	438	166	16
CN16 181	27.91143296	84.50204602	424	89	24
CN16 182	27.89545001	84.539636	294	240	31
CN16 183	27.88968201	84.53976802	334	178	31
CN16 184a	27.88459503	84.54014403	304	256	44
CN16 184b	27.88566667	84.53980556	316	252	14
CN16 185	27.881771	84.543605	305	305	43
CN16 186	27.87695099	84.53937097	277	300	38
CN16 187	27.81550703	84.51769	311	315	38
CN16 188	27.81933697	84.49570896	237	270	42

CN16 189	27.82039602	84.48220496	279	51	74
CN16 190	27.823082	84.47208297	274	248	50
CN16 191	27.82348702	84.46492299	232	242	49
CN16 192	27.82441297	84.46403199	244	301	40
CN16 193	27.82541402	84.46523898	240	263	51
CN16 194	27.830487	84.46821196	258	126	52
CN16 195	27.83208098	84.46730998	262	292	79
CN16 196	27.83401502	84.46296003	232	101	76
CN16 197	27.81877899	84.44372398	293	255	44
CN16 198	27.81500897	84.43974199	258	272	50
CN16 199	27.80827797	84.43248502	252	259	54
CN16 200	27.80125603	84.431964	297	274	64
CN16 201	27.79506298	84.43161104	254	277	58
CN16 202	27.77306501	84.31367003	241	103	49
CN16 203	27.77620596	84.30984604	310	257	52
CN16 204	27.78182896	84.31224704	460	298	66
CN16 205	27.78755497	84.30110003	489	231	54
CN16 206	27.78913496	84.29834398	421	96	68
CN16 207	27.77736501	84.312615	300	305	84
CN16 208	27.77039001	84.31363299	231	92	51
CN16 209	27.76206602	84.31437504	267	82	54
CN16 210	27.74804402	84.31959797	290	285	66
CN16 211	27.74140103	84.34144498	378	256	63
CN16 212	27.74460199	84.38435102	351	260	65
CN16 213	27.73238897	84.39467702	322	260	53
CN16 214	28.55441102	84.23723797	2771	218	32
CN16 215	28.56074799	84.21724596	2751	213	36
CN16 216	28.568846	84.19941396	2798	189	21
CN16 217	28.57295003	84.18378004	3019	234	38
CN16 218	28.57919496	84.17942396	3196	234	39
CN16 219	28.62500098	84.13338996	3258	230	32
CN16 220	28.57058499	84.19731899	2843	193	26
CN16 221	28.55136101	84.26077897	2676	196	20
CN16 222	28.55153896	84.27148199	2709	100	10
CN16 223	28.54969502	84.28150901	2681	-	-
CN16 224	28.52943202	84.31328396	2311	198	32
CN16 225	28.51424402	84.35772398	1871	285	35
CN16 226	28.44799697	84.37372997	1546	277	37
CN16 227	28.42177201	84.40263002	1222	246	35

CN16 228	28.382926	84.400642	1094	225	39
CN16 229	28.37385996	84.40178303	1064	237	38
CN16 230	28.36386102	84.40260697	1031	236	38
CN16 231	28.35619703	84.40253397	1010	258	33
CN16 232	28.35478904	84.402065	1108	257	29
CN16 233	28.35198102	84.403892	989	274	37
CN16 234	28.34694802	84.39996298	994	286	34
CN16 235	28.344256	84.39744003	1045	277	27
CN16 236	28.34037501	84.39648097	1081	285	34
CN16 237	28.33910197	84.396587	981	289	33
CN16 238	28.33399203	84.39762603	971	262	30
CN16 239	28.33299802	84.398168	948	294	27
CN16 240	28.325732	84.39732	965	-	-
CN16 241	28.32103604	84.399491	965	262	15
CN16 242	28.31628903	84.39907199	1019	294	22
CN16 243	28.31024199	84.39511104	1001	290	24
CN16 244	28.30610803	84.38783999	956	281	15
CN16 245	28.29971096	84.37771599	966	288	38
CN16 246	28.29571196	84.37548799	914	267	36
CN16 247	28.29062004	84.37495901	933	310	27
CN16 248	28.28582601	84.36281498	872	312	31
CN16 249	28.25829699	84.365221	794	266	14
CN16 250	28.25566197	84.36762501	751	-	-
CN16 251	28.25052797	84.37082497	769	298	13
CN16 252	28.24500496	84.37235501	759	-	-
CN16 253	28.21587701	84.38442998	770	16	36
CN16 254	28.21356302	84.39054499	786	299	11
CN16 255	28.19210803	84.40905198	722	328	44
CN16 256	28.18185604	84.42545998	705	308	23
CN16 257	28.16984	84.43441504	715	256	14
CN16 258	28.15180499	84.43927998	594	274	33
CN16 259	28.08799901	84.447381	574	110	16
CN16 260	28.03388301	84.461345	430	107	32
CN16 261	28.02349498	84.458482	417	99	40
CN16 262	27.91383999	84.54368798	309	273	53
CN16 263	27.92597598	84.55727303	369	123	12
CN16 264	27.78475	84.83136111	468	295	32
CN16 267	28.15158333	84.44513889	674	331	60
CN16 268	28.19311111	84.46141667	844	326	37

CN16 269	27.19938889	84.488	-	306	45
CN16 270	28.19683333	84.49916667	921	288	40
CN16 271	28.19602778	84.51063889	993	305	64
CN16 272	28.19144444	84.51630556	1070	314	62
CN16 273	28.18927778	84.5215	1268	301	31
CN16 274	28.19566667	84.51827778	1274	305	12
CN16 275	28.19680556	84.51516667	1210	326	21
CN16 276	28.17636111	84.45575	630	313	24
CN16 265	27.78475	84.83136	468	53	64
CN16 266	27.79158	84.82903	408	269	67

Appendix B Muscovite $^{40}Ar/^{39}Ar$ (Mar) ages

ID	Longitude	Latitude	Elevation (m)	Age (Ma)	Error (2σ)	Type	Article	Region
-	84.79890	28.07910	992	7	0.1	Bedrock	Copeland91	BG-Trishuli
-	84.84820	28.23300	1891	3.1	0.1	Bedrock	Copeland91	BG-Trishuli
-	84.86890	28.35790	2060	5.4	0.1	Bedrock	Copeland91	BG-Trishuli
-	84.87160	28.39840	2811	9.4	0.1	Bedrock	Copeland91	BG-Trishuli
-	84.88380	28.27110	1882	3.8	0.1	Bedrock	Copeland91	BG-Trishuli
-	85.01180	28.08650	987	32.9	0.1	Bedrock	Copeland91	BG-Trishuli
GA-66	85.20000	28.23000	4713	4.76	0.1	Bedrock	harrison	BG-Trishuli
-	84.84060	27.77190	525	19.4	-	Bedrock	Herman et al 2010	BG-Trishuli
-	84.86200	27.64880	1035	17.9	-	Bedrock	Herman et al 2010	BG-Trishuli
-	84.86500	27.72430	1792	18.5	-	Bedrock	Herman et al 2010	BG-Trishuli
-	84.87190	27.66500	1507	17.9	-	Bedrock	Herman et al 2010	BG-Trishuli
-	84.87360	27.75210	986	18.1	-	Bedrock	Herman et al 2010	BG-Trishuli
-	84.87570	27.75990	748	18.2	-	Bedrock	Herman et al 2010	BG-Trishuli
-	84.88420	27.77390	777	18.5	-	Bedrock	Herman et al 2010	BG-Trishuli
-	84.91510	27.73560	1443	18	-	Bedrock	Herman et al 2010	BG-Trishuli
-	84.91610	27.71790	1437	19.2	-	Bedrock	Herman et al 2010	BG-Trishuli
-	84.91930	27.76440	804	16.9	-	Bedrock	Herman et al 2010	BG-Trishuli
-	84.92530	27.68290	1958	16.7	-	Bedrock	Herman et al 2010	BG-Trishuli
-	84.92590	27.60420	657	19.9	-	Bedrock	Herman et al 2010	BG-Trishuli
-	84.94390	27.60940	948	19.9	-	Bedrock	Herman et al 2010	BG-Trishuli
-	84.94500	27.62350	1279	19.5	-	Bedrock	Herman et al 2010	BG-Trishuli
-	84.94710	27.63790	1003	19.2	-	Bedrock	Herman et al 2010	BG-Trishuli
-	84.98860	27.64710	1379	19.5	-	Bedrock	Herman et al 2010	BG-Trishuli

-	84.99140	27.66740	1708	18	-	Bedrock	Herman et al 2010	BG-Trishuli
-	85.00033	27.79967	441	15.1	-	Bedrock	Herman et al 2010	BG-Trishuli
-	85.01880	27.80440	688	15.5	-	Bedrock	Herman et al 2010	BG-Trishuli
-	85.02020	27.72230	1274	15.2	-	Bedrock	Herman et al 2010	BG-Trishuli
-	85.03270	27.78060	642	15.1	-	Bedrock	Herman et al 2010	BG-Trishuli
-	85.04870	27.68990	1357	16.1	-	Bedrock	Herman et al 2010	BG-Trishuli
-	85.05650	27.63840	1853	18	-	Bedrock	Herman et al 2010	BG-Trishuli
-	85.05778	27.54444	1226	19.6	-	Bedrock	Herman et al 2010	BG-Trishuli
-	85.06580	27.49970	1010	21	-	Bedrock	Herman et al 2010	BG-Trishuli
-	85.07050	27.60910	2097	18.1	-	Bedrock	Herman et al 2010	BG-Trishuli
-	85.08560	27.55740	1930	17.9	-	Bedrock	Herman et al 2010	BG-Trishuli
-	85.08630	27.52190	781	18.5	-	Bedrock	Herman et al 2010	BG-Trishuli
-	85.10194	27.65972	1991	20.5	-	Bedrock	Herman et al 2010	BG-Trishuli
-	85.10470	27.53510	907	17.6	-	Bedrock	Herman et al 2010	BG-Trishuli
-	85.13270	27.58270	2224	16.8	-	Bedrock	Herman et al 2010	BG-Trishuli
-	85.13620	27.62520	1693	16.5	-	Bedrock	Herman et al 2010	BG-Trishuli
-	85.13980	27.60520	1790	16.6	-	Bedrock	Herman et al 2010	BG-Trishuli
-	85.15250	27.83917	874	13.6	-	Bedrock	Herman et al 2010	BG-Trishuli
-	85.16620	27.89520	514	225	0.1	Bedrock	Herman et al 2010	BG-Trishuli
-	85.17040	27.60340	1944	16.5	-	Bedrock	Herman et al 2010	BG-Trishuli
-	85.23060	27.78640	1312	13.5	-	Bedrock	Herman et al 2010	BG-Trishuli
-	85.23990	27.81020	1864	12	-	Bedrock	Herman et al 2010	BG-Trishuli
-	85.25120	27.54230	1688	19.2	-	Bedrock	Herman et al 2010	BG-Trishuli
-	85.25120	27.51940	1074	22	-	Bedrock	Herman et al 2010	BG-Trishuli
-	85.25150	27.88970	573	17	0.1	Bedrock	Herman et al 2010	BG-Trishuli
-	85.25220	27.88410	585	65	0.1	Bedrock	Herman et al 2010	BG-Trishuli
-	85.27760	27.52240	2156	22	-	Bedrock	Herman et al 2010	BG-Trishuli

-	85.30300	27.97770	1848	11.6	0.1	Bedrock	Herman et al 2010	BG-Trishuli
-	85.33740	28.10990	3189	9.9	0.1	Bedrock	Herman et al 2010	BG-Trishuli
L118	85.32831	28.16474	1913	2.3	0.4	Bedrock	Macfarlane et al.Tect.1993	BG-Trishuli
CN16-036	84.83924	28.11037	587	5.3	0.19	Bedrock	Ghoshal et al., 2020	BG-Trishuli
CN16-034	84.86010	27.94910	1185	31	6	Bedrock	Ghoshal et al., 2020	BG-Trishuli
CN16-037	84.90406	28.31831	1208	4.37	0.07	Bedrock	Ghoshal et al., 2020	BG-Trishuli
CN16-017	85.27541	28.08754	2022	410	80	Bedrock	Ghoshal et al., 2020	BG-Trishuli
CN16-016	85.32276	28.14202	1781	12	3	Bedrock	Ghoshal et al., 2020	BG-Trishuli
CN16-007	85.36367	28.24641	1787	5.4	0.6	Bedrock	Ghoshal et al., 2020	BG-Trishuli
01WBS8	84.80134	28.06633	754	356.9	-	Detrital*	Wobus et al., 2003	BG-Trishuli
01WBS7	84.82965	28.12123	1309	5.9	-	Detrital*	Wobus et al., 2003	BG-Trishuli
01WBS6	84.85002	28.15876	1733	8.7	-	Detrital*	Wobus et al., 2003	BG-Trishuli
01WBS5	84.86927	28.22481	1271	7	-	Detrital*	Wobus et al., 2003	BG-Trishuli
01WBS4	84.90066	28.28713	969	6.47	-	Detrital*	Wobus et al., 2003	BG-Trishuli
03WTS1	85.16800	27.96098	591	1690.3	-	Detrital*	Wobus et al., 2006	BG-Trishuli
01WTS1	85.18494	28.04336	1512	637	-	Detrital*	Wobus et al., 2006	BG-Trishuli
03WTS4	85.19779	28.10189	1679	879.3	-	Detrital*	Wobus et al., 2006	BG-Trishuli
02WTS4	85.31629	28.12759	2090	7.2	-	Detrital*	Wobus et al., 2006	BG-Trishuli
DH76	84.56918	28.00163	0	257	1	Bedrock	Catlos01	Marsyangdi
MA67	84.3396	28.23981	0	7.1	0.3	Bedrock	Bollingeretal2004	Marsyangdi
MA64	84.33297	28.24811	0	5.5	0.2	Bedrock	Bollingeretal2004	Marsyangdi
MA65	84.3384	28.24539	0	6.6	0.2	Bedrock	Bollingeretal2004	Marsyangdi
MA63	84.33387	28.25052	0	4.1	0.2	Bedrock	Bollingeretal2004	Marsyangdi
MA62	84.33553	28.25293	0	5.2	0.1	Bedrock	Bollingeretal2004	Marsyangdi
MA61	84.339	28.25429	0	10	1	Bedrock	Bollingeretal2004	Marsyangdi
AP668	84.5804	28.1345	0	9	0.1	Bedrock	Copeland91	Marsyangdi
MA69	84.359331	28.24311	0	6.1	0.2	Bedrock	Bollingeretal2004	Marsyangdi
MA60	84.355331	28.260666	0	6.1	0.4	Bedrock	Bollingeretal2004	Marsyangdi
MA59	84.355998	28.263777	0	4.3	0.2	Bedrock	Bollingeretal2004	Marsyangdi
MA77	84.374886	28.241777	0	6	0.2	Bedrock	Bollingeretal2004	Marsyangdi
MA74	84.37422	28.244221	0	5.8	1	Bedrock	Bollingeretal2004	Marsyangdi

Lc1	84.41583333	28.19138889	600	15.4	0.1	Bedrock	Arita et al. 1997	Marsyangdi
MA86	84.385108	28.235555	0	10.9	0.3	Bedrock	Bollingeretal2004	Marsyangdi
01NL02*	84.421233	28.333433	1400	2.46	0.2	Bedrock	Huntington & Hodges, 2006	Marsyangdi
MA81	84.334665	28.329776	0	2.4	0.1	Bedrock	Bollingeretal2004	Marsyangdi
NBE-6	84.4016	28.3256	1010	5.8	0.2	Bedrock	Huntington et al., 2021	Marsyangdi
01NL03*	84.424817	28.337133	1695	3.32	0.2	Bedrock	Huntington & Hodges, 2006	Marsyangdi
01NL04*	84.426467	28.3405	1981	3.84	0.08	Bedrock	Huntington & Hodges, 2006	Marsyangdi
01NL05*	84.430267	28.34535	2314	4.13	0.5	Bedrock	Huntington & Hodges, 2006	Marsyangdi
JP-01-4	84.2919	28.3134	2538	5	0.1	Bedrock	Huntington et al., 2021	Marsyangdi
01NL06*	84.438133	28.35275	2697	4.98	0.1	Bedrock	Huntington & Hodges, 2006	Marsyangdi
JP-00-02	84.3552	28.3701	2870	6	0.3	Bedrock	Huntington et al., 2021	Marsyangdi
JP-00-04	84.3793	28.3702	2020	4.4	0.2	Bedrock	Huntington et al., 2021	Marsyangdi
01NL07*	84.44605	28.3621	3032	3.49	0.09	Bedrock	Huntington & Hodges, 2006	Marsyangdi
JP-00-05	84.3871	28.3714	1770	4	0.2	Bedrock	Huntington et al., 2021	Marsyangdi
JP-00-01	84.35	28.382	3105	17.2	0.4	Bedrock	Huntington et al., 2021	Marsyangdi
JP-01-7	84.3501	28.3821	3137	4.08	0.08	Bedrock	Huntington et al., 2021	Marsyangdi
JP-00-07	84.4029	28.3874	1210	4.5	0.2	Bedrock	Huntington et al., 2021	Marsyangdi
01NL08*	84.451433	28.38085	3345	5.1	0.2	Bedrock	Huntington & Hodges, 2006	Marsyangdi
NBE-5	84.4052	28.3914	1100	5.7	0.4	Bedrock	Huntington et al., 2021	Marsyangdi
01NL09	84.4565	28.3917	3642	3	0.1	Bedrock	Huntington et al., 2021	Marsyangdi
01JA01	84.45	28.3952	3370	3.3	0.1	Bedrock	Huntington et al., 2021	Marsyangdi
JP-00-09	84.3948	28.4028	2170	3.2	0.1	Bedrock	Huntington et al., 2021	Marsyangdi
01JA04‡	84.4324	28.39861667	2376	4.09	0.2	Bedrock	Huntington et al., 2021	Marsyangdi
01JA08	84.4109	28.4019	1331	3.1	0.1	Bedrock	Huntington et al., 2021	Marsyangdi
01JA02‡	84.44663333	28.3984	3080	2.58	0.2	Bedrock	Huntington et al., 2021	Marsyangdi
01JA06	84.4203	28.4024	1649	3.5	0.2	Bedrock	Huntington et al., 2021	Marsyangdi
01JA05	84.43	28.4013	2139	5.2	0.2	Bedrock	Huntington et al., 2021	Marsyangdi
01JA03	84.442	28.4022	2706	4.4	0.1	Bedrock	Huntington et al., 2021	Marsyangdi

NBE-13	84.4019	28.4222	1320	6.9	0.3	Bedrock	Huntington et al., 2021	Marsyangdi
JP-00-12	84.3363	28.4133	3543	8.8	0.2	Bedrock	Huntington et al., 2021	Marsyangdi
JP-00-11	84.3282	28.4178	3795	7.1	0.2	Bedrock	Huntington et al., 2021	Marsyangdi
01TA01	84.3784	28.471	1331	5	0.2	Bedrock	Huntington et al., 2021	Marsyangdi
01TA03	84.3841	28.4752	2432	5.2	0.2	Bedrock	Huntington et al., 2021	Marsyangdi
01TA04	84.3852	28.4796	2814	7	0.2	Bedrock	Huntington et al., 2021	Marsyangdi
01TA02	84.3858	28.4715	2232	10.8	0.5	Bedrock	Huntington et al., 2021	Marsyangdi
01TA05	84.3894	28.4829	3191	7	0.1	Bedrock	Huntington et al., 2021	Marsyangdi
01DA01	84.4033	28.4916	4496	8	0.2	Bedrock	Huntington et al., 2021	Marsyangdi
01DA04	84.3944	28.4932	3770	3.1	0.1	Bedrock	Huntington et al., 2021	Marsyangdi
01DA02	84.4007	28.4952	4232	12	0.2	Bedrock	Huntington et al., 2021	Marsyangdi
01DA08	84.3695	28.5126	2440	6.8	0.1	Bedrock	Huntington et al., 2021	Marsyangdi
ArB-02-08	84.2551	28.5041	2670	14.56	0.06	Bedrock	Huntington et al., 2021	Marsyangdi
NBE-12	84.3436	28.5334	2070	6.7	0.2	Bedrock	Huntington et al., 2021	Marsyangdi
01CH04	84.2243	28.5187	4134	10.5	0.2	Bedrock	Huntington et al., 2021	Marsyangdi
NBE-8A	84.2607	28.5614	2640	17.2	0.3	Bedrock	Huntington et al., 2021	Marsyangdi
02RM18	84.2588	28.5629	2560	15.11	0.07	Bedrock	Huntington et al., 2021	Marsyangdi
02RM36	84.1967	28.5749	2520	16.44	0.06	Bedrock	Huntington et al., 2021	Marsyangdi
ArB-02-01	84.211	28.643	3095	16.37	0.06	Bedrock	Huntington et al., 2021	Marsyangdi
DH54	84.74666	28.20784	-	2.64	0.03	Bedrock	Catlos2000	Daraundi
DH51	84.72698	28.18659	-	2.8	0.3	Bedrock	Catlos2000	Daraundi
DH70	84.75532	28.22555	-	2.8	0.1	Bedrock	Catlos2000	Daraundi
DH57	84.74273	28.21886	-	3.3	0.1	Bedrock	Catlos2000	Daraundi
DH43	84.70849	28.17163	-	3.4	0.3	Bedrock	Catlos2000	Daraundi
DH64	84.76083	28.2405	-	4.4	0.1	Bedrock	Catlos2000	Daraundi
DH31	84.66048	28.10592	-	4.85	0.04	Bedrock	Catlos2000	Daraundi
DH66	84.74942	28.22948	-	5.7	0.1	Bedrock	Catlos2000	Daraundi
-	84.745	28.3473	-	6.1	0.1	Bedrock	Copeland91	Daraundi
DH39	84.6711	28.12362	-	6.28	0.03	Bedrock	Catlos2000	Daraundi
DH59	84.74627	28.22712	-	7.9	0.6	Bedrock	Catlos2000	Daraundi
-	84.5804	28.1345	-	9	0.1	Bedrock	Copeland91	Daraundi

DH34	84.67268	28.11103	-	9.2	0.1	Bedrock	Catlos2000	Daraundi
DH27	84.65942	28.091388	-	12.1	0.1	Bedrock	Catlos2000	Daraundi
DH17	84.660193	28.072739	-	12.3	0.1	Bedrock	Catlos2000	Daraundi
DH13	84.656862	28.066017	-	36.8	0.1	Bedrock	Catlos2000	Daraundi
DH2	84.61798	28.00793	-	125	1	Bedrock	Catlos2000	Daraundi
DH76	84.56918	28.00163	-	257	1	Bedrock	Catlos2000	Daraundi
-	84.6178	27.9116	-	398	0.1	Bedrock	Copeland91	Daraundi
01WBS3	84.72468112	27.97151093	-	929.5	0	Detrital	Wobus2006	Daraundi
01WBS2	84.72349139	27.95247524	-	1163	0	Detrital	Wobus2006	Daraundi
01WBS1	84.73538869	27.90726548	-	1392.5	0	Detrital	Wobus2006	Daraundi

Appendix C Zircon Fission Track (ZFT) ages

ID	Longitude	Latitude	Elevation (m)	Age (Ma)	Error (2σ)	Source	Region
FT-JP-00-03	84.3656	28.3668	2540	1.8	0.4	Blythe et al., 2007	Marsyangdi
FT-JP-00-02	84.35523333	28.37008333	2870	1.6	0.4	Blythe et al., 2007	Marsyangdi
FT-JP-00-04	84.37931667	28.37023333	2020	1.8	0.4	Blythe et al., 2007	Marsyangdi
FT-JP-00-01	84.35	28.38195	3105	1.9	0.4	Blythe et al., 2007	Marsyangdi
FT-JP-00-06	84.39498333	28.37586667	1450	0.8	0.2	Blythe et al., 2007	Marsyangdi
FT-JP-00-09	84.3948	28.4028	2170	1.8	0.4	Blythe et al., 2007	Marsyangdi
FT-JP-00-08	84.40101667	28.40296667	1850	1.2	0.2	Blythe et al., 2007	Marsyangdi

Appendix D Zircon (U-Th)/He (ZHe) ages

ID	Longitude	Latitude	Age (Ma)	Error (2σ)	Article	Region
CN16 004	85.15397200	27.85350001	5.61	0.11	Ghoshal et al., 2020	BG-Trishuli
CN16 007	85.36366601	28.24641304	1.24	0.65	Ghoshal et al., 2020	BG-Trishuli
CN16 016	85.32276199	28.14202398	1.17	0.12	Ghoshal et al., 2020	BG-Trishuli
CN16 017	85.27540701	28.08754002	1.39	0.08	Ghoshal et al., 2020	BG-Trishuli
CN16 018	85.22443104	28.06546301	1.71	0.15	Ghoshal et al., 2020	BG-Trishuli
CN16 019	85.20261596	27.99269903	2.59	0.11	Ghoshal et al., 2020	BG-Trishuli
CN16 020	85.14891403	27.92008803	3.91	0.22	Ghoshal et al., 2020	BG-Trishuli
CN16 032	84.84990598	27.85011800	5.61	0.49	Ghoshal et al., 2020	BG-Trishuli
CN16 033	84.87545100	27.88243904	5.67	0.65	Ghoshal et al., 2020	BG-Trishuli
CN16 034	84.86009502	27.94910400	4.76	1.29	Ghoshal et al., 2020	BG-Trishuli
CN16 036	84.83924001	28.11037098	2.09	0.09	Ghoshal et al., 2020	BG-Trishuli
CN16 037	84.90405601	28.31830597	1.15	0.08	Ghoshal et al., 2020	BG-Trishuli
CN16 048	84.89063901	28.26516696	0.97	0.28	Ghoshal et al., 2020	BG-Trishuli
CN16 064	84.88041703	28.17197202	1.19	0.14	Ghoshal et al., 2020	BG-Trishuli
CN16 069	84.76636103	28.03586097	3.03	2.30	Ghoshal et al., 2020	BG-Trishuli
CN16 084	84.90636103	27.56565901	7.44	0.20	Ghoshal et al., 2020	BG-Trishuli
CN16 092	84.86702803	27.56349999	7.91	4.76	Ghoshal et al., 2020	BG-Trishuli
CN16 102	85.09667398	27.52989904	8.74	0.53	Ghoshal et al., 2020	BG-Trishuli
CN16 103	85.04448197	27.49512998	7.91	0.72	Ghoshal et al., 2020	BG-Trishuli
PL3	85.09250000	27.56480000	8.42	0.36	Herman et al., 2010	BG-Trishuli
PL4	85.08780000	27.56760000	8.95	0.32	Herman et al., 2010	BG-Trishuli
PL5	85.08560000	27.56690000	9.08	0.85	Herman et al., 2010	BG-Trishuli
PL6	85.07740000	27.57030000	9.2	0.52	Herman et al., 2010	BG-Trishuli
PL7	85.08400000	27.59010000	9.46	0.76	Herman et al., 2010	BG-Trishuli
Mr-20	84.43385	27.80171	4.43	0.06	Robinson et al., 2021	Marsyangdi
Mr-17	84.40756	27.89709	5.09	0.06	Robinson et al., 2021	Marsyangdi
Mr-121	84.3972	27.95818	2.91	0.04	Robinson et al., 2021	Marsyangdi
MG-3	84.420116	27.940691	5.9	2.6	Cross, 2014	Marsyangdi
MG-14	84.555083	27.943517	4.7	0.4	Cross, 2014	Marsyangdi
MG-18	84.4588	28.023467	3.1	0.4	Cross, 2014	Marsyangdi
MG-16	84.541333	28.074467	3.1	0.4	Cross, 2014	Marsyangdi
Mr-12	84.43941	28.16397	2.25	0.04	Robinson et al., 2021	Marsyangdi
Mr-7	84.36641	28.25744	1.45	0.03	Robinson et al., 2021	Marsyangdi

Mr-4	84.39621	28.33984	0.77	0.01	Robinson et al., 2021	Marsyangdi
CN16 227	84.40263	28.421772	0.74	0.01	Ghoshal et al., 2021	Marsyangdi
CN16 225	84.357724	28.514244	0.85	0.07	Ghoshal et al., 2021	Marsyangdi
CN16 220	84.197319	28.570585	5.68	0.26	Ghoshal et al., 2021	Marsyangdi
CN16 162	84.672478	28.118175	3.18	0.45	This study	Daraundi
CN16 168	84.663911	28.108741	2.94	0.12	This study	Daraundi
MG-16	84.541333	28.074467	3.1	0.4	Cross, 2014	Daraundi
MG-14	84.555083	27.943517	4.7	0.4	Cross, 2014	Daraundi

Appendix E Apatite Fission Track (AFT) ages

ID	Longitude	Latitude	Age (Ma)	Error - 2σ (Ma)	Article	Region
KN237	85.29400000	27.96500000	2.8	2.4	Herman et al. 2010	BG-Trishuli
KN299	84.99900000	27.78100000	5	2.6	Herman et al. 2010	BG-Trishuli
KN272	85.26600000	27.49600000	4.9	1.2	Herman et al., 2010	BG-Trishuli
KN109	85.31300000	27.80100000	4.4	0.8	Herman et al., 2010	BG-Trishuli
KN100	85.35300000	27.84600000	6.1	2.8	Herman et al., 2010	BG-Trishuli
NP05.06	85.14722222	27.92002778	3.1	0.8	Robert et al. 2009	BG-Trishuli
NP05.07	85.15472222	27.92933333	3.4	1	Robert et al. 2009	BG-Trishuli
NP05.08	85.18430556	27.97488889	1.7	0.4	Robert et al. 2009	BG-Trishuli
NP05.14	85.31638889	28.14002778	0.4	0.2	Robert et al. 2009	BG-Trishuli
NP05.15	85.20277778	27.99263889	2.9	0.6	Robert et al. 2009	BG-Trishuli
NP05.17	85.12722222	27.73558333	2.1	2	Robert et al. 2009	BG-Trishuli
NP05.18	85.09916667	27.66283333	1.9	0.6	Robert et al. 2009	BG-Trishuli
NP05.20	85.08055556	27.62197222	4.7	1.6	Robert et al. 2009	BG-Trishuli
NP05.21	85.08861111	27.60533333	6.5	1.2	Robert et al. 2009	BG-Trishuli
NP05.22	85.08438889	27.59100000	7.2	0.8	Robert et al. 2009	BG-Trishuli
NP05.23	85.07305556	27.57536111	8.6	1	Robert et al. 2009	BG-Trishuli
NP05.24	85.04833333	27.55122222	5.9	1.4	Robert et al. 2009	BG-Trishuli
T6	85.20888889	28.01313889	1.4	0.6	Robert et al. 2009	BG-Trishuli
T7	85.22361111	28.06597222	1.4	0.4	Robert et al. 2009	BG-Trishuli
T9	85.31388889	28.10963889	1.4	0.6	Robert et al. 2009	BG-Trishuli
T10	85.32638889	28.10311111	1.6	0.6	Robert et al. 2009	BG-Trishuli
T11	85.33138889	28.10733333	1.4	0.8	Robert et al. 2009	BG-Trishuli
NBE-2	84.4583333	28.02455	3.8	1	Burbank et al., 2003	Marsyangdi
JP-FT-01-5	84.3050167	28.2837167	0.6	1.2	Blythe et al., 2007	Marsyangdi
JP-FT-01-4	84.2919167	28.3134333	0.9	0.6	Blythe et al., 2007	Marsyangdi
01-NL-01	84.4072333	28.3239333	1.9	2.2	Blythe et al., 2007	Marsyangdi
JP-FT-01-8	84.3589333	28.3320333	1.8	0.8	Blythe et al., 2007	Marsyangdi
NBE-4	84.4015833	28.3256333	1.9	2.2	Burbank et al., 2003	Marsyangdi
01-NL-02	84.4212333	28.3334333	0.6	0.4	Huntington et al., 2006	Marsyangdi
01-NL-03	84.4248167	28.3371333	0.5	0.4	Huntington et al., 2006	Marsyangdi
01-NL-04	84.4264667	28.3405	0.8	0.4	Huntington et al., 2006	Marsyangdi
ArB-02-14	84.26581	28.36749	0.6	0.2	Blythe et al., 2007	Marsyangdi
01-NL-05	84.4302667	28.34535	0.9	0.4	Huntington et al., 2006	Marsyangdi

01-NL-06	84.4381333	28.35275	0.8	0.8	Huntington et al., 2006	Marsyangdi
JP-FT-01-2	84.2539333	28.38285	0.8	0.4	Burbank et al., 2003	Marsyangdi
FT-JP-00-03	84.3656	28.3668	1.6	0.6	Blythe et al., 2007	Marsyangdi
FT-JP-00-02	84.3552333	28.3700833	1.9	0.8	Blythe et al., 2007	Marsyangdi
FT-JP-00-04	84.3793167	28.3702333	1.4	0.6	Blythe et al., 2007	Marsyangdi
FT-JP-00-05	84.38705	28.3714	0.9	0.6	Blythe et al., 2007	Marsyangdi
01-NL-07	84.44605	28.3621	1.6	0.8	Blythe et al., 2007	Marsyangdi
FT-JP-00-01	84.35	28.38195	2.5	1	Blythe et al., 2007	Marsyangdi
JP-FT-01-7	84.3500667	28.3821167	1.4	0.6	Blythe et al., 2007	Marsyangdi
FT-JP-00-06	84.3949833	28.3758667	0.6	0.4	Blythe et al., 2007	Marsyangdi
ArB-02-11	84.24836	28.40295	1.1	0.6	Blythe et al., 2007	Marsyangdi
FT-JP-00-07	84.4028833	28.3873667	0.7	0.4	Burbank et al., 2003	Marsyangdi
01-NL-08	84.4514333	28.38085	0.8	0.4	Blythe et al., 2007	Marsyangdi
ArB-02-12	84.27002	28.40975	0.6	0.4	Blythe et al., 2007	Marsyangdi
NBE-5	84.4051833	28.3913667	0.4	0.4	Burbank et al., 2003	Marsyangdi
FT-JP-00-09	84.3948	28.4028	1.1	0.6	Blythe et al., 2007	Marsyangdi
01-JA-07	84.413	28.4007833	0.5	0.4	Blythe et al., 2007	Marsyangdi
01-JA-01	84.4499667	28.3952	1.7	2.4	Blythe et al., 2007	Marsyangdi
FT-JP-00-08	84.4010167	28.4029667	1	0.8	Blythe et al., 2007	Marsyangdi
01-JA-08	84.4108833	28.4019167	0.3	0.2	Blythe et al., 2007	Marsyangdi
01-JA-04	84.4324	28.3986167	1	0.6	Blythe et al., 2007	Marsyangdi
01-JA-06	84.4203	28.4024333	0.5	0.4	Blythe et al., 2007	Marsyangdi
01-JA-02	84.4466333	28.3984	0.8	0.6	Blythe et al., 2007	Marsyangdi
01-JA-05	84.4299667	28.4013333	0.6	0.4	Blythe et al., 2007	Marsyangdi
FT-JP-00-10	84.3707167	28.41105	1.6	1	Blythe et al., 2007	Marsyangdi
01-JA-03	84.44195	28.40215	0.6	1	Blythe et al., 2007	Marsyangdi
01-NL-10	84.4632	28.40025	0.5	0.6	Blythe et al., 2007	Marsyangdi
01-NL-11	84.47505	28.4161833	0.9	0.8	Blythe et al., 2007	Marsyangdi
ArB-02-10	84.23903	28.409	1.2	0.4	Blythe et al., 2007	Marsyangdi
JP-FT-01-1	84.2386333	28.4104167	1.6	0.8	Blythe et al., 2007	Marsyangdi
NBE-13	84.2606667	28.4222333	0.3	0.4	Burbank et al., 2003	Marsyangdi
01-TA-04	84.3851833	28.47955	0.6	0.6	Blythe et al., 2007	Marsyangdi
01-TA-05	84.38935	28.4828667	0.5	0.2	Blythe et al., 2007	Marsyangdi
01-TA-06	84.3926667	28.48545	0.3	0.6	Blythe et al., 2007	Marsyangdi
01-DA-01	84.4032833	28.4916333	0.9	0.8	Blythe et al., 2007	Marsyangdi
01-DA-04	84.3943833	28.4932	1.7	1.2	Blythe et al., 2007	Marsyangdi
01-DA-04 peg	84.3943833	28.4932	1.1	0.6	Blythe et al., 2007	Marsyangdi
01-DA-02	84.4007	28.49515	0.6	0.6	Blythe et al., 2007	Marsyangdi
01-DA-03	84.3972	28.4945167	0.9	0.6	Blythe et al., 2007	Marsyangdi

01-DA-05	84.3862167	28.4947667	1.6	1.2	Blythe et al., 2007	Marsyangdi
01-DA-05 peg	84.3862167	28.4947667	1.1	0.6	Blythe et al., 2007	Marsyangdi
01-DA-06	84.3734667	28.5075	0.3	0.2	Blythe et al., 2007	Marsyangdi
01-DA-06 peg	84.3734667	28.5075	1.2	1	Blythe et al., 2007	Marsyangdi
01-DA-07	84.3731667	28.5099	0.5	0.6	Blythe et al., 2007	Marsyangdi
FT-1-97	84.3034167	28.4936	1.2	0.6	Burbank et al., 2003	Marsyangdi
01-DA-08	84.36945	28.5126	0.4	0.4	Blythe et al., 2007	Marsyangdi
NBE-11	84.3606833	28.5106167	0.5	0.4	Burbank et al., 2003	Marsyangdi
01-DA-09	84.3622667	28.5129167	0.1	0.2	Blythe et al., 2007	Marsyangdi
01-DA-10	84.3606	28.5157	0.3	0.2	Blythe et al., 2007	Marsyangdi
FT-2-97	84.3034333	28.5026333	0.9	0.6	Blythe et al., 2007	Marsyangdi
FT-3-97	84.30655	28.5161667	1	1	Blythe et al., 2007	Marsyangdi
NBE-9	84.3435833	28.5293833	0.9	0.6	Burbank et al., 2003	Marsyangdi
NBE-10	84.3435833	28.5332833	0.5	0.4	Burbank et al., 2003	Marsyangdi
01-CH-02	84.2272	28.5042	0.8	0.8	Blythe et al., 2007	Marsyangdi
FT-4-97	84.3208833	28.53	0	0.4	Burbank et al., 2003	Marsyangdi
01-CH-03	84.2243833	28.5100167	2.4	1.2	Blythe et al., 2007	Marsyangdi
01-CH-04	84.22425	28.5187167	0.3	0.2	Blythe et al., 2007	Marsyangdi
01-CH-01	84.2279833	28.5351167	1.5	1.2	Blythe et al., 2007	Marsyangdi
01-CH-05	84.2256167	28.5386167	0.6	0.6	Blythe et al., 2007	Marsyangdi
01-CH-06	84.2309833	28.54715	0.6	0.4	Blythe et al., 2007	Marsyangdi
NBE-8a	84.2606667	28.5613833	0.4	0.4	Burbank et al., 2003	Marsyangdi
01-CH-07	84.2324833	28.55425	0.5	0.4	Blythe et al., 2007	Marsyangdi
NBE-8	84.1965833	28.5703167	2.3	3.2	Blythe et al., 2007	Marsyangdi
ArB-02-07	84.219	28.616	0.8	0.4	Blythe et al., 2007	Marsyangdi
ArB-02-01	84.211	28.643	0.6	0.4	Blythe et al., 2007	Marsyangdi
ArB-02-06	84.23346	28.66744	1.2	0.6	Blythe et al., 2007	Marsyangdi
ArB-02-05	84.2463	28.68889	0.9	0.4	Blythe et al., 2007	Marsyangdi
ArB-02-04	84.26422	28.71889	0.5	0.6	Blythe et al., 2007	Marsyangdi
ArB-02-03	84.2601	28.71838	1.2	0.6	Blythe et al., 2007	Marsyangdi
ArB-02-02	84.26456	28.73742	0.6	0.4	Blythe et al., 2007	Marsyangdi
MR4	84.39621	28.33984	1.4	1	Robinson et al., 2021	Marsyangdi
MR12	84.43941	28.16397	1.8	0.7	Robinson et al., 2021	Marsyangdi
MR121	84.3972	27.95818	1.4	0.6	Robinson et al., 2021	Marsyangdi